UNIVERSITÀ DEGLI STUDI DI PADOVA

TÉCNICO LISBOA

Università degli Studi di Padova

Centro interdipartimentale "Centro Ricerche Fusione"

Universidade de Lisboa

Instituto Superior Técnico (IST)

JOINT RESEARCH DOCTORATE IN FUSION SCIENCE AND ENGINEERING

Cycle XXVIII

Thermo-hydraulic models and analyses for design optimization of cooling circuits and components of SPIDER and MITICA experiments

Coordinator:

Prof. Paolo Bettini

Supervisors:

Prof. Piergiorgio Sonato

Dr. Mauro Dalla Palma

Dr. Francesco Fellin

Ph.D Student: Matteo Zaupa

Padova, January 2016

<<The Stone Age did not end for lack of stone, and the Oil Age will end long before the world runs out of oil>>

Sheikh Zaki Yamani

To my family

Abstract

ITER is the next milestone towards the development of a controlled thermonuclear fusion reactor. Based on the tokamak concept, among the systems used to heat the plasma, the Neutral Beam Injector (NBI) plays a fundamental role. The particle energy levels up to 1 MeV, the heating power to deliver to the plasma up to 16.5 MW and the steady state condition up to 3600 s, have never been simultaneously achieved before in such kind of device. A Neutral Beam Test Facility has been realised in Padova (Italy) at Consorzio RFX in order to host two experiments (SPIDER and MITICA) and solve the scientific and technological gaps.

The research activity presented in this thesis work has been carried out in the framework of the development of the ITER full scale negative ion source (SPIDER) and of the full injector prototype for the ITER neutral beam (MITICA).
The thesis is focused on two main topics: development of thermo-hydraulic one-dimensional models with 3D sub-modelling, and customization of a finite element code for coupled 1D-3D thermo-hydraulic analyses.

Proper models of the MITICA beam source, neutraliser and residual ion dump cooling systems have been developed since they are required, in support of the design, in order to predict under steady state conditions the flow partitioning, the coolant temperatures and pressure drops in complex and delicate pipework networks; all these results are useful, as boundary conditions, for further detailed simulations oriented to the localised heat transfer coefficients. The hydraulic behaviour of the components have been simulated both with analytical models and detailed 3D computational fluid dynamics (CFD) analyses. The optimised cooling circuits have been proposed and then implemented for the construction of the MITICA components.

The coupled 1D-3D thermo-hydraulic analyses have been dedicated to the SPIDER beam dump (already procured) made of CuCrZr hypervapotrons as high heat flux elements. Suitable correlations for localised heat transfer coefficients and pressure drop for forced-convection and sub-cooled surface boiling in hypervapotron geometry have been implemented in a new customised FE code to allow coupled thermo-hydraulic analyses in two-phase heat transfer. The customized code has been used to carry out detailed simulations of the local heat transfer mechanisms occurring along the cooling channels under different particle beam scenarios (in terms of divergence, halo fraction and horizontal misalignment). A synthesis of the simulation results has been undertaken by identifying in the model the locations of the thermocouples used during operations. The analysis results characterise the thermo-hydraulic behaviour of the beam dump to be used as a possible beam diagnostic in synergy with tomography and spectroscopy.

Riassunto

ITER costituisce la prossima tappa verso lo sviluppo di un reattore a fusione termonucleare. Basato sul concetto tokamak, utilizza diversi sistemi di riscaldamento per il plasma, tra questi sistemi l'iniettore di fascio di neutri gioca un ruolo fondamentale. Il livello di energia delle particelle fino a 1 MeV, la potenza di riscaldamento da rilasciare al plasma fino a 16.5 MW e l'operatività in condizioni stazionarie fino a 3600 s, non sono mai state simultaneamente raggiunte in macchine di questo tipo. Una Neutral Beam Test Facility è stata realizzata a Padova (Italia) presso il Consorzio RFX al fine di ospitare due esperimenti (SPIDER e MITICA) e colmare le lacune scientifiche e tecnologiche.

L'attività di ricerca presentata in questo lavoro di tesi si inserisce nel contesto dello sviluppo di una sorgente a ioni negativi delle dimensioni pari a quelle richieste per ITER (SPIDER) e al prototipo di iniettore di fascio di neutri per ITER (MITICA).
La tesi è focalizzata su due argomenti principali: sviluppo di modelli termo-idraulici uno-dimensionali con sotto-modelli 3D, e l'adattamento di un codice agli elementi finiti per svolgere analisi termo-idrauliche accoppiate 1D-3D.

Sono stati sviluppati appropriati modelli per i circuiti di raffreddamento di MITICA beam source, neutraliser, e residual ion dump in quanto necessari, in supporto alla progettazione, al fine di predire la distribuzione delle portate, le temperature e le cadute di pressione; tali risultati risultano particolarmente utili per successive analisi dettagliate orientate al calcolo del coefficiente di scambio termico locale. Il comportamento idraulico dei componenti è stato simulato sia con modelli analitici, che attraverso simulazioni CFD dettagliate. I circuiti di raffreddamento ottimizzati sono stati adottati per la realizzazione dei componenti di MITICA.

Le analisi termo-idrauliche accoppiate 1D-3D sono state svolte per il componente SPIDER beam dump costituito di hypervapotron, realizzati in lega di CuCrZr, come elementi di scambio termico. In un nuovo codice agli elementi finiti sono state implementate opportune correlazioni per il coefficiente di scambio termico locale e per la perdita di pressione in regimi di convezione forzata ed ebollizione nucleata con vena fluida sottoraffreddata. L'adattamento di tale codice ha permesso di svolgere simulazioni dei diversi meccanismi di scambio termico che si verificano lungo i canali di raffreddamento con differenti scenari di fascio (in termini di divergenza, frazione di halo e disallineamento orizzontale). Una sintesi dei risultati è stata svolta identificando nel modello la posizione delle termocoppie usate durante le operazioni. I risultati caratterizzano il comportamento termo-idraulico del beam dump come possibile diagnostica di fascio in sinergia con tomografia e spettroscopia.

Index

Chapter 1
Fusion and NBI

Environmental concerns and limited energy resources appear today as one of the most challenge for the human kind. Energy from nuclear fusion could represent an innovative way for the electricity production being sustainable, greenhouse gases free, intrinsically safe, with abundant fuel resources and without nuclear waste burden for future generations.

Far from being commercially available, the international community is focused on the research. In particular the nuclear fusion obtained by magnetic fields, to confine an ionized gas in a vacuum chamber of toroidal shape, is one of the most promising concepts for a future fusion reactor.

The first part of this chapter is dedicated to a short introduction of nuclear fusion and the ITER project, while the aim of the second part is given an overview of the ITER Neutral Beam Test Facility named PRIMA.

1.1 Thermonuclear fusion

Nuclear fusion is the reaction between two light nuclei that fuse into a heavier one, releasing energetic reaction products.
For the production of nuclear energy three reactions that involve hydrogen isotopes (deuterium and tritium) and helium-3 may be advantageous.
The most promising fusion reaction is:

$$D + T \rightarrow He^4\ (3.5MeV) + n\ (14.1MeV) \qquad \text{Eq. 1}$$

This reaction involves the fusion of a deuterium nucleus with a tritium nucleus and produces a high-energy neutron and a 3.5 MeV alpha particle. Because of tritium does not exist in nature, it has to be produced in the nuclear reactor from lithium by:

$$Li^6 + n \rightarrow He + T + 4.8\ MeV$$
$$Li^7 + n \rightarrow He + T + n - 2.5\ MeV \qquad \text{Eq. 2}$$

The reason the D-T reaction is preferred to other reactions is shown in in Figure 1-1 where the cross sections as function of the deuteron energy is reported: its cross-section is considerably higher compare to the other reaction, except at impractically high energy.

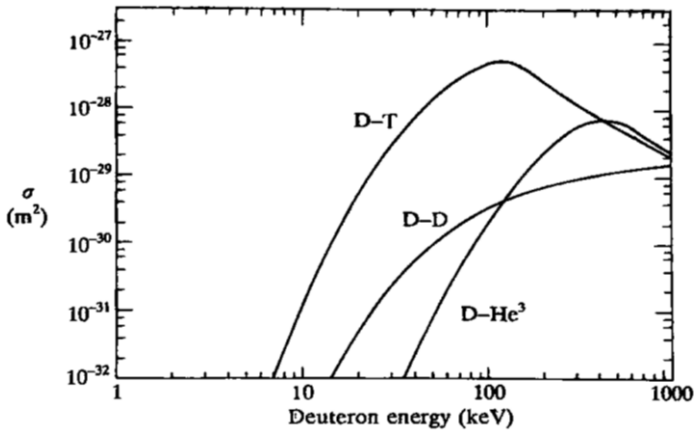

Figure 1-1 Cross-sections for the reactions D-T, D-D and D-He3 [1]

Fusion research is split in two main branches: magnetic and inertial confinement. Since this thesis work is devoted to some analyses and design of the Neutral Beam Injector for a fusion machine based on magnetic confinement, just this technology will be briefly described.

Tokamak (a Russian acronym meaning “toroidal chamber with magnetic coils”) is the most promising candidate for producing controlled thermonuclear fusion power. This kind of device is essentially made of a toroidal vacuum chamber surrounded by a set of coils (Figure 1-2). The plasma is confined by using a strong magnetic field created by the toroidal coils around the vacuum vessel. Achieving a stable plasma equilibrium requires magnetic field lines that move around the torus in a helical shape. Such a helical field can be generated by adding a poloidal field, created by a toroidal electric current that flows inside the plasma, to the toroidal one. This current is induced inside the plasma by a central solenoid.
Additional poloidal field coils are used mainly for the plasma shaping and stability.

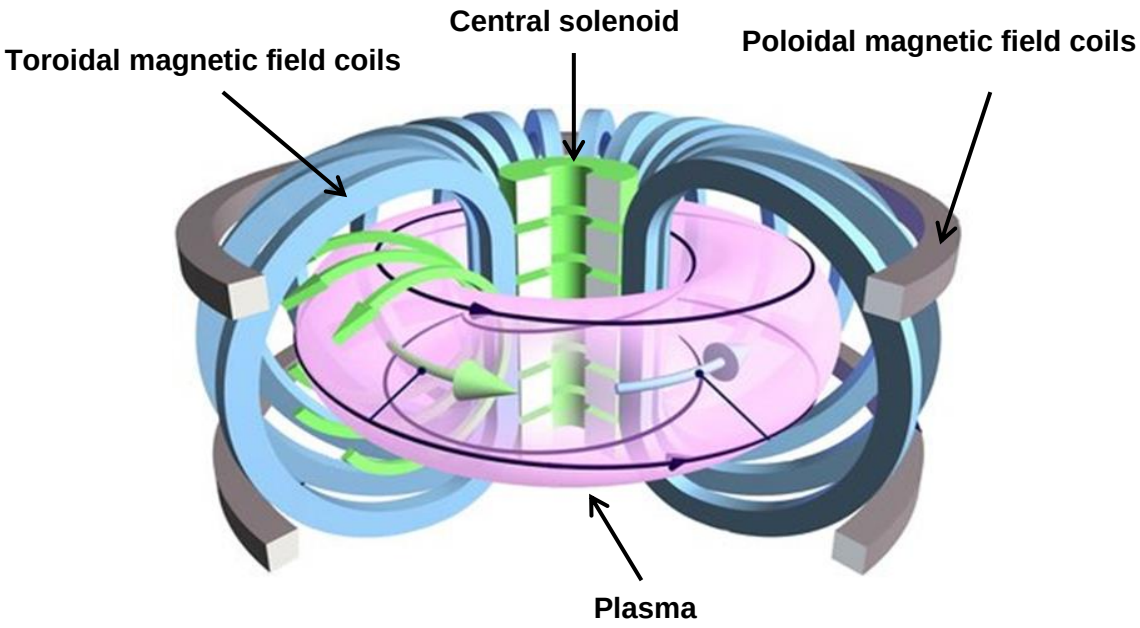

Figure 1-2 General sketch of a Tokamak device

The balance of a fusion reactor is given by:

$$\frac{\partial W}{\partial t} = P_R + P_H - P_L \qquad \text{Eq. 3}$$

where W is the plasma energy density ($W \sim 3nT$ by assuming equals the ion and the electron density and temperature), P_R is the power per unit volume produced by the fusion reactions, P_H the auxiliary heating per unit volume and P_L the power loss per unit volume.

Ignition is defined as the condition wherein the heating of the plasma given by the fusion reactions is sufficient to replace the energy losses without using external heating. It can be calculated considering that must be $P_R \geq P_L$, the result is known as Lawson criterion [2] or triple product:

$$n\tau_E T \geq 3 \times 10^{21} [m^{-3} keV\ s] \qquad \text{Eq. 4}$$

The triple product gives the requirements in terms of plasma density (n), temperature (T) and confinement time (τ_E) in order to have a burning plasma.

In Figure 1-3 the values of the triple product achieved in the most important tokamak experiments are mapped. It is possible to find out the progress toward the ignition and how in the last decades the research have produced more and more encouraging results. The last step, proving the nuclear fusion feasibility, is missing and ITER could help in discovering this region.

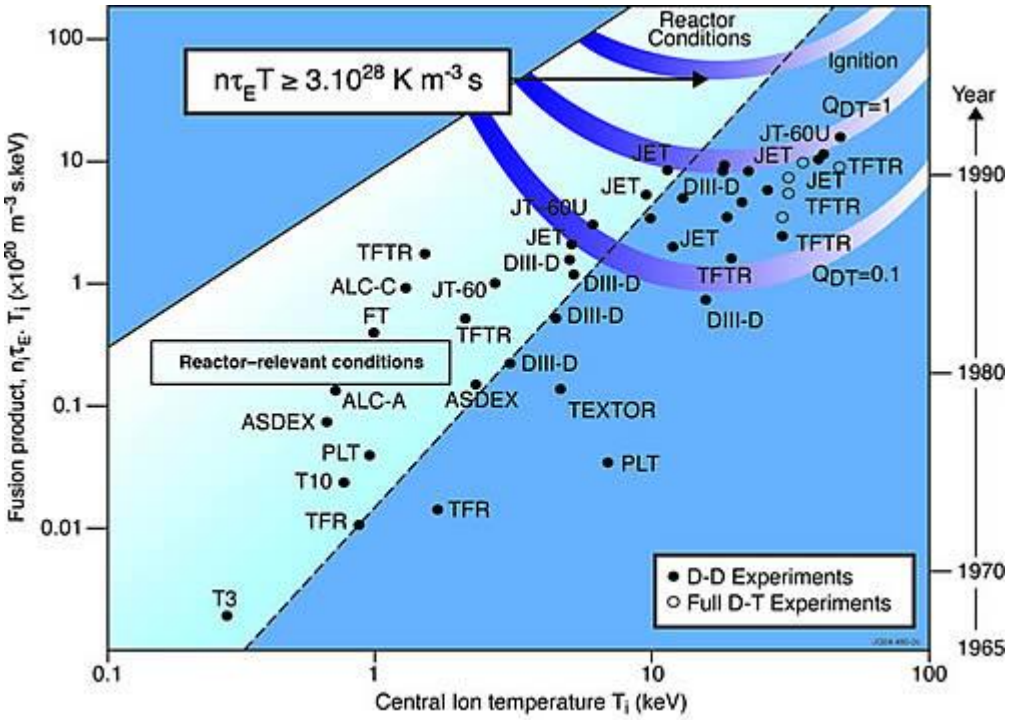

Figure 1-3 **Triple product as a function of ion temperature for different tokamak experiment and for D-T reactions**

1.2 ITER

ITER is the next milestone towards the development of a reactor based on the controlled thermonuclear fusion reactions.
In Cadarache (France), 35 nations are collaborating to build the world's largest tokamak, designed to prove the feasibility of fusion as a large-scale. The ITER project is an agreement between seven international parties: European Union, United States of America, China, South Korea, Japan, India and Russian Federation.

ITER will be the first fusion device to produce net energy and maintain fusion for long periods of time.
The experimental campaign that will be carried on this device is crucial to advancing fusion science and preparing the way for the fusion power plants of tomorrow. With ten times the plasma volume of the largest machine operating today, ITER would offer the possibility of studying new physical regimes and technological issues allowing to make a straightforward step towards the demonstration of a nuclear fusion power plant.

The main technical data and parameters of the ITER experiment are listed in Table 1-1. ITER has been designed to produce 500 MW of thermal fusion power from 50 MW of input power with an amplification factor *Q* (the ratio between the power produced by the fusion with respect to the external power supplying the reactor) of 10. As first of all fusion experiments in history to produce net energy gain, the electricity production is not foreseen. Scientists are confident that the plasmas in ITER will not only produce much more fusion energy, but will remain stable for longer periods of time achieving a deuterium-tritium plasma in which the reaction is sustained through internal heating.
Another mission of the device is to prove the feasibility of producing tritium within the vacuum vessel. The world supply of tritium (used with deuterium to fuel the fusion reaction) is not sufficient to cover the needs of future power plants. ITER will provide a unique opportunity to test mockup in-vessel tritium breeding blankets in a real fusion environment.

A cutway of ITER is shown in Figure 1-4 with the indication of the main components. Starting from the outside the stainless steel cryostat (about 29 m x 29 m) ensures a vacuum and cold environment, and surrounds the vacuum vessel and the superconducting magnets. It is used also to protects the reactor from external damages. Ten thousand tonnes of superconducting magnets will produce the magnetic fields to initiate, confine, shape and control the plasma. The stainless steel vacuum vessel allows the vacuum environment and acts as a first safety containment barrier. The blanket shields the interior part of the steel vacuum vessel and the external components from the heat load and high-energy neutron fluxes produced during the fusion reactions. On the bottom side of the vacuum vessel the divertor has the main functions of withstands the highest heat flux of the machine and control the exhaust of waste gas and impurities from the reactor. Three kind of auxiliary heating system are foreseen: neutral beam injectors, ion cyclotron antenna and electron cyclotron antenna. The maximum total power that these systems will supply is 73 MW: 33 MW from the neutral beam injectors (two NBIs - each one delivering a deuterium beam of 16.5 MW with particle energies of 1 MeV - are currently foreseen for ITER), 20 MW from the ion cyclotron antenna and 20 MW from the electron cyclotron antenna.

Table 1-1 Main ITER parameters

Total fusion power	500 MW
Amplification factor Q	~10
Plasma inductive burn time	≥400 s
Plasma major radius (R0)	6.2 m
Plasma minor radius (r)	2.0 m
Plasma current (Ip)	15 MA
Safety factor (q)	3
Toroidal magnetic field (B)	5.3 T
Electron density (ne)	$1020m^{-3}$
Average ion temperature <Ti>	8.0 keV
Average electron temperature <Te>	8.8 keV
Plasma total external heating	~ 50 MW
Neutral Beam Injector	33 MW
Electron cyclotron antenna (170 GHz)	20 MW
Ion cyclotron antenna (50 MHz)	20 MW
Plasma type	deuterium-tritium
Plasma volume	840 m

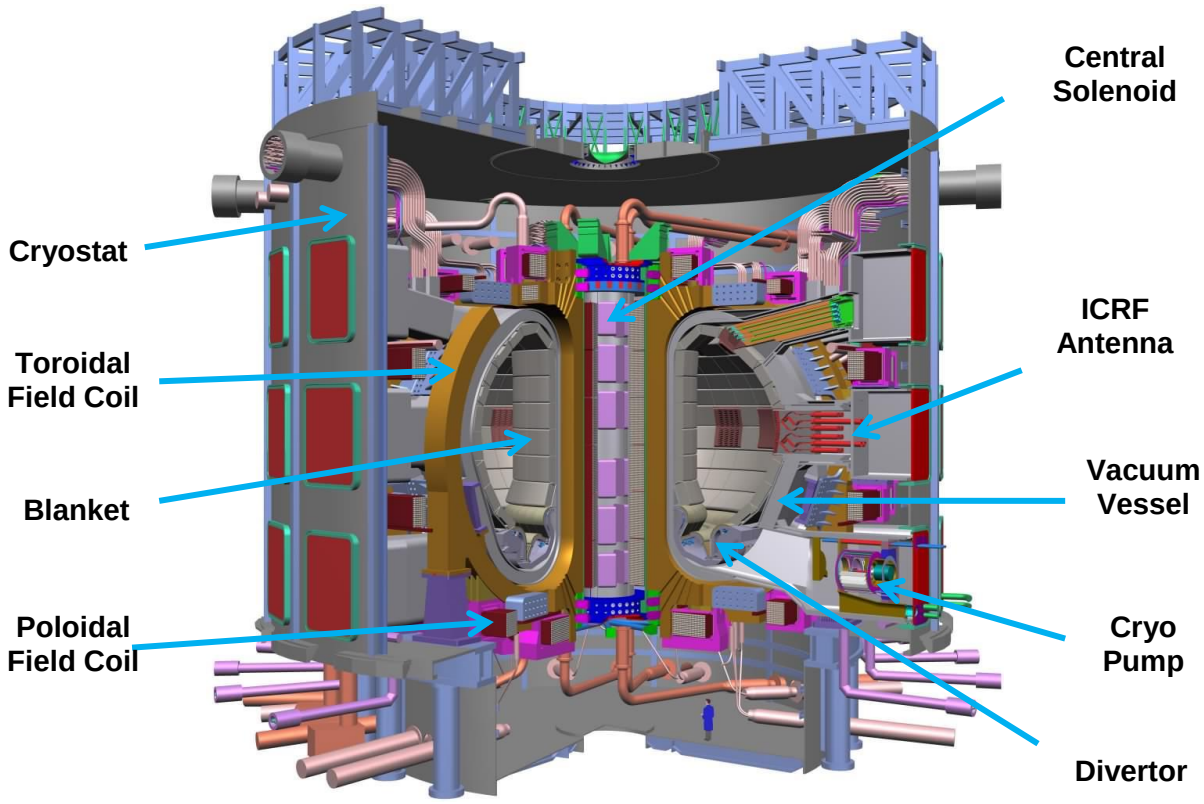

Figure 1-4 3D cutaway model of ITER

1.3 NBI for fusion

The main function of the NBI is to inject uncharged high-energy particles into the plasma where, by means of collisions, they transfer their energy to the plasma particles and increase the global temperature.
In the ASDEX tokamak (in 1982), the injection of such beams caused spontaneous transition to a regime (called *H-mode*) characterised of an enhanced confinement with a transport barrier at the plasma edge [3]. Moreover, the NBI system is also capable to increase the efficiency of the current drive (essential for study advanced scenario in ITER).

Only neutral particles can be injected in the plasma, otherwise the electrically-charged ions would be deflected by the strong magnetic field around the machine. In order to accelerate these particles to the required energy before the injection, an indirect way has to be follow: in principle positive or negative ions has to be generated; then they have to be accelerated trough grids at different voltages; at this point, ones the ions have the right energy is possible to neutralise them by using a neutral gas stripper in which charge exchange processes occur; the resulting beam is then filtered in a residual ion dump by using electric field to deflect the ions which did not get the neutralisation; finally the neutral beam can be injected in the plasma. As the neutrals enter the plasma, they are quickly ionized and remain trapped by the magnetic field of the device.

Even if NBIs have been extensively used in the past fusion machines, the large plasma volume of ITER imposes new requirements: in order to penetrate far enough into the plasma the particles must move three to four times faster than in previous systems. The beam power has to be deposited inside the so-called *H-mode* barrier (located between $0.9 < r/a < 1$, where r is the distance from the plasma centre and a is the minor radius of the plasma). For ITER this means that the ions energy must be >300 keV.

The ions created in the source can be either positive or negative, but as shown in Figure 1-5, only NBI based on negative ions can be used in the perspective of a highly energetic beam.

ITER will use two NBIs to inject 33 MW of either 1 MeV deuterium (D^0) or 870 keV Hydrogen (H^0) into the plasma. A third heating beam may be added later.
A different neutral beam will be used for diagnostic purposes (DNB).

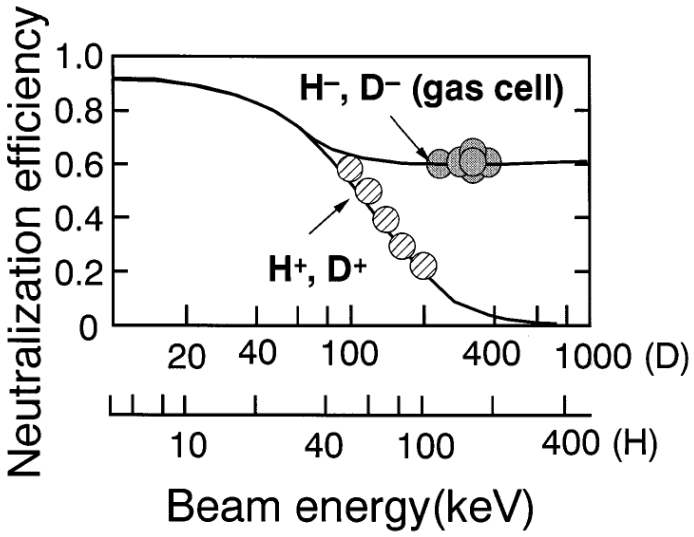

Figure 1-5 **Hydrogen ions neutralisation efficiency as a function of energy, measured in the NBIs at JT-60U [4]**

1.4 PRIMA Test Facility

As the required technology for the ITER NBIs is well beyond to the present performance for similar systems, it has been decided to build a new test facility to solve the scientific gap.
This ITER Neutral Beam Test Facility, named PRIMA (Padova Research on ITER Megavolt Accelerator), is under construction in Padova (Italy).

PRIMA will be host two experimental devices (and all the auxiliary systems): SPIDER and MITICA.
SPIDER is a full size plasma source with low voltage extraction and MITICA a full size neutral beam injector at full beam power.

The buildings are already realised and they have been erected in the National Research Council (C.N.R.) area of Padova, close to the 380 kV power station which already supplies the existing RFX machine. The project insists on an area of 17500 m^2 and the floors covered by the building are approximately 7000 m^2.

In Figure 1-6 a cutway of the main building with the two experiment is given.

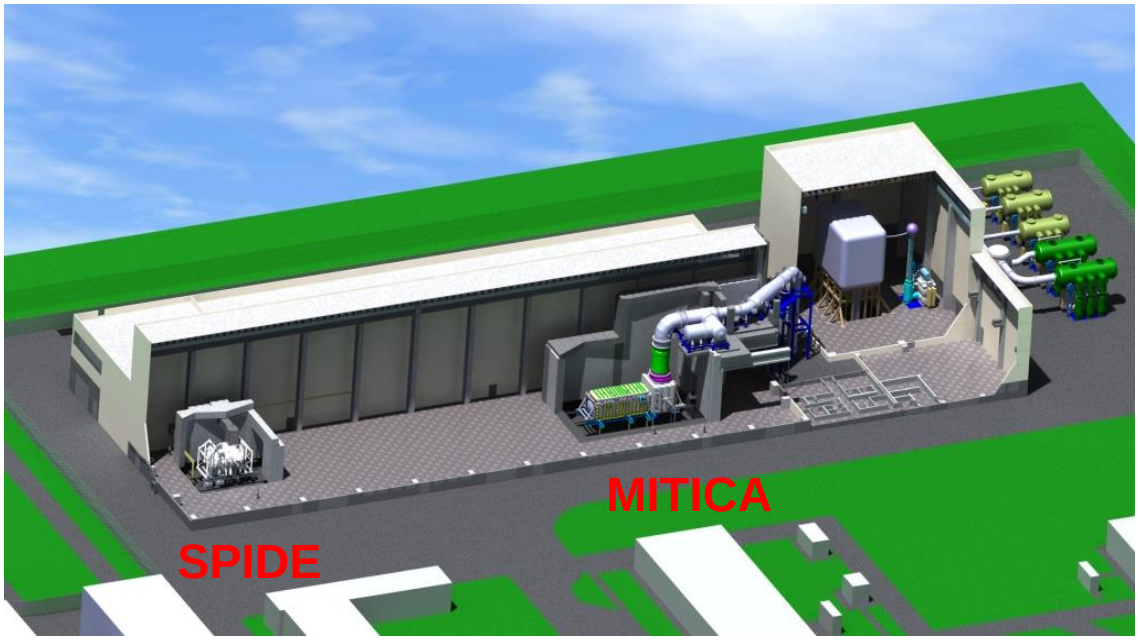

Figure 1-6 Cutway of the PRIMA buildings with a view of the two experiments

The buildings layout is shown in Figure 1-7, three different main buildings are recognizable.

The first building group consist of:

- a main room (1) in which the two devices will be placed within the concrete bunkers (1.02 and 1.03) to shield the neutron fluxes. This room covers a surface of 3000 m^2. A crane of 50 tons of capacity will allow the movements of the components and neutron shielding concrete beams and block. Between the two devices a wide free space (~ 1000 m^2) is foreseen to storage materials, to

assembly the components and to perform site acceptance tests on the components.

- In the rooms (2) and (4) the auxiliary systems for cooling, cryogenic and vacuum are installed. Two cranes (10 tons each) have been foreseen.
- The electric power supplies, the transformers, the switchboards and the diagnostic and control systems for SPIDER will be located in the room (6).
- In the room (7) other conventional systems, like buildings power supplies and HVAC plants, are foreseen.

The second building group (entirely dedicated to MITICA) is made of the room (8) where the -1 MV shielded deck, containing power supply systems and other devices set at -1 MV voltage to ground, will be placed, and room (3) for other electric supply systems at reduced voltage.

The last building (12) connects the previous buildings and contains the central control rooms of both the experiments, meeting rooms and server room.

In the external area there are the MITICA acceleration grid power supply (A) (five transformers from -200 to -1000 kV), the underground -1 MV transmission line (G), and two underground water basins for the cooling plant (F).

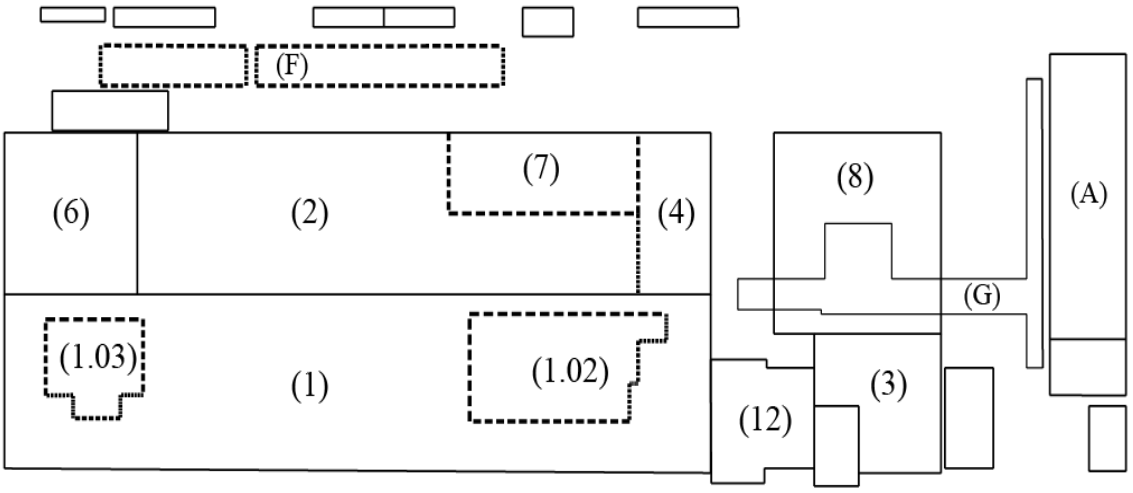

Figure 1-7 PRIMA buildings layout

1.4.1 SPIDER

SPIDER (Source for Production of Ion of Deuterium Extracted from RF plasma) is the full scale ITER NBI source. The aim of this experiment is to address the ITER performance requirements in terms of current density, current density uniformity, limitation of the electron/ion ratio and low source pressure, for the whole operating time (up to 1 hour). The operations on SPIDER are foreseen about 2.5 years before MITICA will start to operate.
An overview of the device is given in Figure 1-8.

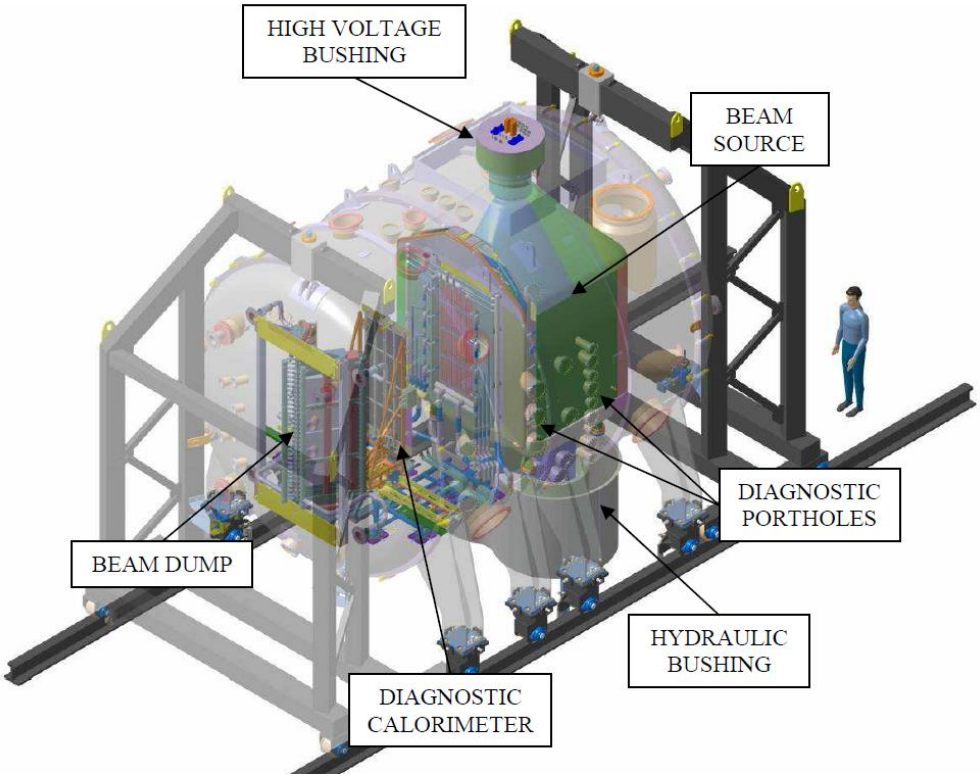

Figure 1-8 Overview of the SPIDER experiment

As SPIDER is focused on the ion source optimisation and not on the entire NBI aspects, it has been designed to accelerate the beam only up to 100 keV, with a total power of 6 MW [5]. It is equipped with eight RF drivers, followed by a plasma expansion chamber and an ion extraction region [5] (see Figure 1-9).

In the driver coils, fed with 1 MHz RF current, the electrons become sufficiently energetic (15-30 eV) to cause collisional ionization and dissociation of the injected gas (hydrogen or deuterium). The results is a plasma mainly constituted by the species e^-, H, H_2, H^+, H_2^+ (and the analogous for deuterium). In the expansion region the electrons are cooled down by a magnetic filter field (produced by a current vertically running through the Plasma Grid itself).
In the expansion chamber, the production of the negative ions is made by the volume processes and surface processes [6]. The surface process dominate: negative ion

production is mainly due to the presence of atomic neutrals which combine with electrons, mostly at the cesiated surface of the Plasma Grid.
The extraction and accelerator system for the SPIDER ion source is composed of three grids: the plasma grid (PG), the extraction grid (EG) and the grounded grid (GG). Each grid is 1600 mm high and 800 mm wide.
The negative ions beamlets are extracted through 1280 apertures: 16 groups that are, in pairs, faced to a single driver; each group has 16 rows and 5 columns of beamlets. Upstream of the PG, a copper bias plate (BP) guarantees the same reference potential all around each beamlet group. The acceleration grid (EG) is biased at 10 kV with respect to the PG. The grounded grid (GG), further downstream, will provide the ions with the last acceleration step of 90 kV.

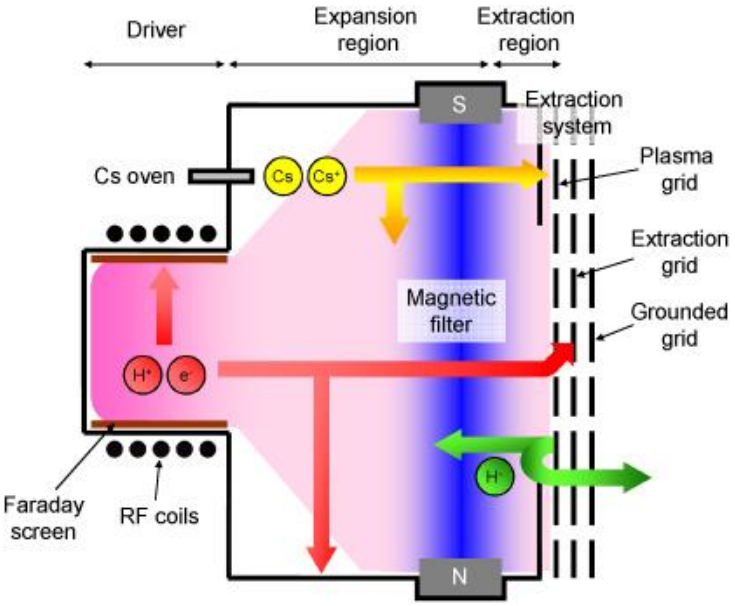

Figure 1-9 Scheme of a RF plasma source

The mission of the SPIDER experiment is to demonstrate the capability of the ion source to guarantee the extraction of a beam energy of 100 keV with a current density of 350 A/m^2 in case of hydrogen and 290 A/m^2 in case of deuterium. The beam shall be well uniform and the number of electrons with respect to the number of ions extracted from the source shall be limited to less than 1. The maximum beam source pressure shall be lower than 0.3 Pa.
The SPIDER nominal parameters are reported in Table 1-2 and an exploded view is given in Figure 1-10

Table 1-2 SPIDER nominal parameters

SPIDER	H	D	Unit
Beam energy	100	100	keV
Extracted current	70	50	A
Extracted current density	>350	>290	A/m^2
Uniformity	±10	±10	%
Maxiumum Beam Source pressure	<0.3	<0.3	Pa
Beam-ON time up to	3600	3600	s
Co-extracted electron fraction (e^-/H^- or e^-/D^-)	<0.5	<1	

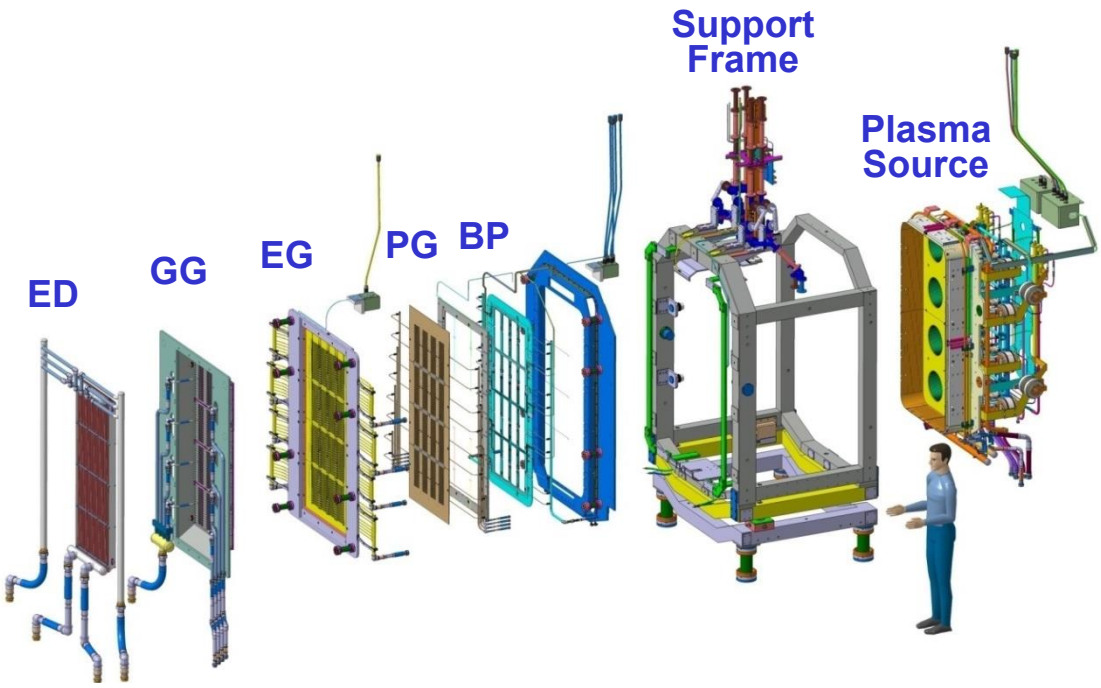

Figure 1-10 Exploded view of the SPIDER beam source

1.4.2 MITICA

MITICA (Megavolt ITER injector & Concept Advancement) is the full scale prototype for the ITER heating neutral beam injector [7].
The injector has been designed to deliver about 16.5 MW neutral beam of deuterium/hydrogen particles obtained from a precursor beam of negative ions accelerated to 1 MeV.

MITICA share the same Ion Source (made of the Plasma Source, the Bias Plate, the Plasma Grid and the Extraction Grid) of SPIDER [8]. The difference in the Ion Source between the two experiments is given by the hydraulic connections: to allow a higher flexibility to possible modifications, flanged connections are foreseen for SPIDER while welded connections are mandatory for MITICA. The other difference is the accelerating grid system of the extracted beam.

The ion source is held at −1 MV, thus the ions are accelerated up to ground potential by five different grids at different potential (by steps of 200 kV between each grid couples). The system made of the five accelerating grids is named Accelerator. The composition of the ion source and the accelerator is called Beam Source.
At the end of the accelerator the beam passes through the neutraliser and electron dump (NED) in order to generate a neutral beam. The NED is constitute of four vertical channels where the collision of the negative ions with the cloud of hydrogen/deuterium gas leads not only the formation of neutral particles but also positive and negative ions due to different processes like simple stripping of the outer electron, double stripping and re-ionization.
Following the neutraliser the beam passes through the residual ion dump (RID) which acts as an electrostatic field deflecting the undesired charged particles onto a set of plates.
Finally the neutral beam dumps onto the calorimeter made of two panels arranged in a V-shape. In the ITER NBI, the calorimeter will be opened to allow the beam to reach the plasma inside the tokamak passing along the duct line.
Large cryopumps are placed on each side of the beam path and the beamline components (neutraliser, residual ion dump and calorimeter) inside the injector to reduce the pressure downstream of the accelerator and downstream of the neutralizer exit. The pressure downstream of the accelerator must be low in order to minimize losses in the accelerator. The pressure downstream of the neutralizer must be low in order to minimize re-ionization of the neutral particles by collision with the background gas.

An exploded view of MITICA is shown in Figure 1-11, while Table 1-3 listed the nominal parameters of the injector.

Table 1-3 MITICA nominal parameters

MITICA	H	D	Unità
Neutral beam power	16.5	16.5	MW
Beam energy	870	1000	keV
Acceleration current	49	40	A
Maximum Beam Source pressure	<0.3	<0.3	Pa
Beamlet divergence	≤7	≤7	mrad
Beam-ON time up to	3600	3600	s
Co-extracted electron fraction (e^-/H^- or e^-/D^-)	<0.5	<1	

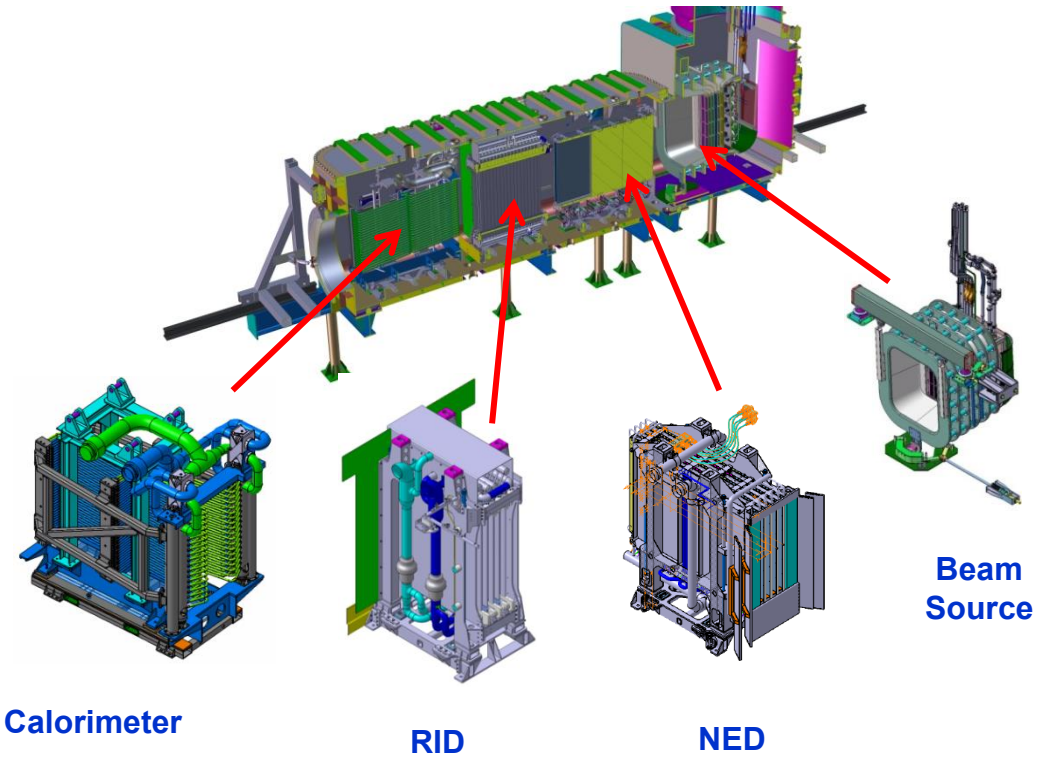

Figure 1-11 Exploded view of MITICA with the relevant components

1.4.3 Coolant supply and requirements

A large amount of thermal power (up to 70 MW) has to be removed from the in-vessel components and from the auxiliary systems of the two experiments. A large cooling plant has been designed [9] and is now under construction at PRIMA site.

The cooling plant (sketched in Figure 1-12) is composed of three main heat transfer systems exchanging the thermal power between them, the experimental test facilities and the environment. The Primary Heat Transfer System (PHTS) is made of ten closed primary circuits (PC) directly connected to the test facilities for cooling, thermal control and calorimetric purposes. They are filled with pure water (acting as dielectric fluid) because of the high voltages in some components.
The two Secondary Heat Transfer System (SHTS) exchange the thermal power between the primary circuits and the water basins. They are filled with normal water allowing a significant reduction of the PHTS circuits extension, and they also act as a safety barrier. The Tertiary Heat Transfer System (THTS) are hydraulic circuits that transfer the thermal power from the water basins to the environment via cooling towers and dry coolers.

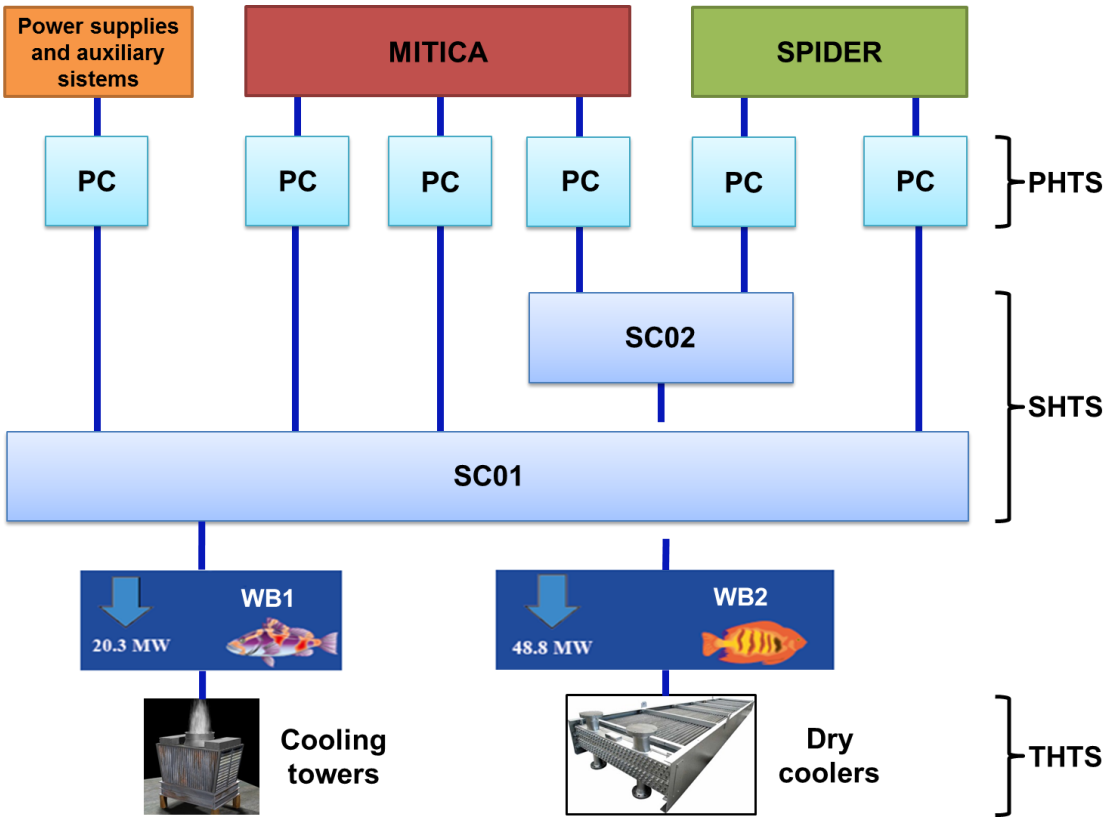

Figure 1-12 Sketch of the PRIMA cooling plant

The cooling plant has been designed in order to work with variable heat loads but keeping the inlet temperature of the coolant constant by using variable speed pumps and two-way valves to regulate the flow rates.
Two water basins (WB) are present in the cooling plant to store large amount of thermal energy. The capacities of the basis are 315 m^3 for the WB1 and 545 m^3 for the WB2. They allow a significant reduction of the installed active power of heat rejection: 6 MW of cooling towers and 17 MW of air coolers compared to 70 MW of the total thermal loads (11 MW from SPIDER and 58.4 MW from MITICA).

The cooling plant has been designed taking in account two different operative scenarios [9]: the first one (ITER-like scenario, to test the full NBI performance) foreseen two long pulses of 3600 s each one at the maximum power for MITICA only (Figure 1-13), while in the second one (typical experimental scenario) MITICA and SPIDER are foreseen two work both in parallel with ten pulses of 300 s each one during the entire day (Figure 1-14).

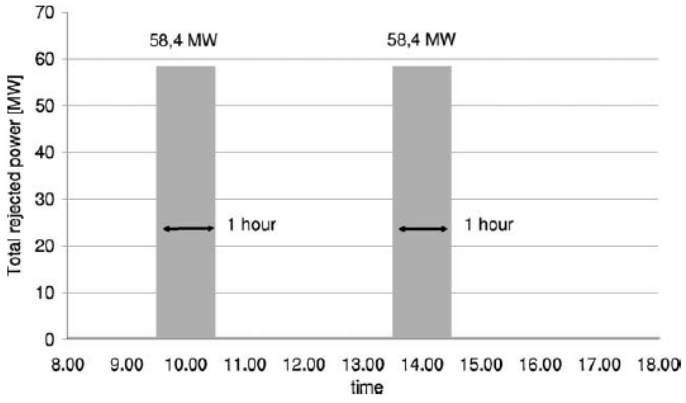

Figure 1-13 MITICA full power long pulses

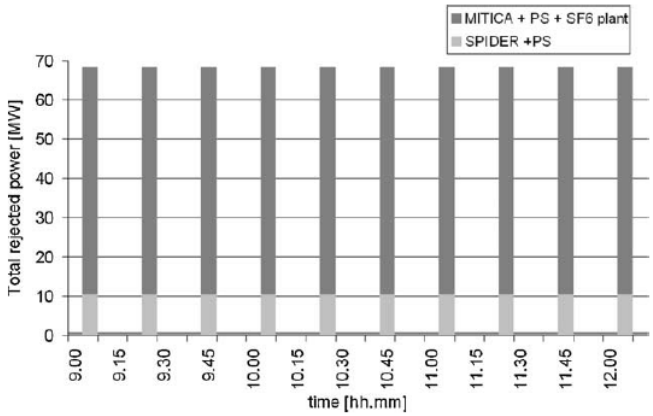

Figure 1-14 SPIDER and MITICA simultaneous operations

Two independent Chemical Control Systems (CCS) based on ultrafiltration, reverse osmosis and electro-deionisation allow water treatment and filtration providing the following pure water type:

- water W-I, with electrical resistivity between 5 and 10 MΩ•cm at 25 °C for the MITICA component (beam source and accelerator)
- water W-II, with electrical resistivity between 1 and 2 MΩ•cm at 25 °C for the MITICA ground potential components and for the SPIDER components (except beam source);
- water W-III, with electrical resistivity between 3.3 and 5 MΩ•cm at 25 °C for the SPIDER and MITICA ion source power supplies;
- water DW, with electrical resistivity between 0,05 and 0,1 MΩ•cm at 25 °C for the MITICA SF6 plant.

The main thermo-hydraulic parameters for the in-vessel components are listed in Table 1-4 for SPIDER and in Table 1-5 for MITICA. For simplicity the same parameters for the primary circuits linked with the power supplies and auxiliaries are not reported.
These parameters, in particular the mass flow rate, the inlet temperature and pressure, constitute the main boundary conditions for the following analyses.

Table 1-4 Thermo-hydraulic requirements for the SPIDER in-vessel components
(+) 40 kW and 80 kW are the powers of the instantaneous heater [10]

Primary Circuit	***Component***	***Max power [kW]***	***Mass flow rate [kg/s]***	***T_{inlet} [°C]***	***P_{inlet} [MPa]***	***Fluid***
PC02	RF coils	25	0.5	20÷35	2.0	W-II
	Extraction grid	1000	11	20÷35		
	Grounded grid	700	8	20÷35		
	Electron Dump	1000	31	20÷35		
PC03	Faraday shields lateral wall 1	240	2.5	35÷45	2.0	W-II
	Faraday shields lateral wall 2	240	2.5	35÷45		
	Faraday shields back plate	73	2	35÷45		
	Driver Plates	160	3	35÷45		
	Source case lateral wall	100	2	35÷45		
	Bias plate	10 +40 (+)	0.125	35÷150		
	Plasma grid	20 +80 (+)	0.125	35÷150		
PC04	Beam dump	6100	64	20÷55	1.0	W-II

Table 1-5 Thermo-hydraulic requirements for the MITICA in-vessel components
(+) 120 kW is the power of the instantaneous heater [10]

Primary Circuit	***Component***	***Max power [kW]***	***Mass flow rate [kg/s]***	***T_{inlet} [°C]***	***P_{inlet} [MPa]***	***Fluid***
PC05	Grid 1 MAMuG (-800 kV)	2000	19.5	25÷45	2.0	W-I
	Grid 2 MAMuG (-600 kV)	2000	19.5	25÷45		
	Grid 3 MAMuG (-400 kV)	2000	19.5	25÷45		
	Grid 4 MAMuG (-200 kV)	2000	19.5	25÷45		
	Grounded grid + frame	2000	19.5	25÷45		
PC06	RF coils	2595	33	35÷45	2.0	W-I
	Faraday Shields Source Case					
	Extraction grid					
	Plasma grid and bias plate	30 +120 (+)	0.25	35÷150		
PC07	NED	6000	80	20÷55	2.0	W-II
	RID	17200	100	20÷55		
	Calorimeter	19460	100	20÷55		

Chapter 2
Thermo-hydraulic 1D models with 3D sub-modelling

The high heat fluxes on the accelerating grids due to stray particles, the temperature control required for optimal caesium deposition on plasma grid and plasma source walls, the highly concentrated load on the back plate due to back streaming ions, and the delicate RF drivers, make the MITICA beam source a very challenging system in which the correct predictions of the flow rate partitioning and coolant temperature are mandatory. The beam line components also deal with severe heat loads, high coolant temperature and pressure, thermal control of bulk materials and surfaces. By using one-dimensional models, several steady state thermo-hydraulic simulations have been carried out to analyse and evaluate possible modifications of the cooling circuits.

2.1 One-dimensional model

In fusion machines one of the most challenging issue, from an engineering point of view, is the reliability of the components faced to the plasma and to the particle beam. The high heat fluxes and power densities they are subjected to, make the cooling capability of these components one of the crucial aspects during the design phase.
Thermo-hydraulic analyses are thus essential to design actively cooled components and relevant cooling circuits that ensure the correct flow rate, coolant temperature and pressure drop for the thermal control.

3D computational fluid dynamics (CFD) simulations allow detailed prediction of the physical phenomena and, as they have been largely used and validated, usually with acceptable margin of error. On the contrary they are very time consuming and they cannot be used to simulate local effects of very large components and systems.
When working with large cooling systems that incorporate different parallel branches interfaced with different components, 1D CFD simulations are the common choice because, even if they are not able to predict detailed results, they allow fast simulations and act as versatile tools suitable to evaluate the correctness of the cooling circuits and to analyse the general thermo-hydraulic parameters.

1D codes use elements with input/output nodes where analytical equations are applied to manipulate the input parameters and give to corresponding outlet. The general governing equations for the thermo-hydraulic analyses for each elements are the conservation of mass (Eq. 5), of energy (Eq. 6) and momentum (Eq. 7). They ensure that the same amount of energy, mass and momentum that goes into a control volume then leave it.
These equations are used to calculate the flow into and out of the components as a function of the pressure. Flow is then eliminated from the equations using continuity at each node and the resulting pressures are substituted back into the component

equations to calculate new estimates of the flows. The process is iteratively repeated until stable values are achieved.

$$\frac{\partial \rho}{\partial t} + \frac{\partial}{\partial x}(\rho u) + \frac{\partial}{\partial y}(\rho v) + \frac{\partial}{\partial z}(\rho w) = 0 \qquad \text{Eq. 5}$$

$$Ein + Eg - Eout = Est \qquad \text{Eq. 6}$$

$$\begin{aligned} \rho g_x - \frac{\partial p}{\partial x} + \mu\left(\frac{\partial^2 u}{\partial x^2} + \frac{\partial^2 u}{\partial y^2} + \frac{\partial^2 u}{\partial z^2}\right) &= \rho \frac{du}{dt} \\ \rho g_y - \frac{\partial p}{\partial y} + \mu\left(\frac{\partial^2 v}{\partial x^2} + \frac{\partial^2 v}{\partial y^2} + \frac{\partial^2 v}{\partial z^2}\right) &= \rho \frac{dv}{dt} \\ \rho g_z - \frac{\partial p}{\partial x} + \mu\left(\frac{\partial^2 w}{\partial x^2} + \frac{\partial^2 w}{\partial y^2} + \frac{\partial^2 w}{\partial z^2}\right) &= \rho \frac{dw}{dt} \end{aligned} \qquad \text{Eq. 7}$$

From the Navier-Stokes equations (Eq. 7) the Bernoulli's equation can be derived:

$$\frac{v^2}{2g} + z + \frac{p}{\rho g} = C \qquad \text{Eq. 8}$$

where v is the bulk velocity [m/s], g is the gravitational acceleration [m/s^2], z is the elevation [m], p is the static pressure [Pa] and ρ the fluid density [kg/m^3].

The MITICA beam source, neutraliser and residual ion dump are actively cooled by complex hydraulic networks made of a large number of pipes, manifolds, junctions, bends and experimental components. Their cooling system have been modelled and analysed with 1D CFD codes, simulating non-linear behaviour introduced by material properties depending on local temperature.
Different software have been used (e.g. Flowmaster [11] and ANSYS APDL [12]) and also the analyses have been performed with different aims: the flow partitioning for the beam source has been simulated in order to design the arrangement of the cooling system, the coolant outlet temperature for the neutraliser to verify the PED (Pressure Equipment Directive) requirements, the flow uniformity and the boiling margin for the residual ion dump have been controlled. The results are useful, as boundary conditions, for further detailed simulations oriented to the localised heat transfer coefficients.

The mentioned software use the well-known analytical models to simulate the standard components (like pipes and bends), while complex geometries whose hydraulic behaviours are not available in literature have been studied by detailed 3D CFD simulations. The 3D analyses have been carried out by imposing different values of mass flow rate as boundary condition in order to get the characteristic curves (pressure drop vs. mass flow rate) which allow to simulate the component as a localised pressure drop to fully characterize the circuit. Other cooling elements as swirl tubes, often used in fusion applications but not present in the commercial software, have been simulated by using appropriate correlations.

The integrated models have been developed with the following procedure: the cooling networks made of one-dimensional elements have been made by considering all the geometrical parameters (length of pipes, internal diameters and curvature radius of the bends) taken from the 3D geometrical model. The standard components (like pipes and bends) have been simulated with the analytical models, while for the experimental components with particular geometry, the information coming from the 3D CFD simulations have been used.

In the following a description of the mathematical models used in Flowmaster and ANSYS APDL are reported.

2.2 Flowmaster 1D elements

Flowmaster is a 1D thermo-fluid software package to analyse complex pipework net providing a graphical virtual environment where it is possible to design, refine and test the entire fluid flow system. It is based on Don Miller's "Internal Flow Systems" [14] .
The mathematical models used by Flowmaster are reported in the following.

2.2.1 Pipe

The pipe component (Figure 2-1) models the pressure drop along a straight pipe assuming a constant cross section area.

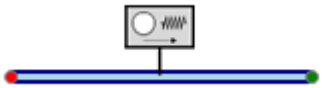

Figure 2-1 Pipe symbol in Flowmaster code

The distributed pressure drop is calculated with the Darcy-Weisbach equation:

$$\Delta p = f \frac{L}{D} \frac{\rho v^2}{2} \qquad \text{Eq. 9}$$

where Δp is the pressure drop [Pa], f is the friction factor [-], L is the pipe length [m], D is the pipe diameter [m], ρ is the fluid density [kg/m^3] and v is the fluid velocity [m/s].

The friction factor f is computed with the Colebrook-White equations:

- laminar flow (Re<2000): $f = f_l = \frac{64}{Re}$
- fully turbulent flow (Re>4000):

$$f = f_t = \frac{0{,}25}{\left[\log\left(\frac{k}{3{,}7D} + \frac{5{,}74}{Re^{0{,}9}}\right)\right]^2} \qquad \text{Eq. 10}$$

- transitional flow (2000<Re<4000): $f = x f_t + (1 - x) f_t$

$$x = \frac{Re}{2000} - 1$$

2.2.2 Bend

The bend component (Figure 2-2) models the distributed and localised pressure drop in bends.

Figure 2-2 Bend symbol in Flowmaster code

The localized pressure drop given by the bend is calculated by the equation:

$$\Delta p = \frac{k\dot{m}^2}{2\rho A^2} \qquad \text{Eq. 11}$$

where Δp is the pressure drop [Pa], k is the loss coefficient [-], $\dot{m}$ is the mass flow rate [kg/s], ρ is the fluid density [kg/m^3] and A is the cross section [m^2].

The loss coefficient k is given, for fully turbulent flow, by

$$k = k_b C_{Re} C_f \qquad \text{Eq. 12}$$

The three terms in Eq. 12 are respectively the loss coefficient of the bend (obtainable by Figure 2-3), a correction for the Reynolds Number (Figure 2-4) and a correction for the friction factor (equals to the ratio between the friction factor for the rough pipe and the friction factor for a smooth pipe).

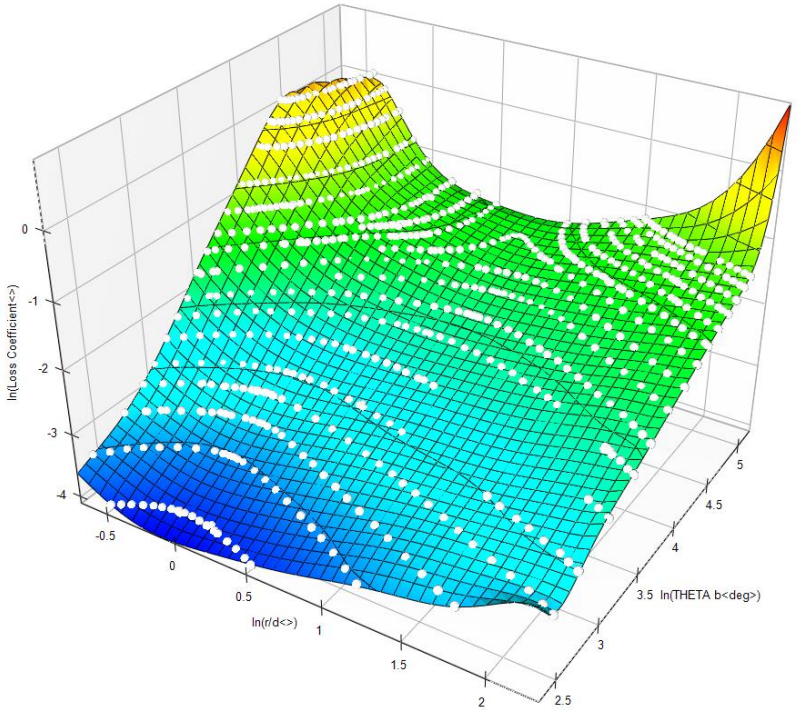

Figure 2-3 **Bend loss coefficient in function of the ratio between the curvature radious and the diameter (*ln(r/d)*) and the degree of the inclination (*ln(THETA b)*)**

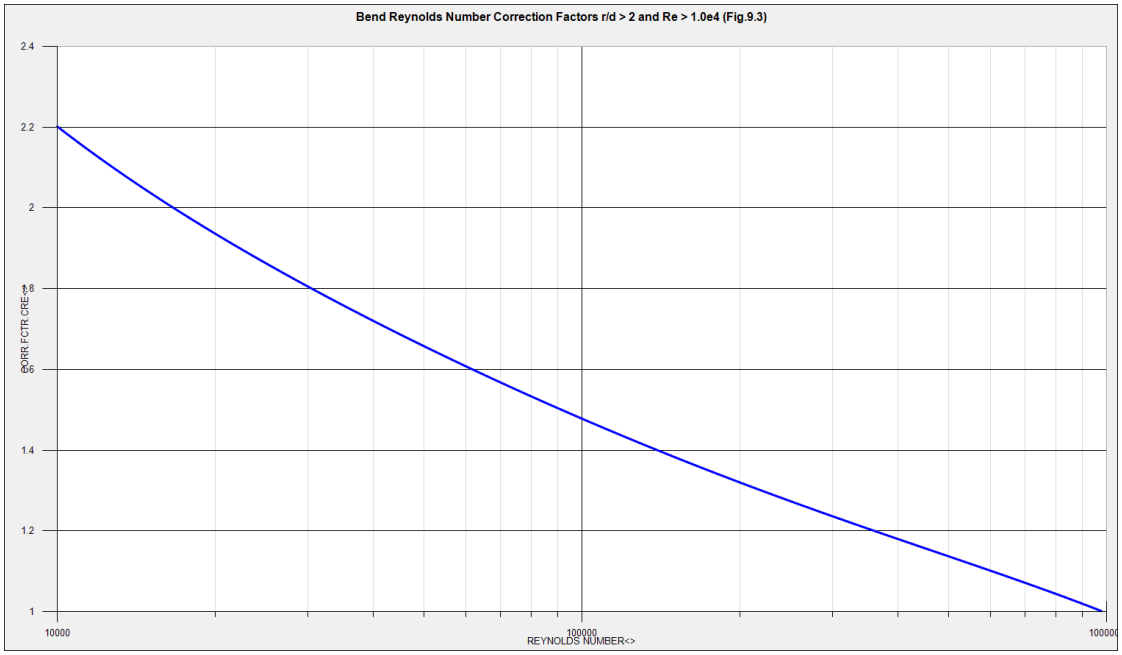

Figure 2-4 **Reynolds number correction**

2.2.3 T-joint

The T-joint component has been used in the cooling circuit in order to replicate the behaviour of the manifolds. The component symbol is shown in Figure 2-5

Figure 2-5 T-joint symbol in Flowmaster code

The localized pressure drop given by the bend is calculated by the equation:

$$\Delta p_{ij} = C_{Re} \frac{k_{ij} \dot{m}^2}{2\rho A^2} \qquad \text{Eq. 13}$$

where C_{Re} is the correction factor of Reynolds Number [-], Δp_{ij} is the pressure drop between two nodes i and j [Pa], k_{ij} is the loss coefficient between the two nodes [-], $\dot{m}$ is the mass flow rate [kg/s], ρ is the fluid density [kg/m^3] and A is the cross section [m^2].

The loss coefficient k_{ij} is given by different curves depending on whether the flow is. The curves are not shown, for simplicity.

2.2.4 Discrete loss

The discrete loss component (Figure 2-6) provides a way of modelling a pressure drop by defining a fixing value of the loss or a curve which describes the trend of the loss as function of the flow rate.

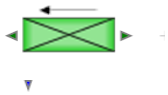

Figure 2-6 Discrete loss symbol in Flowmaster code

2.2.5 Heat exchanger

The heat exchanger component (Figure 2-7) is an electric resistance that provides heating to the fluid by defining the thermal power:

$$P_{th} = \dot{m}\, c_p\, (T_o - T_i) \qquad \text{Eq. 14}$$

where P_{th} is the thermal power [kW], $\dot{m}$ is the mass flow rate [kg/s], c_p is the specific heat [kJ/(kg K)], T_o and T_i the outlet and inlet fluid temperature [°C].

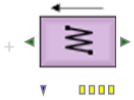

Figure 2-7 Heat exchanger symbol in Flowmaster code

2.3 ANSYS APDL

ANSYS APDL can be used as 1D code to solve complex hydraulic networks. The one-dimensional element to be used is *fluid116* (Figure 2-8). It allows the simulation of pipes, manifolds and other cooling elements. It is an element with the ability to conduct heat and transmit fluid between its two primary nodes. The element may have two different types of degrees of freedom, temperature and/or pressure.

Fluid116 can have a friction factor to calculate the distributed pressure drop, and a loss coefficient (K_{loss}) for carry out the local pressure drop (i.e. bends, change of sections, inlet and outlet).

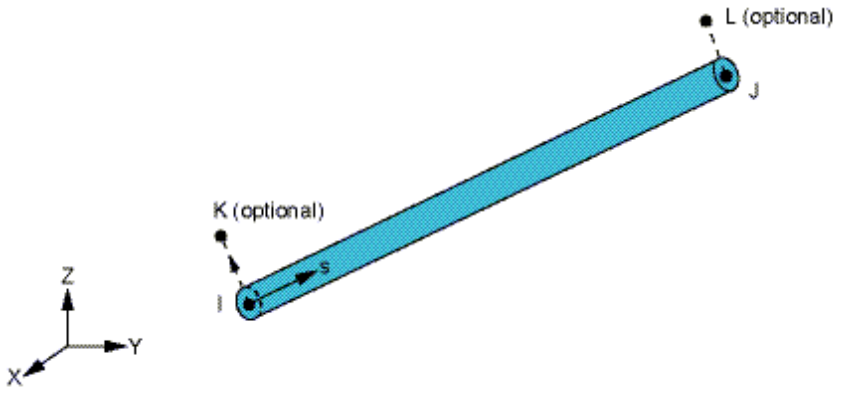

Figure 2-8 Element *Fluid116*

2.4 Beam Source

The MITICA beam source is composed of a radio frequency (RF) based ion source for negative ions generation and a five step electrostatic accelerator with multi-aperture grids (MAMuG) for ions accelerations [15]. An overall section view of the beam source is shown in Figure 2-9.

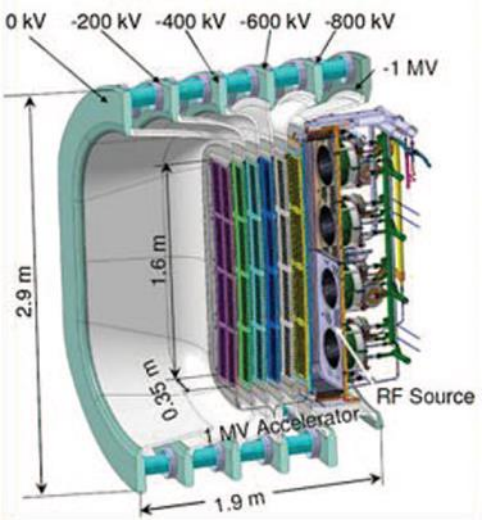

Figure 2-9 Section view of the MITICA beam source

The MITICA beam source is cooled down by six cooling circuits: one for the entire ion source and then one for each accelerating grid. As the accelerating grids have a devoted cooling system which fill only their four segments, their hydraulic pipework has not been analysed. On the other side the hydraulic networks for the ion source and for the grounded grid and electron dump needed of detailed models in order to analyse the flow partitioning of the coolant within each components.

The two integral thermo-hydraulic models of the cooling systems have been realised and analysed by using Flowmaster code.

2.4.1 Ion Source

In paragraph 1.4.1 it has been already explained how a RF ion source works. Figure 2-10 shows the MITICA ion source where the complexity of the system is recognizable.

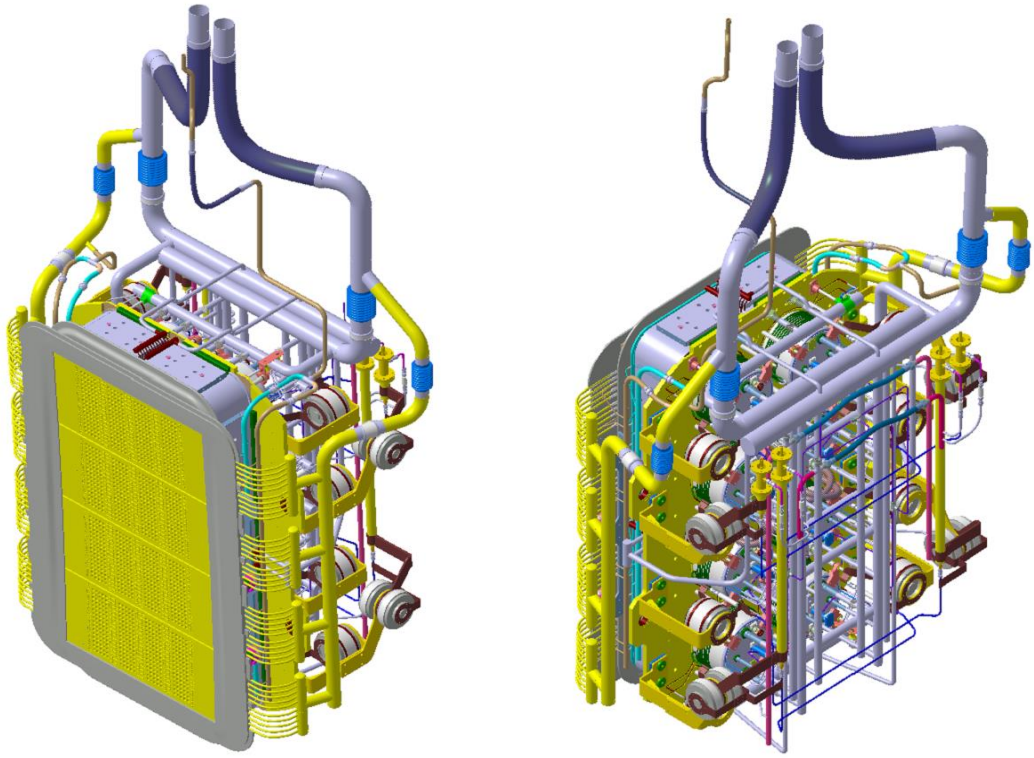

Figure 2-10 **Two views of the MITICA ion source: all the components and the cooling circuits are shown.**

The drivers' plate is composed of two different plates: the rear drivers plate and the plasma drivers plate. The rear drivers plate is a stainless steel plate with the function of support the drivers; the plasma driver plate (PDP) is a CuCrZr alloy plate which facing the plasma allows the thermal expansion [8]. Stripping reactions in the accelerator are expected to generate back-streaming positive ions [16] which dumping on the PDP impose a dedicated cooling circuits to carry out the heat loads.
The source case lateral wall (SCLW) which surround the entire RF source is divided in six sectors with cooling ducts machined on the internal surface.
The drivers are the cylindrical structures where the flow current, running through the RF Coils, transfers the power and generates the plasma. High heat loads are foreseen on the drivers because of the interaction with the back-streaming positive ions [8] and two separate cooling circuits are devoted to remove these loads: the Faraday Shield Lateral Wall (FSLW) and the Faraday Shield Back Plate (FSBP).

The extractor is made of the Bias Plate (BP), the Plasma Grid (PG) and the Extraction Grid (EG). Each grid is composed of four segments made by electro-deposition of pure copper onto a copper base plate. Channels with small cross section area run inside the grids allowing the cooling.

2.4.1.1 CFD Sub-Modelling

Because of the particular geometry of the main experimental components, the hydraulic behaviour of complex geometries whose models are not available in literature, have been analysed and characterised with three dimensional CFD code (e.g. ANSYS CFX [13]). The *k-ε* turbulence model has been used for all the simulations.
For each component three different analyses at different inlet mass flow rates have been carried out in order to get the characteristic curves (pressure drop vs. mass flow rate) to be inserted in the one-dimensional model where they are simulated as localised pressure drop.

The Plasma Driver Plate (PDP) is composed of four identical quarters in which the water flows along two different branches named Channel 1 and Channel 2. One quarter is recognizable in Figure 2-11. The obtained results are listed in Table 2-1. The total heat load on the PDP is 520 kW [18] (65 kW for each channel).

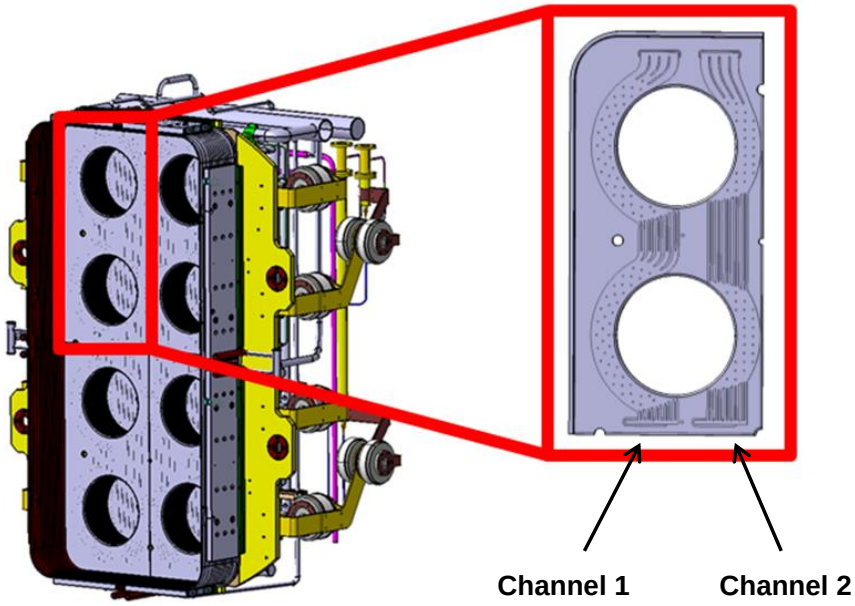

Figure 2-11 Magnification of one quarter Plasma Driver Plate

Table 2-1 PDP Channel 1 and Channel 2: pressure drop as function of mass flow rate [17]

PDP Channel 1		PDP Channel 2	
Mass flow rate [kg/s]	**Pressure drop [kPa]**	**Mass flow rate [kg/s]**	**Pressure drop [kPa]**
1.125	102	1.125	131
2.25	397	2.25	516
3.375	885	3.375	1160

The Source Case Lateral Wall (SCLW) is divided in six parts (Figure 2-12). One sixth has been simulated and the results are listed in Table 2-2 The total heat load on the SCLW is 20 kW [19] (3.33 kW each sixth).

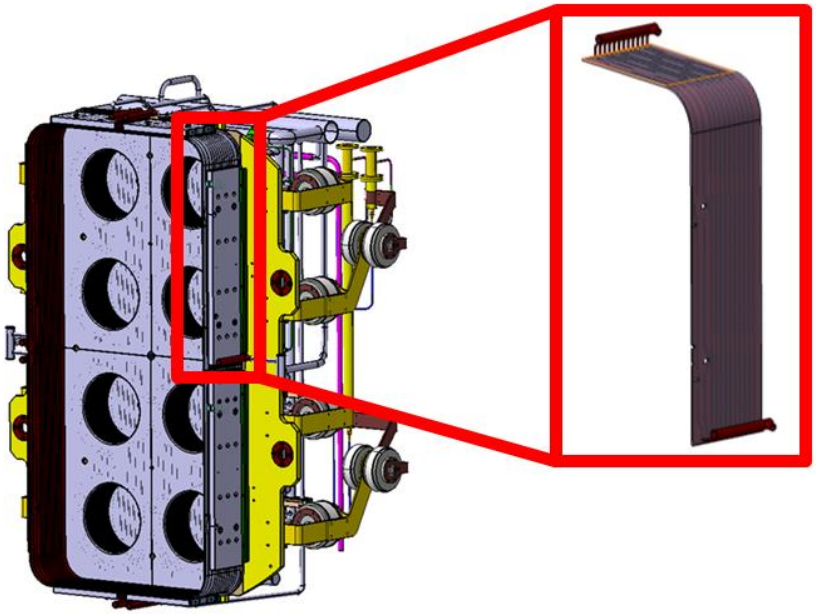

Figure 2-12 Magnification of one sixth Source Case Lateral Wall

Table 2-2 SCLW: pressure drop as function of mass flow rate [19]

Mass flow rate [kg/s]	Pressure drop [kPa]
0.25	44
0.5	177
1	708

The obtained results of the Faraday Shield Lateral Wall (FSLW) (Figure 2-13) and the Faraday Shield Back Plate (FSBP) (Figure 2-14) are listed in Table 2-3. The thermal load for each FSLW is 40 kW [20] and for each FSBP 75 kW [21].

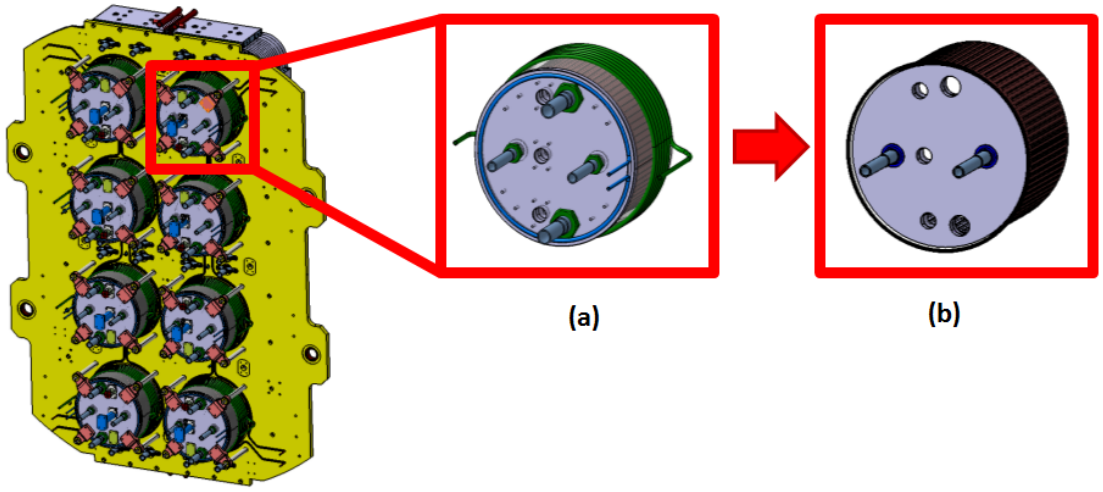

Figure 2-13 **Magnification of one Driver (a) and one FSLW (b)**

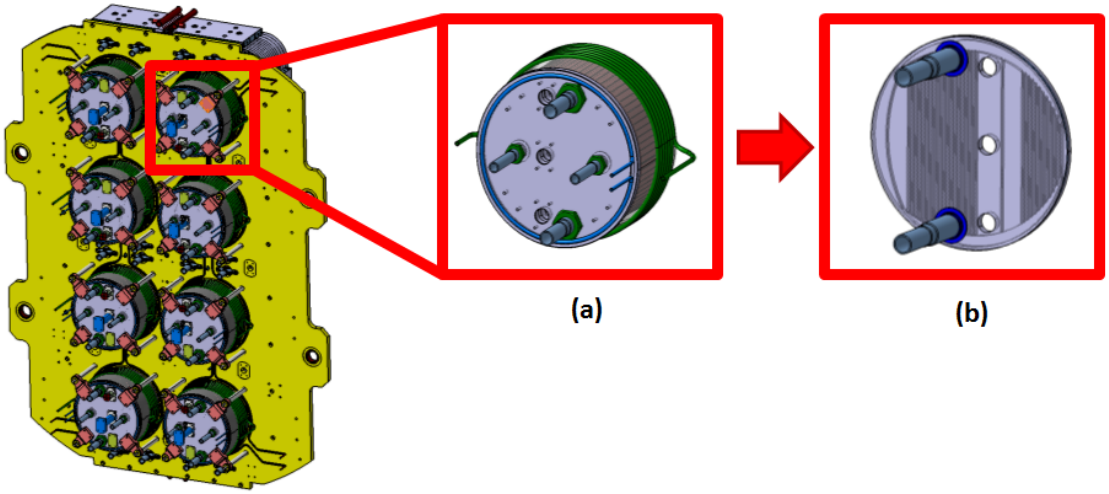

Figure 2-14 **Magnification of one Driver (a) and one FSBP (b)**

Table 2-3 **FSLW and FSBP: pressure drop as function of mass flow rate [20][21]**

FSLW		FSBP	
Mass flow rate [kg/s]	**Pressure Drop [kPa]**	**Mass flow rate [kg/s]**	**Pressure Drop [kPa]**
0.3	62	0.5	17
0.45	135	1.5	137
0.625	251	2	238

The RF Coil (Figure 2-15) has been simulated with the following main parameters of the mesh:

- **maximum element size**: 1 mm;
- **inflation layer**: 5 layers, first layer with height of 0.1 mm and grow rate equals to 1.2;
- **number of elements**: 2.76×10^6.

The meshed model is shown in Figure 2-16.

The pressure drop results are listed in Table 2-4 and plotted in Figure 2-17. The thermal load expected at each RF Coil is of 5.7 kW [22].

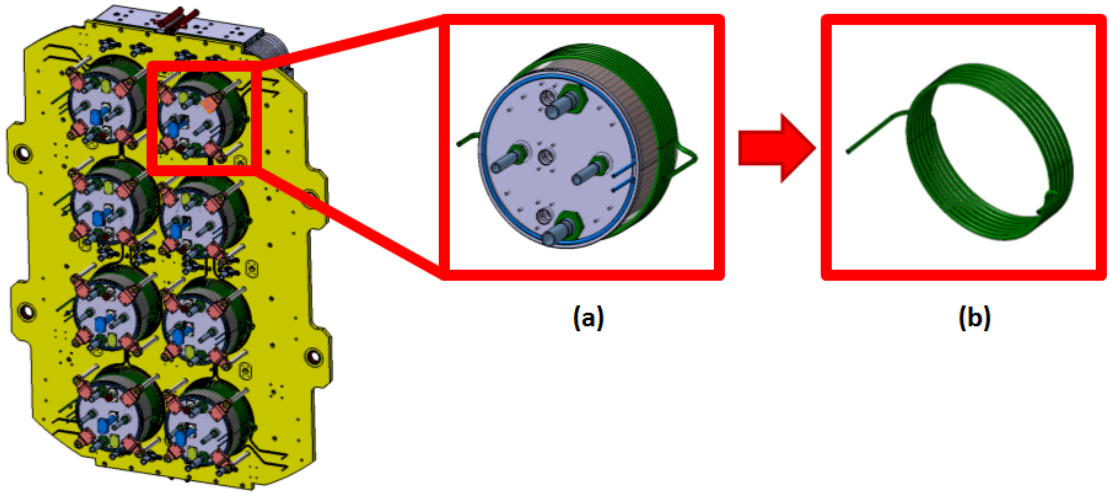

Figure 2-15 Magnification of one Driver (a) and one RF coil cooling circuit (b)

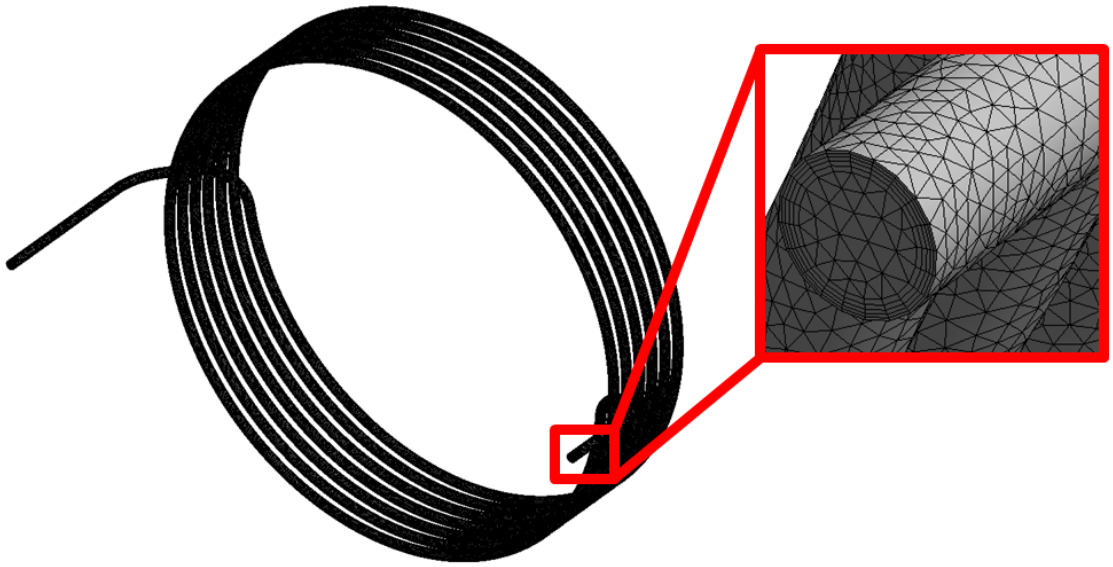

Figure 2-16 Overview of the mesh for the RF Coil

Table 2-4 **RF Coil: pressure drop as function of mass flow rate**

Mass flow rate [kg/s]	Pressure Drop [kPa]
0.0625	73
0.125	253
0.25	863

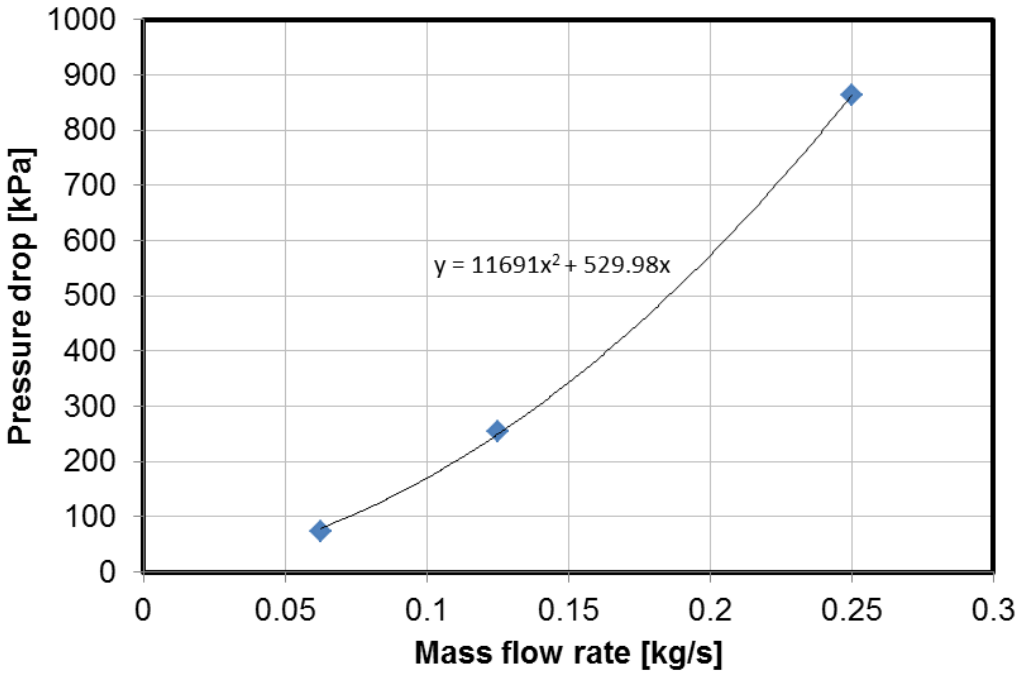

Figure 2-17 **RF Coil: characteristic curve pressure drop vs. mass flow rate**

The Plasma Grid, Bias Plate and Extraction Grid belong to the MITICA Extractor and are shown in Figure 2-18.

The Plasma Grid is composed of four identical segments, for each one the nominal mass flow rate is 0.125 kg/s and the corresponding pressure drop is 6 kPa [23]. The characteristic curve (pressure drop vs. mass flow rate) has been assumed with an ideal parabolic trend. The heat load for each PG segment is 6.2 kW.

The Extraction Grid is composed of four identical segments, for each one the nominal mass flow rate is 1.255 kg/s and the corresponding pressure drop is 102 kPa [23]. The characteristic curve (pressure drop vs. mass flow rate) has been assumed with an ideal parabolic trend. The heat load for each EG segment is 135.25 kW [10].

The Bias Plate (BS) has been simulated directly in Flowmaster by using the *pipe* elements. The total heat load on the grids is 6 kW.

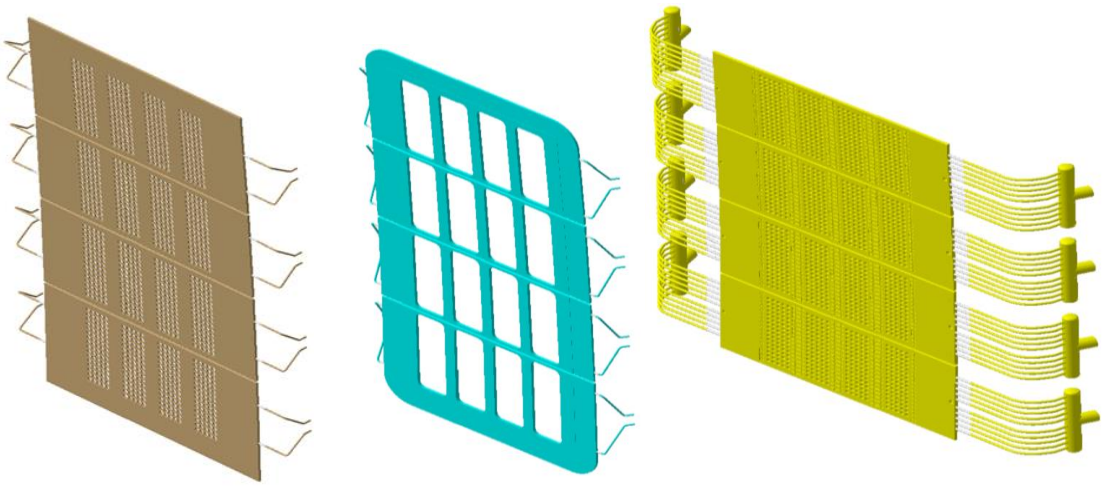

Figure 2-18 MITICA Extractor: Plasma Grid (a), Bias Plate (b) and Extraction Grid (c)

2.4.1.2 Integrated RF ion source cooling circuit model

In Figure 2-19 and Figure 2-20 the implemented cooling circuit model of the MITICA beam source is shown. The model replicates the geometry in only two dimensions and, being a schematic representation, the actual position in the space of the various parts isn't important. The experimental components mentioned in the previous paragraph have been simulated by using discrete losses with the calculated pressure drop curves, followed by heat exchangers thermally loaded with the nominal power. In Table 2-5 the values used in the one-dimensional model for the pressure drops and for the thermal loads are listed and it is possible to note that, compared to the values stated in the previous paragraph, for the PG and the EG there is a variation in the mass flow rate and in the thermal power. The motivation is that the PG has been simulated by using 2 parallel branches for each grid segment (8 parallel channels in total). For each branch the pressure drop has been kept equals to the entire pressure drop of one grid segment, while the flow rate and the thermal power have been split in 8 channels. The same procedure has been done to simulate the EG by using 10 branches for each grid segment (40 channels in total).

Table 2-5 Mass flow rate, corresponding pressure drop and thermal load for each 1D element

Component	Mass flow rate [kg/s]	Pressure drop [MPa]	Pth [kW]
PDP Channel 1	1.125	102	65
	2.25	397	
	3.375	885	
PDP Channel 2	1.125	131	65
	2.25	516	
	3.375	1156	
SCLW	0.25	44	3.33
	0.5	177	
	1	708	
FSLW	0.3	62	40
	0.45	135	
	0.625	251	
FSBP	0.5	17	75
	1.5	137	
	2	238	
FS Coil	0.0625	73	5.7
	0.125	253	
	0.25	863	
PG	0.0078	2	3.1
	0.0156	6	
	0.0172	7	
EG	0.0628	26	13.525
	0.1255	102	
	0.1381	123	

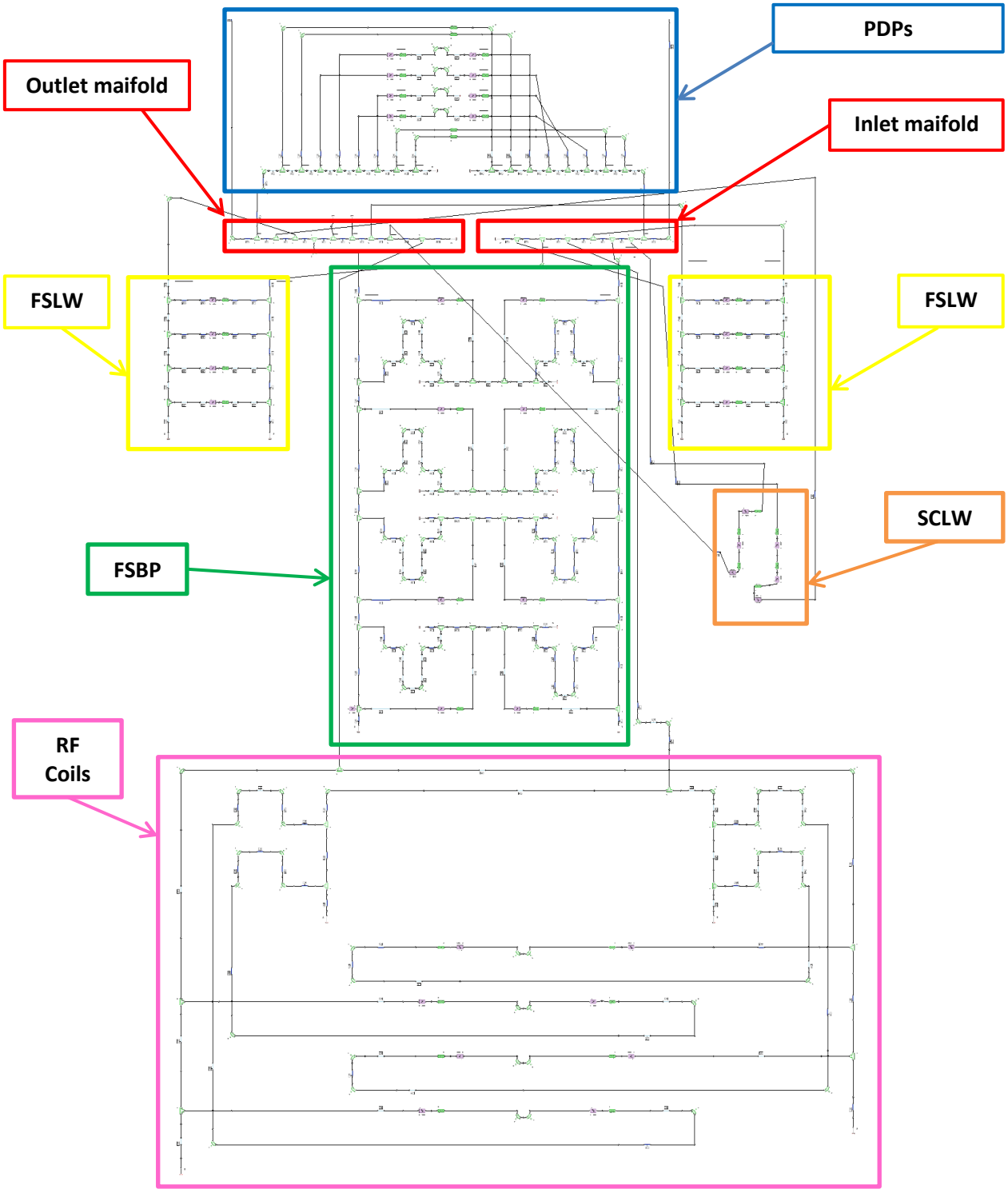

Figure 2-19 Overview of the RF Ion Source hydraulic network in Flowmaster

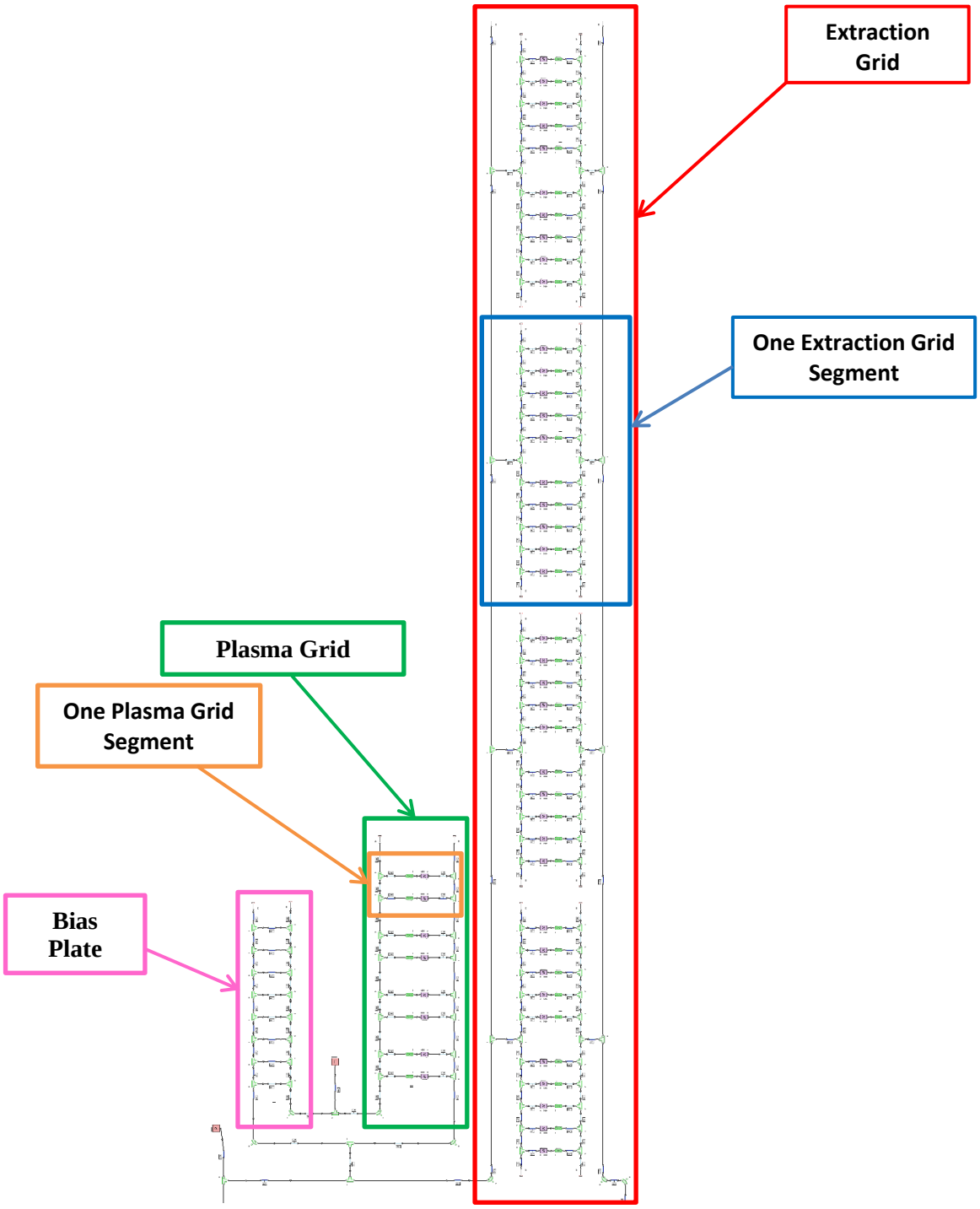

Figure 2-20 Overview of the Extractor hydraulic network in Flowmaster

2.4.1.3 Results

The CFD 1D thermo-hydraulic model has been used to evaluate the mass flow rate partitioning and outlet coolant temperatures in each cooling circuit in different scenarios and within different design.

In the following the results of the simulations are reported using the nomenclature shown in Figure 2-21, Figure 2-22 and Figure 2-23.

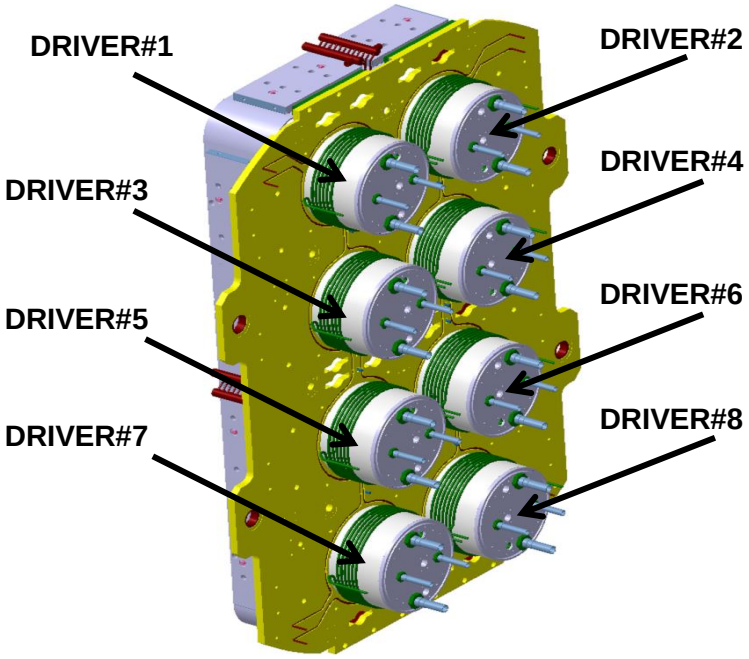

Figure 2-21 **Nomenclature of the components used to show the results. Each Driver is composed of three cooling circuits: FSLW, FSBP and RF Coil**

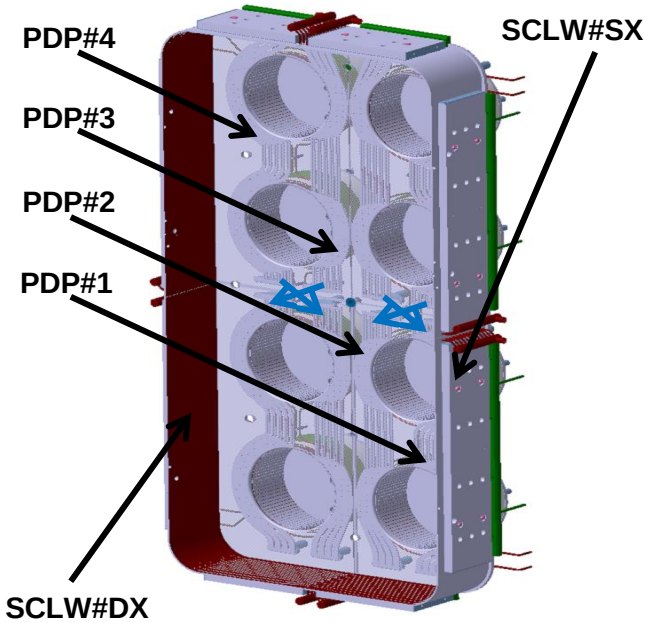

Figure 2-22 **Nomenclature of the components used to show the results**

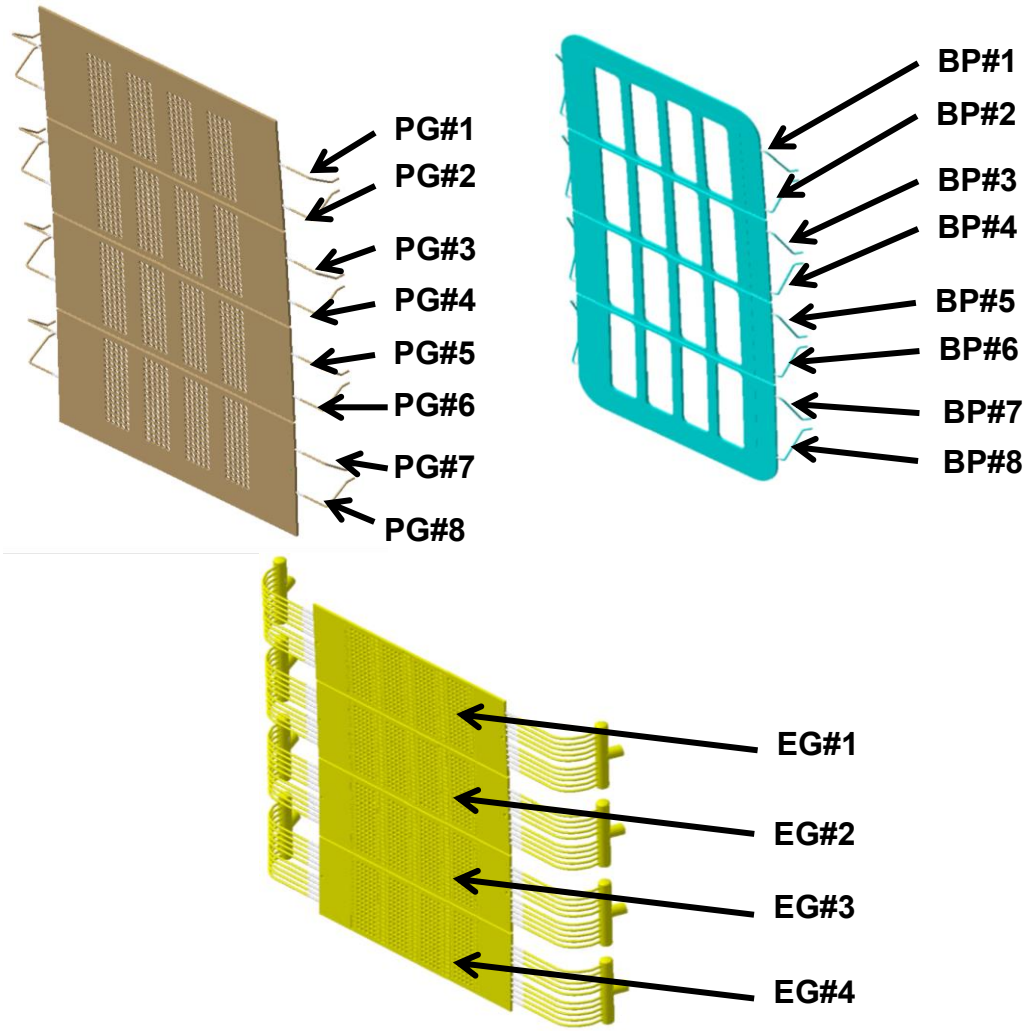

Figure 2-23 **Nomenclature of the components used to show the results**

2.4.1.3.1 Reference design

The first analysed design is sketched in Figure 2-24.

The boundary conditions for cooling water in the nominal case are the following:

- the total mass flow rate at main inlet is 33 kg/s;
- the water temperature at the main inlet is 35 °C;
- another inlet is present in order to feed the Plasma Grid and Bias Plate, here the total mass flow rate is 0.25 kg/s while the inlet water temperature is 150 °C;
- the pressure at the common outlet is 1.5 MPa;
- the heat loads are those listed in Table 2-5.

The detailed results are listed in Table 2-6 and shown in Figure 2-25 and Figure 2-26 where the normalised mass flow rate (calculated over the nominal desired value) and the outlet temperature are plotted.

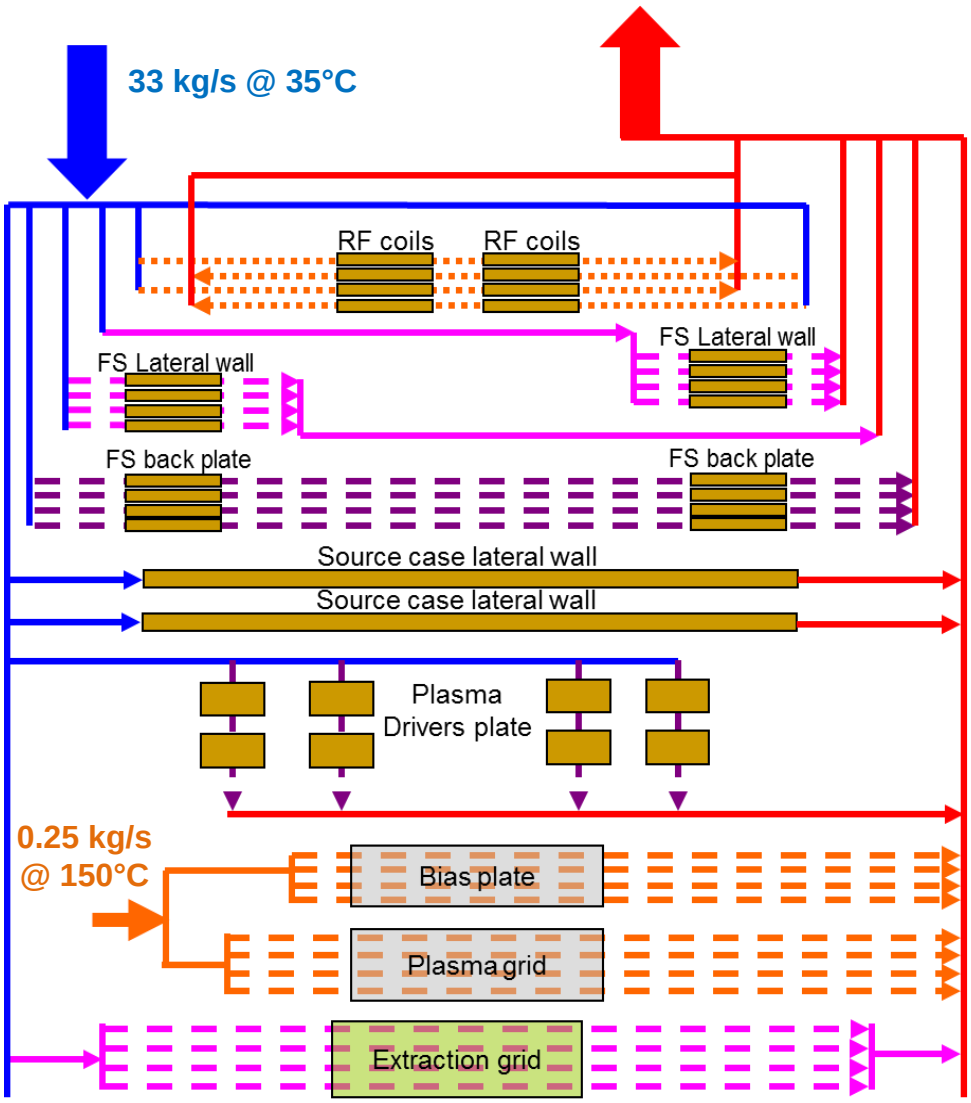

Figure 2-24 Sketch of the previous MITICA Beam Source cooling design

Table 2-6 Mass flow rate and coolant outlet temperature in the reference design

Component	Mass flow rate [kg/s]	Nominal mass flow rate [kg/s]	Percentage change [%]	Outlet temperature [°C]
PDP#1	1.243	2.25	-45	60.1
PDP#2	1.246	2.25	-45	60
PDP#3	1.259	2.25	-44	59.8
PDP#4	1.257	2.25	-44	59.8
FSLW#1	0.93	0.625	49	45.4
FSLW#2	1.021	0.625	63	44.4
FSLW#3	0.869	0.625	39	46.1
FSLW#4	0.955	0.625	53	45.1
FSLW#5	0.826	0.625	32	46.7
FSLW#6	0.909	0.625	45	45.6
FSLW#7	0.776	0.625	24	47.4
FSLW#8	0.855	0.625	37	46.3
FSBP#1	1.41	2	-30	47.8
FSBP#2	1.415	2	-29	59.7
FSBP#3	1.385	2	-31	48
FSBP#4	1.387	2	-31	60.2
FSBP#5	1.366	2	-32	48.2
FSBP#6	1.364	2	-32	60.6
FSBP#7	1.356	2	-32	48.3
FSBP#8	1.355	2	-32	60.8
RF_Coil#1	0.082	0.1	-18	51.7
RF_Coil#2	0.082	0.1	-18	68.3
RF_Coil#3	0.083	0.1	-17	67.8
RF_Coil#4	0.083	0.1	-17	51.4
RF_Coil#5	0.079	0.1	-21	52.2
RF_Coil#6	0.079	0.1	-21	69.4
RF_Coil#7	0.08	0.1	-20	69
RF_Coil#8	0.08	0.1	-20	52
SCLW#DX	0.394	0.5	-21	41.1
SCLW#SX	0.4	0.5	-20	41.1
BP#1	0.011	0.0156	-29	166.3
BP#2	0.007	0.0156	-55	176.7
BP#3	0.006	0.0156	-62	178.0
BP#4	0.006	0.0156	-62	178.0
BP#5	0.006	0.0156	-62	178.0
BP#6	0.006	0.0156	-62	178.0
BP#7	0.007	0.0156	-55	176.8
BP#8	0.01	0.0156	-36	167.1
PG#1	0.025	0.0156	60	177.6
PG#2	0.025	0.0156	60	178
PG#3	0.024	0.0156	54	178.9
PG#4	0.024	0.0156	54	179.2
PG#5	0.023	0.0156	47	179.9
PG#6	0.023	0.0156	47	180.2
PG#7	0.023	0.0156	47	180.5
PG#8	0.022	0.0156	41	182.3
EG#1	3.394	1.255	170	44.6
EG#2	3.37	1.255	169	44.7
EG#3	3.356	1.255	167	44.7
EG#4	3.342	1.255	166	44.8

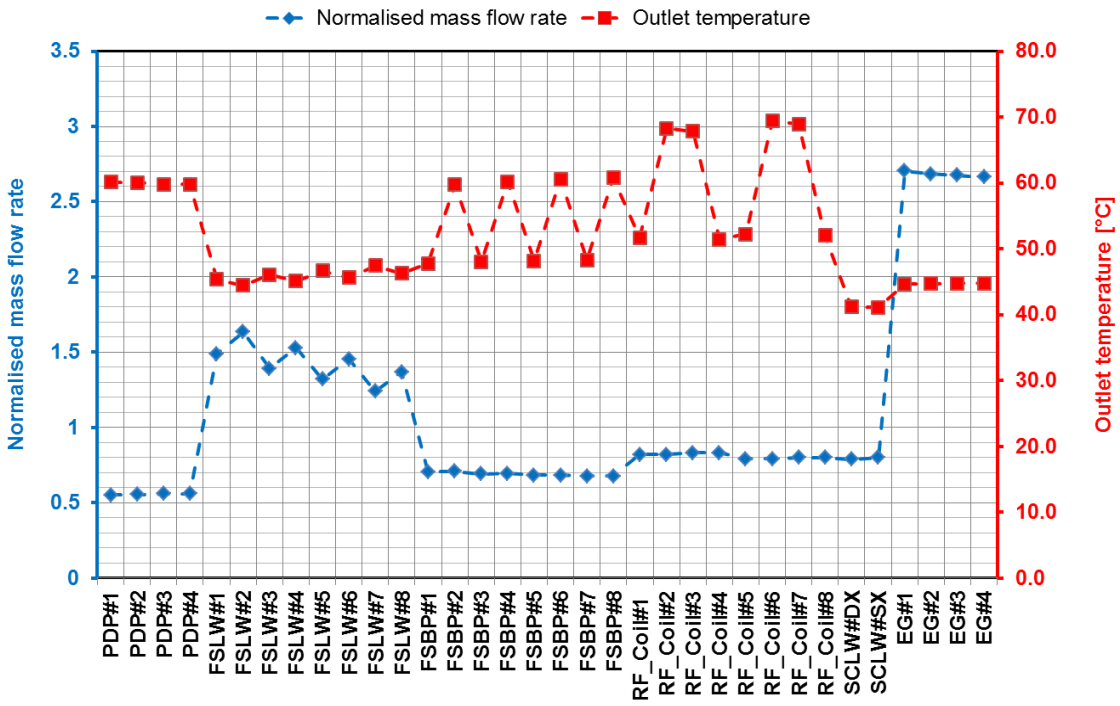

Figure 2-25 **Normalised mass flow rate (calculated over nominal value) and coolant outlet temperature in the reference design for PDP, FSLW, FSBP, RF Coils, SCLW, EG**

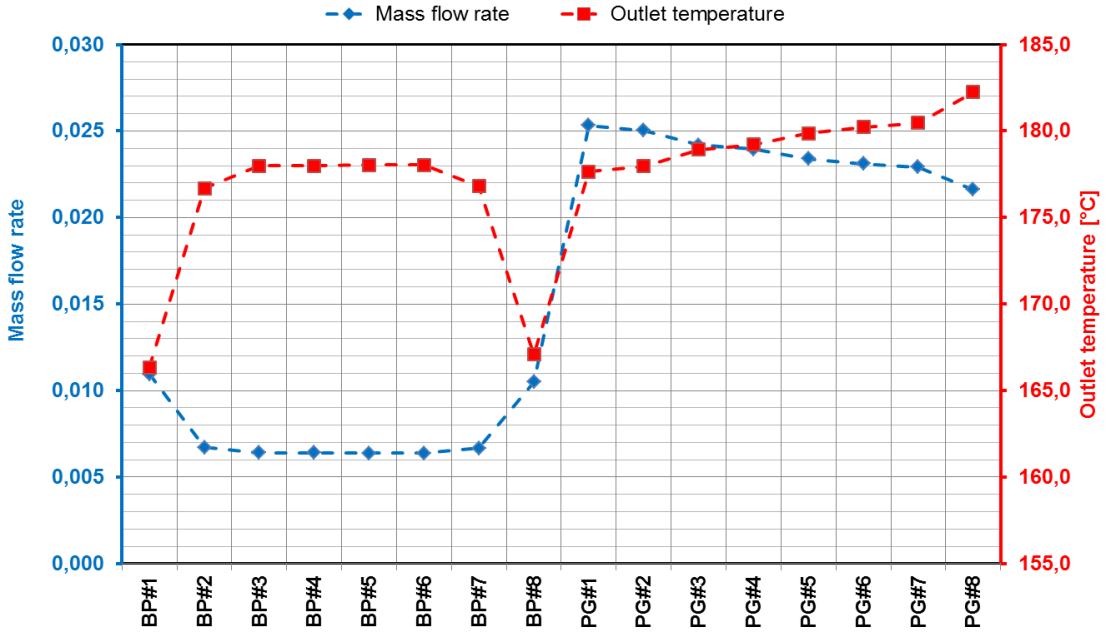

Figure 2-26 **Normalised mass flow rate (calculated over nominal value) and coolant outlet temperature in the reference design for BP and PG**

According to the results of the simulation, the total pressure drop of the entire cooling circuit is 370 kPa and the coolant outlet temperature 50.6 °C.
In the model there are two different inlets (with a fixed flow rate) and a single outlet (with a fixed pressure), due to this fact there are two different pressure drops in the network: one for the main circuit and one for the Plasma Grid and Bias Plate circuit. The situation is only imaginary: in reality, the flow balance will be done by using regulating valves and the pressure drop of the parallel circuit will be the same. Here has been assumed that the total pressure drop is dominated by the main circuit.

The cooling system which supplies the coolant water can vary the mass flow rate during the operations. Different case studies have been simulated to check the flow partitioning, the outlet coolant temperatures, and the total pressure drop. Only the mass flow at the main inlet has been changed while the flow rate for the Plasma and Bias Plate has been fixed at 0.25 kg/s:

- SCENARIO#1: total mass flow rate equals to 16.5 kg/s (50% of the nominal mass flow);
- SCENARIO#2: total mass flow rate equals to 24.75 kg/s (75% of the nominal mass flow);
- SCENARIO#3: total mass flow rate equals to 36.3 kg/s (110% of the nominal mass flow).

In all the possible scenarios mentioned above the temperature of the water at the main inlet has been set to 35 °C and the thermal loads on the components are always the nominal value. The results are listed in Table 2-7.

The maximum temperatures (~90 °C) have been found at the RF Coils in the SCENARIO#1, which is the lowest mass flow scenario. Although this temperature is fully acceptable, this scenario is not considered as an operational one, but could occur in case of a failure in the cooling system. The proper accelerator grid alignment can be obtained by controlling the grid thermal elongation, thus in SCENARIO#2 and #3 the cooling water flow is modulated to obtain this effect.

The total pressure drop of the circuit and the outlet temperature of the water in the different cases are reported Table 2-8. In Figure 2-26 the characteristic pressure drop of the entire cooling circuit is plotted.

Table 2-7 Mass flow rate partitioning and outlet temperature in different scenario

	SCENARIO#1 (9.75 kg/s)		SCENARIO#2 (14.63 kg/s)		SCENARIO#3 (21.45 kg/s)	
Component	**Mass flow rate [kg/s]**	**Outlet temperature [°C]**	**Mass flow rate [kg/s]**	**Outlet temperature [°C]**	**Mass flow rate [kg/s]**	**Outlet temperature [°C]**
PDP#1	0.796	74.09	1.042	64.88	1.313	58.76
PDP#2	0.798	73.98	1.045	64.81	1.317	58.70
PDP#3	0.806	73.59	1.056	64.50	1.330	58.46
PDP#4	0.804	73.59	1.054	64.55	1.329	58.49
FSLW#1	0.427	57.41	0.563	52.06	1.114	43.67
FSLW#2	0.433	57.14	0.570	51.85	1.216	42.95
FSLW#3	0.425	57.56	0.559	52.17	1.042	44.26
FSLW#4	0.430	57.28	0.566	51.96	1.137	43.50
FSLW#5	0.423	57.66	0.557	52.25	0.993	44.72
FSLW#6	0.428	57.38	0.564	52.03	1.084	43.92
FSLW#7	0.420	57.79	0.553	52.35	0.933	45.34
FSLW#8	0.426	57.51	0.561	52.13	1.019	44.48
FSBP#1	0.898	54.99	1.181	50.22	1.490	47.08
FSBP#2	0.901	73.67	1.185	64.46	1.496	58.38
FSBP#3	0.881	55.37	1.159	50.51	1.464	47.30
FSBP#4	0.882	74.48	1.161	65.06	1.466	58.84
FSBP#5	0.869	55.66	1.143	50.73	1.444	47.47
FSBP#6	0.867	75.12	1.141	65.55	1.442	59.22
FSBP#7	0.863	55.81	1.135	50.84	1.434	47.56
FSBP#8	0.861	75.40	1.133	65.76	1.433	59.38
RF_Coil#1	0.049	63.02	0.067	55.38	0.087	50.68
RF_Coil#2	0.049	90.94	0.067	75.71	0.087	66.31
RF_Coil#3	0.049	90.19	0.068	75.15	0.089	65.86
RF_Coil#4	0.049	62.64	0.068	55.10	0.089	50.45
RF_Coil#5	0.047	63.90	0.065	56.05	0.084	51.20
RF_Coil#6	0.047	92.69	0.065	77.04	0.084	67.35
RF_Coil#7	0.048	91.97	0.066	76.50	0.086	66.93
RF_Coil#8	0.048	63.54	0.066	55.78	0.086	50.99
SCLW#DX	0.256	44.39	0.332	42.25	0.416	40.84
SCLW#SX	0.258	44.30	0.336	42.18	0.422	40.76
EG#1	1.299	59.93	2.492	48.04	3.695	43.85
EG#2	1.297	59.97	2.473	48.14	3.669	43.91
EG#3	1.296	59.99	2.463	48.20	3.654	43.94
EG#4	1.295	60.01	2.452	48.25	3.639	43.98

Table 2-8 **System pressure drop and outlet temperature in different scenario**

	Total Pressure Drop [kPa]	Outlet temperature [°C]
SCENARIO#1	150	67
SCENARIO#2	258	56
SCENARIO#3	414	50

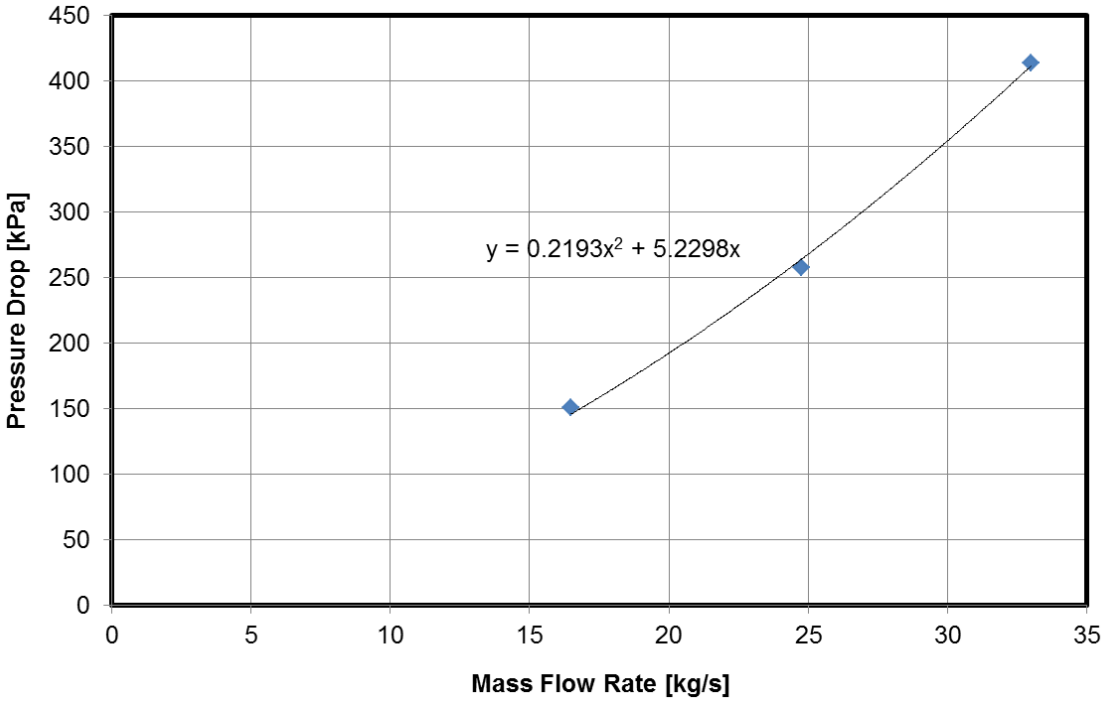

Figure 2-27 **Characteristic curve *Pressure Drop vs. Mass Flow* rate for the entire RF ion source cooling system**

As shown in Figure 2-25 and Figure 2-26 the expected flow partitioning in the components is so far to be acceptable. In particular, a too low flow rate is foreseen in PDP and FSBP, while an higher flow rate is foreseen in FSLW and EG. The flow distribution in the BP and PG has been considered acceptable.
In the following several different attempts to modify the cooling circuits are presented.

2.4.1.3.2 PDP connection modification

In order to increase the flow rate in the Plasma Driver Plate, a new possible connections of the different PDP channels has been analysed by using the one-dimensional model. In Figure 2-28 is shown a sketch of the new possible design: all the elements, named Channel 1 and Channel 2, are parallel connected in order to reduce the pressure drop and increase the mass flow.

The boundary conditions are the following:

- the total mass flow rate at main inlet is 33 kg/s;
- the water temperature at the main inlet is 35 °C;
- another inlet is present in order to feed the Plasma Grid and Bias Plate, here the total mass flow rate is 0.25 kg/s while the inlet water temperature is 150 °C;
- the pressure at the common outlet is 1.5 MPa;
- the heat loads are those listed in Table 2-5.

The results are shown in Figure 2-29 and Figure 2-30 where the nomenclature is the same used before with the exception of the PDP for which have been used that of Figure 2-28. By looking at the results for the PDP is clear that this solution is not able to solve the flow partitioning issue: the total mass flow rate into the entire PDP grid is higher compared to the reference design, but in each single channel, about half the flow rate is expected. According to the results of the simulation, the total pressure drop of the entire cooling circuit is 317 kPa and the coolant outlet temperature is 50.9 °C.

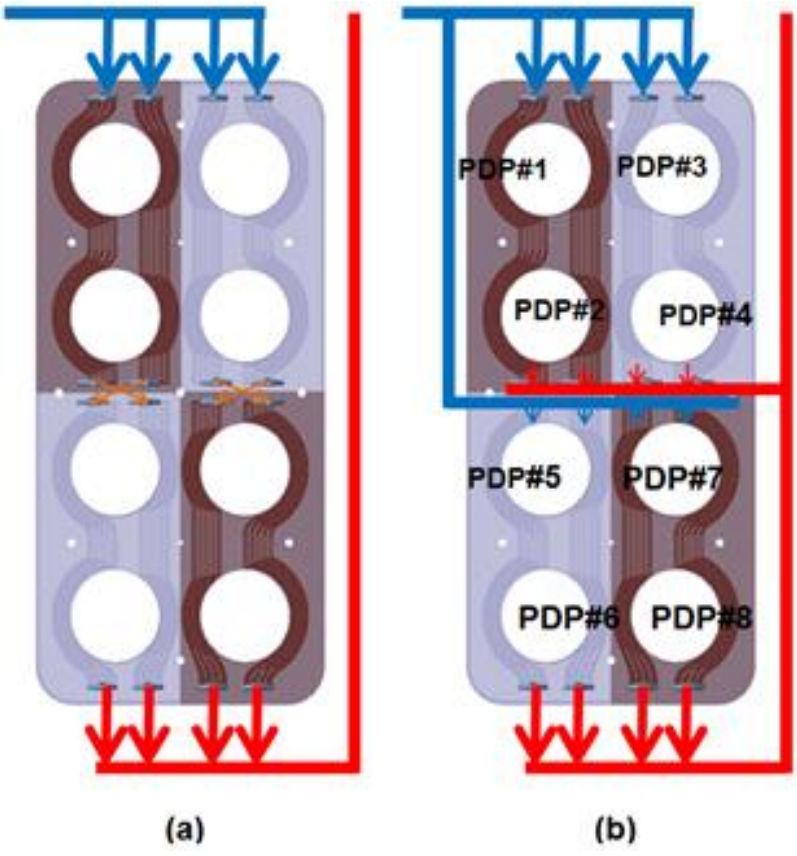

Figure 2-28 Cooling connection of the Plasma Drivers Plate: (a) actual pipe line layout; (b) new pipe line layout investigated

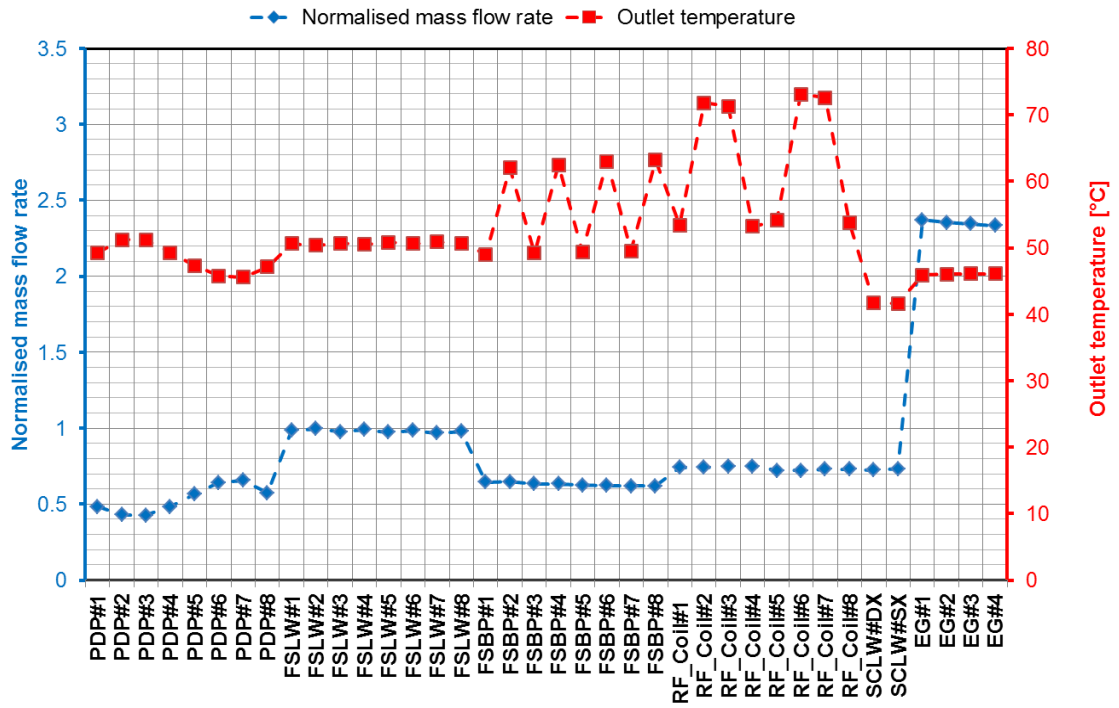

Figure 2-29 **Normalised mass flow rate (calculated over nominal value) and coolant outlet temperature for PDP, FSLW, FSBP, RF Coils, SCLW, EG, in case of parallel connection of all the PDP channels**

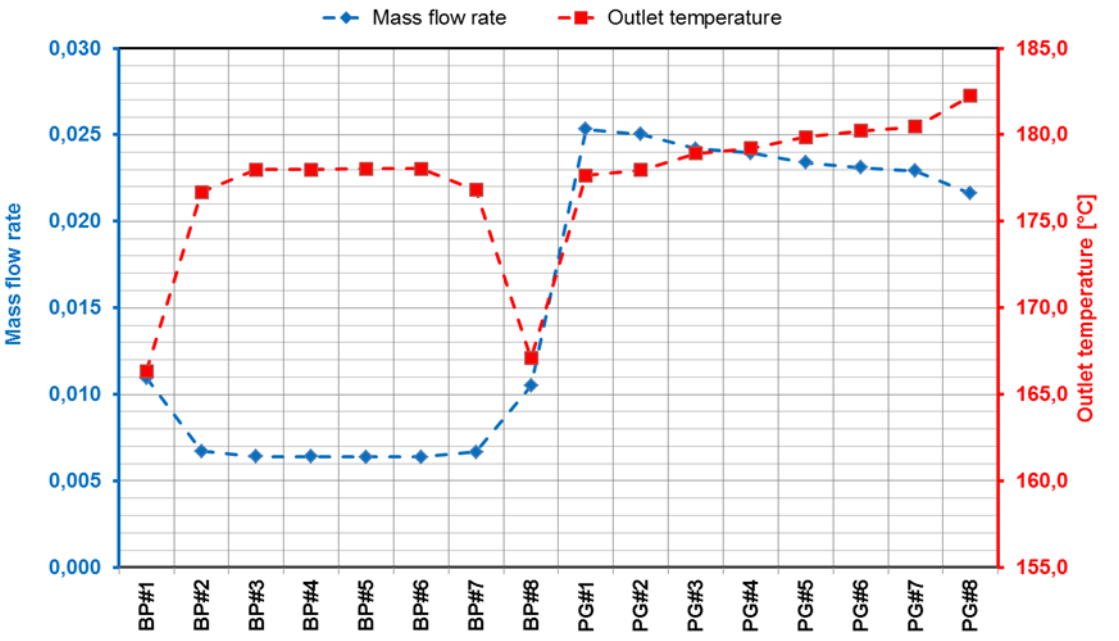

Figure 2-30 **Normalised mass flow rate (calculated over nominal value) and coolant outlet temperature for BP and PG, in case of parallel connection of all the PDP channels**

2.4.1.3.3 EG manifolds modification

A different attempt to increase the mass flow through the PDP channels has been the restriction of the diameters that feed the Extraction Grid in order to reduce the mass flow in this component. By taking in account the nominal mass flow rate foreseen for the Extraction Grid (5.02 kg/s) and for each Extraction Grid segment (1.255 kg/s), an optimization has been done in order to select the correct pipe diameters with an acceptable fluid velocity.

In the reference design, with respect to Figure 2-31, the diameters are:

- PART#1: DN 2'';
- PART#2: DN 1''1/2;
- PART#3: DN 1''1/2.

To increase the pressure drop by reducing the diameters, and accepting a fluid velocity (in the nominal case) of about 3÷4 m/s (Table 2-9), in the one-dimensional model the dimensions have been changed as in the following:

- PART#1: DN 1''1/2;
- PART#2: DN 3/4'';
- PART#3: DN 3/4''.

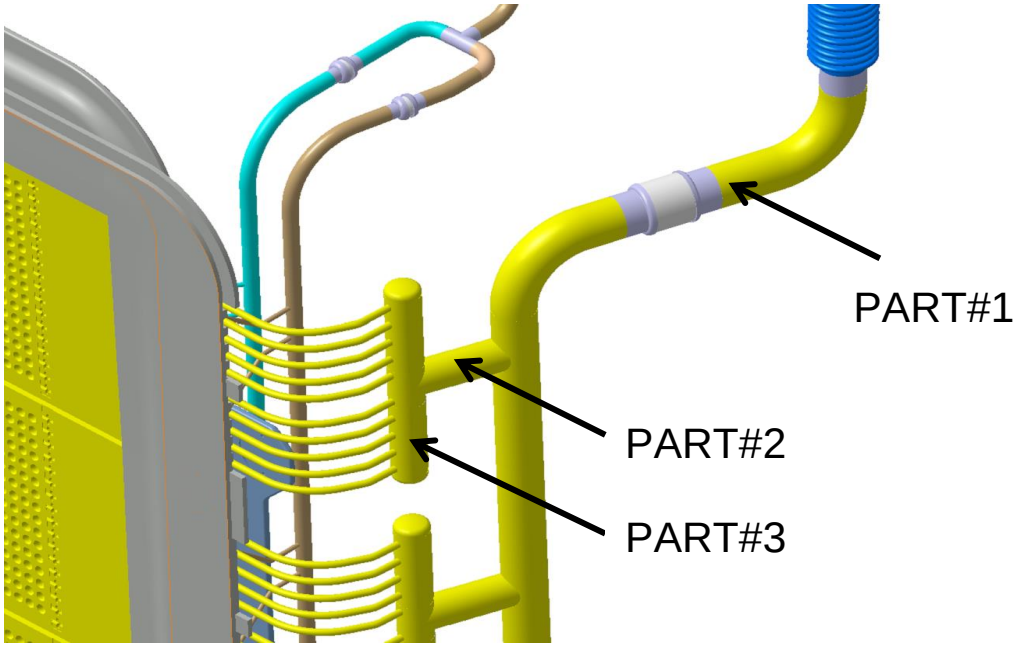

Figure 2-31 Extraction Grid manifolds diameters

Table 2-9 Extraction Grid manifolds: diameters optimisation

PART#1					**PART#2 and PART#3**				
Nominal mass flow 5.02 kg/s					Nominal mass flow 1.255 kg/s				
DN	OD	t	ID	v	DN	OD	t	ID	v
	mm	mm	mm	m/s		mm	mm	mm	m/s
2"	60.32	3.91	52.5	2.32	1"1/2	48.26	3.68	40.9	0.96
1"1/2	**48.26**	**3.68**	**40.9**	**3.83**	1"1/4	42.16	3.56	35.04	1.30
1"1/4	42.16	3.56	35.04	5.22	1"	33.4	3.38	26.64	2.26
1"	33.4	3.38	26.64	9.02	**3/4"**	**26.67**	**2.87**	**20.93**	**3.65**

The boundary conditions are the following:

- the total mass flow rate at main inlet is 33 kg/s;
- the water temperature at the main inlet is 35 °C;
- another inlet is present in order to feed the Plasma Grid and Bias Plate, here the total mass flow rate is 0.25 kg/s while the inlet water temperature is 150 °C;
- the pressure at the common outlet is 1.5 MPa;
- the heat loads are those listed in Table 2-5.

The results are shown in Figure 2-32 and Figure 2-33. The flow rate in each EG segment is about 2.4 kg/s (instead of 3.4 kg/s of the reference design): by reducing the pipe diameters is possible to reduce the mass flow in the EG but the gained flow is distributed among all the other components and an improvement of the PDP cooling is not recognizable.

According to the results of the simulation, the total pressure drop of the entire cooling circuit is 445 kPa and the coolant outlet temperature 60 °C.

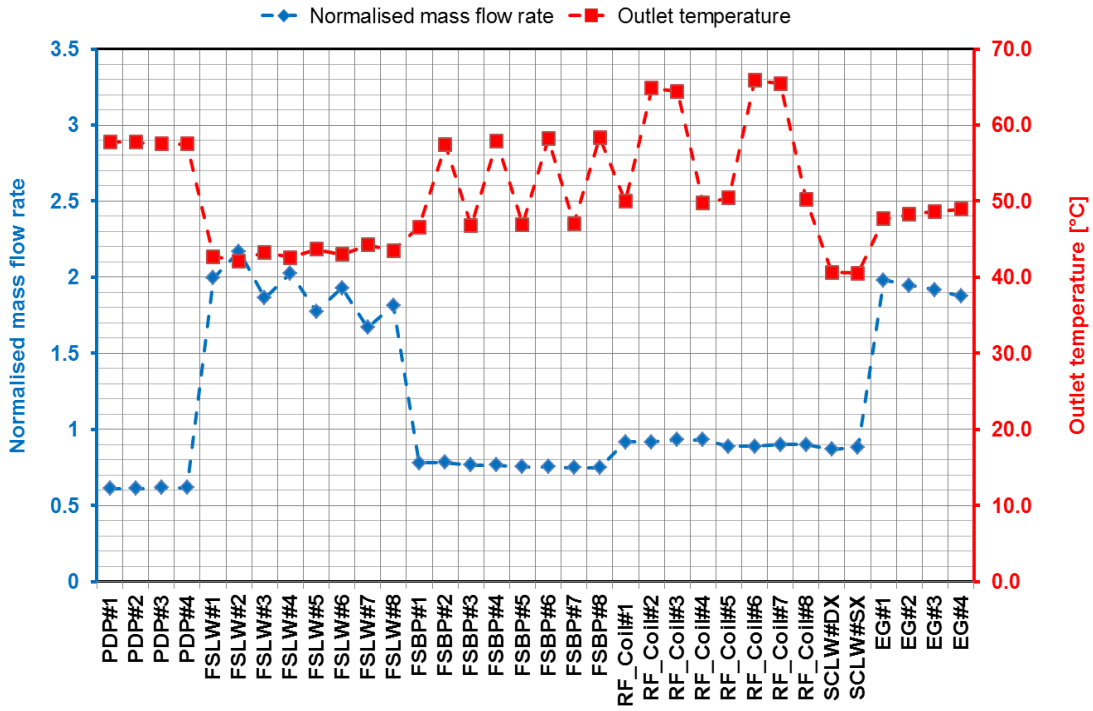

Figure 2-32 **Normalised mass flow rate (calculated over nominal value) and coolant outlet temperature for PDP, FSLW, FSBP, RF Coils, SCLW, EG, in case of EG manifolds optimized**

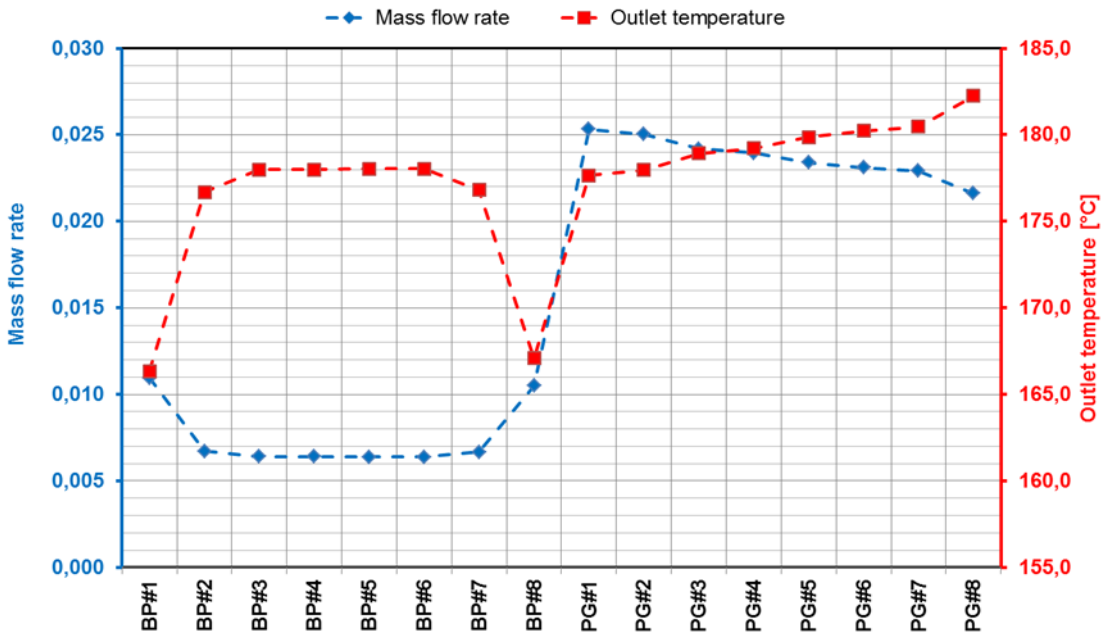

Figure 2-33 **Normalised mass flow rate (calculated over nominal value) and coolant outlet temperature for BP and PG, in case of EG manifolds optimized**

2.4.1.3.4 New design A

Compared to the reference design the following modifications have been implemented:

- PDP channels all parallel connected;
- EG manifolds optimized as discussed in paragraph 2.4.1.3.3;
- a localised pressure drop of 440 kPa has been put at the EG outlet in order to get the required mass flow;
- four parallel connections of FSLW with two FSLW in series instead of eight parallel different connections.

In Figure 2-34 the sketch of the circuits is shown.

The boundary conditions are the following:

- the total mass flow rate at main inlet is 33 kg/s;
- the water temperature at the main inlet is 35 °C;
- another inlet is present in order to feed the Plasma Grid and Bias Plate, here the total mass flow rate is 0.25 kg/s while the inlet water temperature is 150 °C;
- the pressure at the common outlet is 15 bar;
- the heat loads are those listed in in Table 2-5.

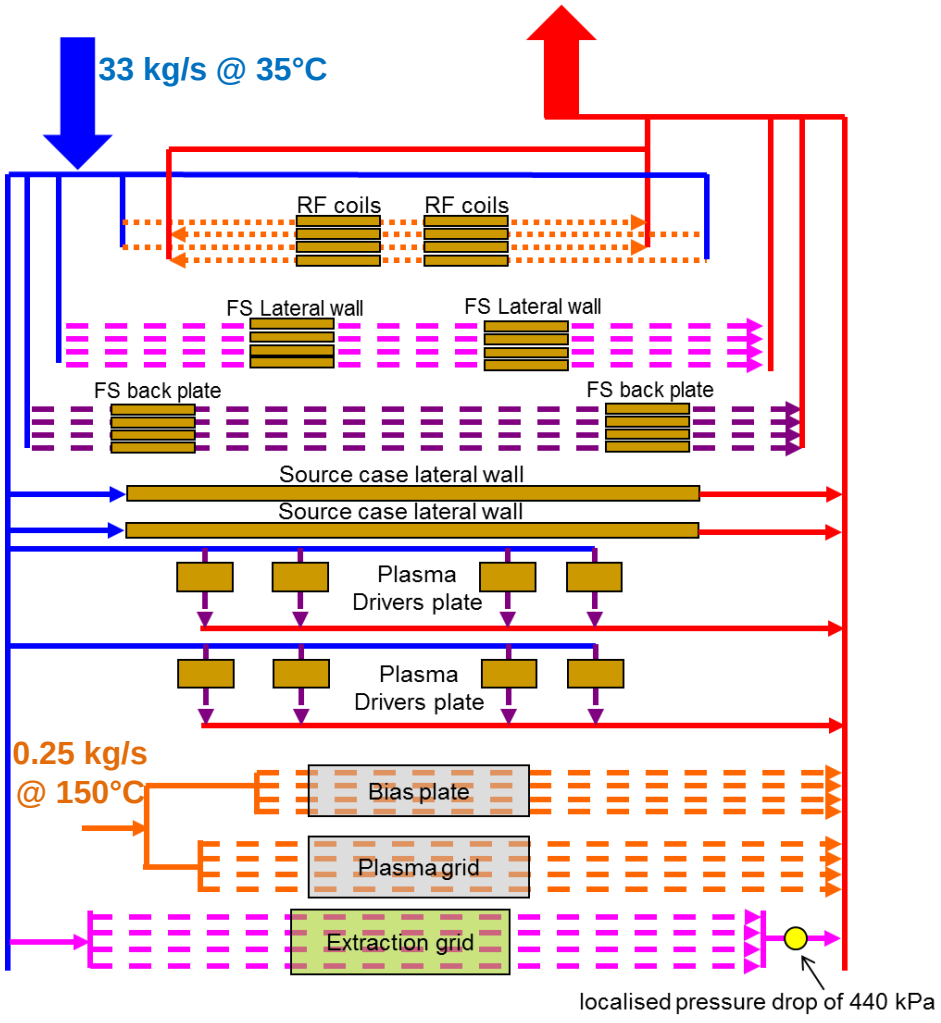

Figure 2-34 Sketch of the design A for the MITICA Beam Source cooling

The results are plotted in Figure 2-35 and Figure 2-36. The total pressure drop of the entire cooling circuit is 650 kPa and the coolant outlet temperature 51 °C.
As shown in Figure 2-35, with the mentioned modifications, a good flow balancing has been achieve and only the FSLW has still an higher mass flow rate.

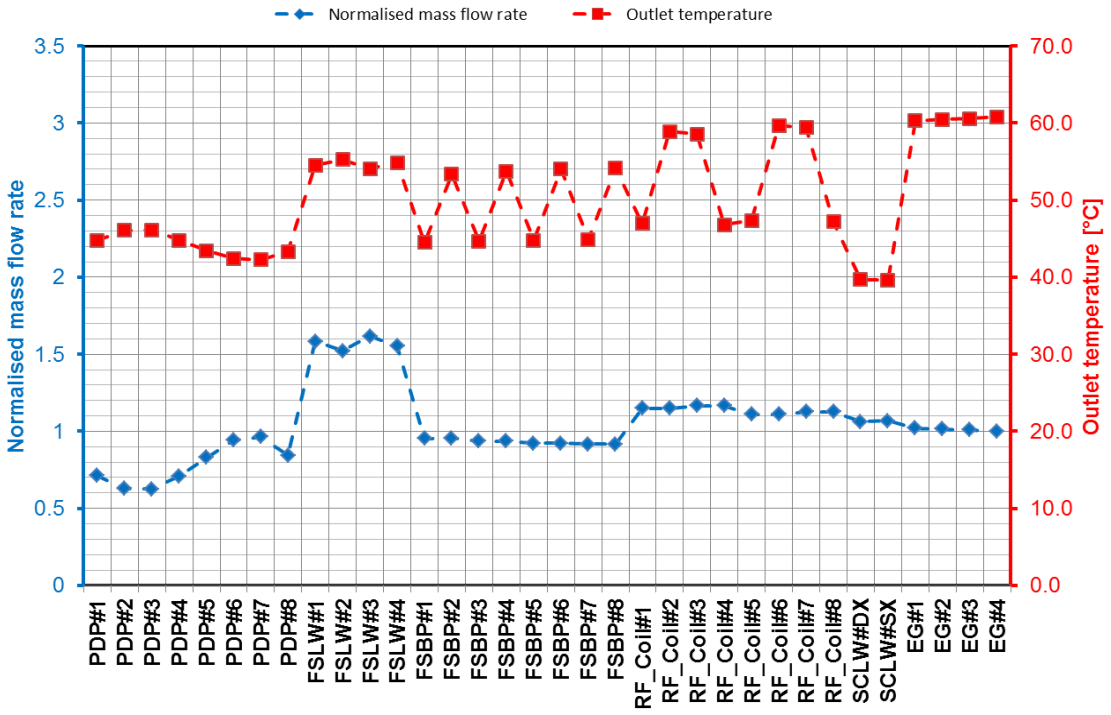

Figure 2-35 **Normalised mass flow rate (calculated over nominal value) and coolant outlet temperature in the design A for PDP, FSLW, FSBP, RF Coils, SCLW, EG**

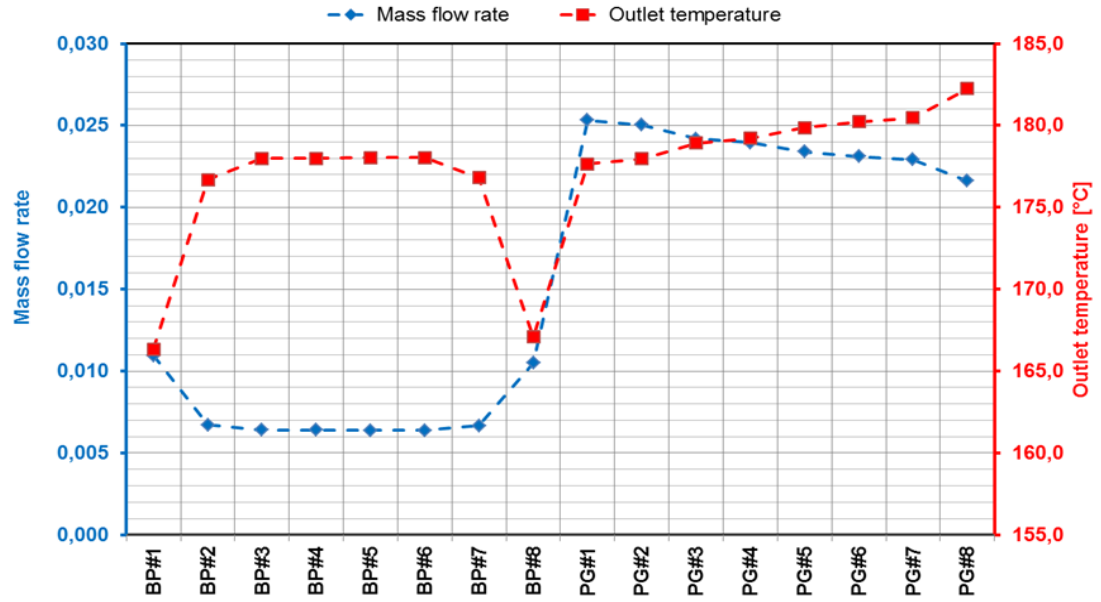

Figure 2-36 **Normalised mass flow rate (calculated over nominal value) and coolant outlet temperature in the design A for BP and PG**

2.4.1.3.5 New design B

Compared to the reference design the following modifications have been implemented:

- PDP channels all connected in parallel;
- EG manifolds optimized as discussed in paragraph 2.4.1.3.3;
- a localised pressure drop of 440 kPa has been put at the EG outlet in order to get the required mass flow;
- two localised pressure drops of 330 kPa have been put at the two FSLW outlet in order to get the required mass flow.

The boundary conditions are the following:

- the total mass flow rate at main inlet is 33 kg/s;
- the water temperature at the main inlet is 35 °C;
- another inlet is present in order to feed the Plasma Grid and Bias Plate, here the total mass flow rate is 0.25 kg/s while the inlet water temperature is 150 °C;
- the pressure at the common outlet is 15 bar;
- the heat loads are those listed in Table 2-5.

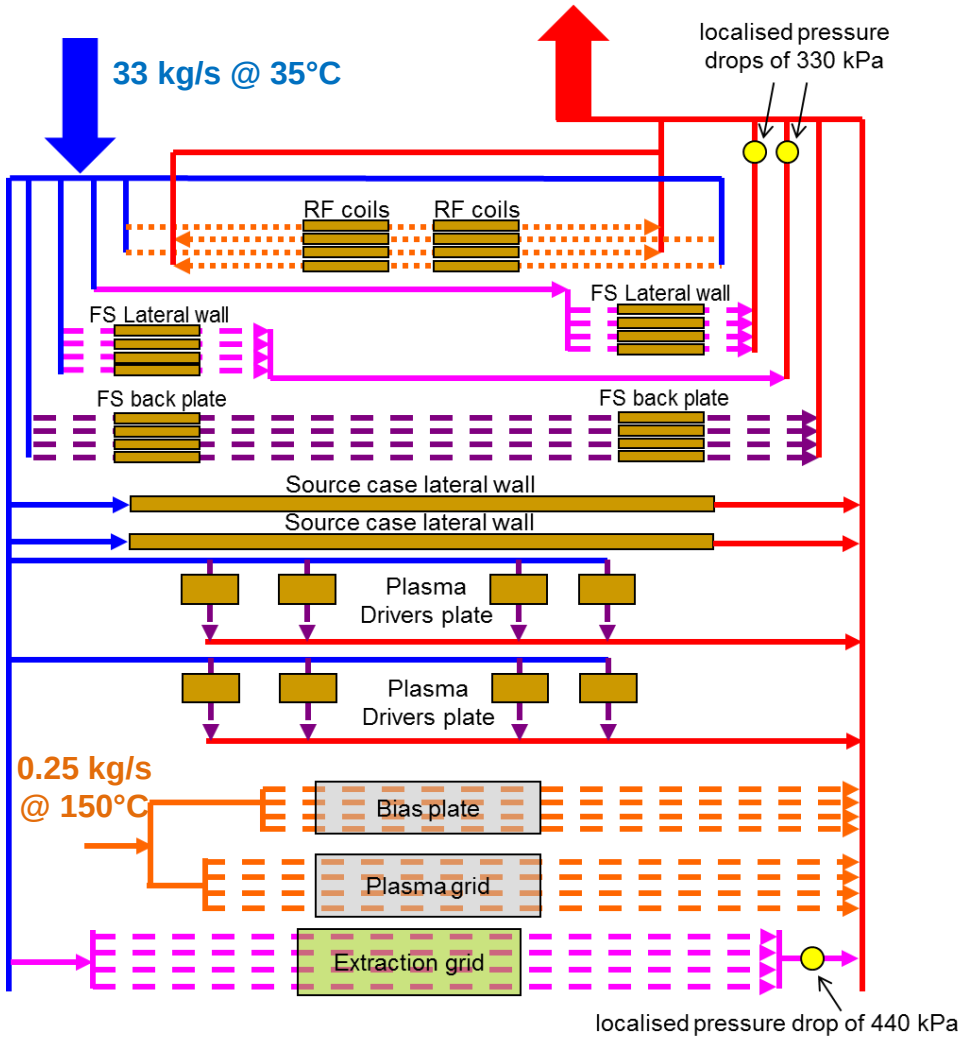

Figure 2-37 Sketch of the design B for the MITICA Beam Source cooling

The results are plotted in Figure 2-38 and Figure 2-39. The total pressure drop of the entire cooling circuit 620 kPa and the coolant outlet temperature is 51 °C.

As shown in Figure 2-38 the proposed modifications allow to achieve a really good flow balancing. The mass flow in some PDP channels is still under the nominal value, but is not possible to reach the nominal value in all the channels by using a total parallel connection which would requires 18 kg/s only for the PDP.

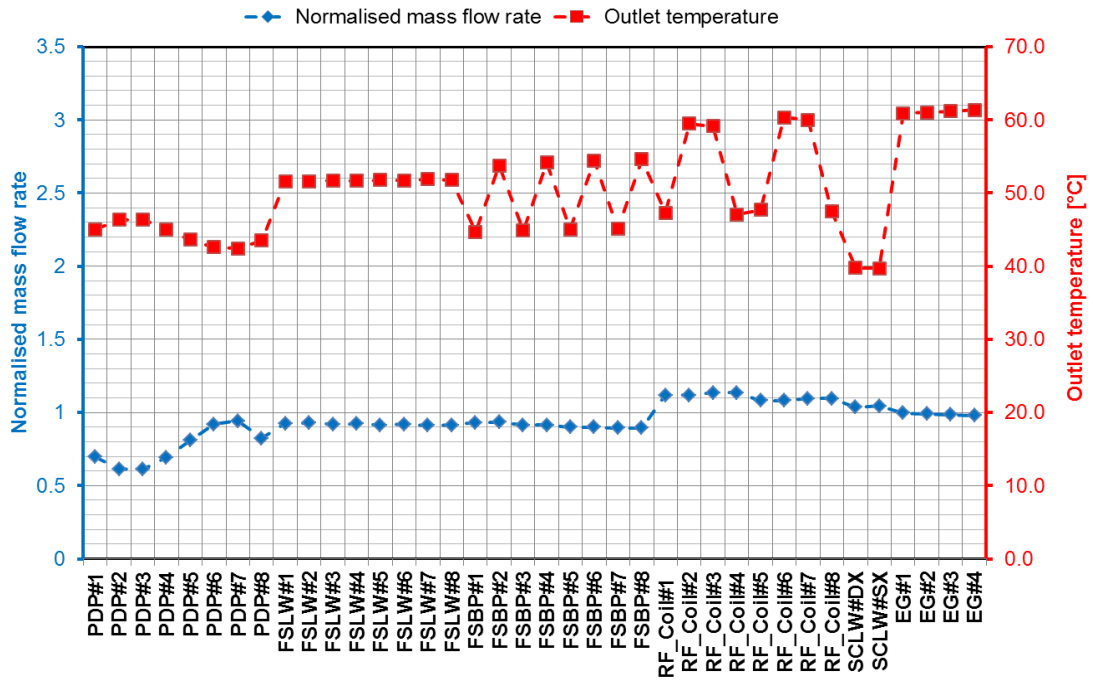

Figure 2-38 **Normalised mass flow rate (calculated over nominal value) and coolant outlet temperature in the design B for PDP, FSLW, FSBP, RF Coils, SCLW, EG**

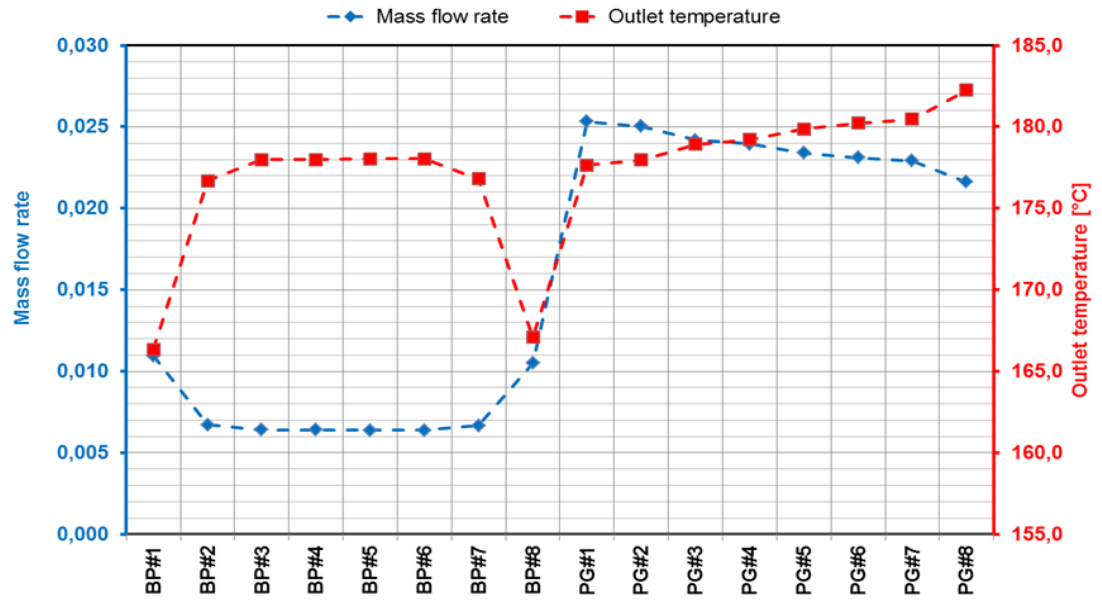

Figure 2-39 **Normalised mass flow rate (calculated over nominal value) and coolant outlet temperature in the design B for BP and PG**

2.4.1.4 Discussion

The developed integrated model of the MITICA RF ion source cooling system has been used as a versatile tool to analyse the proposed design. As the results didn't fulfil the requirements in terms of flow partitioning, different arrangements of the cooling circuit have been simulated.

First of all single minor modifications have been implemented by maintaining the original design as far as possible. The resulting improvement of the flow rate partitioning was not sufficient and new arrangements of the components have been modelled.

The best results have been obtained by using the so called design B in which, compared to the previous proposed design, the following modification are required:

- the PDP channels are all parallel connected;
- the EG manifolds have been optimised by reducing the pipe diameter assuming a maximum bulk velocity of about 3÷4 m/s;
- a localised pressure drop of 440 kPa has been inserted at the EG outlet;
- two localised pressure drops of 330 kPa have been inserted at the two FSLW outlets.

By adopting this solution, the total pressure drop of the cooling circuit is 620 kPa (instead of the 370 kPa expected in the first design).

As shown in Figure 2-38 the new design guarantee the correct flow rate in all the component except to the PDP#1, PDP#2, PDP#3 and PDP#4 for whom the water flowing in the channels is about 40% less than the desired value. The major constrain is given by the total inlet mass flow rate, thus by adopting an arrangement in which the PDPs are in parallel connected, the nominal required flow rates are not achieving everywhere.

The design B has been officially adopted for the MITICA RF ion source.

2.4.2 Grounded Grid and Electron Dump

The MITICA Grounded Grid (GG) and Electron Dump (ED) are cooled down by a common cooling system (shown in Figure 2-40).

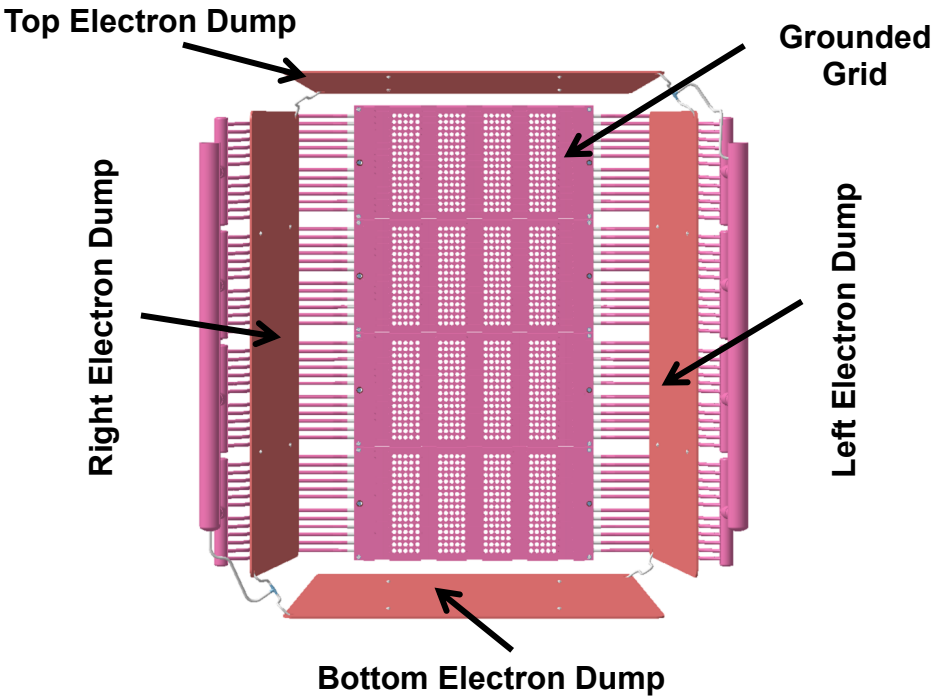

Figure 2-40 Overview of the grounded grid and electron dump cooling system

The cooling circuit has been analysed in order to get the foreseen mass flow rate partitioning inside each component, the outlet coolant temperature and the pressure drop of the entire system.

The GG is composed of 4 identical segments. Each grid segment is connected to the main manifolds and it is fed in parallel with the others. The ED is made of four panels: the right and top ones are hydraulically connected in series and then fed in parallel with the series of the bottom and left ED panels. The cooling water is derived directly from the main inlet manifold and returns through the main outlet manifold.

2.4.2.1 CFD Sub-Modelling

The Grounded Grid has been analysed by using ANAYS CFX in order to obtain the characteristic curve (pressure drop vs. mass flow rate) of each segment.
The nominal mass flow rate for one segment is 4.7 kg/s and the corresponding pressure drop equals to 414 kPa [23].
An ideal parabolic trend of the pressure drop has been assumed. The total heat load is 1485 kW for the entire Grounded Grid [23].

The cooling channels of the four Electron Dump panels have been simulated directly in Flowmaster by using the *pipe* elements. The total heat load is 7.5 kW for each panel [24].

2.4.2.2 Integrated 1D model

In Figure 2-41 the implemented cooling circuit model of the MITICA GG and ED is shown. The experimental components have been simulated by using discrete losses with the calculated pressure drop curve following by heat exchangers.

Each GG segment has been simulated by using 12 parallel channels where each localise pressure drop has the characteristic curve reported in Table 2-10 and an imposed thermal power of 31 kW. A magnification of one Grounded Grid segment is shown in Figure 2-42 where it is possible to distinguish between the 12 different channels.

Table 2-10 Grounded Grid: pressure drop vs. mass flow rate values

Mass flow rate [kg/s]	Pressure Drop [kPa]
0.20	104
0.39	414
0.59	932

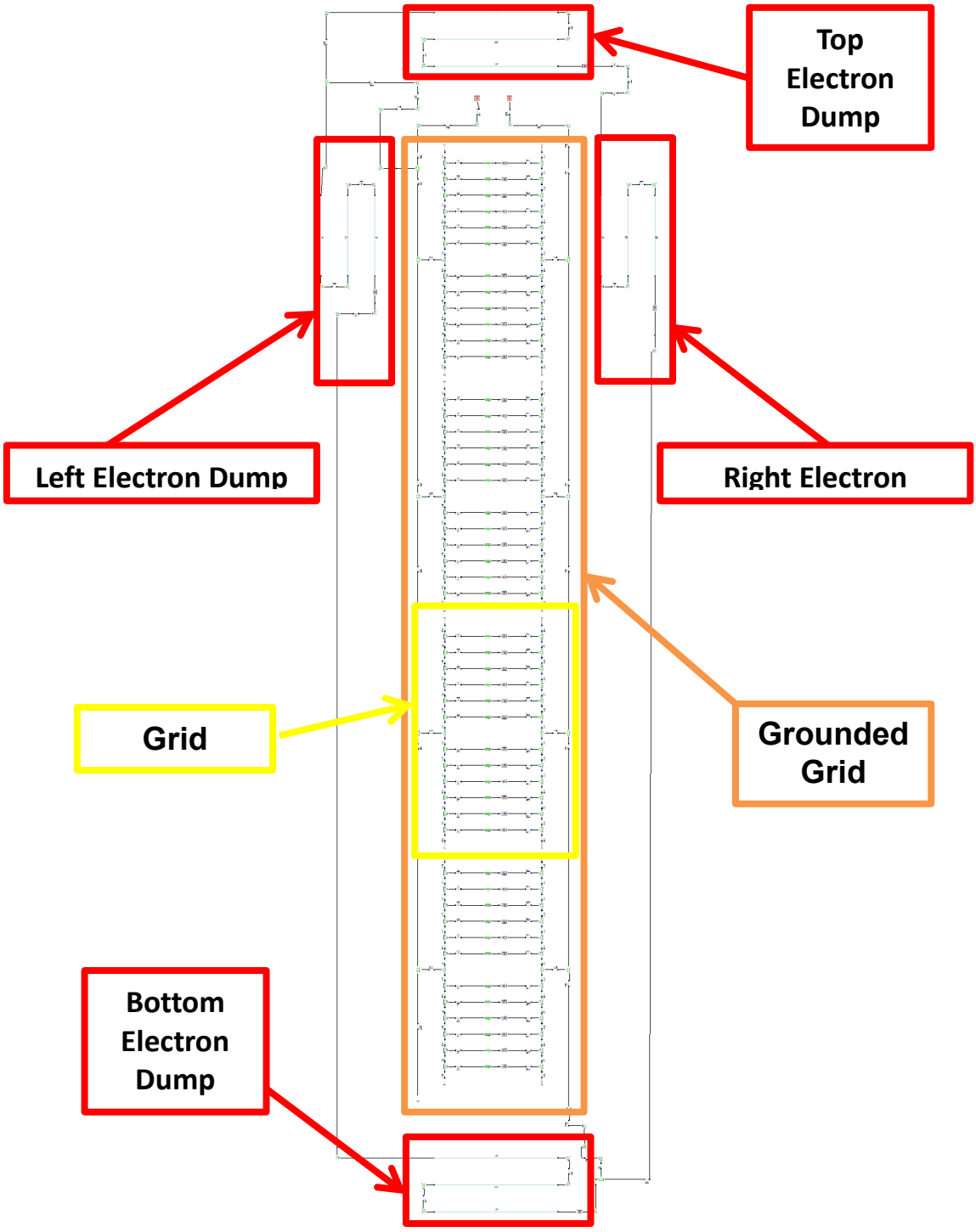

Figure 2-41 Overview of the hydraulic network in Flowmaster

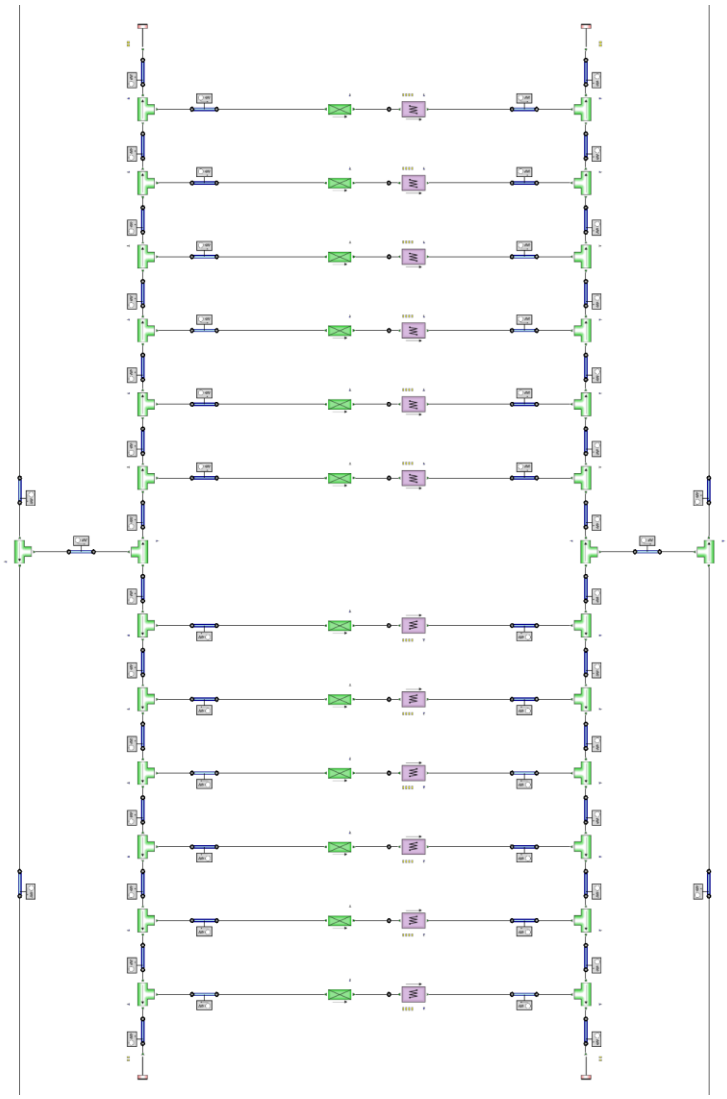

Figure 2-42 Magnification of one Grounded Grid segment

2.4.2.3 Results

The 1D CFD thermo-hydraulic model has been used to evaluate the mass flow rate partitioning and outlet coolant temperatures in each cooling circuit in different scenarios. In the following, the results of the simulations are reported by using the nomenclature shown in Figure 2-43.

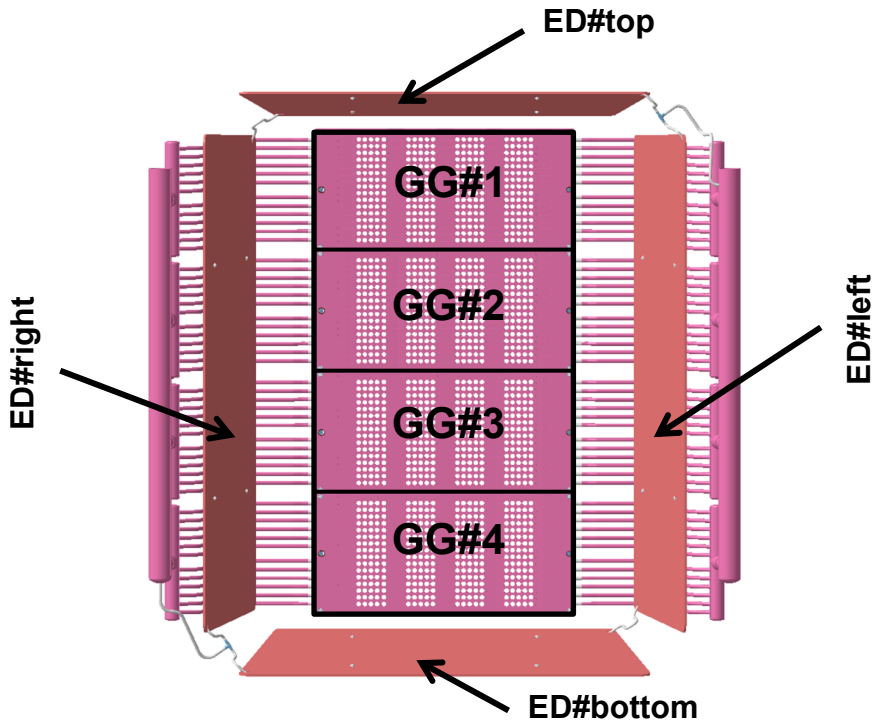

Figure 2-43 Nomenclature of the components used to show the results

2.4.2.3.1 Nominal scenario

The boundary conditions for cooling water in the nominal case are the following:

- the total mass flow rate at the inlet is 19.5 kg/s;
- the water temperature at the inlet is 35 °C.

According to the results of the simulation, the total pressure drop of the entire cooling circuit is 624 kPa and the coolant outlet temperature 54 °C. With respect to the nomenclature in Figure 2-43, the detailed results for each sub-component are reported in Table 2-11 and plotted in Figure 2-44**.**

Table 2-11 **Mass flow rate and coolant outlet temperature in the nominal case**

Component	Mass flow rate [kg/s]	Outlet temperature [°C]
GG#1	4,84	53
GG#2	4,82	54
GG#3	4,81	54
GG#4	4,80	54
ED#bottom	0,11	51
ED#left	0,11	67
ED#right	0,11	51
ED#top	0,11	67

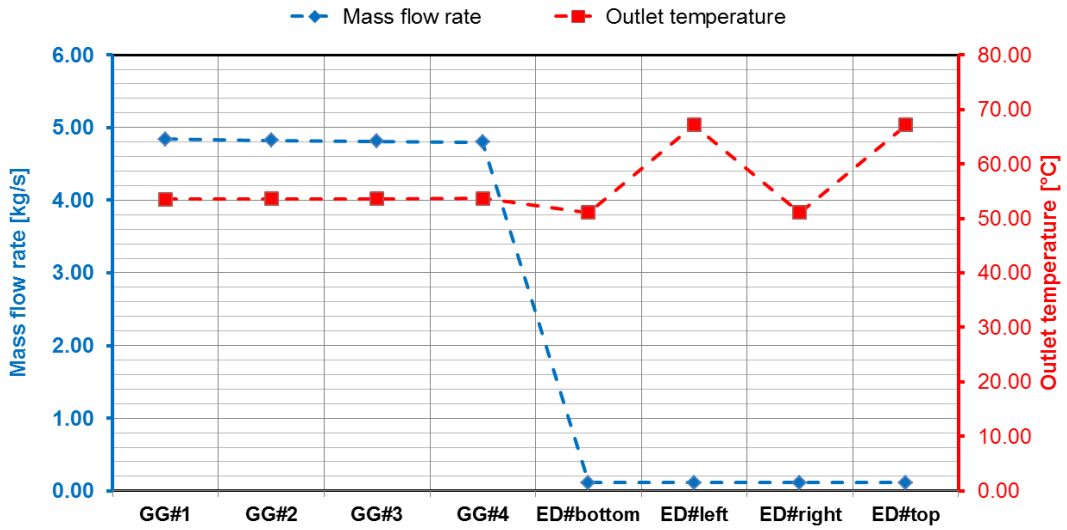

Figure 2-44 **Mass flow rate and coolant outlet temperature in the nominal case**

In order to understand how the pressure drops are distributed along the cooling circuit, with respect to the Figure 2-45, five different parts have been identified and the pressure drop along each part is reported in Table 2-12.
Please note that the Electron Dump cooling circuit is not shown: the total pressure drop is dominated by the Grounded Grid part.

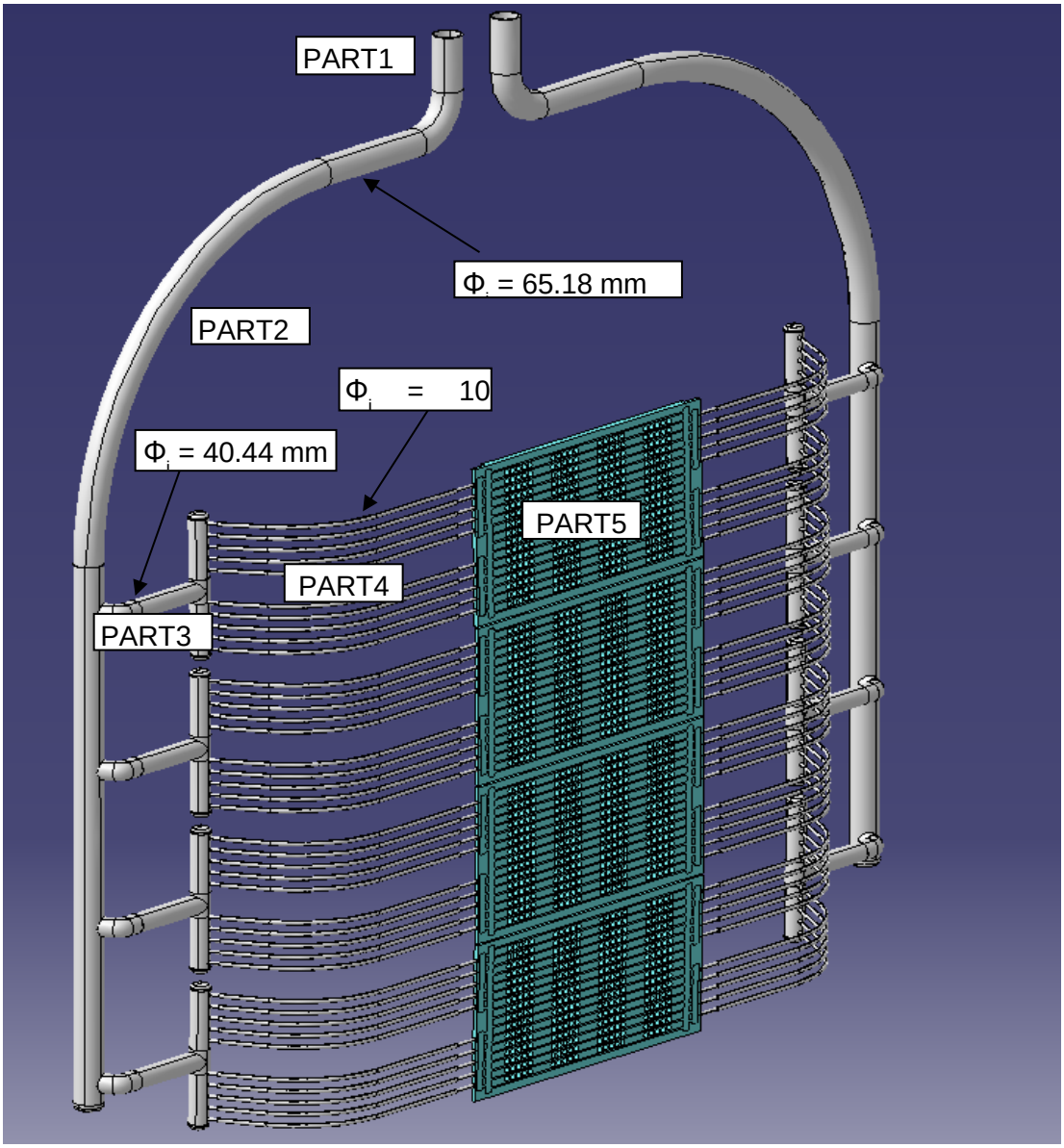

Figure 2-45 **Overview of the cooling system without the electron Dump circuits**

Table 2-12 **Pressure drop distribution along the Grounded Grid cooling system**

Item	Pressure drop [kPa]
PART1	20
PART2	12
PART3	27
PART4	36
PART5	447

2.4.2.3.2 Other possible scenario

The cooling system which supplies the coolant water can vary the mass flow rate during the operations. Different case studies have been simulated to check the flow partitioning and the outlet coolant temperatures:

- SCENARIO#1: total mass flow rate equals to 9.75 kg/s (50% of the nominal mass flow);
- SCENARIO#2: total mass flow rate equals to 14.63 kg/s (75% of the nominal mass flow);
- SCENARIO#3: total mass flow rate equals to 21.45 kg/s (110% of the nominal mass flow).

In all the possible scenarios mentioned above, the temperature of the water at the inlet has been set to 35 °C and the thermal powers on the components are always set to the nominal values (1485 kW for the entire Grounded Grid and 7.5 kW for each Electron Dump panel).

Table 2-13 Mass flow rate partitioning and outlet temperature in different scenarios

	SCENARIO#1 (9.75 kg/s)		SCENARIO#2 (14.63 kg/s)		SCENARIO#3 (21.45 kg/s)	
Component	**Mass flow rate [kg/s]**	**Outlet temperature [°C]**	**Mass flow rate [kg/s]**	**Outlet temperature [°C]**	**Mass flow rate [kg/s]**	**Outlet temperature [°C]**
GG#1	2,42	72	3,63	60	5,32	52
GG#2	2,41	72	3,62	60	5,31	52
GG#3	2,41	72	3,61	60	5,29	52
GG#4	2,40	72	3,60	60	5,28	52
ED#bottom	0,05	68	0,08	57	0,12	50
ED#left	0,05	100	0,08	78	0,12	64
ED#right	0,05	68	0,08	57	0,12	50
ED#top	0,05	100	0,08	78	0,12	64

The water flow distribution among the segments is highly uniform in all the different scenarios.

The maximum temperatures (~100 °C) are found at the Right Electron Dump and Bottom Electron Dump in the SCENARIO#1 which is the lowest mass flow scenario. Although this temperature is fully acceptable, this scenario is not considered as an operational one, but could occur in case of a failure in the cooling system.

The proper accelerator grid alignment can be obtained by controlling the grid thermal elongation, thus in SCENARIO#2 and #3 the cooling water flow is modulated to obtain this effect.

The total pressure drop of the circuit and the outlet temperature of the water in the different cases are reported in Table 2-14. In Figure 2-46 the characteristic pressure drop of the entire cooling circuit is reported.

Table 2-14 System pressure drop and outlet temperature in different scenario

	Total Pressure Drop [bar]	Outlet temperature [°C]
SCENARIO#1	1.58	72.18
SCENARIO#2	3.53	59.85
SCENARIO#3	7.54	52.08

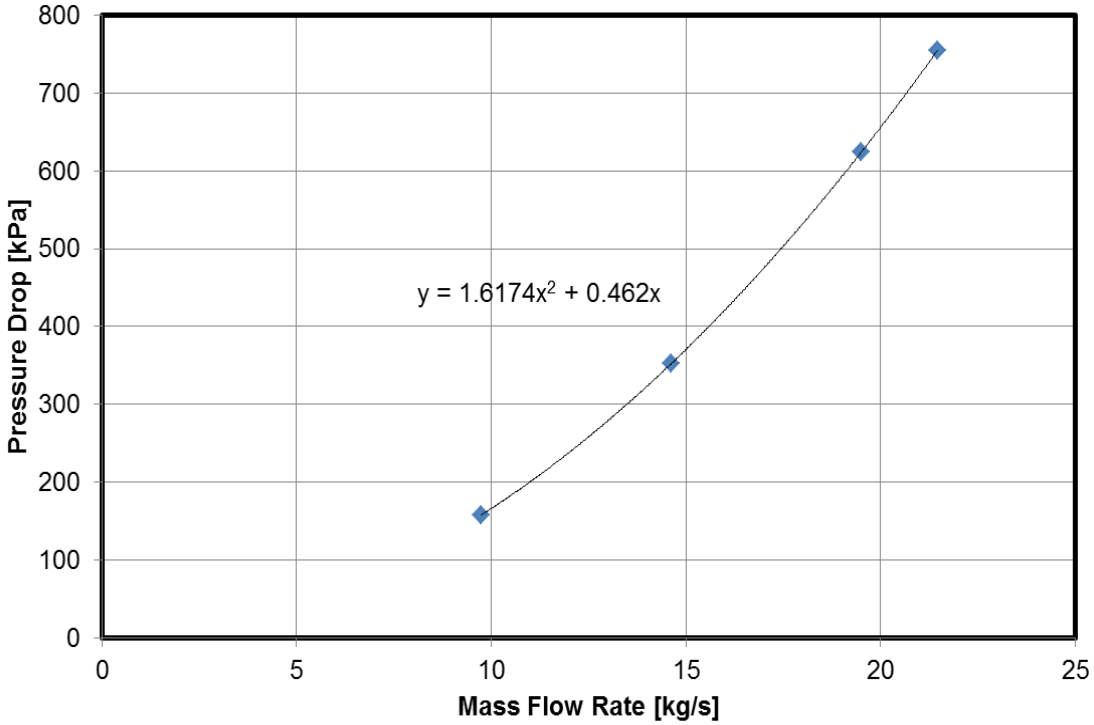

Figure 2-46 Characteristic curve *Pressure Drop vs. Mass Flow* rate for the entire Grounded Grid and Electron Dump cooling system

2.4.2.4 Discussion

The one-dimensional thermo-hydraulic model of the MITICA grounded grid and electron dump has been developed and used to analyse the flow partitioning and the coolant outlet temperature for each active cooled element of the cooling circuit. The results (Figure 2-44) show a flow distribution and outlet temperature fully acceptable. The total pressure drop of the system is equal to 624 kPa with the nominal flow of 19.5 kg/s.

Other scenarios have been simulated in order to characterise the cooling circuit at different mass flow rate (Figure 2-46).

2.5 Neutraliser

The MITICA Neutraliser, being the first Beam line Component (BLC), plays an important role and it is subjected to heating by beam and co-accelerated particles. An isometric view, with the component naming of the visible elements, is shown in Figure 2-47.

The neutralisation of beam ions occurs in the Neutraliser along four vertical channels of rectangular cross-section, each 3 m long and 1.7 m high, laterally delimited by five OFHC copper walls. The panels are cooled down by demineralised water running inside 14 vertical channels (manufactured by deep-drilling). The closed cooling circuit is realised by welded plugs. Other oxygen free (OF) copper panels are placed at the top and bottom sides of the Neutraliser. The edges of the five panels, at the beam entrance section, subjected to high heat loads due to power deposition from accelerated beam ions and electrons that are stripped in the accelerator, are protected by leading edge elements (LEEs) made of CuCrZr alloy with twisted tapes as turbulence promoters. Additional copper panels, placed around the Neutraliser entrance section, constitute the ion and electron dumps that represent a protection against accelerated particles with diverging trajectories towards the cryopumps and vessel [25].

The Neutraliser cooling circuit is shown in Figure 2-48. The design shall guarantee the suitable flow rate partitioning among the different circuits and the analyses have been focused in particular on the bulk coolant temperature: a maximum outlet temperature of 110 °C must be guaranteed inside the panel channels, according to requirements from PED (Pressure Equipment Directive) hazard classification, in order to simplify the procedure to affix the CE marking. The same requirement is not foreseen for the LEEs because of their small water volume.

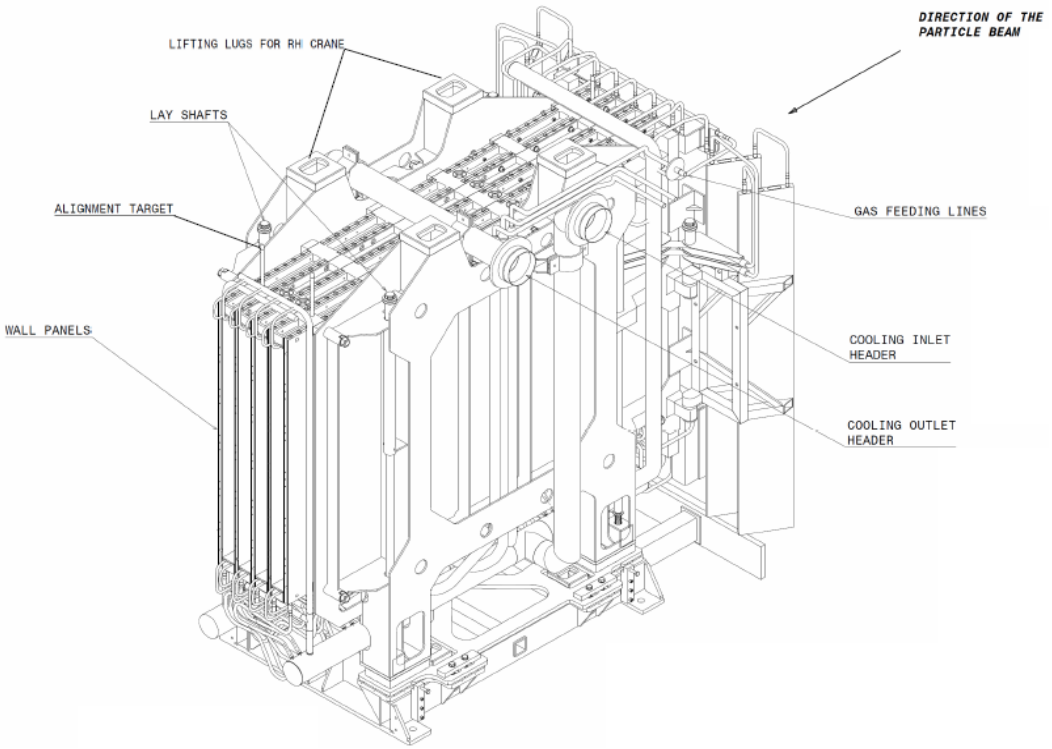

Figure 2-47 Isometric NED view and naming of the main visible elements

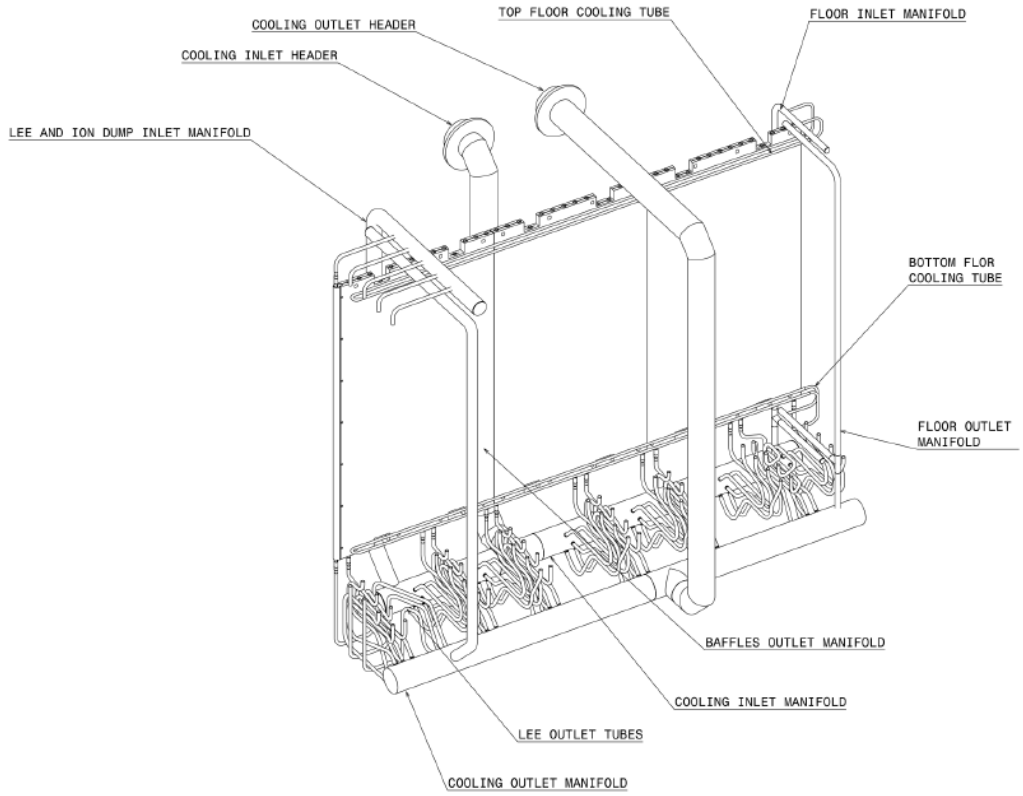

Figure 2-48 NED cooling circuit view and its main elements; a vertical panel is also shown

2.5.1 Thermal Loads

The thermal loads on the actively cooled elements depend on the beam parameters. The reference beamlet parameters are defined by maximum deposition of power onto the component: 7 mrad beam core divergence, 30 mrad halo divergence with 15% halo power fraction; this beamlet scenario has been considered.

The cooling circuit simulation considers as input data the values of heat power due to ions and electrons [26] calculated by means of the codes Trigo and Backscat [27].

As shown in Figure 2-49, each panel is divided into 14 sectors; this sub-division replicates the scheme of the cooling circuits that are composed by 14 vertical segments, thus, the sectors represent the surfaces from which the heat is collected by each single segment. The upstream sector (1/14 of the surface, first from left) of each panel is shadowed by the previous panel or by the leading edge element, and receives less beam halo power. In the attempt of uniformly collect the halo power, the positioning of the channel circuit inside the panels is therefore non-symmetrically placed, and the surface is divided in accordance.

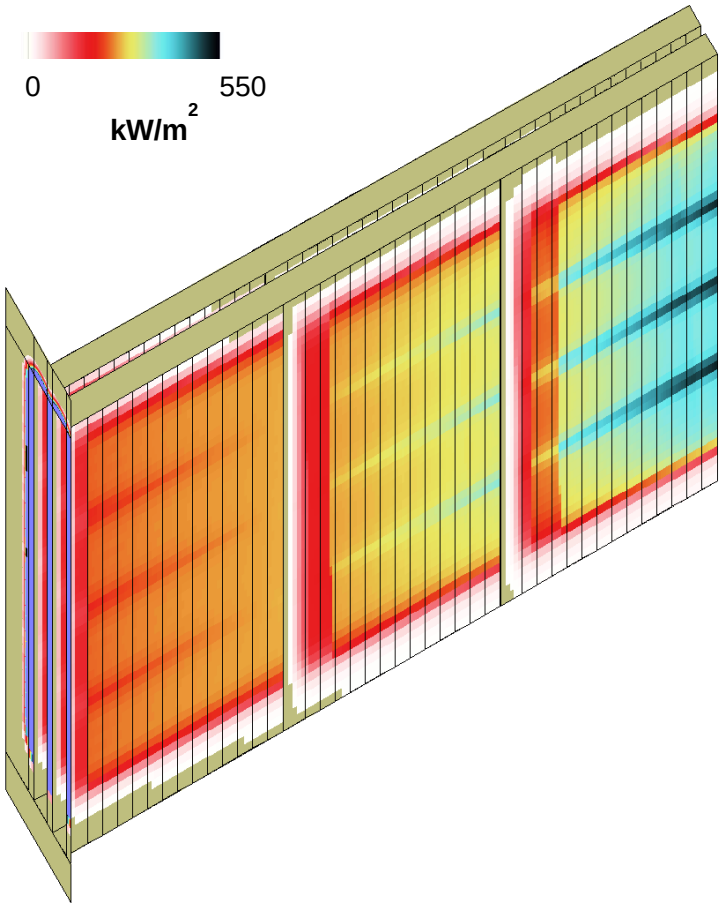

Figure 2-49 **Power densities on the surfaces dividing the panels according to the cooling circuit routing**

2.5.2 Sub-Modelling of piping elements

Because of the particular geometry of some piping elements, the development of sub-models is needed in order to predict their hydraulic behaviour.

In particular the following sub-models have been obtained:

1) swirl tube;
2) expansion joint pipes.

2.5.2.1 Swirl channels modelling

Twisted tapes are foreseen inside the *Leading Edge Elements* (LEE) as turbulence promoters. The hydraulic behaviour of these elements have been characterised by using analytical formulas in order to find the characteristic curve pressure drop vs. mass flow rate.

The hydraulic diameter is defined as:

$$D_h = \frac{4A}{P_w} = D_i \frac{\pi D_i - 4\delta}{2D_i + \pi D_i - 2\delta} \qquad \text{Eq. 15}$$

where A is the flow area [m^2], P_w the wetted perimeter [m], D_i the inner diameter and δ the twisted tape thickness [m]

The Reynolds number, referred to the hydraulic diameter and swirl flow, is given by Eq. 16 ($K_{sw}=\pi D_h/pitch$ is the twist ratio, and *pitch* is the distance between two homologous consecutive elements of the inserted twisted tape [m], D_h the hydraulic diameter [m], v is the axial component of the fluid velocity [m/s], ρ_b is the mass density of the bulk [kg/m^3], μ_b is the dynamic viscosity of the bulk [Pa s]).

$$Re_{sw} = (1 + K_{sw}^2)^{0.5} \left(\frac{v\, \rho_b D_h}{\mu_b} \right) \qquad \text{Eq. 16}$$

The non-linear Colebrook-White correlation for turbulent flow [29] modified in order to take in account the swirl flow, has been used for the friction factor f_{sw} calculation (in the Fanning form):

$$\frac{1}{\sqrt{4f_{sw}}} = -2\, log_{10}\left(\frac{2.51}{Re_{sw}\sqrt{4f_{sw}}} + \frac{\varepsilon_r}{3.71}\right) \qquad \text{Eq. 17}$$

where $\varepsilon_r=\varepsilon/D_h$ is the reduce roughness.

Finally, the pressure drop along the swirl channel is given by:

$$\Delta p = 4f_{sw} \frac{L}{D_h}\, \rho_b (1 + K_{sw}^2)^{\frac{3}{2}}\, \frac{v^2}{2} \qquad \text{Eq. 18}$$

where L is the tube length [m].

A Matlab [28] routine has been implemented to solve the above listed equations. The characteristic pressure drop curve shown in Figure 2-50 have been obtained for the following geometrical parameters:

- internal diameter: 18 mm;
- pitch: 70 mm;
- tape thickness: 4 mm;
- length: 1.85 m.

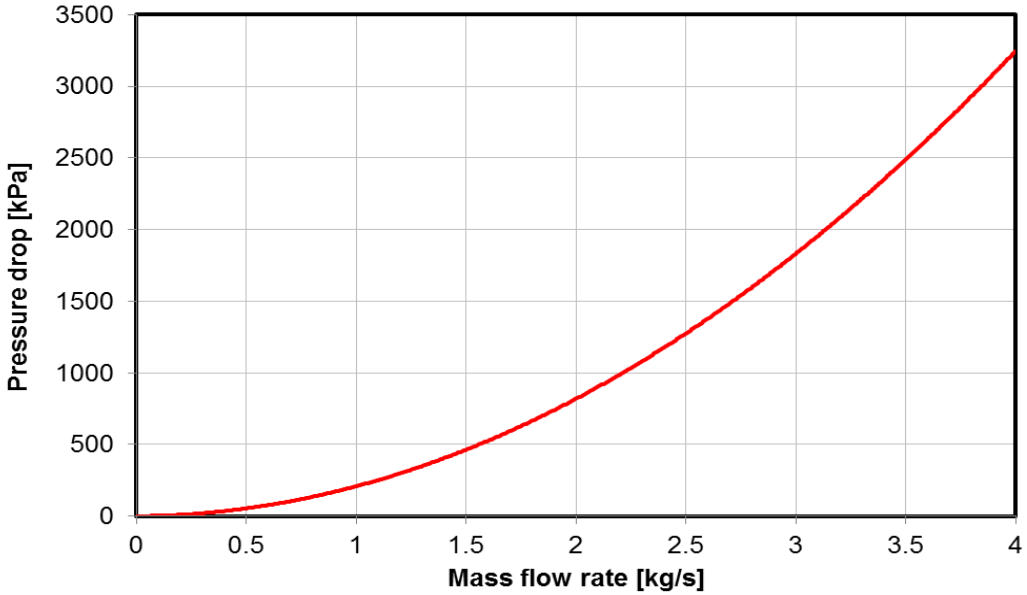

Figure 2-50 **Leading Edge Element: characteristic curve Pressure drop vs. Mass flow rate**

2.5.2.2 Expansion joint pipes modelling

The hydraulic behaviour of the expansion joint pipes (Figure 2-51) have been analysed with ANSYS CFX in order to obtain the characteristic curve *Pressure drop vs. Mass flow rate* to be used in the global model of the cooling circuit. The sub-models have been simulated by using the *k-ε* turbulent model. These joints consist of bent tubes providing some flexibility to accommodate differential thermal expansions of end parts connected by the tubes.

Two main groups of expansion joints are recognizable: the *Leading edge outlet expansion joints* and the *Panel inlet/outlet expansion joints.*

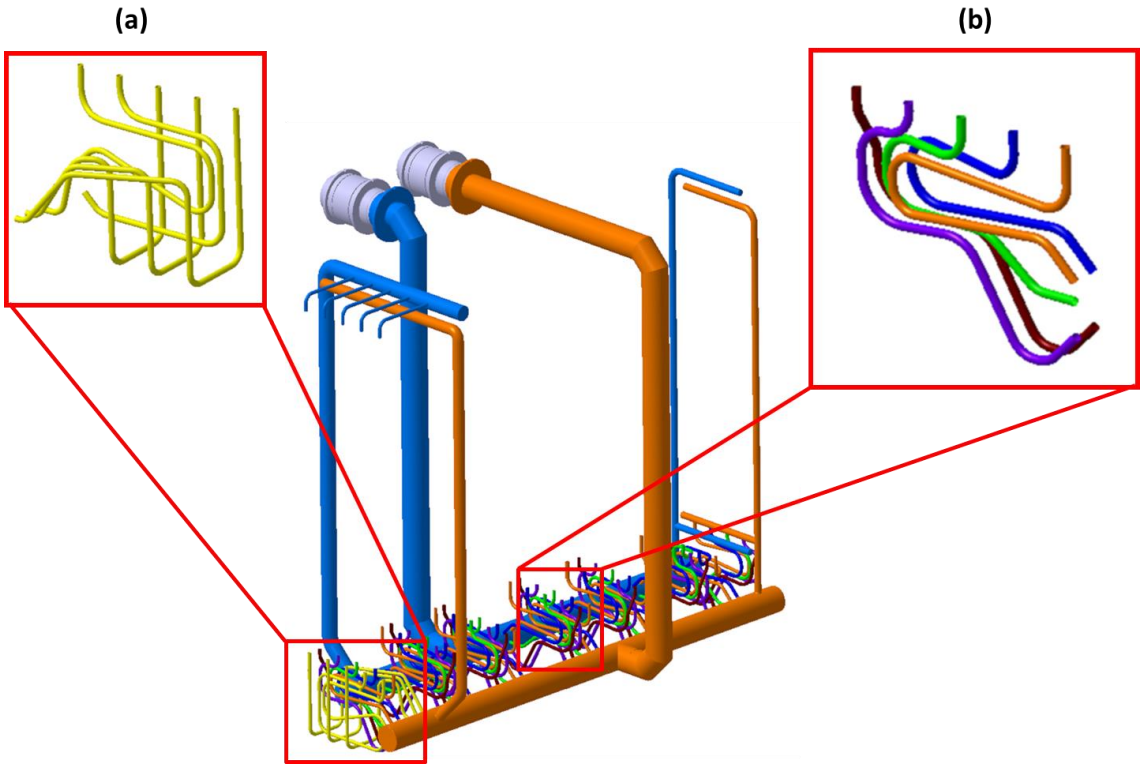

Figure 2-51 **Expansion joints: magnifications of the two main groups. (a) Leading edge outlet expansion joints; (b) Panel inlet/outlet expansion joints**

For the *Leading edge outlet expansion joints* (one of them is visible in Figure 2-52) the following main mesh parameters have been used and the results are shown in Figure 2-53 with the characteristic parabolic trend:

- **maximum element size**: 1 mm;
- **inflation layer**: 5 layers, first layer height equals to 0.5 mm and grow rate equals to 1.2;
- **number of elements**: 2.9×10^6.

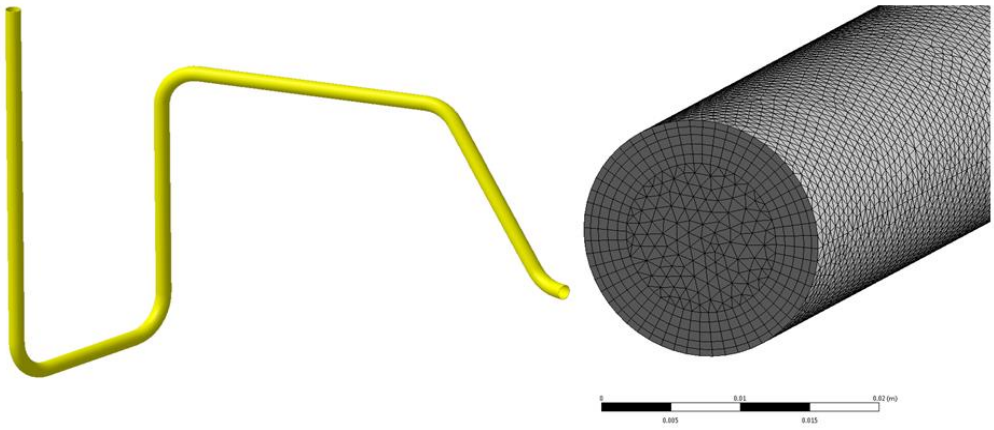

Figure 2-52 **Leading edge outlet expansion joint #1: overview and magnification of the mesh**

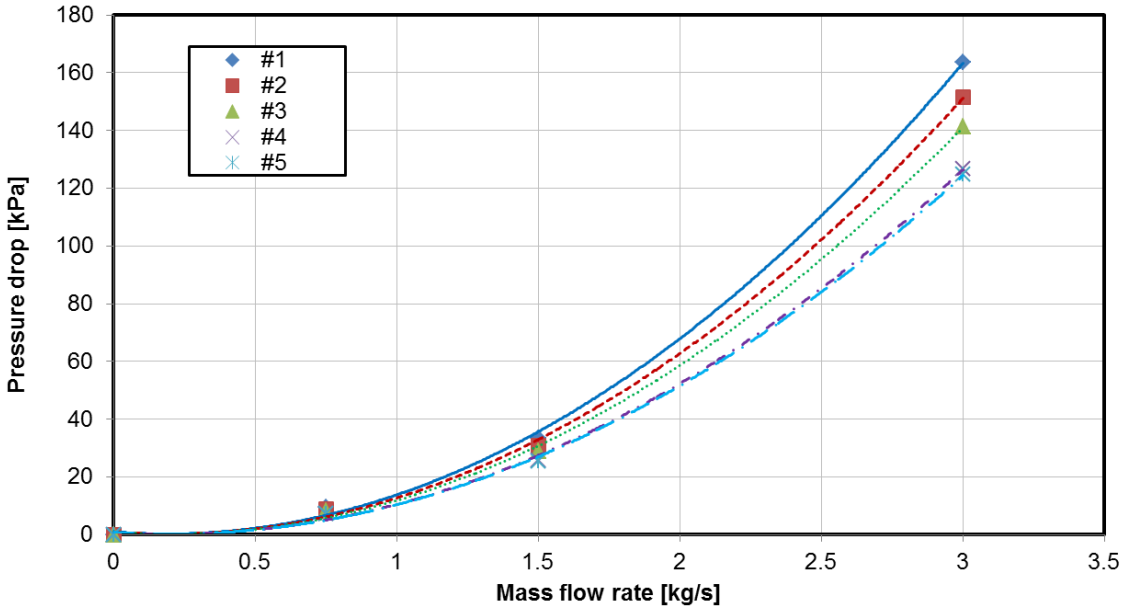

Figure 2-53 **Leading edge outlet expansion joints: characteristic curve *Pressure drop vs. Mass flow rate***

The same analyses have been carried out for the *Panel inlet/outlet expansion joints* and the results are in Figure 2-54.

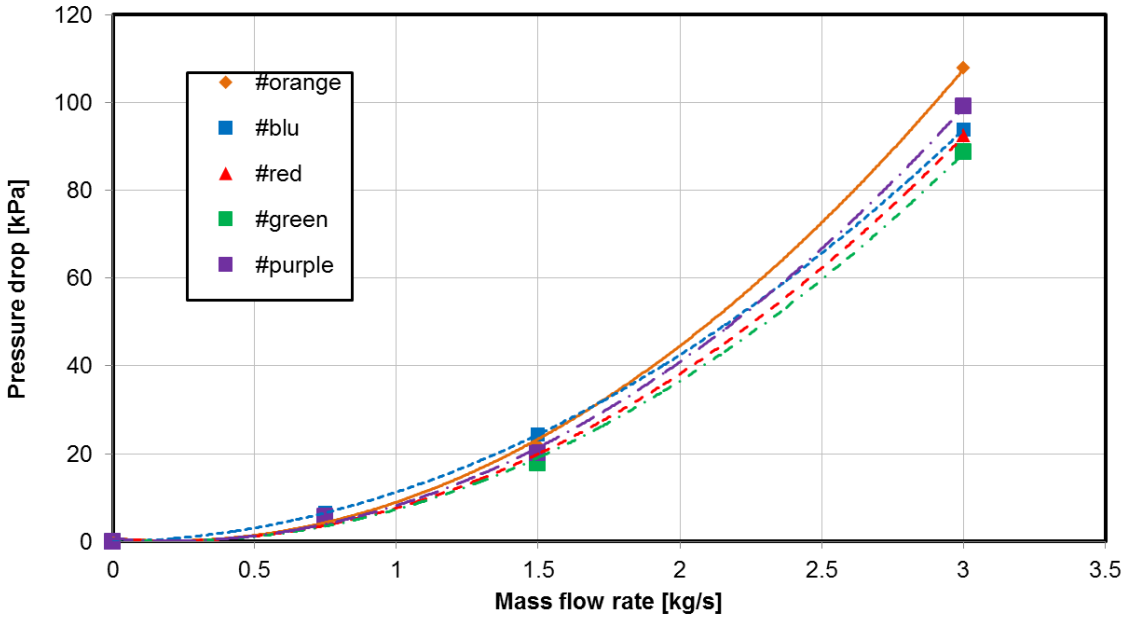

Figure 2-54 **Panel inlet/outlet expansion joints: characteristic curve *Pressure drop vs. Mass flow rate***

2.5.3 Integrated Neutraliser cooling circuit model

The following cooling circuits have been identified and they are sketched in Figure 2-55:

- five vertical panels within which the cooling circuits are separated in two lines, the downstream circuits and the upstream circuits (D and U). Due to the expected power density distribution on the panel surfaces, the upstream circuits are longer than the downstream circuits;
- the top spacer cooling circuits (TS) and the bottom spacer cooling circuits (BS);
- the cooling circuits inside the *Leading Edge Elements* (LEE);
- the cooling circuit inside the *Ion Dump* (ID);
- the cooling circuit inside the *Electron Dump* (ED);
- the cooling circuits inside the *Right Electron Dump* (RED);
- the cooling circuits inside the *Left Electron Dump* (LED).

The thermo-hydraulic 1D model (Figure 2-56) has been made with Flowmaster code and it has been used to evaluate the mass flow rate partitioning and outlet coolant temperatures in each cooling circuit.

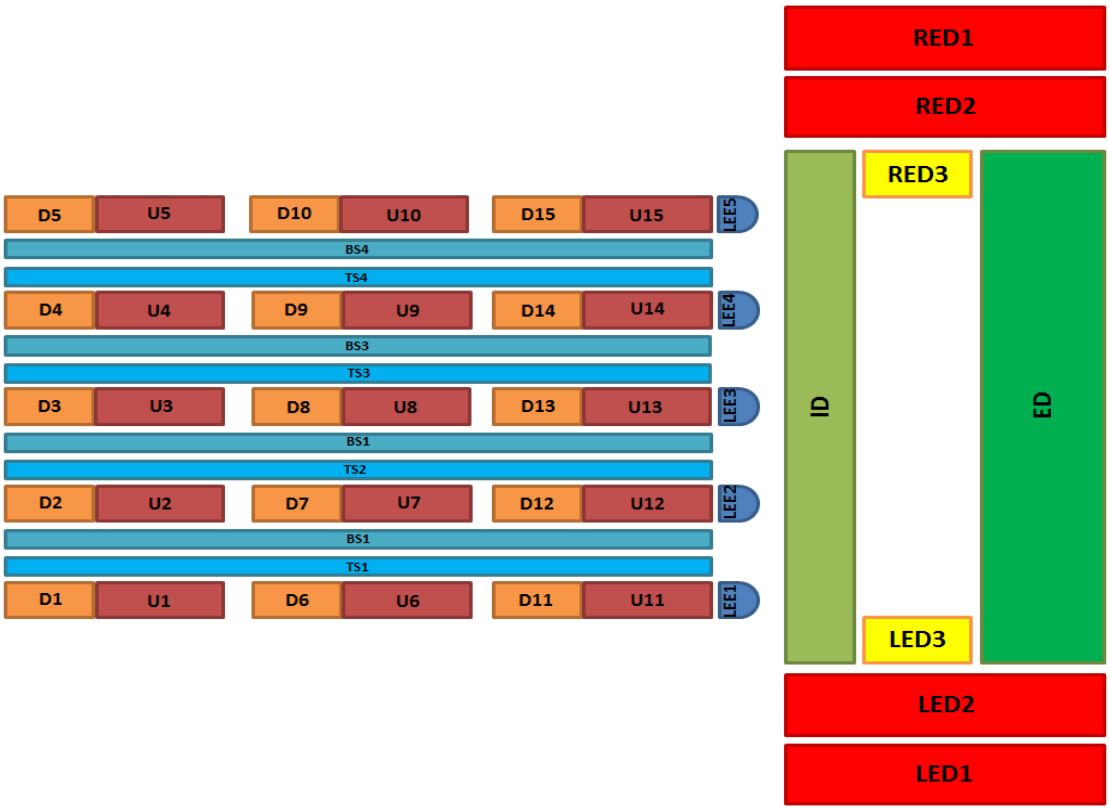

Figure 2-55 Cooling scheme of the Neutraliser

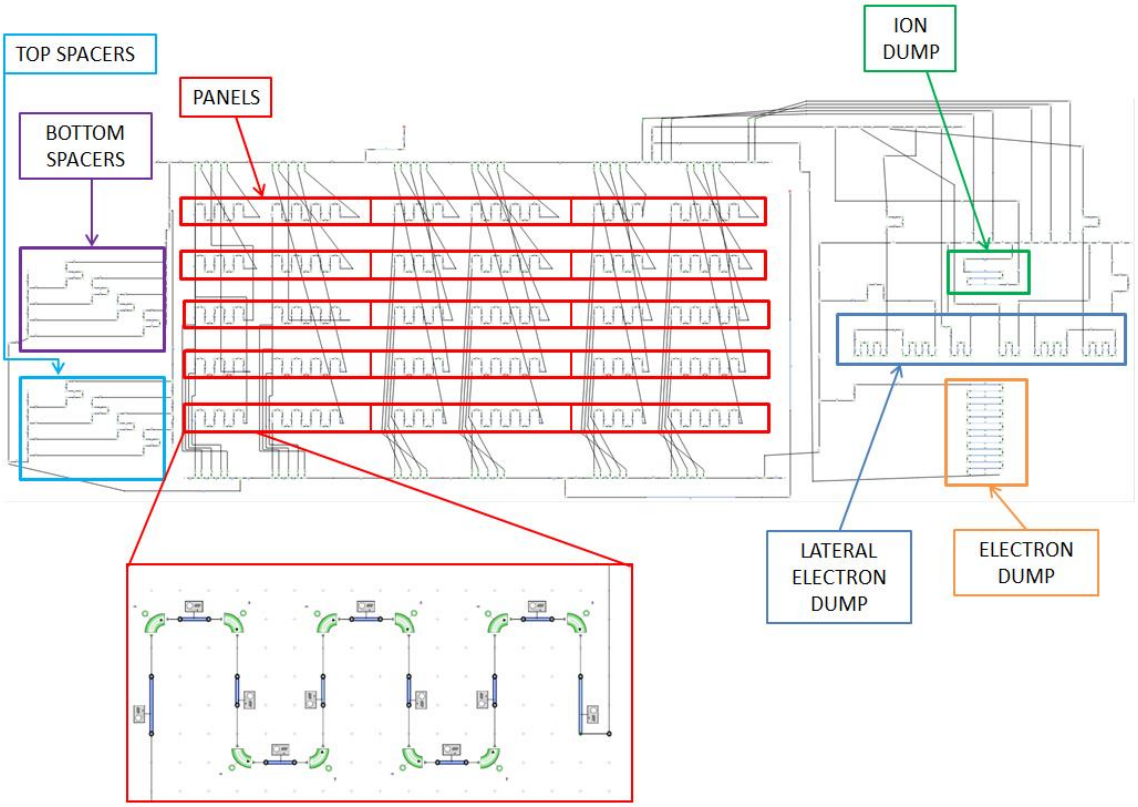

Figure 2-56 **Entire view of the model created in Flowmaster of the Neutraliser cooling system. Due to its large extension the figure is not really understandable but all the cooling circuits are indicated and a magnification of a small part is present in the bottom part**

2.5.4 Results

Even if the PRIMA cooling plant is able to supply the MITICA Neutraliser up to 80 kg/s with inlet water temperature within the range of 20÷55 °C [10], the operations on ITER are foreseen with 50÷55 kg/s at 35 °C, the remaining mass flow rate is considered unnecessary.

Two different scenarios have been taken in account:

- SCENARIO#1 in which the total mass flow rate is 50 kg/s;
- SCENARIO#2 in which the total mass flow rate is 55 kg/s.

The inlet water temperature for both the cases is 35 °C and the outlet pressure has been set at 1.7 MPa.

Figure 2-57 shows the mass flow rate and the water velocity inside each component for both the scenarios. The total pressure drop for the SCENARIO#1 is 300 kPa, while 360 kPa has been found for the SCENARIO#2.

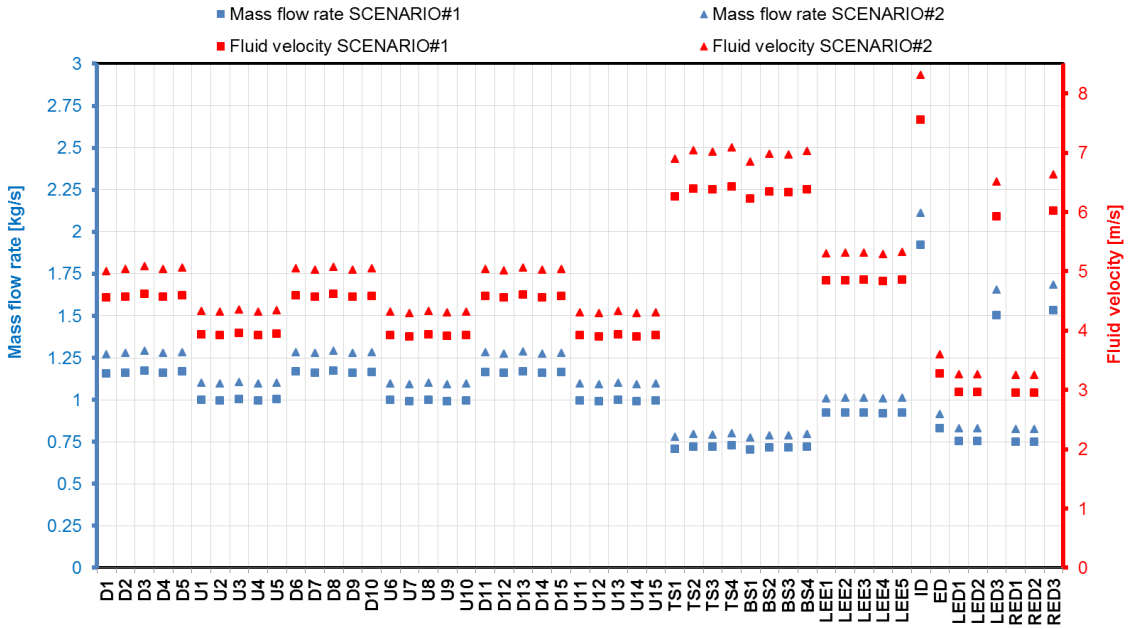

Figure 2-57 Mass flow rate partitioning for the Neutraliser cooling system

Figure 2-58 shows the coolant outlet temperature for all the components for both the scenarios. The maximum outlet temperatures are 87 °C for the panels and 106 °C for the three central LEEs with a total mass flow rate of 50 kg/s and inlet temperature of 35 °C. The maximum outlet temperatures decrease to 83 °C for the panels and 100 °C for the three central LEEs when the total mass flow rate is 55 kg/s and the inlet temperature is equals to 35 °C.

In order to consider the different operating conditions of the inlet water temperature (20÷55 °C), in Figure 2-59 vertical bars are used to show the resulting outlet temperature range in case of 50 kg/s of inlet mass flow rate. The maximum temperature is 107 °C for the panels and 126 ° for the LEEs.
The same plot, in case of 55 kg/s as inlet mass flow rate, is shown in Figure 2-60 where the maximum temperature is 103 °C for the panels and 120 ° for the LEEs.

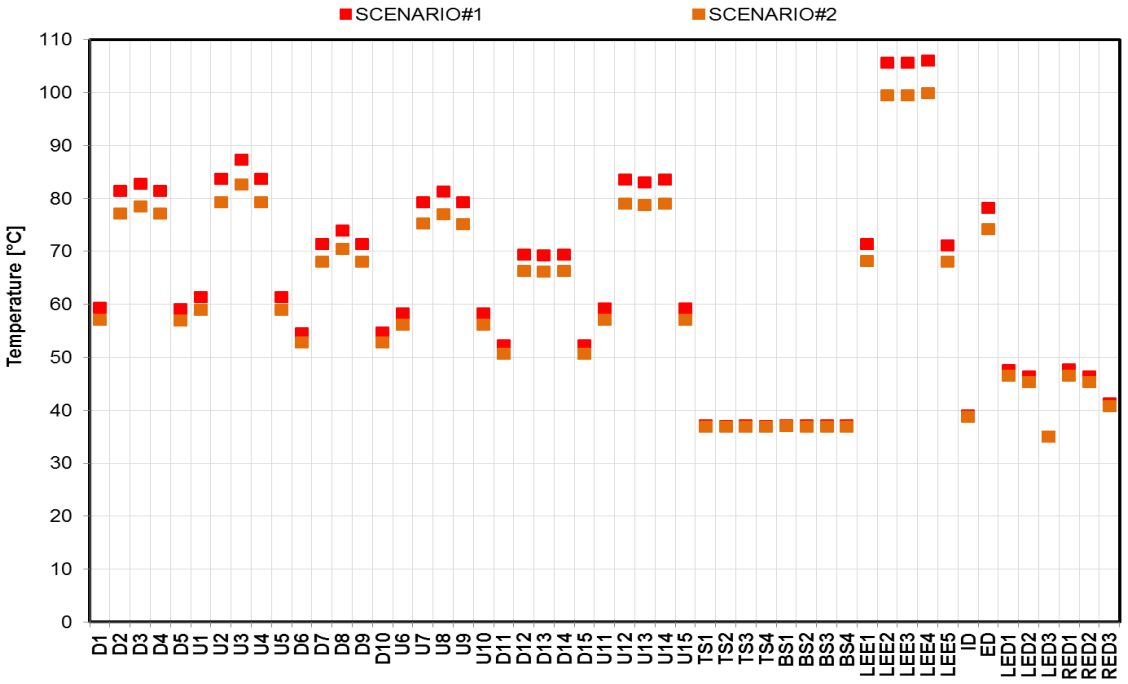

Figure 2-58 **Outlet coolant temperatures for SCENARIO#1 and SCENARIO#2. For both the scenarios the inlet temperature is equals to 35 °C (ITER requirement)**

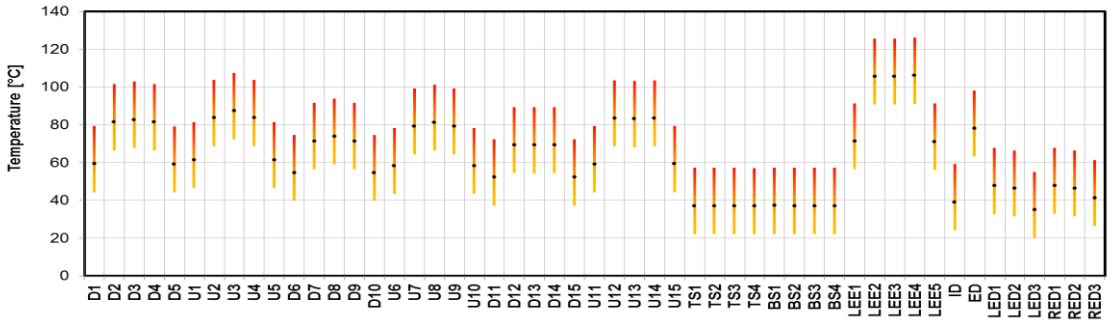

Figure 2-59 **Influence of inlet coolant temperature in outlet coolant temperatures in the case of SCENARIO#1 (total mass flow rate equals to 50 kg/s)**

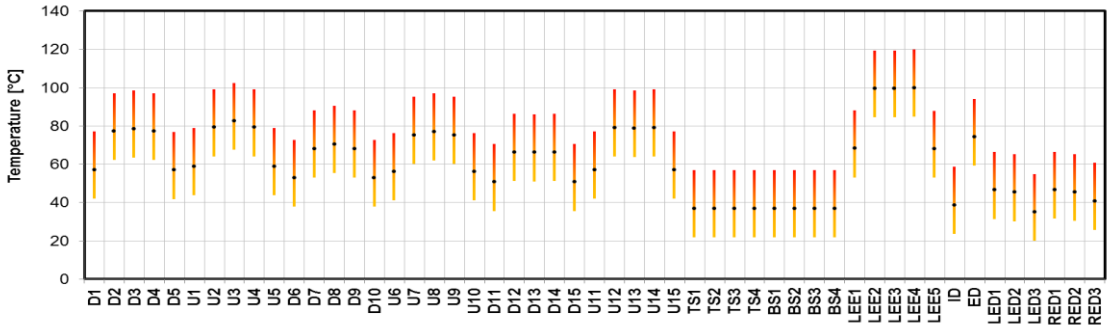

Figure 2-60 **Influence of inlet coolant temperature in outlet coolant temperatures in the case of SCENARIO#2 (total mass flow rate equals to 55 kg/s)**

2.5.5 Discussion

A one-dimensional model has been developed as a versatile tool in order to have a complete characterisation of the MITICA Neutraliser cooling system. The flow partitioning and the outlet temperature of each active cooled element have been analysed.

The maximum outlet temperatures are 87 °C for the panels and 106 °C for the three central LEEs with a total mass flow rate of 50 kg/s. The maximum outlet temperatures decrease to 83 °C for the panels and 100 °C for the three central LEEs with a total mass flow rate of 55 kg/s. These maximum temperatures have been calculated for the operation in the ITER HNB injectors at full beam power with inlet water temperature of 35 °C.

A maximum coolant temperature of 110 °C should be guaranteed inside the panels channels, according to requirements from PED (Pressure Equipment Directive) hazard classification, in order to simplify the procedure to affix the CE marking.
The PRIMA cooling plant supplies the Neutraliser within coolant temperature in the range of 20÷55 °C. Thus, by fixing the mass total inlet mass flow rate at 50 kg/s, the maximum temperature for the panel channels is 107 °C. This value has not been considered sufficiently below the limit of 110 °C. An increased inlet mass flow rate (up to 55 kg/s) has been proposed, and accepted by ITER, because the maximum outlet temperature for the panel channels decreases at 103 °C, allowing to simplify the procedure to affix the CE marking.

The total pressure drop of the cooling system is equals to 300 kPa in case of the SCENARIO#1 with 50 kg/s of mass flow, and 360 kPa for the SCENARIO#2 with 55 kg/s of total mass flow.

2.6 Residual Ion Dump

The MITICA Residual Ion Dump (RID) consists of five vertical dump walls, a support frame, manifolds and headers for the water cooling supply (see Figure 2-61 and Figure 2-62). The five walls realise four channels crossed by the particle beam.
Electrostatic fields are used to deflect the ions that are dumped onto the five walls. The fields are produced by applying zero potential to the two external panels and to the central one named grounded walls, and negative potential (- 20kV +/- 5kV @ 50Hz with trapezoidal wave form) to the two remaining named biased walls.

Each dumped panel consists of 18 vertical beam stop elements (BSEs) shown in Figure 2-63 and made of CuCr1Zr alloy (2.3 tons for the 5 walls). The BSEs have a rectangular cross-section (22mmx100mm) with four internal channels of 14mm in diameter for active cooling; the cooling channels are machined by deep drilling from both ends and caps are welded at the end sides to produce the close cooling circuits. AISI 316L twisted tapes with a pitch of 50 mm are inserted inside the cooling channels as turbulence promoters.

The BSEs are supported and positioned at the bottom between the two halves of a panel clamping bar. An upper bar similarly clamps the BSEs top end, but with gaps allowing free thermal expansion of the BSEs in the vertical direction. The wall assembly rests on two transverse bars and its support allows free axial thermal expansion. Walls biased at high voltage are connected to the transverse bars via cylindrical ceramic insulators.

All the manifolds are made of AISI 316L. The panel manifold is a single pipe DN 100 and the main headers are DN 200.

A gas baffle is mounted on the frame at the RID exit section to subdivide the injector volume and therefore to achieve differential pumping for reduction in ITER of re-ionisation losses in the duct liner.

The cooling circuit is shown and sketched in Figure 2-64. All the five walls are hydraulically connected in parallel: three of them (the grounded ones) are top filled and two (biased ones) are bottom filled. Inside the BSEs, the water runs through two swirl tubes in parallel, up to the other edge of the BSE and back (see Figure 2-65).

The RID is fed with 100 kg/s of demineralised water supplied by the PRIMA cooling plant with an inlet range temperature of 20÷55 °C and 2.0 MPa of inlet pressure. The total power to exhaust is up to 18 MW.

The 1D model of the cooling circuit has been developed in ANSYS APDL.

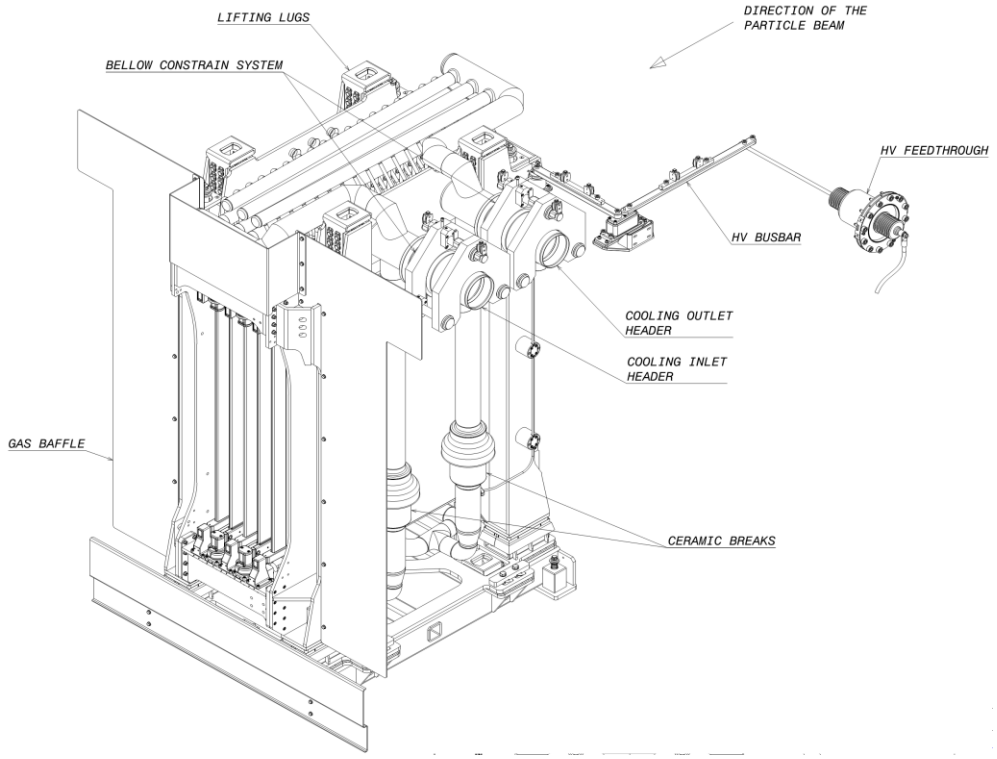

Figure 2-61 MITICA RID assembly, rear-top view

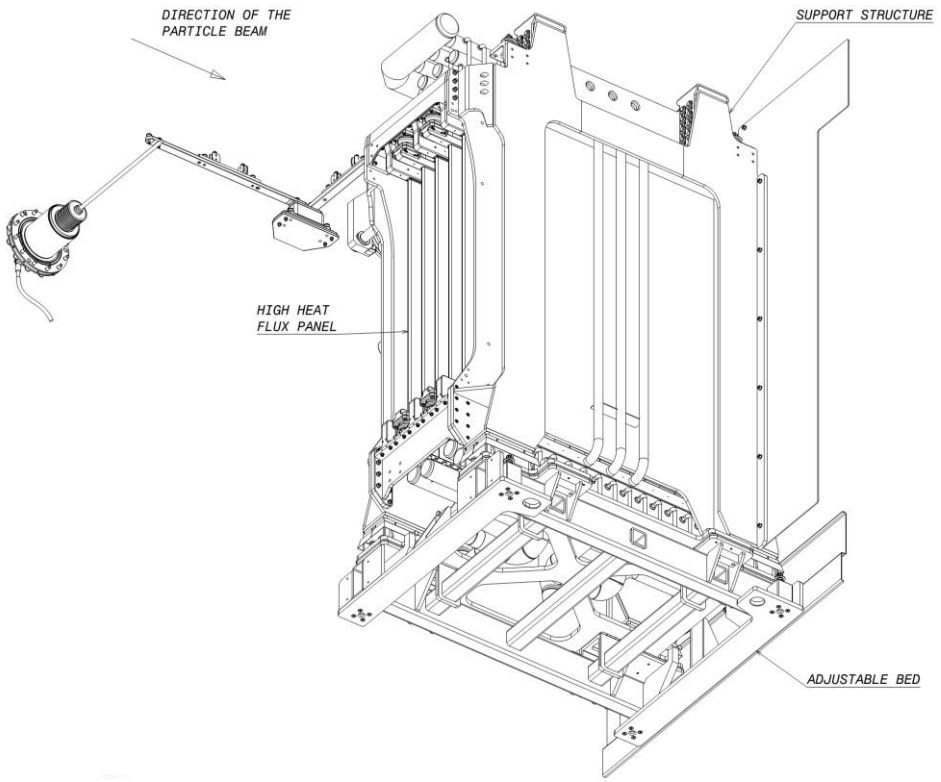

Figure 2-62 MITICA RID assembly, front-bottom view

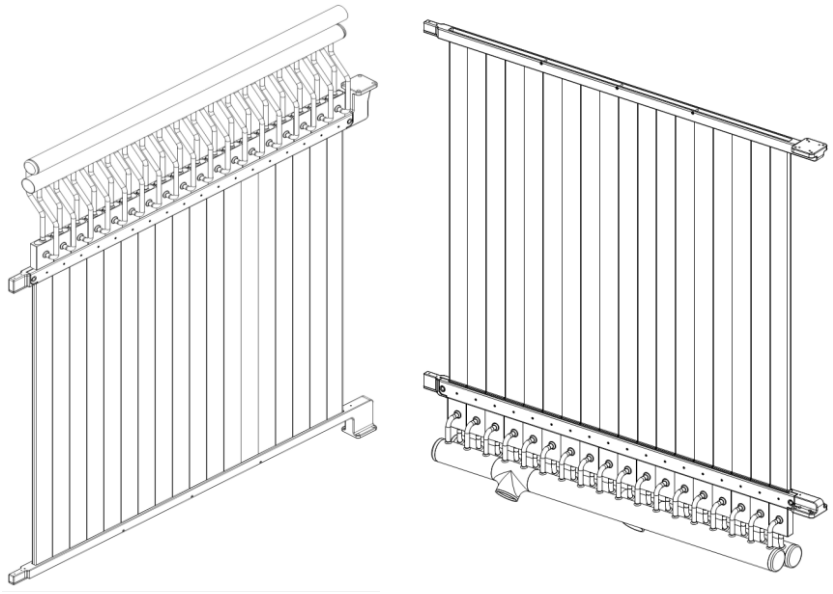

Figure 2-63 MITICA RID wall sub-assemblies with the 18 BSEs

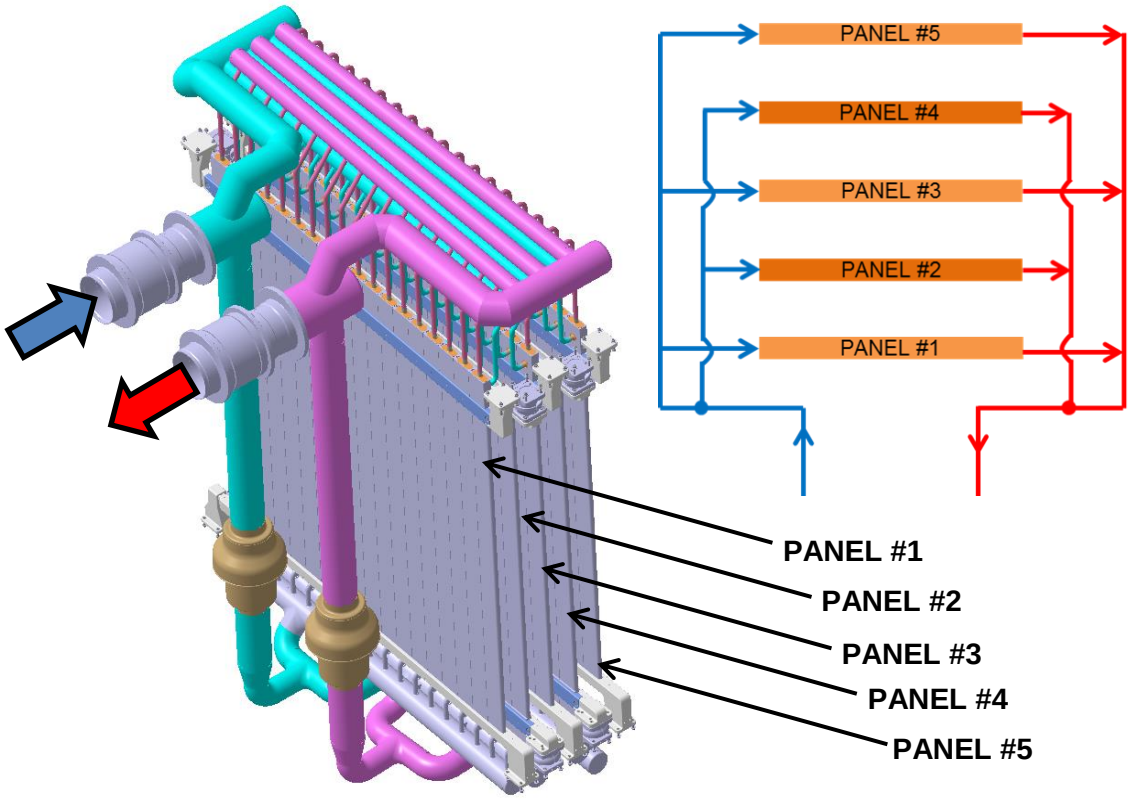

Figure 2-64 RID cooling system: 3D overview and sketch

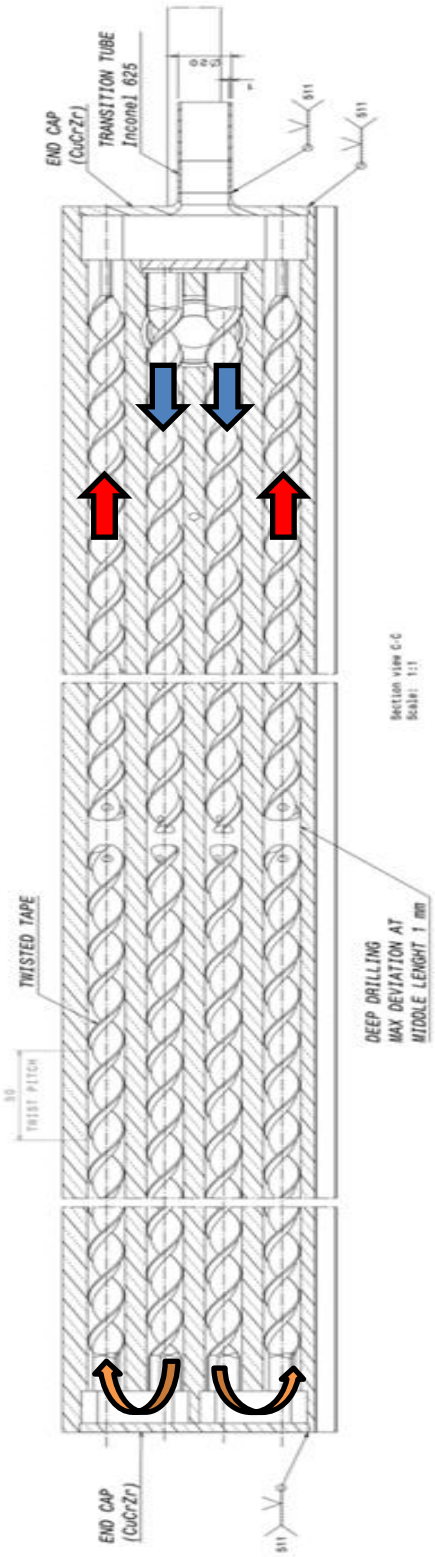

Figure 2-65 BSE magnification with the internal channels

2.6.1 CFD sub-modelling

Because of the particular geometry of the BSE inlet and outlet sections (Figure 2-66), their hydraulic behaviour has been analysed with ANSYS CFX in order to obtain the loss coefficient to be used in global models of the cooling circuit. The *k-ε* turbulence model has been used .

The Total Pressure drops *Δp* have been obtained from the simulations, and the localised loss coefficients have been calculated as:

$$K = \frac{\Delta p}{\rho\left(\frac{v^2}{2}\right)} \qquad \text{Eq. 19}$$

where *K* is the loss coefficient [-], *Δp* the pressure drop [Pa], *ρ* the bulk density of the coolant [kg/m^3] and *v* bulk fluid velocity [m/s].

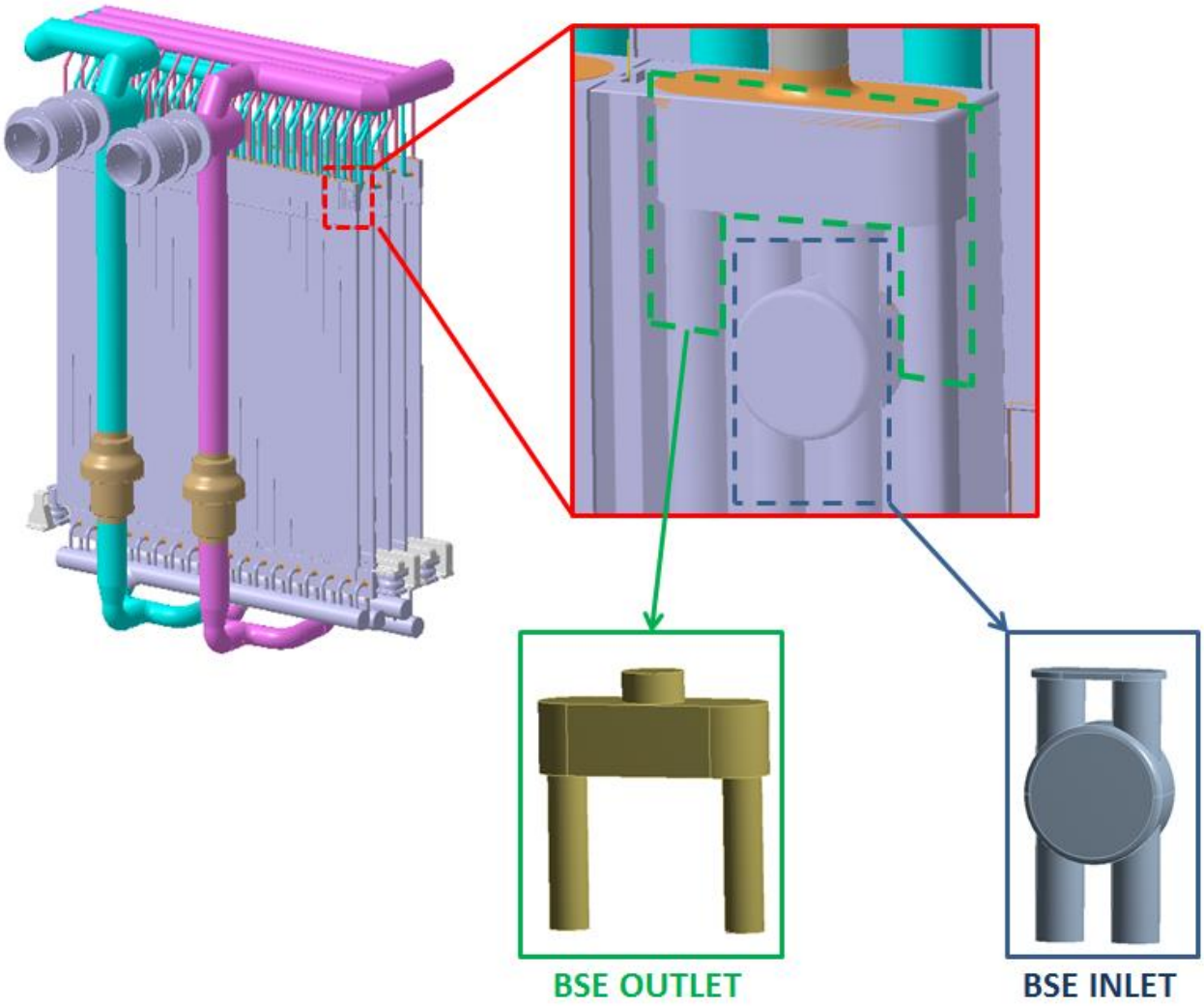

Figure 2-66 RID overview with BSE inlet and outlet magnification

2.6.1.1 BSE inlet

The dependence of the results on the mesh size has been analysed by comparing three different meshes named A, B, C. The nominal mass flow rate (1.1 kg/s) has been used in each simulation. In Table 2-15 the main mesh parameters and the results are reported.

Table 2-15 Main mesh parameters

Mesh name	Elements number [x10^6]	Minimum element size [mm]	Pressure drop [kPa]
A	1.86	1	12.51
B	4.6	0.5	13.54
C	7.75	0.4	15.45

The mesh sensitivity has been evaluated as shown in Figure 2-67 which shows the trend of the pressure drop as function of the mesh number of elements, which can be considered as a quantitative index of the accuracy of the mesh for simulating the coolant flow. The mesh named “C” appears a good mesh, pretty close to the computational limits for a usable CFD model; even though oscillation is found in Figure 2-67 due to simplifications in the convergence criteria, a more sophisticated mesh would not bring big improvements.

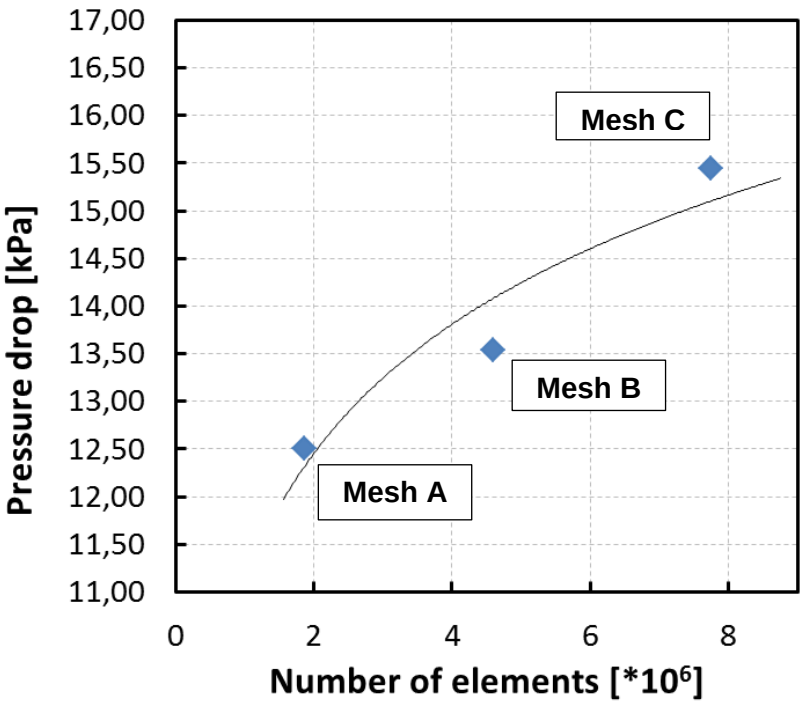

Figure 2-67 Total pressure drop for the BSE inlet with different meshes

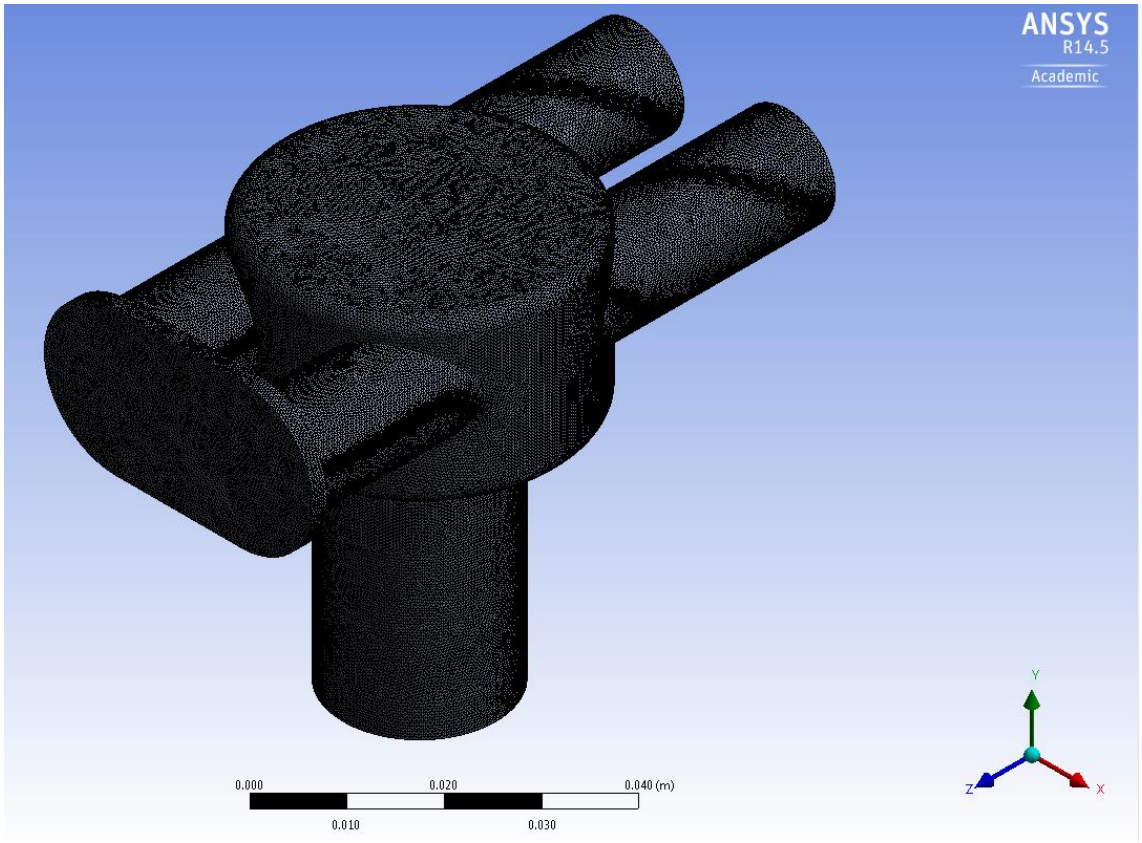

Figure 2-68 **Overview of the mesh for the BSE inlet**

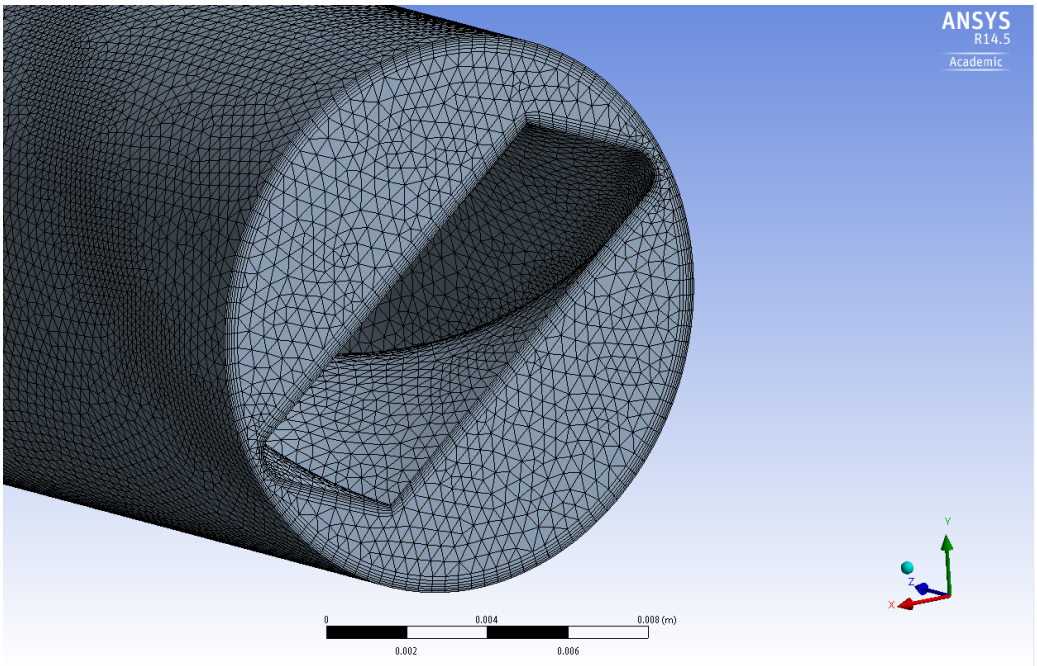

Figure 2-69 **Particular of the inflation layer around the turbulence promoter (6 layers, first layer height equals to 0.04 mm and grow rate equals to 1.2)**

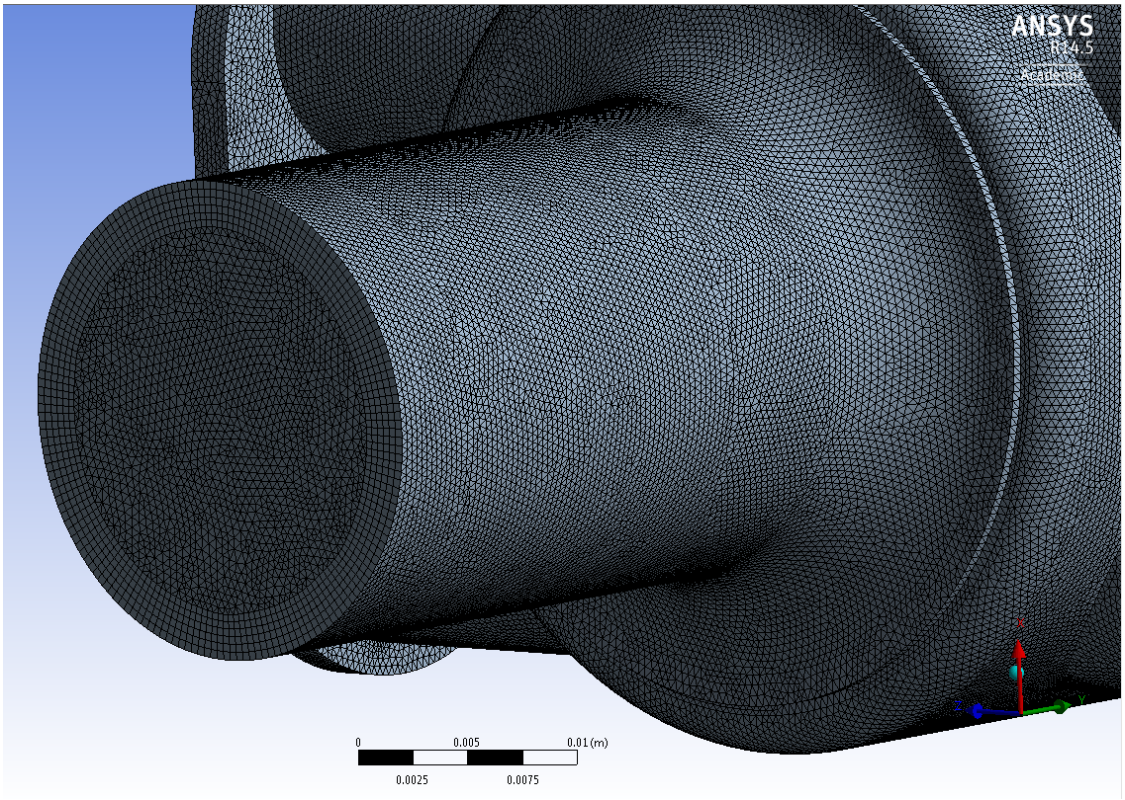

Figure 2-70 Particular of the inflation layer around the inlet pipe (6 layers, first layer height equals to 0.5 mm and grow rate equals to 1.2)

The stream lines and velocity distribution for case C are shown in Figure 2-71.

With the mesh “C” three simulations at different mass flow rate have been carried out, to obtain the loss coefficient as shown in Table 2-16. The values have been calculated by considering an internal diameter of the pipe equals to 18 mm which is the diameter of the tube before the enetrance in the BSE. The loss coefficient is constant at 1.1 kg/s (nominal mass flow rate) and 0.5 kg/s but it grows when the mass flow rate is very low (0.1 kg/s).

The value K=1.65 has been used in the hydraulic model.

Table 2-16 BSE inlet loss coefficient

Mass flow rate [kg/s]	Water velocity [m/s]	Pressure drop [kPa]	*K*
0.1	0.39	0.1616	2.09
0.5	1.96	3.093	1.60
1.1	4.32	15.41	1.65

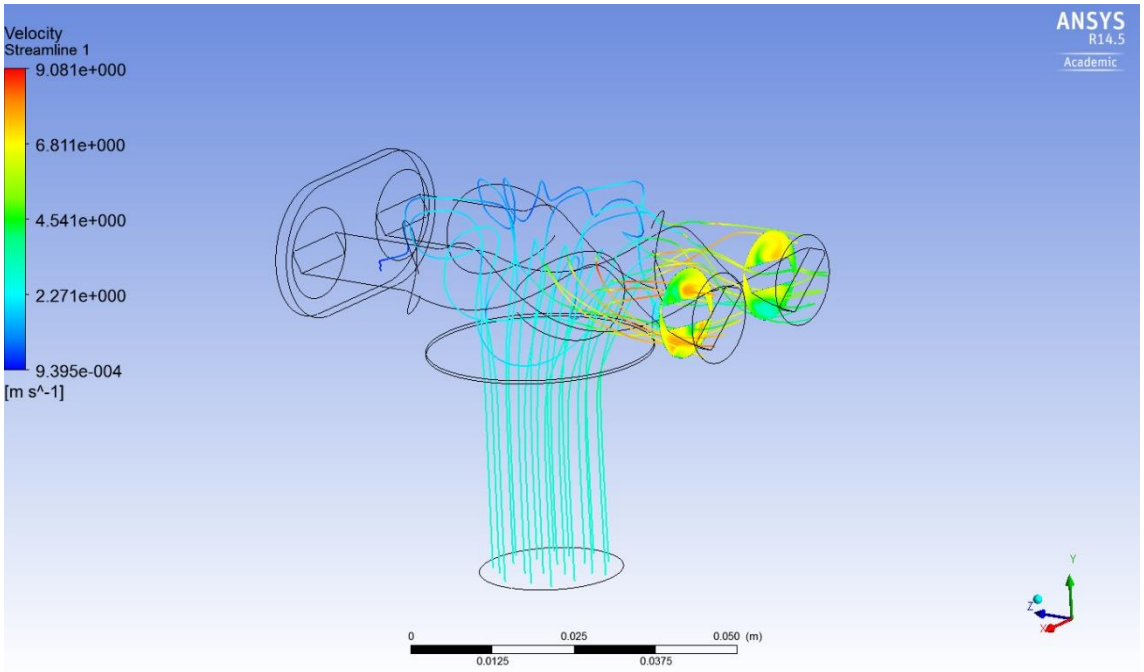

Figure 2-71 Stream lines and velocity distribution

2.6.1.2 BSE outlet

The study of the BSE outlet geometry has been performed with the following main mesh parameters:

- **minimum element size**: 0.4 mm;
- **inflation layer around the turbulence promoter**: 6 layers, first layer height equals to 0.04 mm and grow rate equals to 1.2;
- **inflation layer around the outlet pipe**: 6 layers, first layer height equals to 0.5 mm and grow rate equals to 1.2.
- **number of elements**: 10.6×10^6;

The meshed model is shown in Figure 2-72, Figure 2-73 and Figure 2-74.

For the BSE outlet, a mesh similar to the BSE inlet has been used, and the sensitivity analysis has not been carried out as a certain confidence on the CFD models has been achieved.

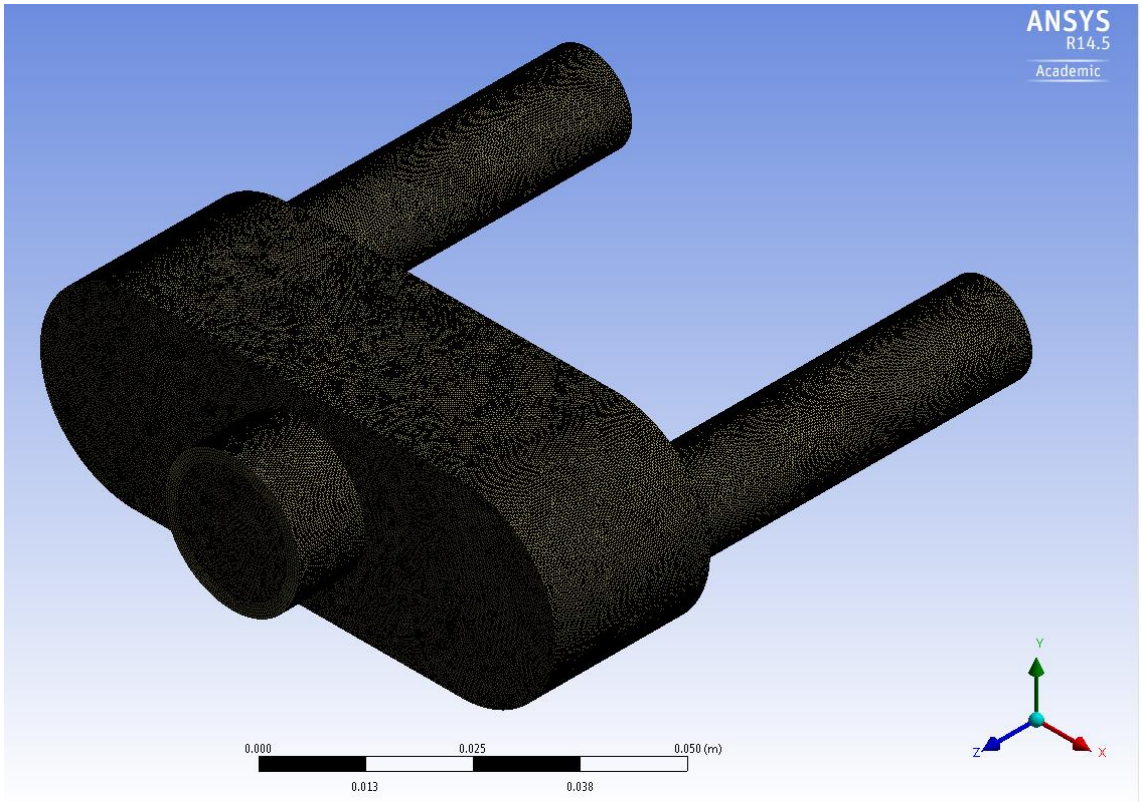

Figure 2-72 **Overview of the mesh for the BSE outlet**

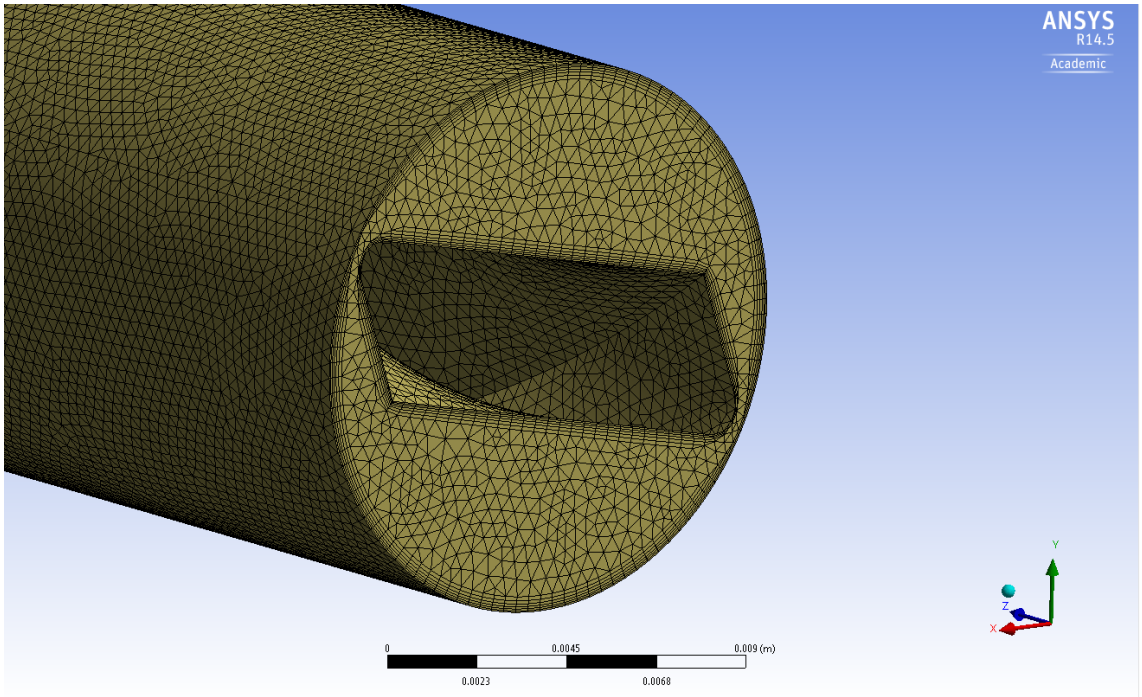

Figure 2-73 **Particular of the inflation layer around the turbulence promoter (6 layers, first layer height equals to 0.04 mm and grow rate equals to 1.2)**

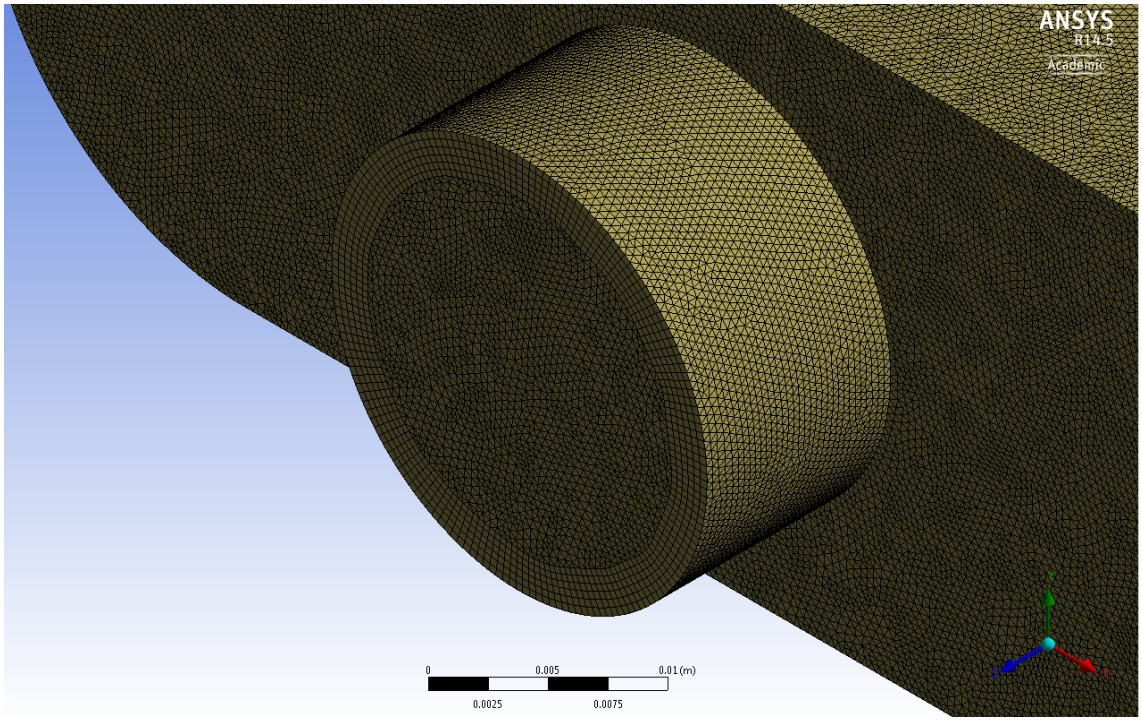

Figure 2-74 **Particular of the inflation layer around the outlet pipe (6 layers, first layer height equals to 0.5 mm and grow rate equals to 1.2)**

The stream lines and velocity distribution are shown in Figure 2-75.

Three simulations at different mass flow rate have been carried out to obtain the loss coefficient, as summarized in Table 2-17. The values have been calculated by considering an internal diameter of the pipe equals to 18 mm which is the diameter of the tube at the BSE outlet. The loss coefficient is constant at 1.1 kg/s (nominal mass flow rate) and 0.5 kg/s but it grow when the mass flow rate is very low (0.1 kg/s).

The value K=3.1 has been used in the hydraulic model.

Table 2-17 **BSE outlet loss coefficient**

Mass flow rate [kg/s]	water velocity [m/s]	Pressure drop [kPa]	*K*
0.1	0.39	0.3279	4.25
0.5	1.96	5.877	3.04
1.1	4.32	28.63	3.06

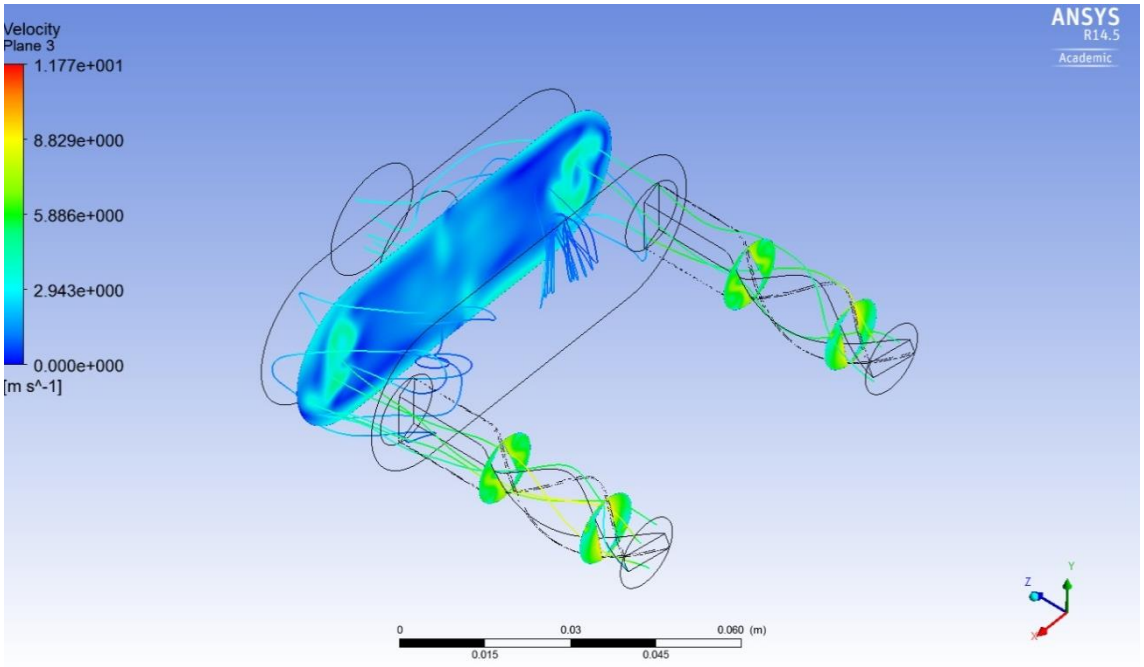

Figure 2-75 Stream lines and velocity distribution on sections of the flow domain

2.6.2 Integrated cooling circuit model

The geometry of the RID cooling system has been replicated in ANSYS APDL (Figure 2-76) by using the one-dimensional element *fluid116* to model pipes, manifolds and swirl tubes.

The material properties of the water have been implemented in the finite element model by using polynomial equations to simulate their proprieties in function of the temperature [61].
Different material properties have been defined for the different friction correlations due to the presence or not of the swirl channel elements and in order to take into account the specific hydraulic diameter. In particular, for the swirl channel the Eq. 15, Eq. 16, Eq. 17 and Eq. 18 have been implemented.
In order to compute the localised pressure drop in bends, T-junction, inlet and outlet, the loss coefficients given in Table 2-18 [63] have been used. As already stated, for the BSE inlet and outlet the localised loss coefficients have been set to 1.65 and 3.1 respectively.

The boundary condition of the one-dimensional model are:

- total mass flow rate: 100 kg/s;
- outlet pressure: 2 MPa.

Table 2-18 Localised loss coefficient

Type of element	*K*
90° bend	0.5
45° bend	0.1
Outlet loss	1
Inlet loss	0.5
T junction through pipe (DN70)	0.3
T junction through pipe (DN125)	0.2
T junction branch pipe (DN70)	1.5

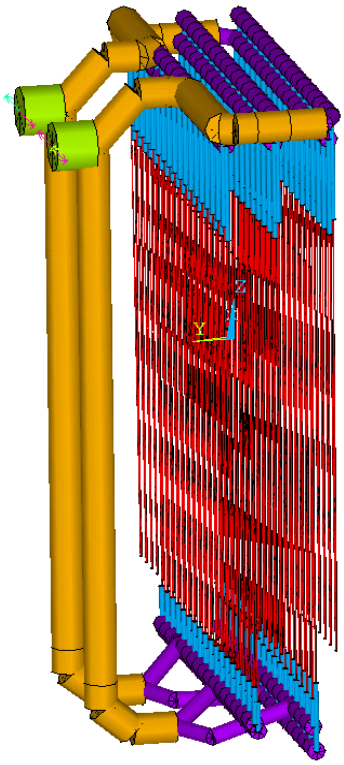

Figure 2-76 One-dimensional model in ANSYS APDL of the RID cooling circuit. Different colours indicate a different material number.

2.6.3 Results

The model has been used as a versatile tool to analysed the flow partitioning of the coolant along each BSE in two different cooling circuit configurations.
For both the configurations the cooling channel diameter inside the RID walls is 14 mm. A balanced solution, which corresponds to identical twisted tapes with 4 mm thickness installed inside all the wall cooling channels, has been compared to an unbalanced solution for which an increasing of the flow rate inside the central BSEs is realised by using different tape thickness.

2.6.3.1 Balanced solution

The balanced solution corresponds to a design in which all the cooling channels inside the BSEs have the same geometrical parameters:

- internal diameter: 14 mm;
- tape thickness: 4 mm;
- tape pitch: 50 mm.

The resulting flow partitioning has been analysed by using the following definition of flow non-uniformity for each panel:

$$\Delta_{\mathrm{flow}} = \frac{\Phi_{\max} - \Phi_{\min}}{\Phi_{\min}} \qquad \text{Eq. 20}$$

where Φ_{max} and Φ_{min} are the maximum and minimum mass flow rate along one BSE.

With respect to the panels numbering shown in Figure 2-64, the flow non-uniformity is:

- panel 1: 1.24 %;
- panel 2: 0.54 %;
- panel 3: 1.25 %;
- panel 4: 0.75 %;
- panel 5: 1.25 %.

An overall non-uniformity can also be calculated considering the absolute maximum and minimum, which is 3.43% (between BSE#18 of panel 2 and BSEs #9 and #10 of panel 5).

Figure 2-77 is a schematic top view of the RID and shows the mass flow rate inside each BSE for each panel. These results mean that the flow is well distributed within each wall panel.
The total pressure drop is 710 kPa (the local pressure along the circuit is shown in Figure 2-78).

The average mass flow rate inside one BSE (1.1 kg/s) has been used to calculate the temperature of the coolant at the outlet of the BSEs (Table 2-19). The maximum foreseen heat loads on the wall are: 547 kW for the double side heated middle panels (panel #2 #3 #4) and 303 kW for the single side heated side panels (panel #1 #5). These thermal powers have been calculated with the BTR code by assuming a gaussian shape of the beam profile passing through each beam channel of the RID [30]. With respect to the saturation temperature (calculated at the minimum possible

pressure) the boiling margin between the bulk and the saturation temperature is 35 °C in the middle panels and 87 °C for the two side panels.

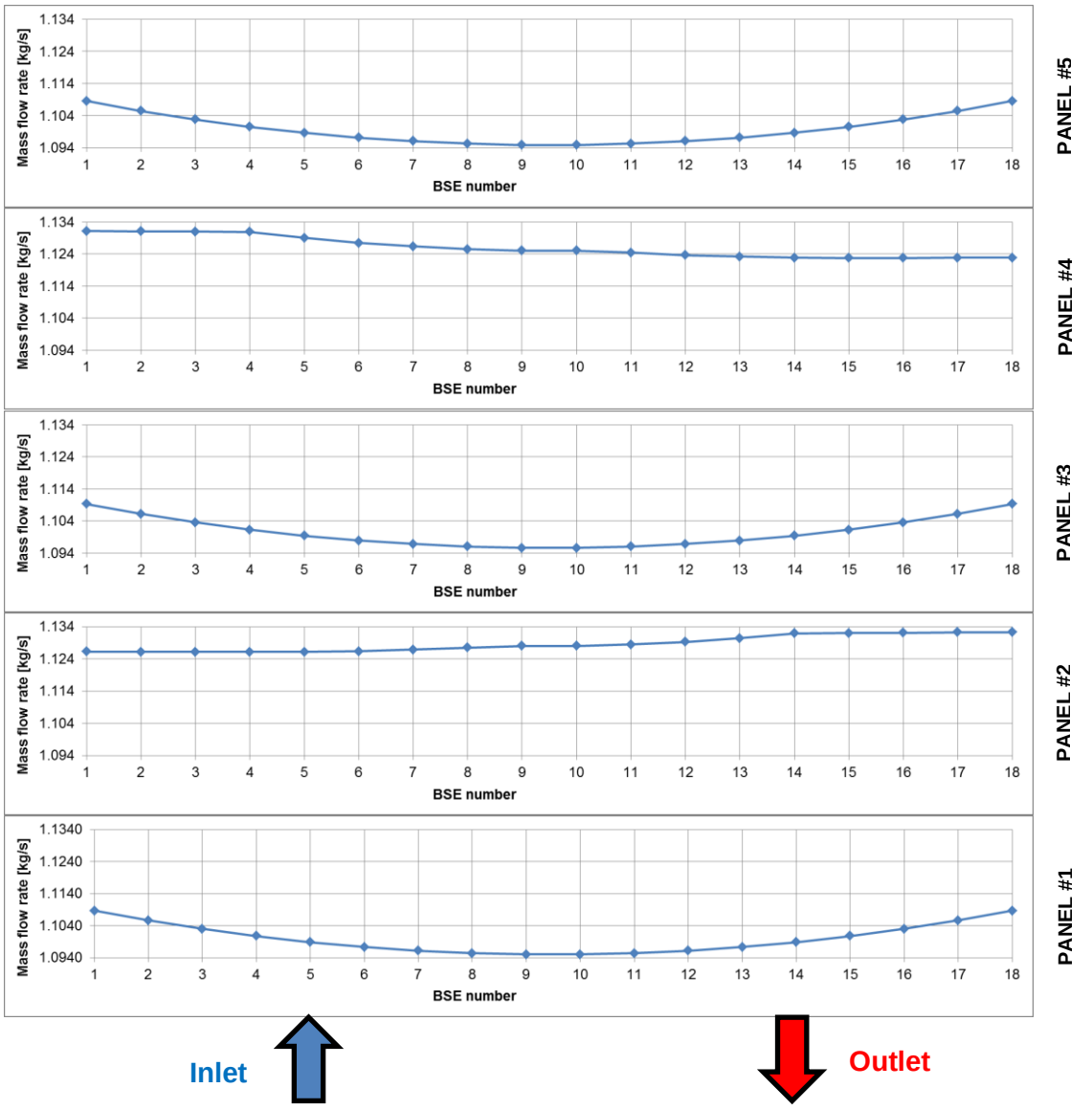

Figure 2-77 Balanced solution: mass flow distribution of the water in BSEs elements

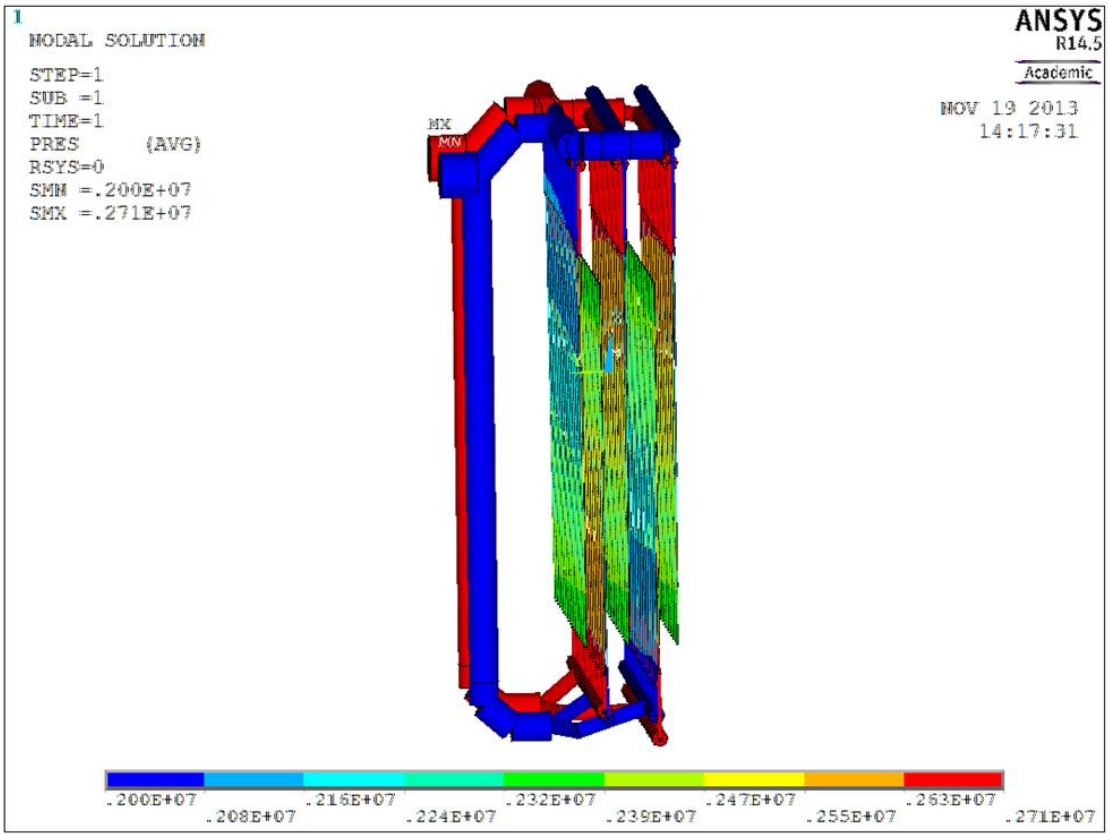

Figure 2-78 **Balanced solution: overview of the local pressure [Pa] in the system**

Table 2-19 **Cooling parameters and boiling margin for the balanced RID cooling scheme**

Total mass flow rate [kg/s]	100	
Tinlet [°C]	38	
	Middle panels	Side panels
m_{panel} [kg/s]	59.4	39.6
m_{BSE} [kg/s]	1.1	1.1
Internal diameter [m]	0.014	0.014
Tape thickness [m]	0.004	0.004
Tape pitch [mm]	50	50
Hydraulic diameter, Dh [m]	6.12E-03	6.12E-03
Heat capacity, c_p [J/(kg °C)]	4200	
BSE max heating power [W]	5.47E+05	3.03E+05
BSE max bulk temp rise, ΔT [°C]	118	66
BSE max bulk outlet temp [°C]	**156**	**104**
Minimum pressure [MPa]	1.29	1.29
Saturation water temperature [°C]	191	191
Boiling margin at the BSE outlet [°C]	**35**	**87**

2.6.3.2 Unbalanced solution

In order to increase the boiling margin a unbalanced solution has been analysed.

Different flow rates are realised in BSEs as twisted tape thickness is properly set: 4 mm thickness of twisted tapes inserted inside all the cooling channels except for the BSEs located in the centre and middle walls for which 2 mm of tape thickness is foreseen to increase the mass flow rate (9 BSE from no. 7 to no. 15, see Figure 2-79).

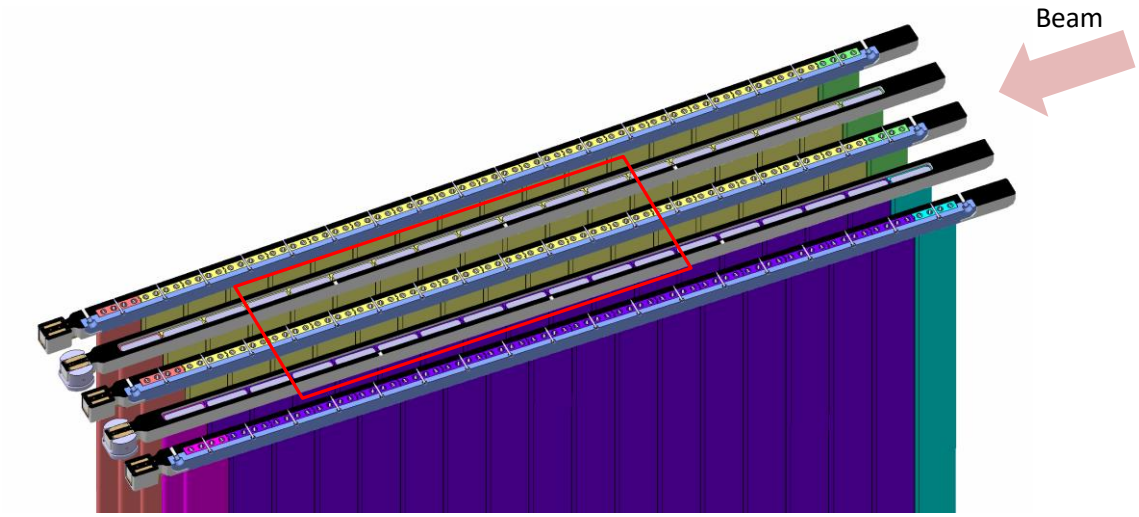

Figure 2-79 Highlighting of BSEs with reduced twisted tape thickness (2 mm)

Figure 2-80 is a schematic top view of the RID and shows the results in terms of mass flow rate inside each BSE for the unbalanced design. The flow non-uniformity has not been considered here because would not make sense. The results clearly show the increased flow rate in the central BSEs with the reduced tape thickness: about 1.35 kg/s are expected in these BSEs while 1.01 kg/s for the other.

The total pressure drop is 610 kPa (the local pressure along the circuit is shown in Figure 2-81).

The outlet temperatures are reported in Table 2-20 in which, for simplicity, only the BSEs with reduced tape thickness have been considered for the middle walls. With respect to the saturation temperature (calculated at the minimum possible pressure) the boiling margin between the bulk and the saturation temperature is 60 °C in the middle panels and 85 °C for the two side panels. Compared to the balanced solution, with the unbalanced design the boiling margin, in the most heated BSEs, is increased from 35 to 60 °C.

This solution has been adopted for the final design of the RID cooling system.

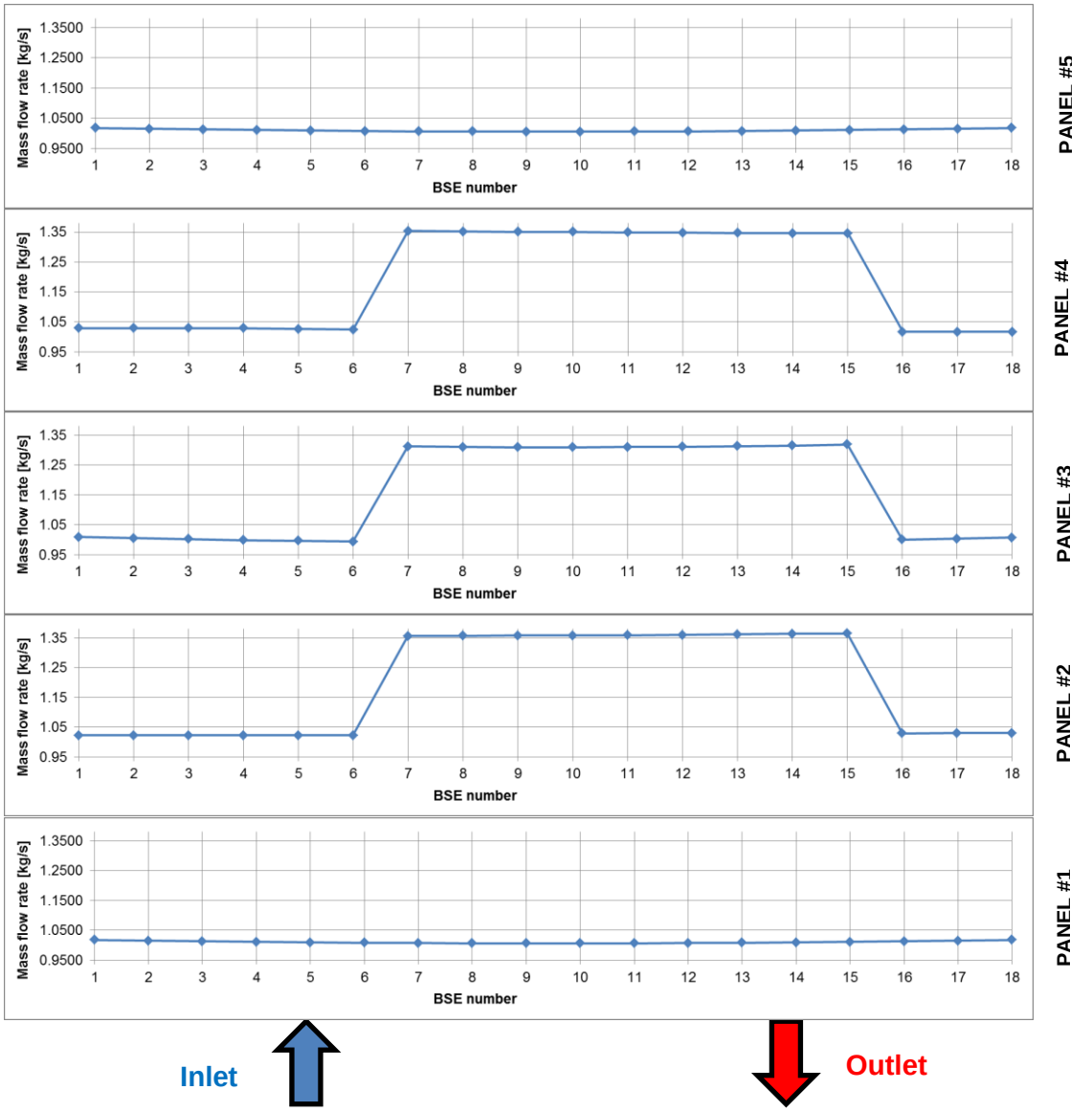

Figure 2-80 **Unbalanced solution: mass flow distribution of the water in BSEs elements**

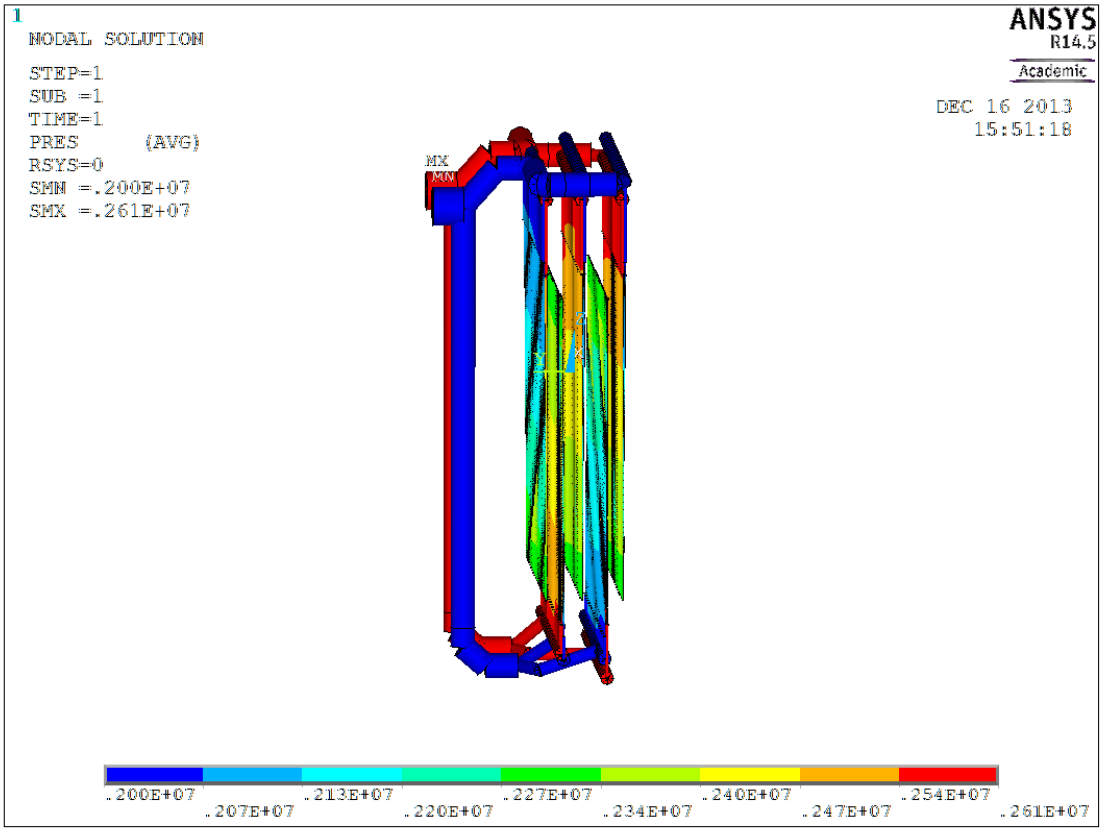

Figure 2-81 **Unbalanced solution: overview of the local pressure [Pa] in the system**

Table 2-20 **Cooling parameters and boiling margin for the unbalanced RID cooling scheme**

Total mass flow rate [kg/s]	100	
Tinlet [°C]	38	
	Middle panels	Side panels
m_{panel} [kg/s]	63.7	36.4
m_{BSE} [kg/s]	1.35	1.01
Internal diameter [m]	0.014	0.014
Tape thickness [m]	0.002	0.004
Tape pitch [mm]	50	50
Hydraulic diameter, Dh [m]	7.41E-03	6.12E-03
Heat capacity, c_p [J/(kg °C)]	4200	
BSE max heating power [W]	5.47E+05	3.03E+05
BSE max bulk temp rise, ΔT [°C]	96	71
BSE max bulk outlet temp [°C]	**134**	**109**
Minimum pressure [MPa]	1.39	1.39
Saturation water temperature [°C]	194	194
Boiling margin at the BSE outlet [°C]	**60**	**85**

2.6.4 Draining and dry procedure

The RID cooling channels have to be dried in order to allow a safe removal from the vacuum vessel of the component without water and contaminants. The draining and drying procedure has not yet been defined, in particular as regards the required blowing out pressure level.
This pressure is estimated, as presented in the following, by considering the cooling circuit geometrical characteristics and by a dedicated CFD sub-modelling of the compressible Nitrogen gas flow inside the BSE channels to be used for this purpose.

The coolant trapped inside the circuits will be evacuated only if the pressure difference applied at its opposite boundaries is greater than the pressure given by the coolant column height that inside the RID panels is $p = \rho\ g\ h$ = 1000x9.81x2.74=26.9 kPa (Figure 2-82). This static pressure must be smaller than the pressure drop for gas flowing across the circuits.
In particular, one can imagine the case in which only one BSE has been fully evacuated, and all the others are partially filled with water; one can imagine as well the case in which all the BSE channels have been evacuated, apart from one. In both extreme cases, the pressure difference between the inlet and outlet manifold will have to be higher than the pressure produced by the coolant column height.

During gas blowing, the pressure losses will determine the pressure difference between the inlet and outlet manifolds. In particular, if the pressure losses in the external circuit are neglected, these pressures will be given uniquely by the gas flow inside the swirl channels. It is to be expected, in any case, that the pressure losses in the gas feeding lines are much smaller than the losses inside the BSEs.

The pressure drop for gas flowing has been estimated with ANSYS CFX considering half the swirl channel inside the BSE.
Figure 2-83 shows the mesh used. The k-ε model has been used in all the simulations with the hypothesis of isothermal gas at 343 K.

As the swirl channel is the element with the highest pressure drop, the other contributions have not been taken in account: in a first approximation their contribution is not significant, moreover in this way we are in conservative hypothesis.

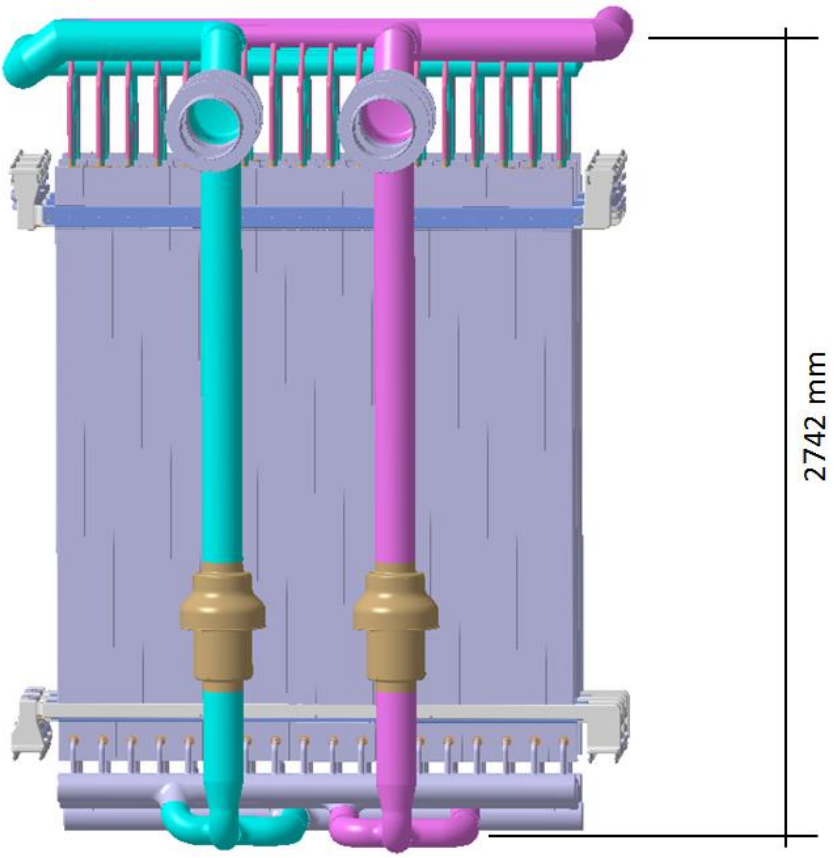

Figure 2-82 **Maximum RID water column height**

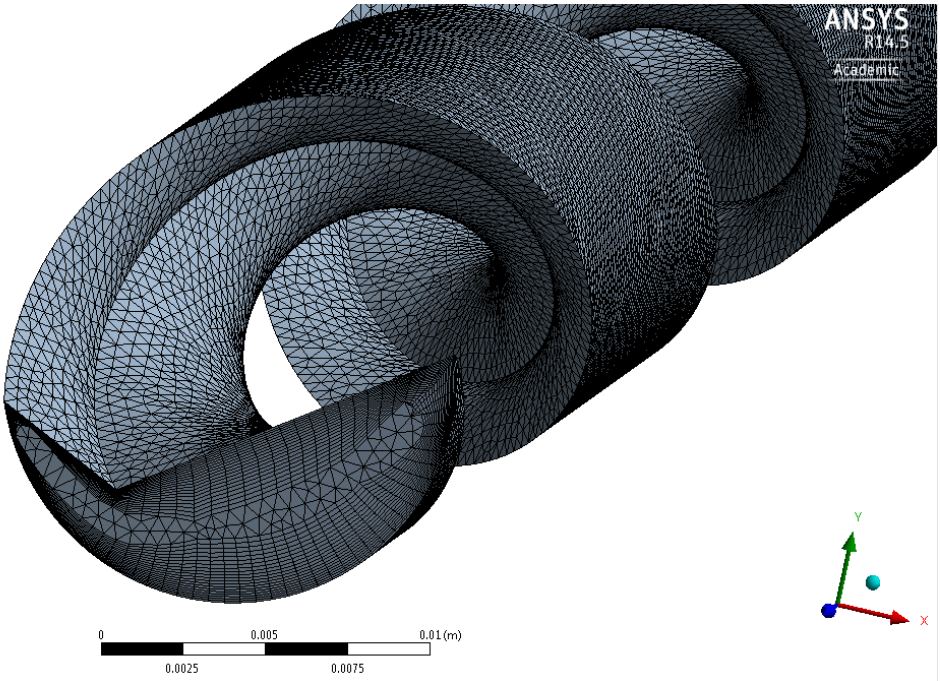

Figure 2-83 **Particular of the inflation layer around the turbulent promoter (20 layers, first layer height equals to 0.06 mm and grow rate equals to 1.05)**

Different scenarios have been simulated by considering different fluid velocity inside the swirl channel. Figure 2-84 shows the pressure drop as function of the fluid velocity for a swirl channel of 3662 mm (1831x2 mm because the path inside the BSE panel is composed by two swirl channels), and Figure 2-85 the stream lines in the case with 30 m/s of inlet fluid velocity.

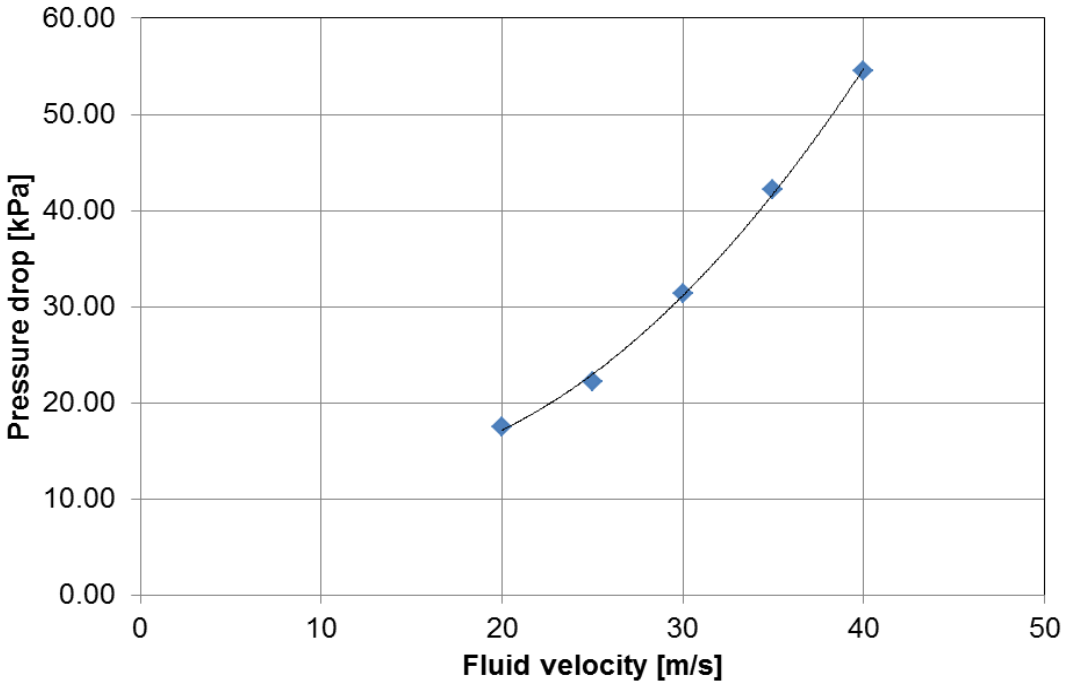

Figure 2-84 **Pressure drop in the swirl channel as function of the fluid velocity**

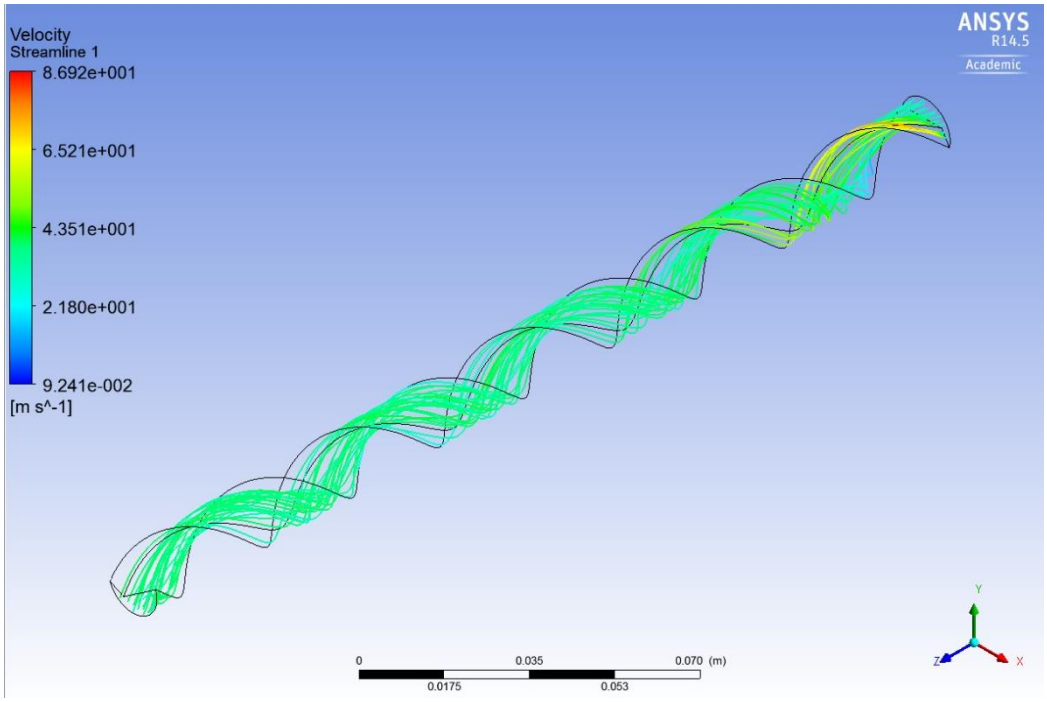

Figure 2-85 **Stream lines inside a portion of the swirl channel in case of inlet Nitrogen velocity of 30 m/s**

Results are reported in Table 2-21 where the inlet pressure ranging between 119 and 156 kPa. By assuming the outlet pressure equals the atmospheric pressure (101 kPa), the inlet pressure for blowing out and draining has been obtained considering: $p_{inlet}=p_{outlet}+\Delta p$.

This calculation gives the minimum nitrogen gas flow rate that must be provided to the RID cooling circuit during blowing-out, in order to realize the pressure drop between the manifolds of 27 kPa.
In the case of evacuation of a single channel, the mass flow rate is 6.54E-3 kg/s; in the case of complete evacuation, with one single BSE channel still to be evacuated, the mass flow rate of 1.18 kg/s will be sufficient (6.54E-3x2x18x5).
Therefore, if additional losses are neglected, a minimum pressure of 133 kPa and mass flow rate of 1.18 kg/s of nitrogen will permit complete blowing out of the RID cooling circuit.

Table 2-21 Swirl channel pressure drop as function of different mass flow rate

Mass flow rate for one swirl channel [kg/s]	Average fluid velocity [m/s]	Swirl channel pressure drop [kPa]	Outlet pressure [kPa]	Inlet pressure [kPa]
4.33E-03	20	17.5	101	119
5.42E-03	25	22.2	101	124
6.54E-03	**30**	**31.4**	**101**	**133**
7.67E-03	35	42.1	101	143
8.82E-03	40	54.5	101	156

2.6.5 Discussion

A one-dimensional FE model has been developed as a versatile tool in order to have a complete characterisation of the RID cooling system. The flow partitioning inside the BSE elements has been analysed.

Two different designs of the cooling circuit have been explored. In the case of homologous BSE channels and nominal flow rate, the results show a very good flow distribution inside each BSE of each panel. The average mass flow rate inside one BSE is about 1.1 kg/s and an overall non-uniformity (calculated between the maximum and the minimum flow found) equal to 3.43% has been calculated. The maximum temperature at the BSE outlet is 156 °C with a boiling margin of 35 °C.
A modification of the design concerns the increase of the flow area inside the BSE (through the reduction of the tape thickness) in order to have a higher mass flow where the thermal power is expected to be higher, in the middle of the RID. A case with 2 mm of tape thickness for the central BSEs and 4 mm for the others have been analysed. The results show a sufficient increase in the mass flow where desired (1.35 kg/s instead of the previous 1.1 kg/s for the most heated BSEs). By using this unbalanced solution, the maximum temperature at the BSE outlet is 134 °C and the boiling margin increases at 60 °C. This second design has been officially adopted for the MITICA RID.

In order to allow a safe removal of the component from the vacuum vessel, the RID cooling channel will have to be dried by using a system able to blow nitrogen inside the BSEs and remove the water trapped inside. The coolant trapped inside the circuits will be evacuated only if the pressure difference applied at its opposite boundaries is greater than the pressure given by the coolant column height inside the RID. The water column height has been calculated analytically, and the nitrogen mass flow rate needed has been computed with CFD analysis. A mass flow of 1.18 kg/s of nitrogen with a minimum pressure of 133 kPa will permit complete blowing out of the RID cooling circuit.

Chapter 3
Combined 1D-3D thermo-hydraulic model

High heat loads, wall temperatures and pressures characterize the SPIDER Beam Dump. Integrated analyses with shared and linked degree of freedom between 1D and 3D models within the non-linear process of the ANSYS APDL finite element code have been carried out in order to examine the sensitivity of the beam dump as diagnostic device.

3.1 SPIDER Beam Dump

The SPIDER Beam Dump has been designed to allow two main functions: dumping all the beam power coming from the RF beam source, and measuring the temperatures on the dumping panels for beam diagnostic.

To limit the incident power density, the Beam Dump consists of two walls arranged in V-shape with an angle between them of 60°. Each panel is composed of 31 actively cooled hypervapotrons (HVs) vertically stacked.
An hypervapotron is a high heat flux element made of finned surface of high conductivity material in which the flow direction is perpendicular to the fins in order to create a turbulent regime.
The HVs are made of CuCrZr alloy in order to absorb a total heat flux of 5 MW in case of D_2 and 6.1 MW in case of H_2 with power densities up to 8 MW/m^2 [31].

Thermal sensors are installed at the outlet of each HV to monitor the temperature of the cooling water for calorimetric purposes, and in the bottom side of the HVs for structural material protection and power deposition profile evaluation.

A picture of the Spider Beam Dump is shown in Figure 3-1. The main dimensions of each panel are: 2060 mm height and 800 mm width.
The detailed drawings, with the thermocouples (TCs) position, of the hypervapotrons intercepting the centre of the beamlet groups (four each panel), are in Figure 3-2 and Figure 3-3 for the left and right panel respectively. Other HVs have a reduced set of holes for TCs: only ten corresponding to the intercept of each beamlet axis. Initially not all holes are equipped with a thermocouple, but only 14 holes of the hypervapotrons intercepting the centre of the beamlet groups, 7 for each beamlet group: one in the centre and three on each side to measure the gradient of the power density profile.

Complete and thorough analyses of thermal exchange inside the HVs have been carried out by means of multiphysics simulations, involving multiple simultaneous physical phenomena and combining thermal conduction with fluid mechanics.

Figure 3-1 Picture of the SPIDER Beam Dump

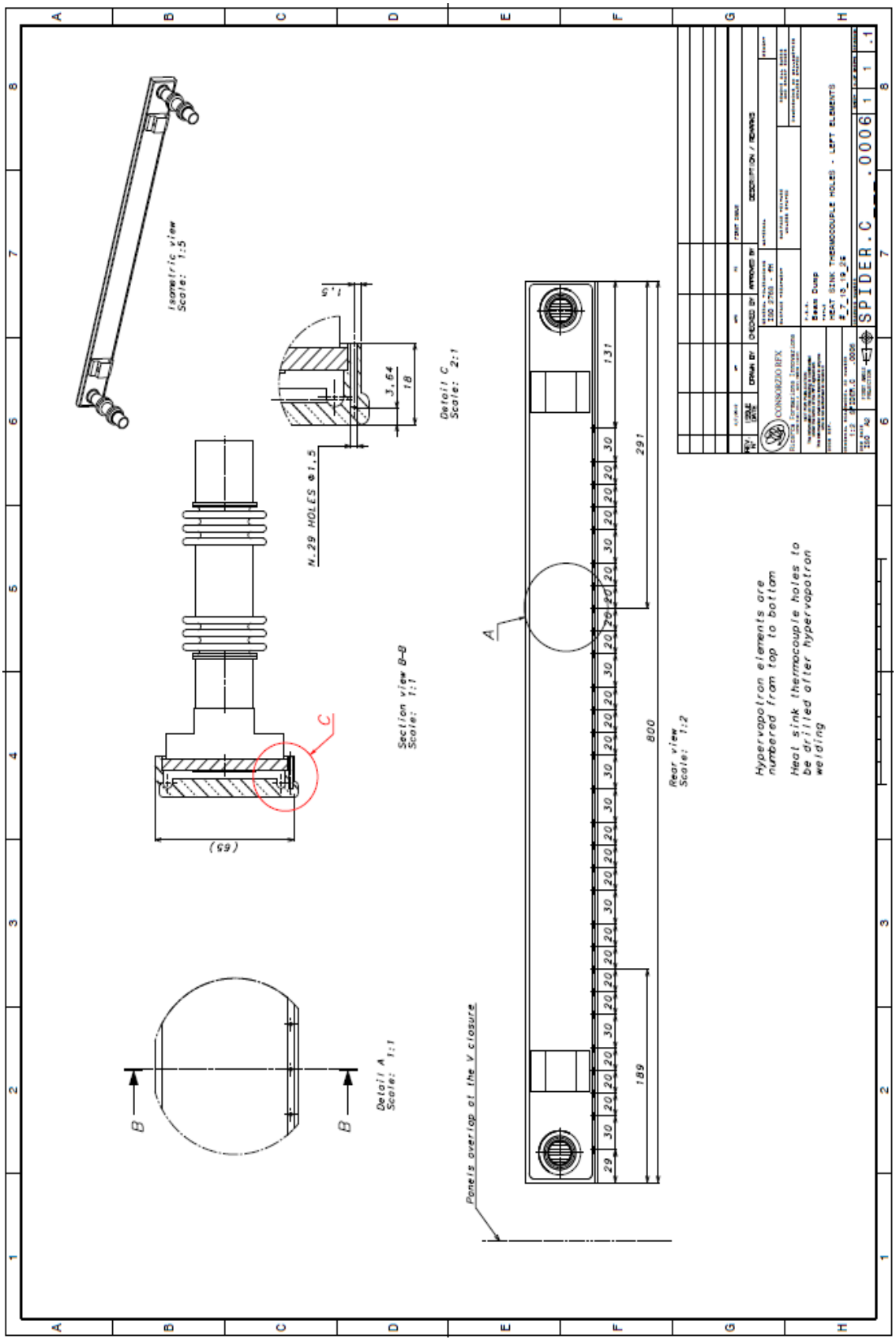

Figure 3-2 **Detailed drawing of one hypervapotron for the left panel with the position of the thermocouples**

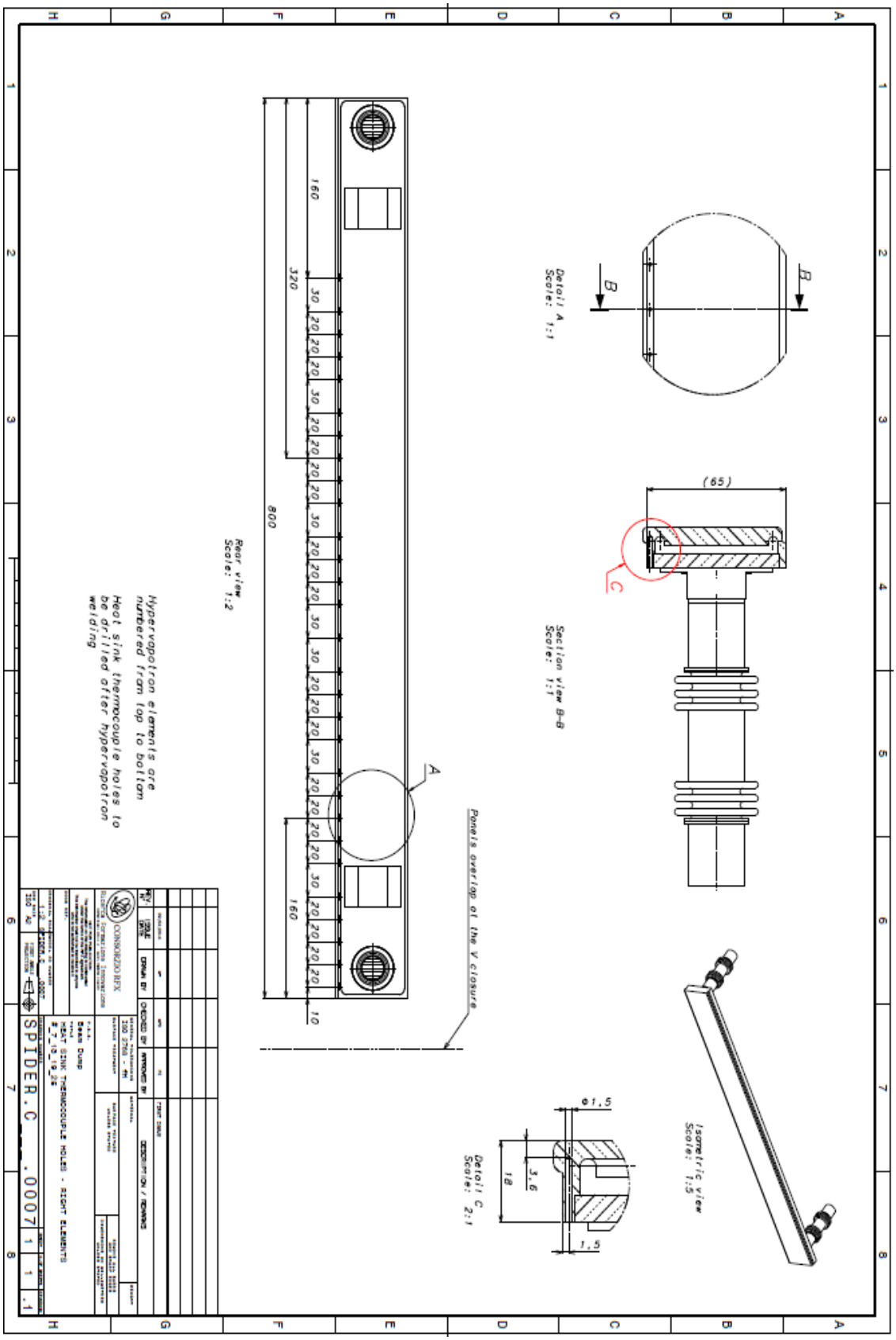

Figure 3-3 **Detailed drawing of one hypervapotron for the right panel with the position of the thermocouples**

3.2 Heat transfer and pressure drop correlations for hypervapotron

Along a hypervapotron, because of a variation of surface temperature, fluid temperature, and pressure, different heat transfer mechanisms can occur simultaneously:

- forced convection;
- transition from forced convection to nucleate boiling;
- nucleate boiling at the channel surface;
- critical heat flux.

Considering the above mechanisms, the heat exchange will occurs in forced-convection surface boiling where three distinct regions can be found [38]. The heat transfer is governed by forced convection at low wall superheat; by increasing the superheat a combined effect of forced convection and surface boiling occurs; at high wall superheat the effect of forced convection seems to disappear and fully developed boiling dominates.

In Figure 3-4 the regions and the temperature trends are shown. From A to B the exchange heat mechanism is forced convection. At a certain point located in B, the wall temperature has exceeded the saturation temperature of the coolant so that the surface has an amount of superheat that allows the bubble nucleation. This point is known as Onset of Nucleate Boiling (ONB) and represents the incipient boiling condition. After the ONB, the heat transfer rate increases because of an increasing amount of vapour, from B to B' the heat transfer mechanism is named Partial Developed Boiling (PDB). Finally at a certain location B' the boiling effect becomes dominant and the region is called Fully Developed Boiling (FDB).

The advantage of using boiling heat transfer is limited by a condition known as Critical Heat Flux (CHF), or alternately Departure from Nucleate Boiling (DNB), which represents the maximum exchanged heat flux that the system can withstand.

At the CHF the presence of bubbles is so high that a vapour film is present along the surface and limits the heat exchange causing a dramatic increase of the wall temperature.

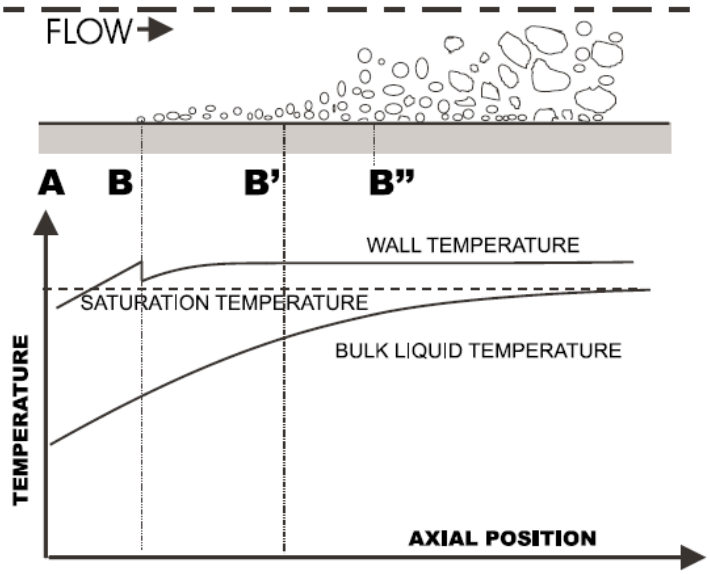

Figure 3-4 **Sub-cooled flow boiling regions: schematic of bubble growth with wall and bulk temperatures along the channel axis [38]**

3.2.1 Forced convection

When the wall temperature at the cooling channel is less than the incipient boiling temperature, the heat transfer method is forced convection. The correlation able to describe the phenomenon is the Modified Dittus Boelter correlation [32][33]:

$$Nu = k\ 0.023(Re)^{0.8}(Pr)^{0.33} \qquad \text{Eq. 21}$$

where *Nu* is the Nusselt Number, *k* an empirical constant used to account the turbulence which occurs in the channel formed by the fins, *Re* the Reynolds Number and *Pr* the Prandt Number.

The amplification factor *k=1.35* has been obtained experimentally and with finite element analyses by Falter for different geometry and flow velocities [34] and used also in [32].

The Reynolds number is:

$$Re = \frac{\rho_b v D_h}{\mu_b} \qquad \text{Eq. 22}$$

where ρ_b is the mass density of the bulk [kg/m^3], *v* the bulk water velocity [m/s], D_h the hydraulic diameter [m] and μ_b the dynamic viscosity of the bulk [Pa s].

The hydraulic diameter to be used in the Reynolds Number is the hydraulic diameter of the flow channel between the fins [34] and is defined as follow (*A* is the flow section, P_w the wetted perimeter, *b* and *h* the dimension of the channel):

$$D_h = \frac{4A}{P_w} = 4\frac{bh}{2(b+h)} \qquad \text{Eq. 23}$$

The Prandt number is defined as:

$$Pr = \frac{\mu_b c_p}{\lambda} \qquad \text{Eq. 24}$$

where c_p is the specific heat of the coolant [J/(kg K)] and λ is the thermal conductivity of the water at the bulk temperature [W/(m K)].

The heat transfer coefficient in single-phase and forced convection for hypervapotron is given by:

$$h_{FC} = \frac{Nu\ \lambda}{D_h} = \ k\ 0.023(Re)^{0.8}(Pr)^{0.33}\frac{\lambda}{D_h} \qquad \text{Eq. 25}$$

The heat flux exchanged in forced convection is (T_w is the channel wall temperature and T_b the temperature of the bulk):

$$q_{FC} = h_{FC}\ (T_w - T_b) \qquad \text{Eq. 26}$$

3.2.2 Onset of nucleate boiling

In steady state condition, in order to activate the bubble nucleation, the surface temperature has to exceed the saturation temperature of the coolant at the local pressure. At the same location, until the temperature of the bulk remains below the saturation, a significant increase in the exchanged heat flux occurs [38]. The process is known as sub-cooled flow boiling.

A procedure for predicting the required conditions to activate the bubble nucleation has been proposed by Hsu and Graham [36] but the solution does not lead to an explicit formula for the incipient heat flux.

Bergles and Rohsenow presented a much more convenient graphical solution which lead to the following expression for the incipient heat flux q_{ONB} [37] (the exchanged heat flux corresponding the ONB point), the equation is valid in the pressure range $0.1034 \leq p \leq 13.79$ MPa [39]):

$$q_{ONB} = 49.2\ \left(\frac{p}{6895}\right)^{1.156}[1.8\ (T_{ONB} - T_{SAT})]^{\frac{2.3}{\left(\frac{p}{6895}\right)^{0.0234}}} \qquad \text{Eq. 27}$$

where p is the local pressure of the water [Pa], T_{ONB} the temperature at which there is the onset of nucleate boiling and T_{SAT} the saturation temperature of the water at the local pressure.

The onset nucleate boiling temperature T_{ONB} is obtained by imposing the equality between the exchanged heat flux in forced convection (Eq. 26) and the incipient heat flux (Eq. 27). The solution has to be found by an iterative process:

$$h_{FC}\ (T_w - T_b) = 49.2\ \left(\frac{p}{6895}\right)^{1.156}[1.8\ (T_{ONB} - T_{SAT})]^{\frac{2.3}{\left(\frac{p}{6895}\right)^{0.0234}}} \qquad \text{Eq. 28}$$

In Eq. 28, T_{SAT} is the saturation temperature at the local pressure and it can be calculated by using the Steltz and Silvestri equation [40] valid in the pressure range 620.52 < *p* < 4688396 Pa:

$$T_{SAT} = 255.38 + \sum_{i=0}^{i=8} A_i [\ln(0.00145\ p)]^i - 273.15$$

$$A_0 = 19.5322$$
$$A_1 = 13.6626$$
$$A_2 = 1.17678$$
$$A_3 = -0.189693$$
$$A_4 = 0.087453$$
$$A_5 = -0.0174053$$
$$A_6 = 0.00214768$$
$$A_7 = -0.138343 * 10^{-3}$$
$$A_8 = 0.38 * 10^{-5}$$

Eq. 29

3.2.3 Fully Developed Boiling

At the onset of nucleate boiling, the heat flux becomes nonlinear with respect to the wall temperature. Where strong nucleate boiling occurs the exchanged heat flux q_{FDB} can be expressed by [37]:

$$q_{FDB} = C\ (T_w - T_{SAT})^n$$ Eq. 30

where *n* is a constant in the vicinity of 4 for most surfaces and *C* a constant function of pressure and fluid-surface combination.

Thom developed a correlation for sub-cooled (or saturated) flow boiling of water under conditions where the nucleate boiling contribution is predominant over forced convection [41]. The equation neglects the channel geometry and the flow rate and it is function of the local pressure and of the difference temperature between the channel wall and the saturation temperature:

$$q_{FDB} = 10^6 \left[\frac{e^{\frac{p}{87*10^5}}}{22.65} (T_w - T_{SAT}) \right]^2$$ Eq. 31

the ranges of validity of Eq. 31 are: 0.50 < *p* <13.8 MPa [39].

Schlosser and Boscary modified the Thom formula by using an exponent equals to 2.8 instead of 2 [42][43]. The correlation has been obtained from experimental campaigns on mockups under thermonuclear fusion conditions but it has been developed for swirl tubes and in literature it has not been found information about other geometries. On the contrary Eq. 31 has been used in [32] for hypervapotron.

3.2.4 Partial Boiling Region

The region between the forced convection and the fully developed boiling is called partial boiling. This transition region, which is frequently neglected, is important to correctly predict the entire heat transfer curve for a particular system.

Different procedures have been proposed [37]:

- McAdams [44] suggested only to use the forced convection and the fully developed boiling curves. The transition point is given by the intersection of the two curves: for wall temperature below this point the forced convection has to be used, while the fully developed boiling curve has to be used above the transition point.
- Kutateladze [45] proposed the following equation that includes a ratio of heat transfer coefficients for fully developed boiling and forced convection:

$$\frac{q_{PBD}}{q_{FC}} = \left[1 + \left\{\frac{\left(\frac{q_{FDB}}{(T_w - T_{SAT})_{FDB}}\right)}{\frac{q_{FC}}{(T_w - T_{SAT})_{FC}}}\right\}^2\right]^{0.5} \qquad \text{Eq. 32}$$

- Rohsenow [46] considered the combined effects of forced convection and nucleate boiling in the transition region as superimposition of the two effects:

$$q = q_{FC} + q_{FDB} \qquad \text{Eq. 33}$$

- K. Engelberg-Forster and R. Greif [47] suggested a method in which the interception between the forced convection curve and the fully developed boiling curve is called (q_0); with this value a new point (q_1) is calculated as follow:

$$q_1 = 1.4\, q_0 \qquad \text{Eq. 34}$$

  q_1 represents the point at which the fully developed boiling occurs; the transition region is located between the incipient boiling and q_1 and it is represented by a straight line, however it's not explained how the incipient boiling point should be found.

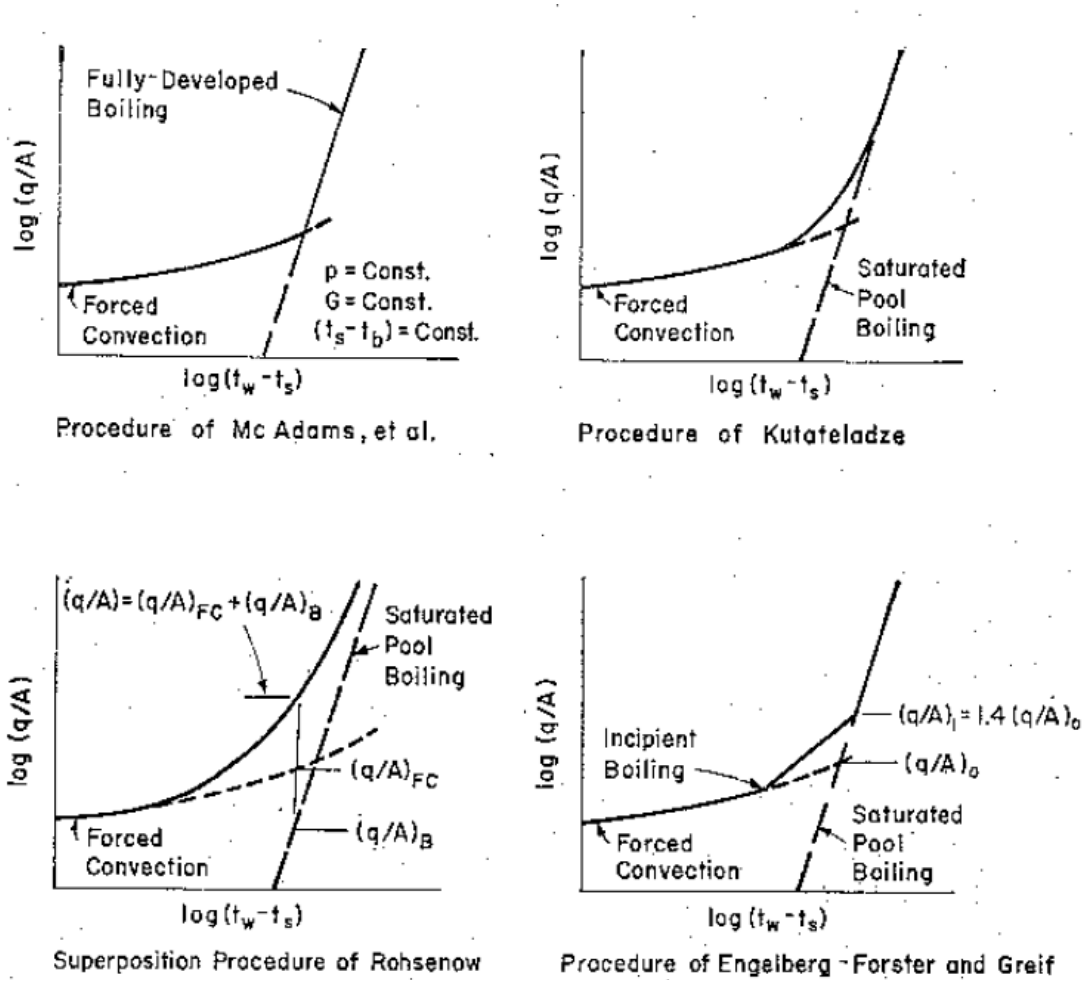

Figure 3-5 Procedures for estimation of heat transfer with forced convection boiling [37]

With other experiments, the constant in Eq. 34 was found to vary from 1.3 to 2.8. A modified Kutateladze correlation has been proposed by Bergles and Rohsenow [37]:

$$q = q_{FC}\left[1+\left\{\frac{q_{FDB}}{q_{FC}}\left(1-\frac{q_{FDBi}}{q_{FDB}}\right)\right\}^2\right]^{0.5} \qquad \text{Eq. 35}$$

where q_{FDBi} is the fully developed boiling heat flux calculated at the incipient boiling. The equation has to be used after the incipient boiling to calculate the heat flux curve which, in this way, asymptotically approaches the fully developed boiling.

3.2.5 Critical Heat Flux

When the Critical Heat Flux (CHF) is achieved, a boiling crisis occurs accompanied by a sudden increase of the surface temperature or deterioration of the heat transfer rate. The CHF imposes a limit in designing and operating boiling heat transfer equipment in power industries such as nuclear fission, fusion, and fossil power plants [48].

As shown in Figure 3-6 after the CHF the wall temperature rises and starts to oscillate. By further increasing the heat flux a region named Film Boiling is reached. Here the surface is entirely covered with steam, the heat exchange is reduced and the wall temperature rises approximately linearly with the heat flux without oscillations.

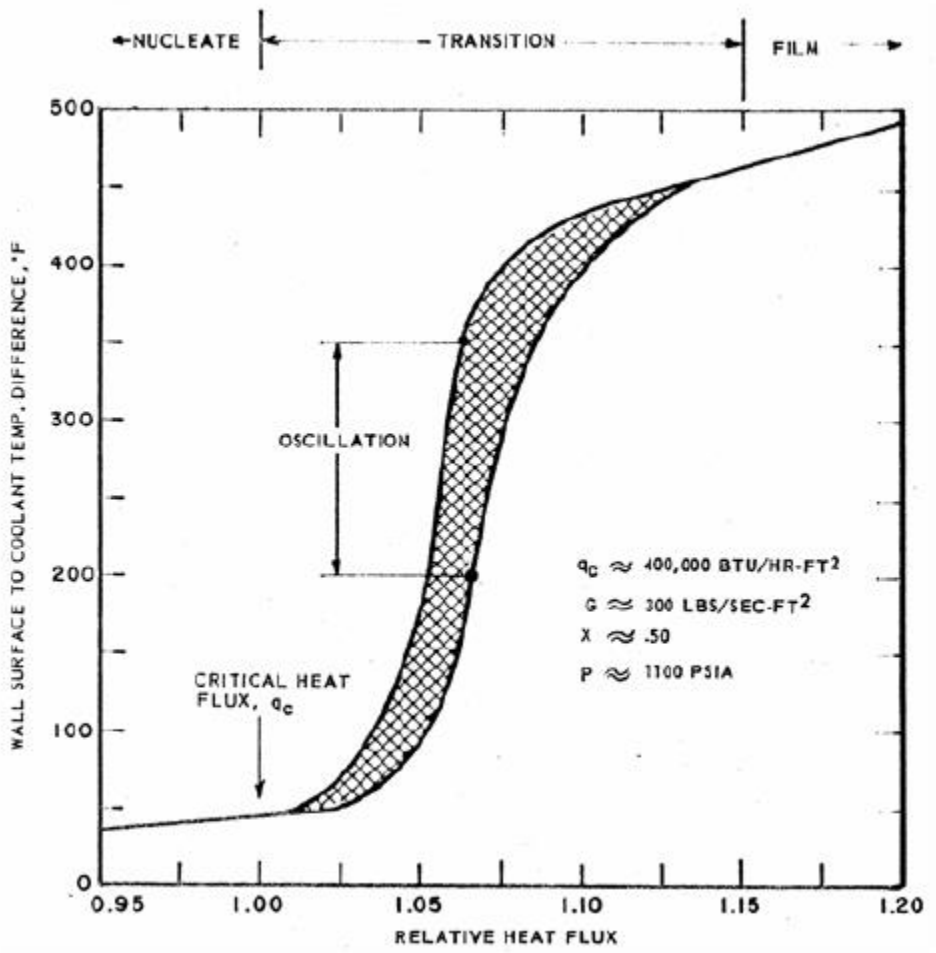

Figure 3-6 Surface temperature as function of heat flux after CHF [49]

As CHF_w is the Critical Heat Flux at the channel wall, the resulting Incident Critical Heat Flux (*ICHF*) has to be carried out by finite element analyses because it depends on the configuration and geometry (Figure 3-7) [50].

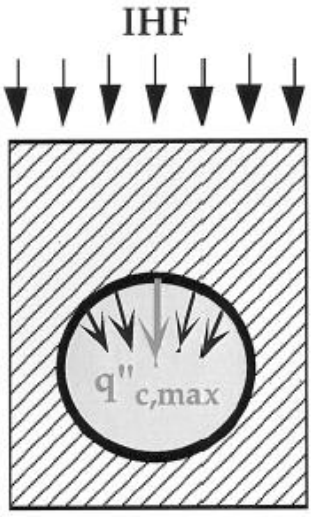

Figure 3-7 **Heat flux at the channel wall (q''_c) for a given incident heat flux (*IHF*) [50]**

In order to increase the CHF in sub-cooled flow boiling conditions several techniques can be used: electrical fields, pressure wave generation, tangential fluid injection, surface roughness, swirl tubes, helically coiled wires and hypervapotron [70].
The design concept of “vapotron” or “hypervapotron” has been proposed initially by Le Franc [67] to provide good heat transfer and CHF performance.
Positive experimental results have been obtained at the Joint European Torus (JET) [68][69] and for the experimental programme supporting the Next European Torus (NET) divertor design [54][55].
Boscary reported that hypervapotron (and swirl tube) are the most efficient cooling technique to remove high incident heat fluxes and at high bulk velocity (10 m/s) an hypervapotron is able to withstand an ICHF 1.4 times higher than a swirl tube with two cooling channels (Figure 3-8) [43].
Cattadori performed experiments on the water cooled hypervapotron CHF taking in account different geometries of the internal fin structure (2 and 4 mm width; 3, 5, 7 mm high; 2 and 4 mm gap between fins) and different coolant thermo-hydraulic parameters (pressure, inlet temperature and bulk velocity) [70]. The maximum obtained CHF has been 29.4 MW/m^2 under the conditions p=0.9 MPa, axial velocity 9 m/s, and inlet temperature 60 °C but the hypervapotron effect (the continuous boiling and condensation between two adjacent fins) has not been detected as it occurs more easily as the coolant velocity and the sub-cooling are low [70].

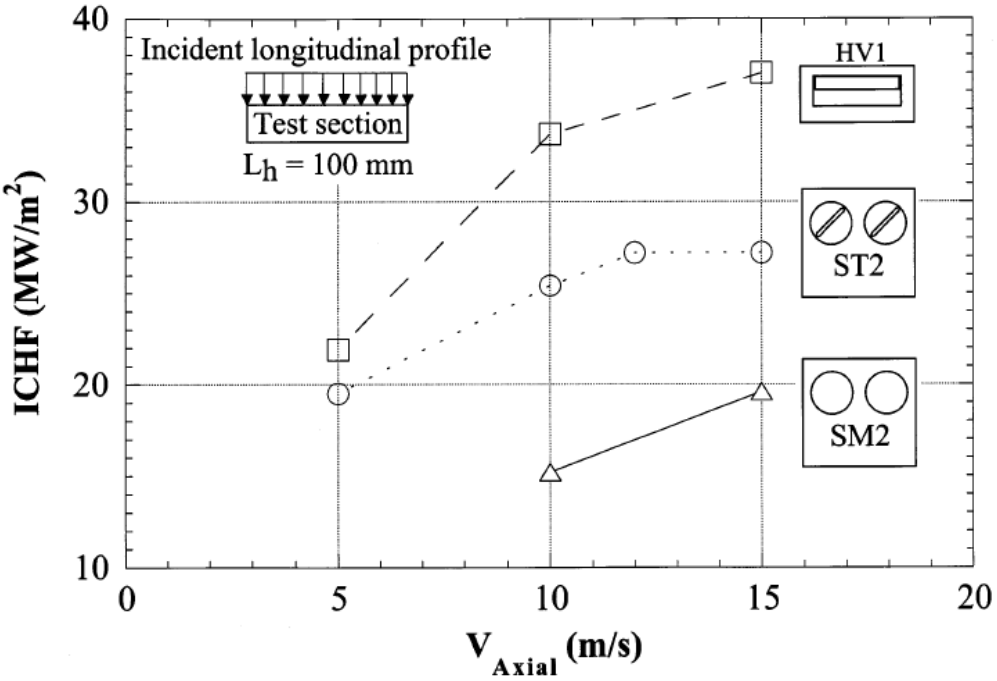

Figure 3-8 **Incident CHF as function of water axial velocity for Association Euratom-CEA tests (width device 27 mm, *p*=3.5 MPa, $\Delta T_{sub,out}$=100°C) [43]**

The evaluation of CHF with high power density, as frequently occurs under fusion condition, is a key factor. The correlations developed for fission reactor have been the starting point and then extended to account the fusion conditions (one-sided heating, peaked heat flux profile, higher flow velocity, higher sub-cooling, lower coolant pressure and lower coolant temperature) [50].

The well-known Tong-75 CHF correlation [51] has been modified by Schlosser et al., in order to fit the CHF under one-side heating data for different cooling channel geometries [50][52][53]:

$$CHF_W = 0.23\, f\, G\, H_{fg} \left[1 + 0.00216 \left(\frac{p}{p_c}\right)^{1.8} Re^{0.5} Ja\right] C_f \qquad \text{Eq. 36}$$

with

$$Re = \frac{G D_h}{\mu_f} \qquad \text{Eq. 37}$$

$$Ja = \frac{\rho_f}{\rho_g} \frac{c_p (T_{SAT} - T)}{H_{fg}} \qquad \text{Eq. 38}$$

$$f = 8\, Re^{-0.6} \left(\frac{D_h}{D_0}\right)^{0.32} \qquad \text{Eq. 39}$$

and where: CHF_w is the CHF at the channel wall [W/m^2], f is the friction factor calculated by Eq. 39, G is the mass velocity of the coolant [kg/(m^2 s)], T is the coolant temperature at a local position [°C], p is the local pressure of the coolant [MPa], p_c is the critical pressure of the water equal to 22.1 MPa, T_{SAT} the saturation temperature corresponding to the pressure p [°C], H_{fg} is the latent heat of vaporization at T_{SAT} [J/kg], Re is the Reynolds Number calculated as reported in Eq. 37, D_h the hydraulic diameter [m], μ_f is the water density at T [kg/m^3], μ_g is the vapour density at T_{SAT} [kg/m^3], Ja is the Jakob number defined as Eq. 38, c_p is the specific heat at T [J/(kg K)], D_0 is the reference diameter equals to 12.7x10^{-3} m and C_f is a factor used to account for the configuration.

In Eq. 36, C_f is a corrective factor to account for the configuration and the incident heat flux profile.

Several design concepts (smooth pipes, swirl tubes, swirl rod inserts and hypervapotrons) with the same external width of 27 mm have been characterized by Schlosser et al. [52]. Conversely, the more the flux is peaked the higher is the CHF, and in this condition is possible to find for one geometry (or for geometries close to) the same corrective factor C_f between uniform heated tube and one side heated without any dependency on the thermal hydraulic condition. However C_f depends on the incident heat flux profile [52].

A corrective factor $C_f = 1.97$ [52][72] can be used for a geometry with the main dimensions as reported in Table 3-1 (with respect to the Figure 3-9). This value doesn't appears appropriate for the considered SPIDER geometry as listed in Table 3-1: the main difference is the HV width.

The influence of the width in the ICHF (the corresponding data for the CHF have not been found) is shown in Figure 3-10 both for uniform power deposition and peaked power density with 90% of the power deposited in a disc of 1.5 mm of diameter.

Because the available information is very scarce, a possible solution would be to use a corrective factor $C_f = 1.2$ [52][72] valid for smooth channel with internal diameter of 10 mm thus ensuring a high safety margin, or alternatively using only the Tong-75 CHF correlation without any corrective factor.

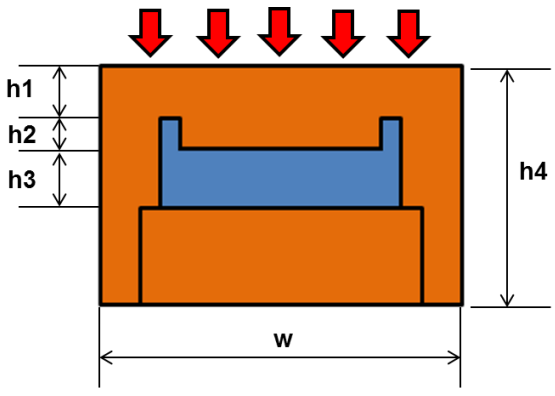

Figure 3-9 HV cross section scheme

Table 3-1 **Comparison of the main geometrical dimension for the hypervapotron used by Schlosser in [52] and foreseen for SPIDER**

	Literature	SPIDER
h1 [mm]	3	4
h2 [mm]	4	4
h3 [mm]	5	4
h4 [mm]	20	18
w [mm]	**27**	**65**
Fins width [mm]	3	3
Groove between fins [mm]	3	3

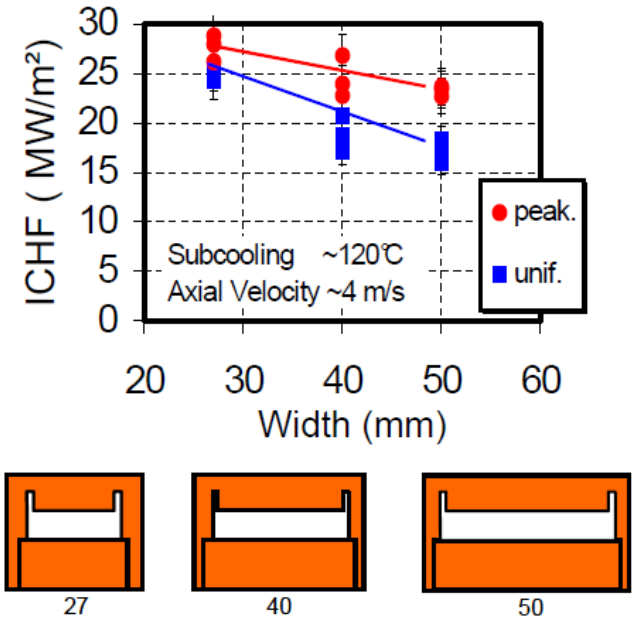

Figure 3-10 **ICHF as function of hypervapotron width [73]**

3.2.6 Pressure Drop

The knowledge of pressure drop is essential in the SPIDER Beam Dump thermo-hydraulic model because the correlations for Partial and Fully Developed Boiling needs the local value of the coolant pressure to calculate the exchanged heat flux.

A summary of hypervapotron pressure drop data in terms of the friction factor as function of the Reynolds number is shown in Figure 3-11.
By using the existing data on hypervapotron geometry [32][34][54][56][57] Baxi proposed the following correlation for friction factor [50][58]:

$$f_{HV} = 0.153\, Re^{-0.2} \qquad \text{Eq. 40}$$

where Eq. 22 and Eq. 23 are still valid.

The pressure drop along the hypervapotron is then calculated as follow:

$$\Delta p = 4\, f_{HV}\, \frac{L}{D_h}\, \rho\, \frac{v^2}{2} \qquad \text{Eq. 41}$$

Where Δp is the pressure drop [Pa], f_{HV} is the friction factor, L is the channel length [m], D_h is the hydraulic diameter [m], ρ is the mass density of the water and v is the bulk velocity [m/s].

The results indicate that the measured friction factors are significantly lower than the predicted values with the Baxi correlation probably due to the poor accounting of entrance/exit effect [50].

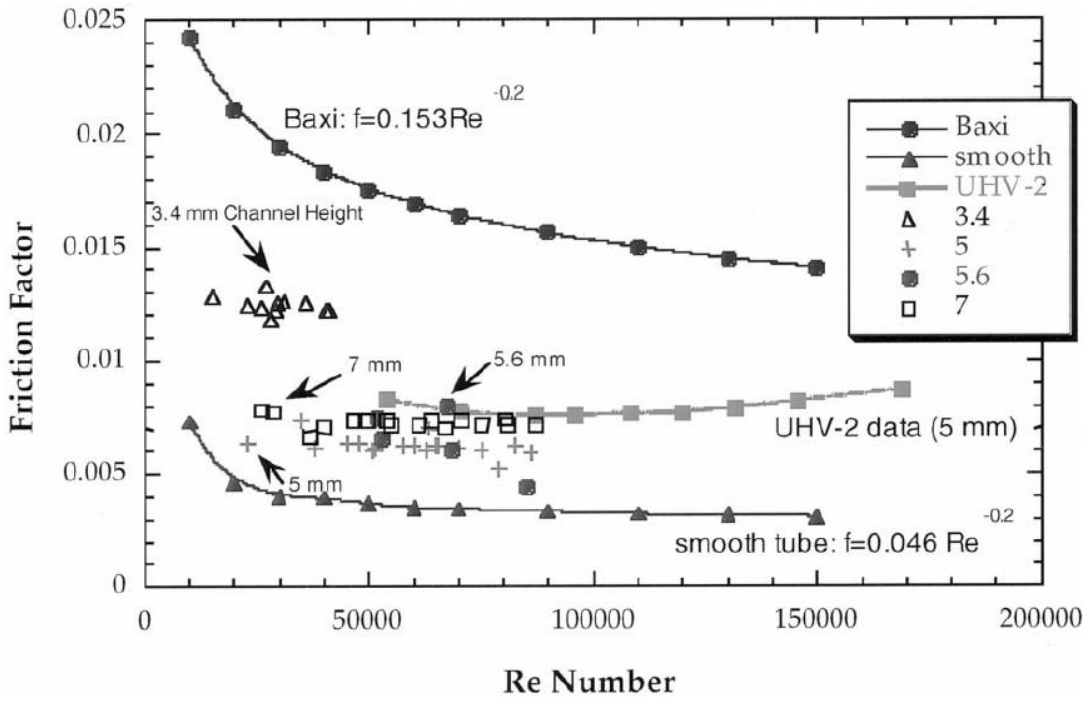

Figure 3-11 Friction factor as function of Reynolds number for hypervapotron geometry and smooth tube for comparison [50]

3.3 ANSYS Customization

The correlations reported in paragraph 3.2 require the calculation of heat flux and pressure drop as a function of local parameters (channel wall and coolant bulk temperature, coolant pressure, saturation temperature and pressure, flow rate, channel geometry, coolant density, velocity, viscosity, and thermal conductibility); these detailed formulations have been programmed in ANSYS APDL finite element code to realise a custom version of the software to be used for special analyses.

The standard ANSYS APDL routines give only the possibility to perform simulations in single-phase heat transfer condition without simulation of nucleate boiling, hence a code customization was required. Furthermore, the customization shall consider the geometry of the heat transfer element and the characteristic conditions for coolant flow and heat transfer.
A user programmable routine with the hypervapotron correlations has been written in FORTRAN and then linked to ANSYS APDL. As the formulas are non-linear, the main program calls the modified routine at each step and for each element to solve iteratively the balance equations and check the convergence criteria.

3.3.1 Material Proprieties

All the materials have been implemented in the finite element model by using polynomial equations to simulate their proprieties as function of temperature.

3.3.2 Water

The thermo-physical proprieties of the water have been obtained from the NIST data [61]. The following properties have been programmed in the model:

- mass density in the range 0÷150 °C (Figure 3-12)

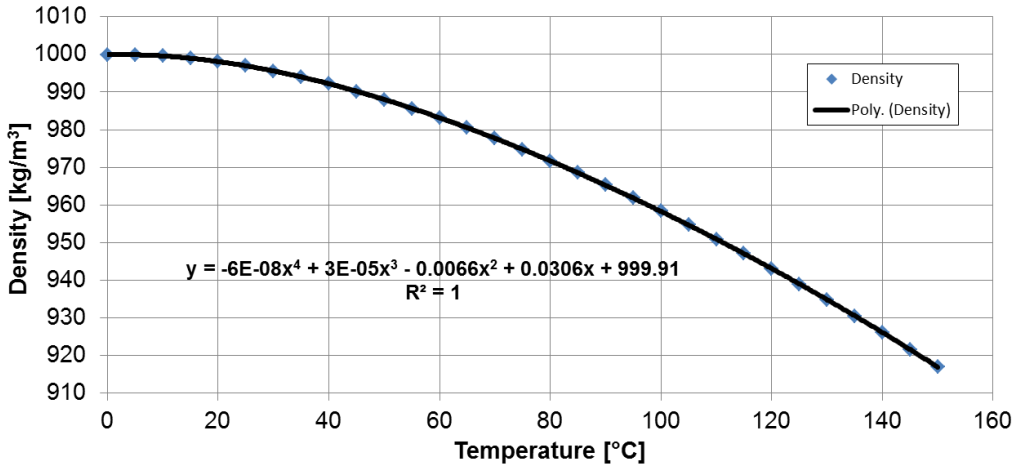

Figure 3-12 Water mass density as function of temperature

- thermal conductivity in the range 0÷150 °C (Figure 3-13)

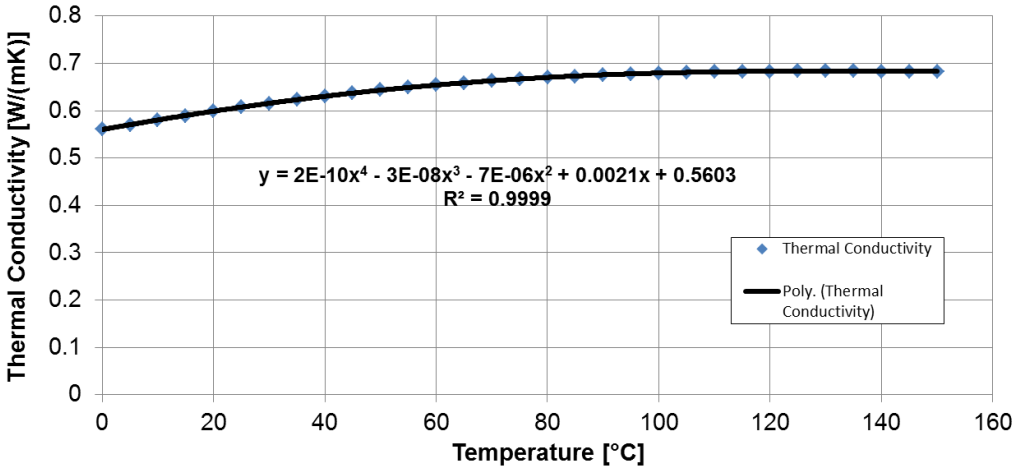

Figure 3-13 Water thermal conductivity as function of temperature

- Specific heat in the range 0÷150 °C (Figure 3-14)

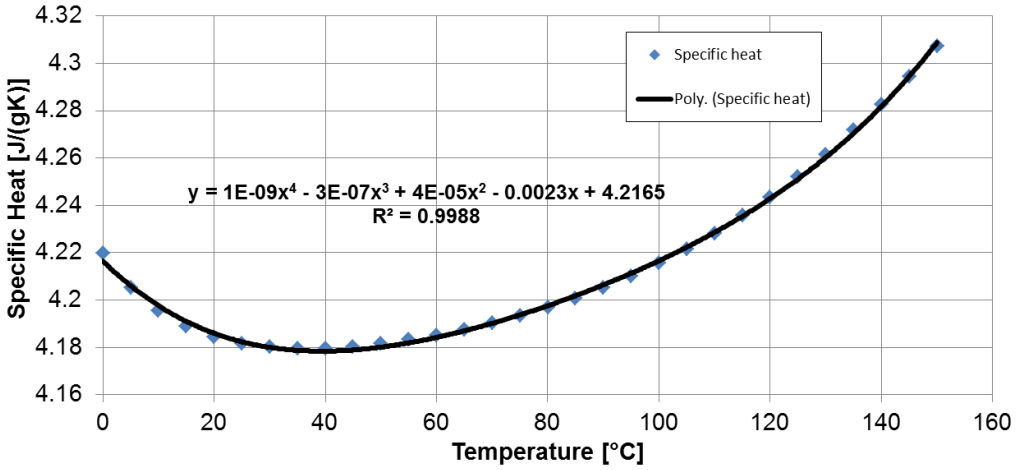

Figure 3-14 Water specific heat as function of temperature

- Dynamic viscosity in the range 0÷150 °C (Figure 3-15)

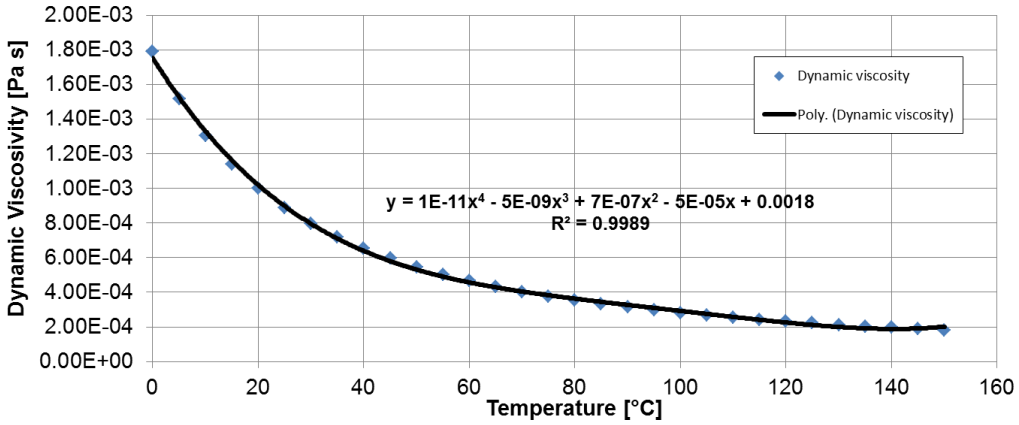

Figure 3-15 Water dynamic viscosity as function of temperature

3.3.3 CuCrZr alloy

The thermal conductibility of the CuCrZr alloy has been obtained from the ITER Documentation [62] (Figure 3-16).

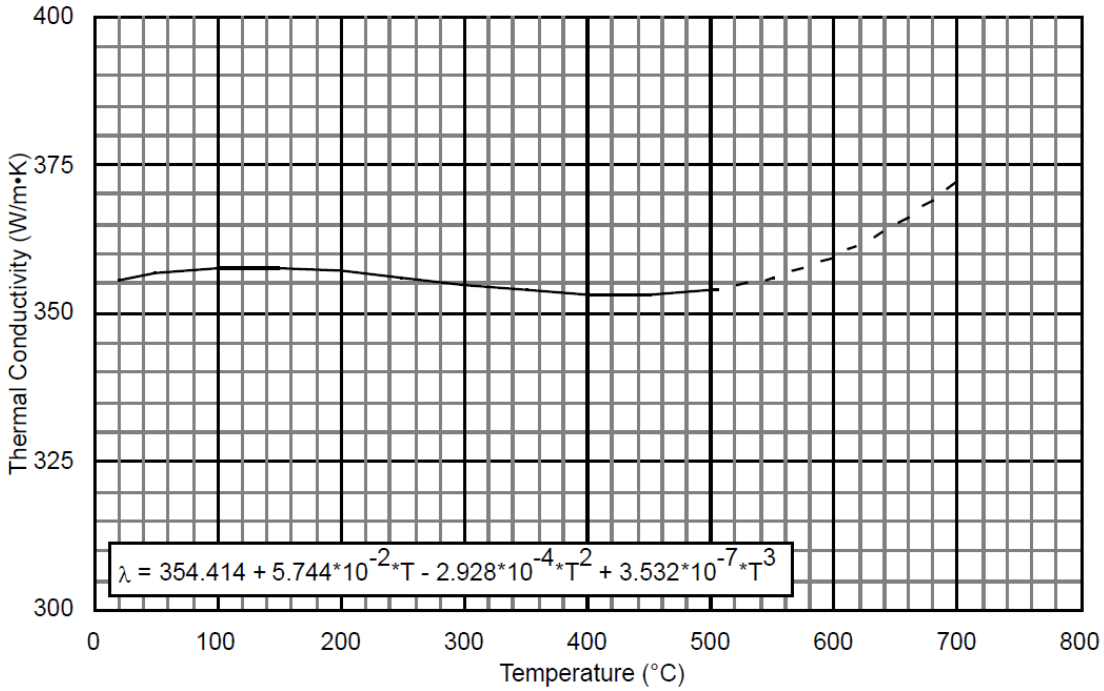

Figure 3-16 Thermal conductibility for unirradieted CuCrZr as function of temperature

3.4 Thermal loads and boundary conditions

The thermal loads on the SPIDER Beam Dump are determined by the beam parameters. They have been calculated by using the vector code Trigo and Backscat Monte Carlo codes [27][59].

The shape of the power density deposition is approximately a bi-gaussian. Each of the gaussian distribution represent a fraction of the beamlet power: one is used for the core fraction with divergence ω_c, and one for the halo fraction with divergence ω_h [60]. The power density is given by:

$$\frac{P_\omega}{P_{tot}} = \left\{ \frac{1-f}{\pi(X\omega_c)^2} exp\left[-\left(\frac{\omega}{\omega_c}\right) \right]^2 + \frac{f}{\pi(X\omega_h)^2} exp\left[-\left(\frac{\omega}{\omega_h}\right) \right]^2 \right\} \qquad \text{Eq. 42}$$

where P_ω is the power density [W/m^2] in the ω direction which is the angle with respect to the beamlet axis, X is the distance from the Grounded Grid (GG), f the fraction of the power present in the halo, P_{tot} the total power of one beamlet.

The starting point of the beamlets are the 1280 apertures on the GG (Figure 3-17) defined by a text file together with the positions of the GG centre and the distance from the beam dump panels obtained from the SPIDER 3D geometrical model.
The two beam dump panel have been assumed as rectangular plane surfaces and regular grids on them have been used as mesh.

Different scenarios have been taken into account as reported in Table 3-2.

The results are available in a plot format (an example of obtained heat loads data is given in Figure 3-18) or in tabular format ready for the load application in ANSYS.

Table 3-2 Beam parameters used for the heat loads on the SPIDER Beam Dump. The horizontal misalignment is positive in the left direction

Scenario	ω_c [mrad]	ω_h [mrad]	f [%]	Horizontal misalignment [rad]
#1a	3	3	15	0
#1b	3	30	15	0
#1c	3	3	15	2
#2a	5	5	15	0
#2b	5	30	15	0
#2c	5	5	15	2
#3a	7	7	15	0
#3b	7	30	15	0
#3c	7	7	15	2

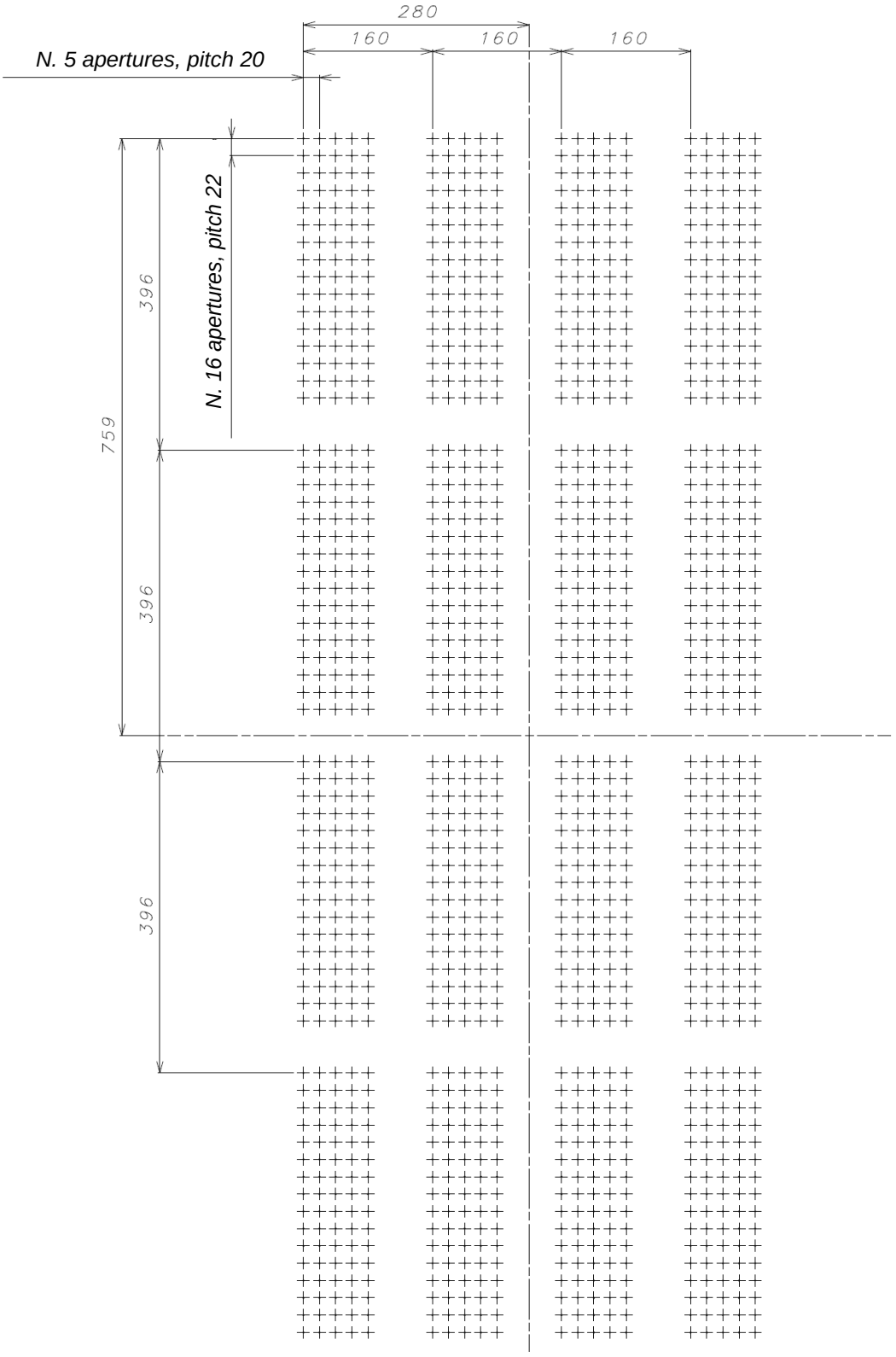

Figure 3-17 Beamlet aperture arrangements on the SPIDER Grounded Grid

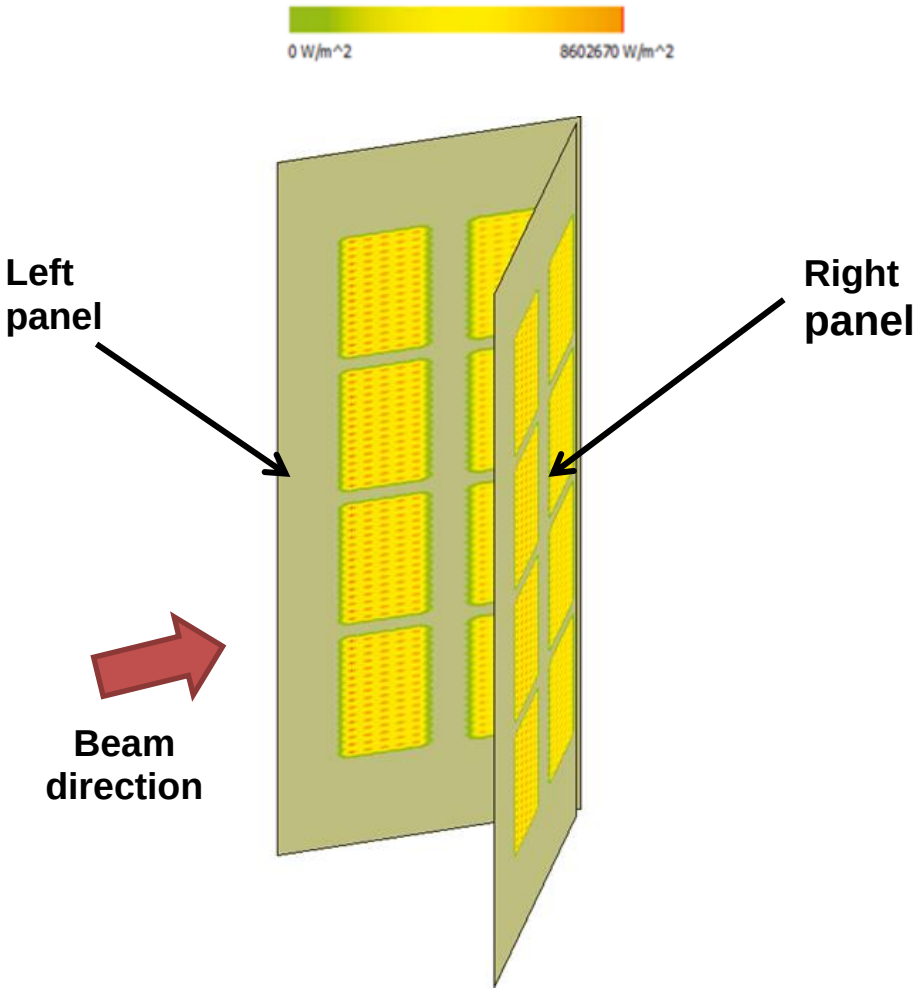

Figure 3-18 **Heat load on the Beam Dump panels in case of Scenario#1a (3mrad divergence, no halo, no misalignment)**

The heat fluxes from the Trigo and Backscat codes have been applied to the external wall of the Beam Dump by using tabulated data and ANSYS ADPL scripts. As the heat fluxes are obtained for simple vertical walls, the values corresponding to the regions in which there are chamfers have been scaled with a factor equals to the cosine of the angle of incidence.
Two examples of heat loads applied on the FE model are shown in Figure 3-19 and Figure 3-20.

The boundary conditions for the simulation are:

- inlet mass flow rate: 32 kg/s [10];
- inlet temperature of the coolant: 20 °C [10];
- outlet pressure: 0.9 MPa.

Note that the total mass flow rate for the Spider Beam Dump is 64 kg/s (32 kg/s for each panel) and the outlet pressure has been set to 0.902 MPa in order to get an inlet pressure equal to 1 MPa [10].

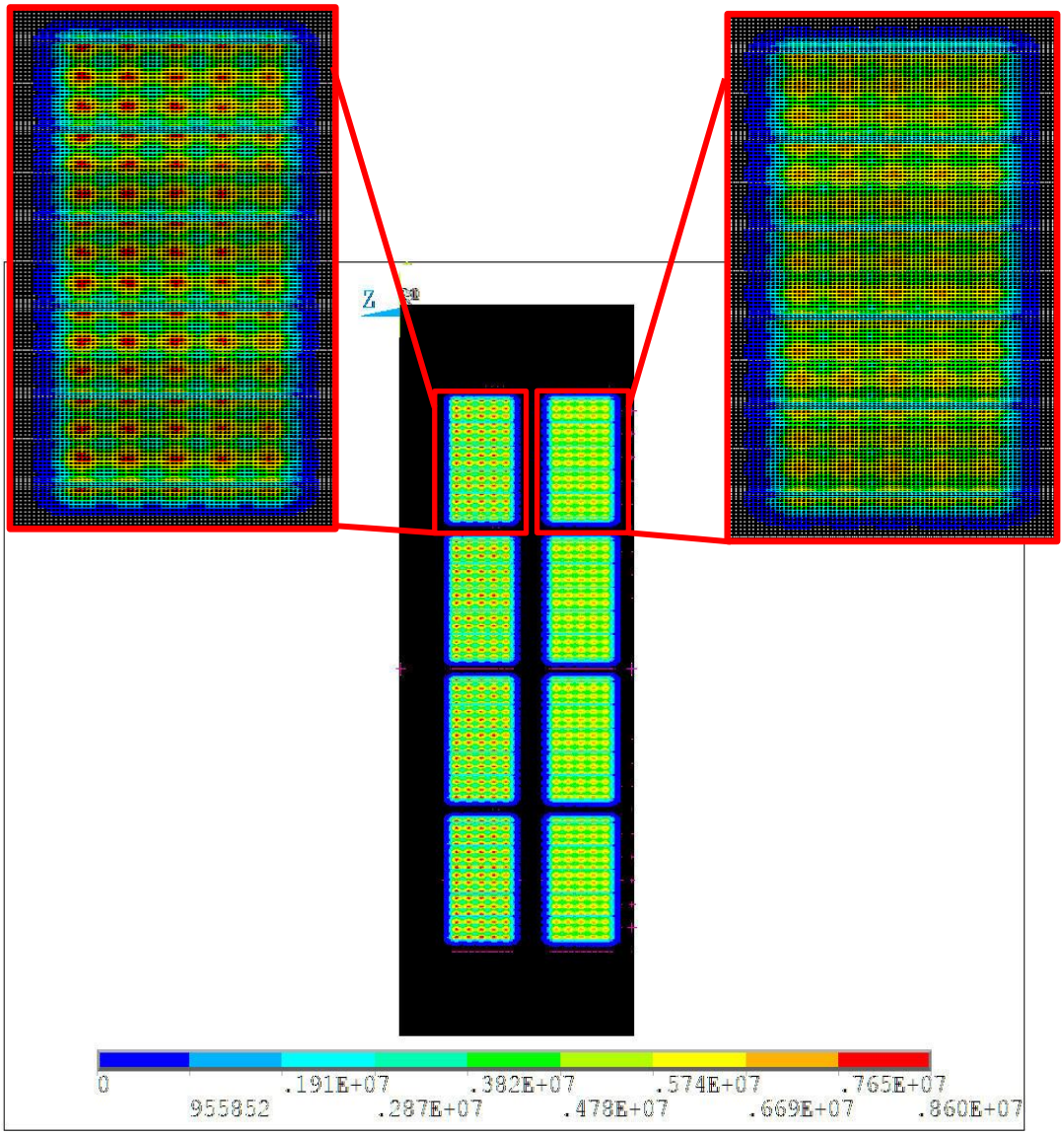

Figure 3-19 **Beam Dump Left Panel: applied heat fluxes [W/m^2] in case of ω_c = 3 mrad and no halo**

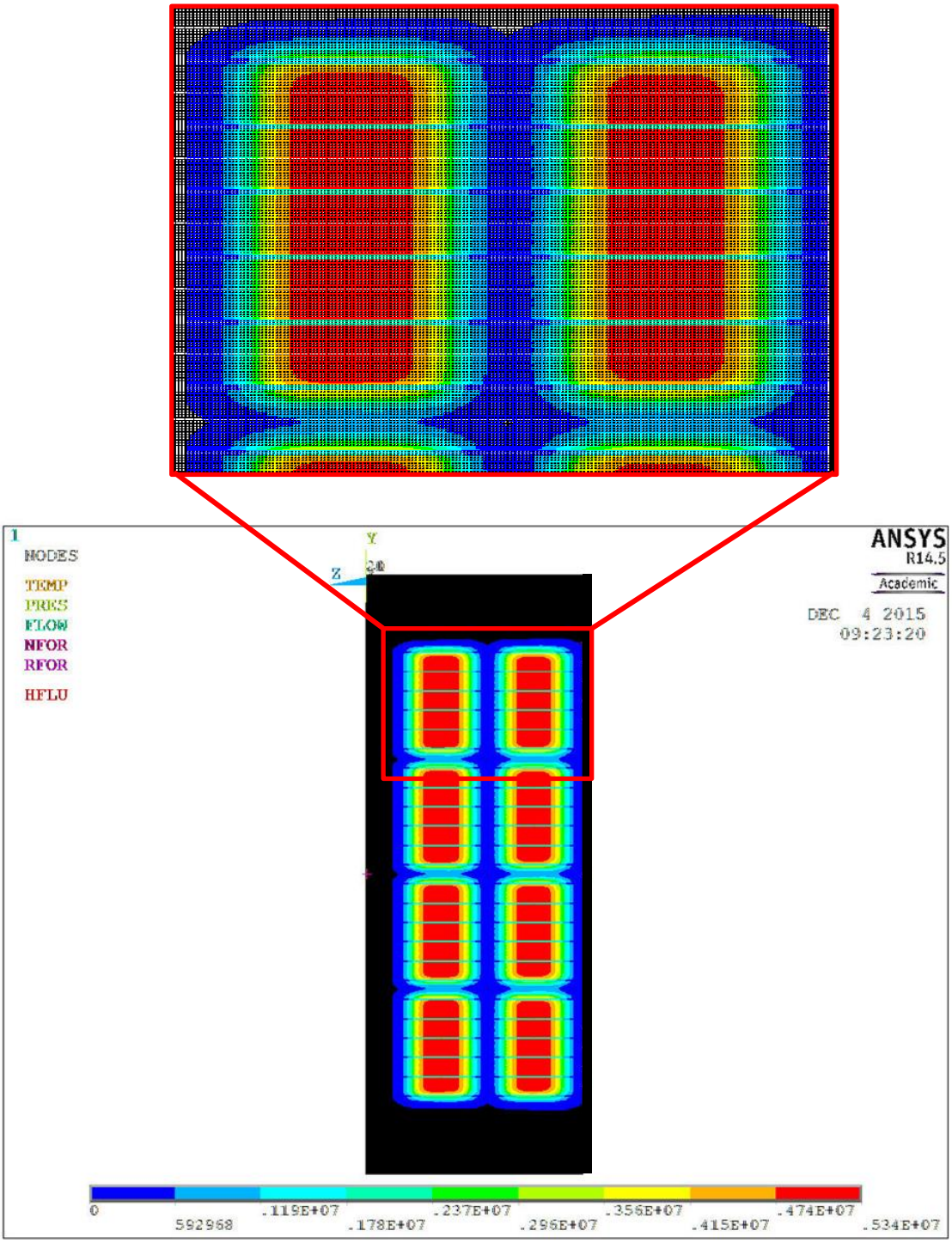

Figure 3-20 **Beam Dump Left Panel: applied heat fluxes [W/m^2] in case of ω_c = 7 mrad and no halo**

3.5 FE Model

The three dimensional coupled solid-fluid model has been developed with the following elements and it is shown in Figure 3-21:

- the element “solid70” is a solid thermal element which has been associated with the material proprieties of the CuCrZr copper alloy;
- the element “fluid116” is a fluid thermal element able to simulate pipes and cooling channel geometries and it has been associated with the water proprieties;
- the element “surf152” is a surface element with the ability to link the fluid elements with the solid ones. It has been associated with the customized routine to transfer the heat flux form the channel surface to the bulk.

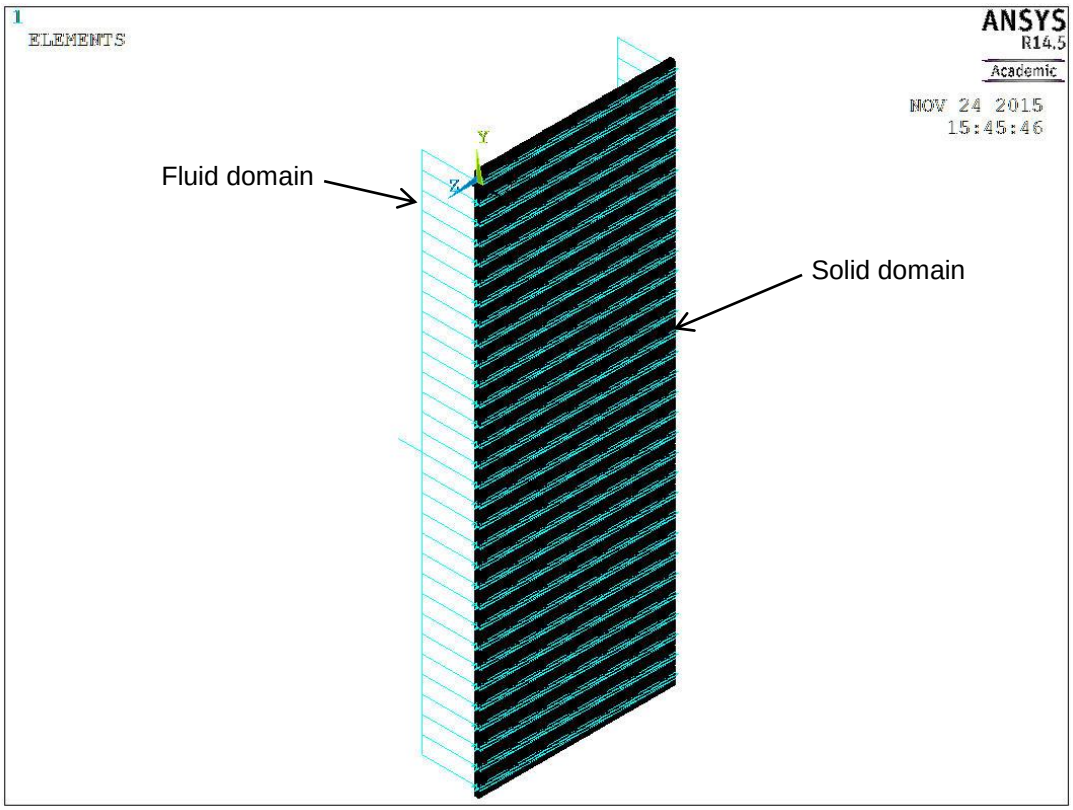

Figure 3-21 Overview of the FE model with elements of the fluid and solid domains

3.5.1 Fluid Domain

The one-dimensional element *fluid116* (already described in 2.3) has been used to simulate pipes, manifolds and hypervapotron channels.
For the standard pipes, the friction factor (and the resulting pressure drop) is automatically calculated in ANSYS APDL, whereas for the hypervapotron channels the Eq. 40 has been included in the code for the friction factor. In order to compute the pressure drop in bends, inlet and outlet, the loss coefficients in Table 3-3 have been used [63].

Table 3-3 Localised loss coefficients

Type of element	K_{loss}
Manifold inlet/outlet	0.2
90° bend	0.5
HV inlet	0.5
HV outlet	1

The overall fluid domain is shown in Figure 3-22 where the dimension of the internal diameter of the pipes and the hydraulic diameter (calculated as in Eq. 23) of the hypervapotron channels are also reported.

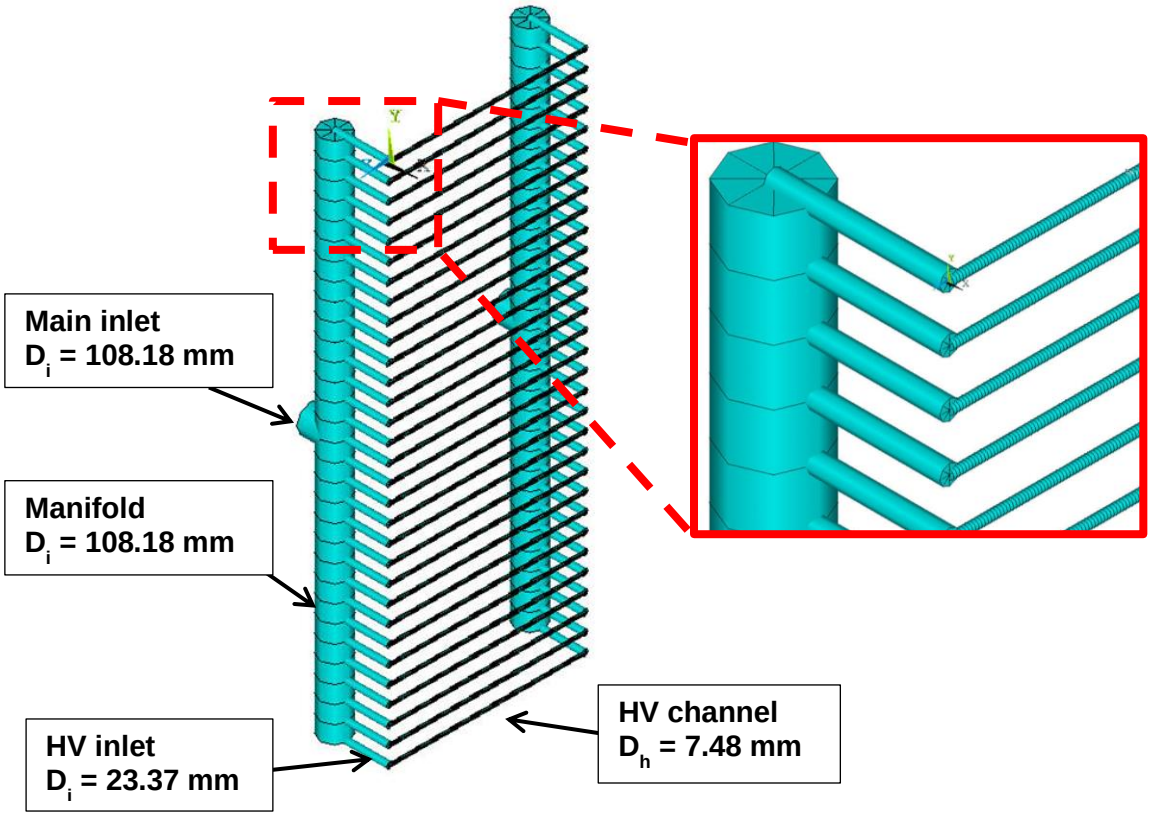

Figure 3-22 Beam Dump model: overview of the fluid domain made of *fluid116* elements

3.5.2 Solid Domain

The element *solid70* (Figure 3-23) has been used to simulate the solid part that constitutes the Beam Dump. *Solid70* is an element with 3-D thermal conduction capability. It has eight nodes with a single degree of freedom (temperature) at each node.

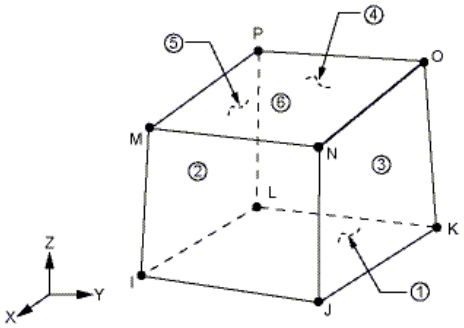

Figure 3-23 ANSYS element *solid70*

In Figure 3-24 the section of one hypervapotron with the main dimensions is reported. The cross section of the flow (57 mm x 4 mm) is modelled without considering the fins (as required for the correlations listed in 3.2.1). The thickness of CuCrZr directly exposed to the beam is 5.7 mm (the real thickness without considering the fins should be 4 mm but a layer of 1.7 mm has been added to account the additional material of the fins, a discussion of this will be given in paragraph 3.6.3).

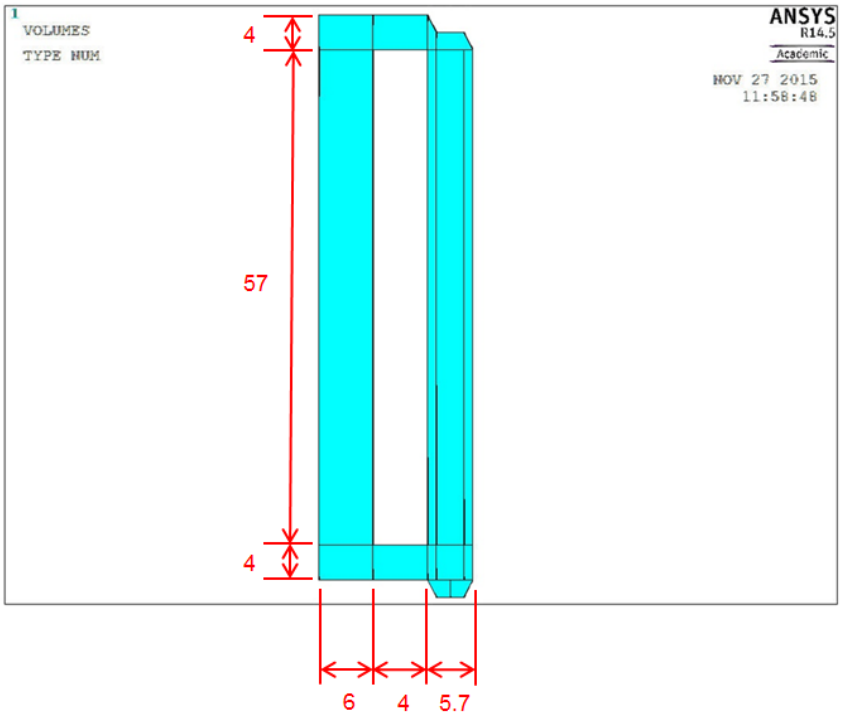

Figure 3-24 Cross section of one hypervapotron with main dimensions in millimetres

3.5.3 Surface elements

The element *surface152* is a thermal surface element that may be overlaid onto an area face of any 3D thermal elements. By using this element type is possible to transfer information from the fluid domain to the solid one (and vice versa) so that the coupled 1D-3D model is realised. This coupling is realised by placing the *surface152* link, named extra node, onto the *fluid116* node.

3.5.4 Mesh

The used mesh consists of more than 11.9 million of elements and a magnified detail is shown in Figure 3-25.

Along the hypervapotron axial direction the same mesh has been used for ANSYS APDL and for the generation of the heat loads in order to get an overlap of the nodes where the heat fluxes have to be imposed.

In the orthogonal direction a fine mesh in the thickness exposed to the beam and a coarser mesh on the back side have been adopted. The finer mesh on the front side allows a much easier convergence because this is the region where the heat transfer mainly occurs. On the contrary, the back side has a coarse mesh which has been adopted because the temperature gradients here are not high and this choice allows faster simulations.

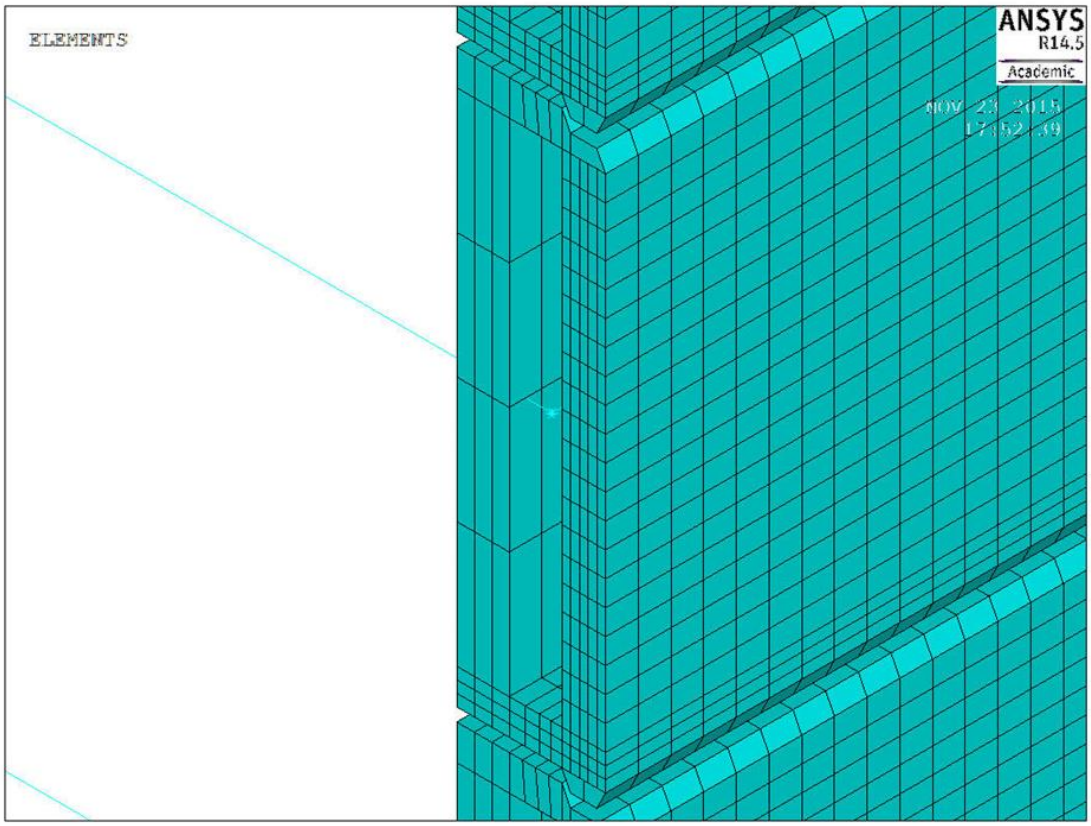

Figure 3-25 Magnification of the mesh used for the SPIDER Beam Dump model

3.6 Results

The thermocouples installed along the hypervapotrons and at each outlet pipe are used for protection of the SPIDER Beam Dump, for calorimetry, and can provide information about the particle beam using the Beam Dump as a diagnostic.

Housings of thermocouples are not modelled in the geometrical model as the good thermal contact realised at the thermocouple-hypervapotron interface will not introduce thermal discontinuities; indeed, the small radial gap of 0.1 mm between thermocouple and hypervapotron will be filled with a thermal conducting silver based cement. Locations of thermocouples are detailed in the following when readings of measurements are discussed.

In the following the results of the carried out simulation listed in Table 3-2 are reported. It has been decided to group these results in order to show the capability of the component to diagnose the beam divergence, the beam halo and the horizontal misalignment.
To facilitate the reading of this paragraph only the main results are reported with the legend given in Figure 3-26

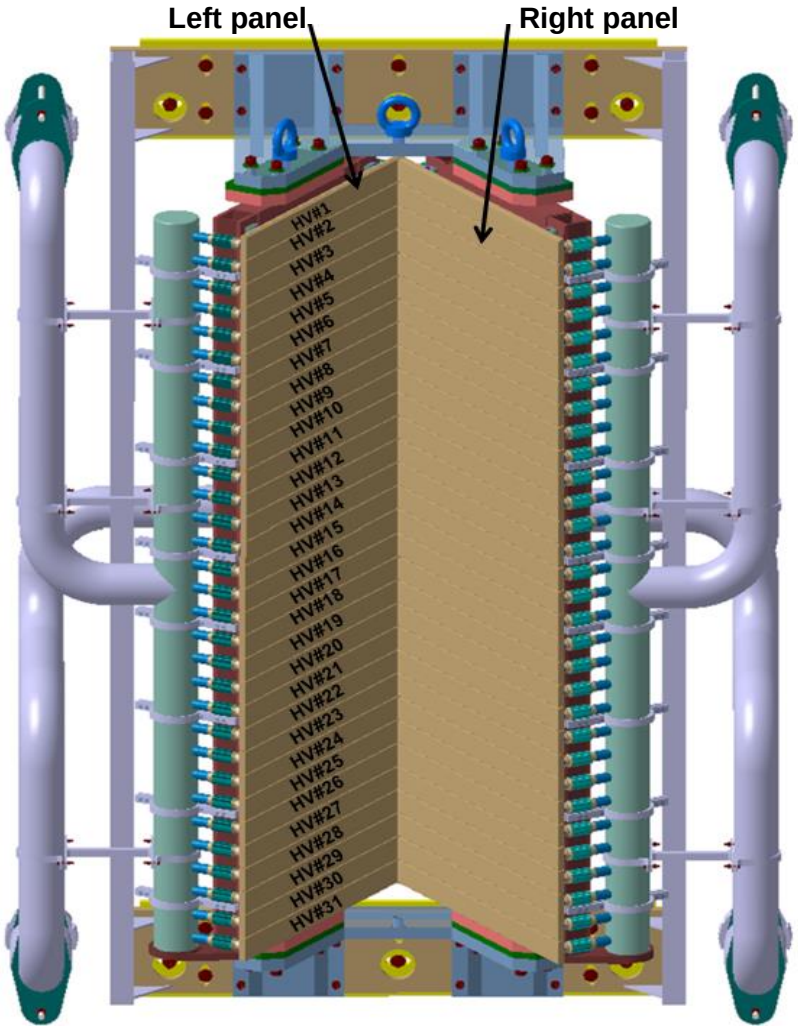

Figure 3-26 SPIDER Beam Dump: legend used for the results

3.6.1 Nominal Conditions

The following results have been obtained in the thermo-hydraulic nominal conditions (determined by the cooling plant) in which the main boundary conditions are:

- Inlet mass flow rate for one panel : 32 kg/s [10];
- Inlet temperature of the coolant: 20 °C [10];
- Outlet pressure: 0.9 MPa.

Note that the outlet pressure has been set to 0.902 MPa in order to get an inlet pressure equal to 1 MPa [10].

A general estimate of the heat transfer expected in the simulation is given in Figure 3-27: the plot gives the heat transfer (q) as function of the wall temperature at the cooling channel (T_w) within the assumptions given in the caption. By considering a bulk temperature of the coolant of 25 °C and a pressure of 1 MPa, the onset of the nucleate boiling (T_{ONB}) occurs at 188 °C. As long as the wall temperature is under that value the heat transfer mechanism is forced convection (q_{FC}); when the T_{ONB} is reached the partial developed boiling starts, causing an increase of the heat transfer.

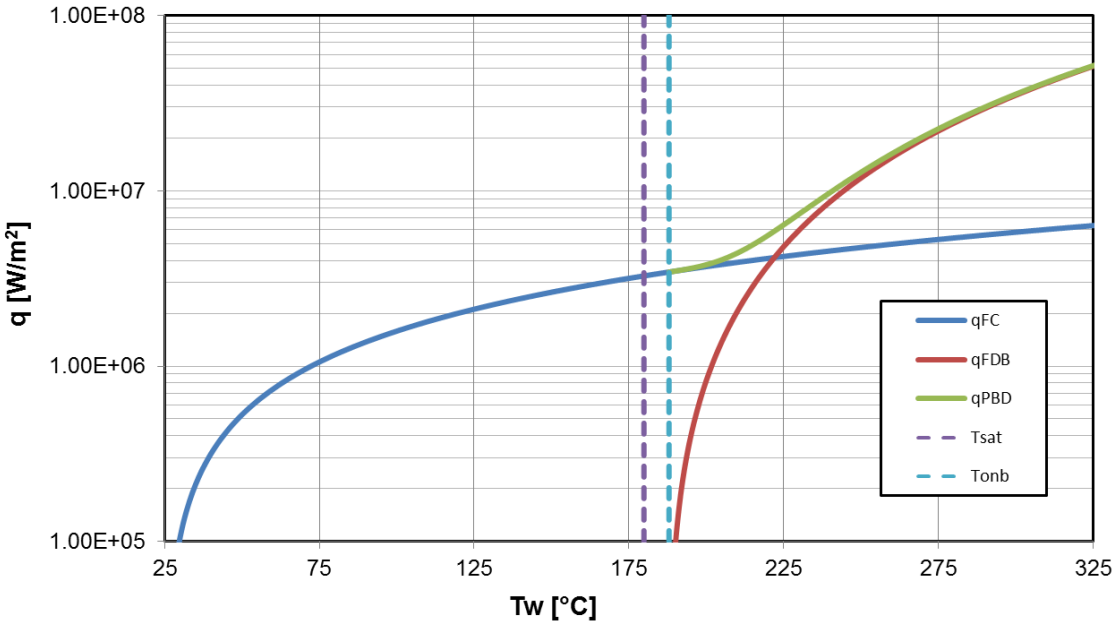

Figure 3-27 **Estimate of heat transfer for hypervapotron geometry with forced convection (q_{FC}), partial developed boiling (q_{PDB}) calculated with the Bergles and Rohsenow procedure and fully developed boiling (q_{FDB}), for T_b=25 °C, p=1 MPa, D_h=7.48 mm and $\dot{m}$=1.03 kg/s**

3.6.1.1 Beam divergence

The divergence of the beamlets can be detected by the shape of the temperature profile along the hypervapotron.

In the hypothesis of no halo ($\omega_h = \omega_c$) and by changing the divergence of the beamlet core (ω_c) the results for the HV#13 are shown in Table 3-4 and in the following.

Table 3-4 HV#13: temperatures at the thermocouples position in different beam scenarios without

	ω_c = 3 mrad	**ω_c = 5 mrad**	**ω_c = 7 mrad**
Thermocouples position [mm]	T [°C]	T [°C]	T [°C]
151	21	25	38
171	34	59	75
191	116	122	121
211	216	180	164
231	191	206	196
251	224	210	206
271	193	209	210
291	222	210	210
311	191	209	209
331	220	209	204
351	192	202	190
371	211	177	162
391	96	112	115
411	42	63	77
431	36	41	53
471	36	43	56
491	46	69	84
511	133	132	130
531	212	181	167
551	197	204	192
571	219	210	206
591	199	211	210
611	219	211	211
631	201	211	210
651	220	212	206
671	202	203	190
691	207	177	164
711	123	130	130
731	57	77	91
751	51	57	69

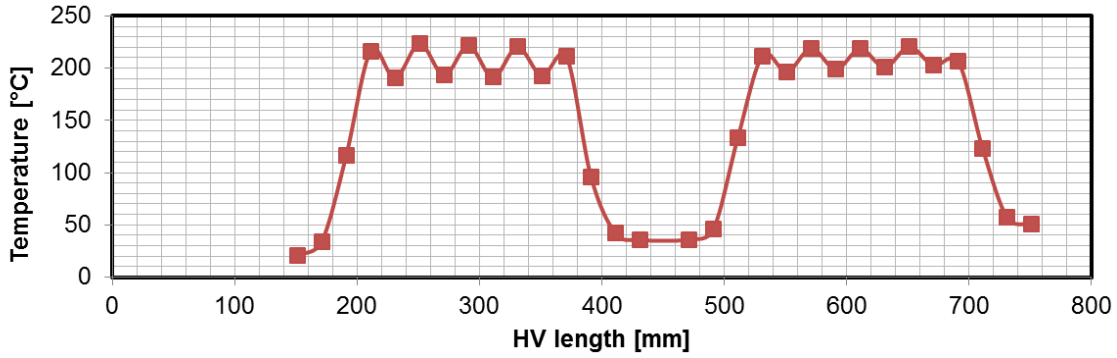

Figure 3-28 **HV#13 left panel: temperatures at 3 mm depth and at the positions of the thermocouples in case of $\omega_c = \omega_h = 3$ mrad (no halo)**

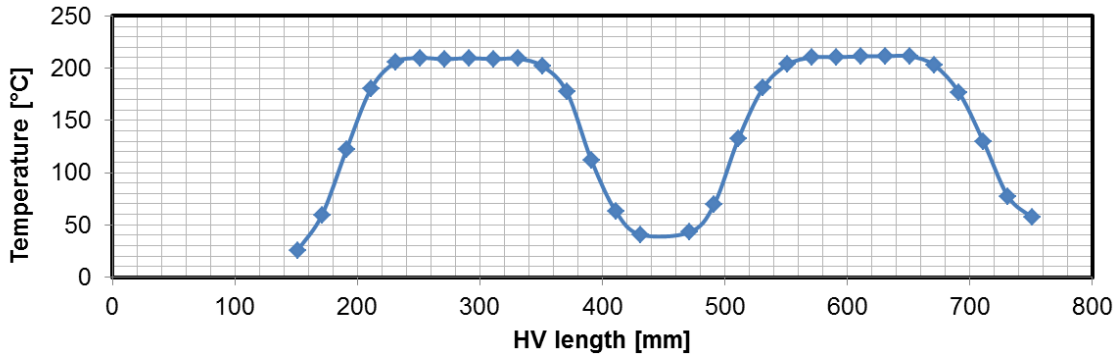

Figure 3-29 **HV#13 left panel: temperatures at 3 mm depth and at the positions of the thermocouples in case of $\omega_c = \omega_h = 5$ mrad (no halo)**

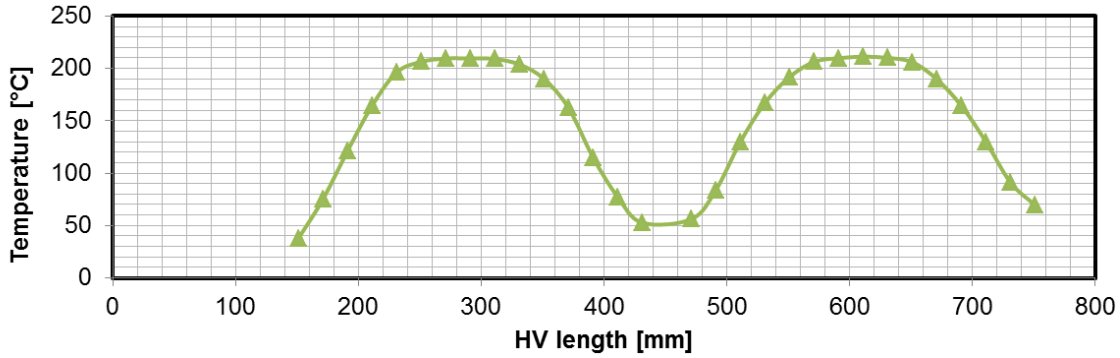

Figure 3-30 **HV#13 left panel: temperatures at 3 mm depth and at the positions of the thermocouples in case of $\omega_c = \omega_h = 7$ mrad (no halo)**

From the Figure 3-28, Figure 3-29 and Figure 3-30 it becomes evident that only in case of 3 mrad of core divergence is possible to detect the peaks and the valleys of temperature caused by the different beamlets; an almost uniform temperature is produced in the central part of the heated regions for larger beam divergence. A comparison of these three cases is shown in Figure 3-31: the higher the core

divergence, the higher the temperatures at the tails of the beam (e.g for the first thermocouple located at 151 mm the temperature is 21 °C in case of ω_c=3 mrad and 38° C in case of ω_c=7 mrad, the percentage increase is therefore of 81%).

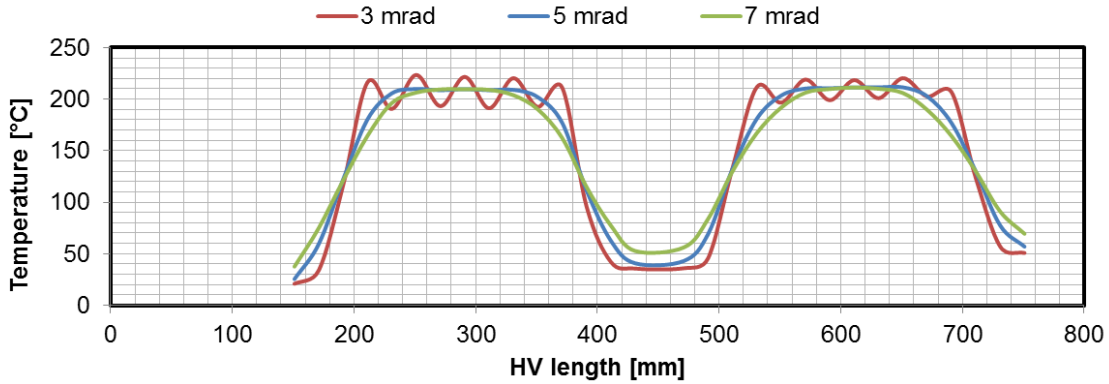

Figure 3-31 **HV#13 left panel: comparison of temperatures at 3 mm depth and at the positions of the thermocouples in case of ω_c = *3 mrad,* ω_c = *5 mrad and* ω_c = *7* mrad (no halo)**

It must be considered that initially not all the housing will be equipped with a thermocouple, but only 14 holes of the hypervapotrons intercepting the centre of the beamlet groups, 7 for each beamlet group: one in the center and three on each side to measure the gradient of the power density profile, as shown in Figure 3-32.

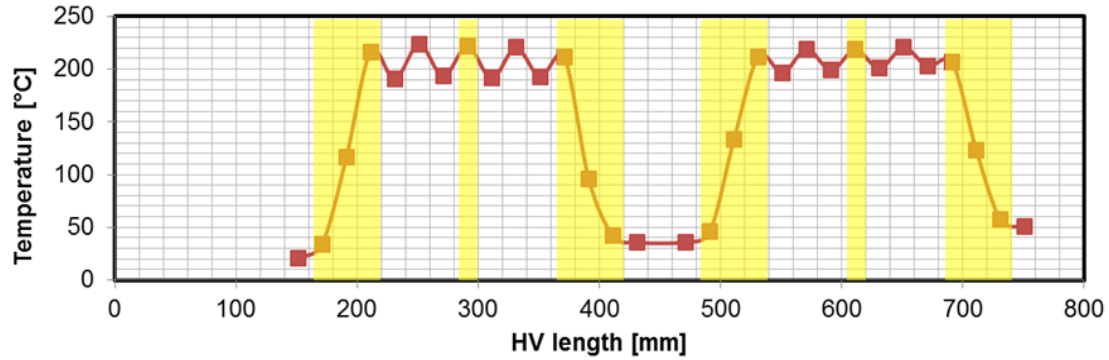

Figure 3-32 **Example of temperatures measured by the thermocouples. Highlighted with yellow bars are the position at which initially the thermocouples will be mounted**

For a better understanding of the difference of the temperature profiles with different beamlet core divergence, the contour plot of the external temperature for the left panel is shown in Figure 3-34 for ω_c = 3, in Figure 3-35 for ω_c= 5 mrad and in Figure 3-36 for ω_c= 7 mrad.

For 3 mrad beamcore divergence, the maximum temperature of 277 °C is visible in Figure 3-34 and this value can be compared with the maximum allowable temperature of the CuCrZr alloy, of which the hypervapotrons are made. This copper alloy reaches an optimum in mechanical strength after a thermal treatment involving solution

annealing and water quenching, followed by a certain amount of cold work, and finally by ageing at an intermediate temperature (450÷500 °C) to decompose the supersaturated solid solution into a fine distribution of Cu_3Zr and Cr precipitates. As ageing can continue after the components are manufactured, temperature-time limits must be considered to preserve the mechanical strength. For a total beam-on time of 5500 hours (common design parameter to ITER HNB injector, MITICA, and SPIDER) [64][65], the mechanical strength will be maintained by limiting the operation temperature at 350 °C (see Figure 3-33).

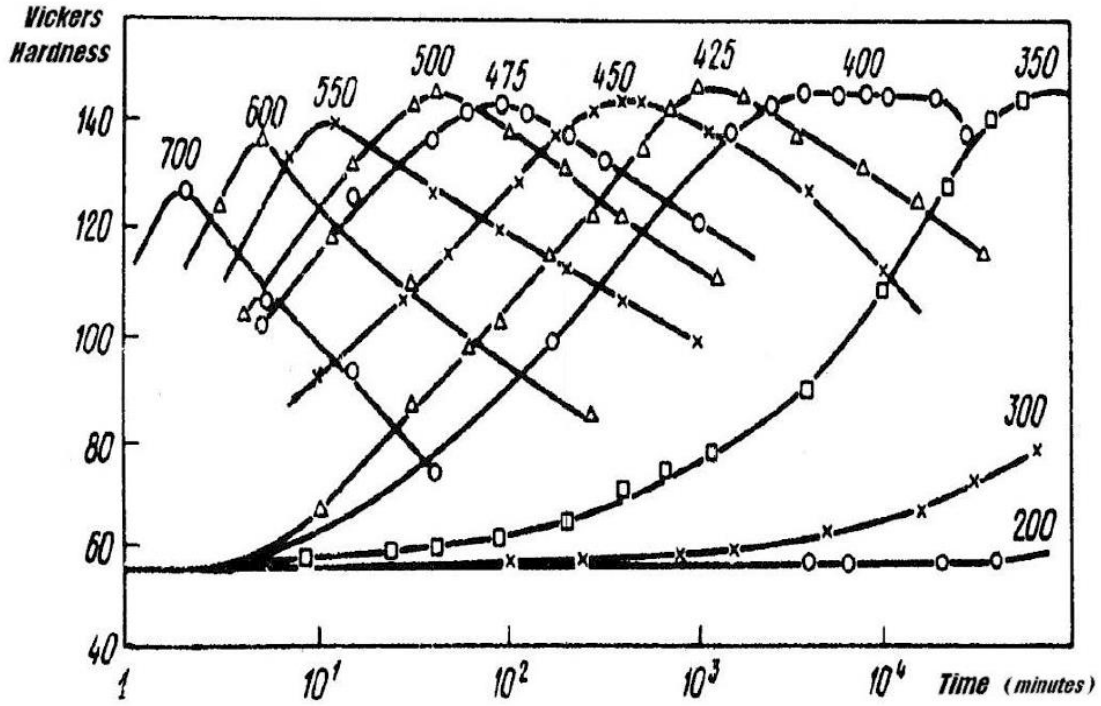

Figure 3-33 Vickers hardness against time for CuCrZr [66]

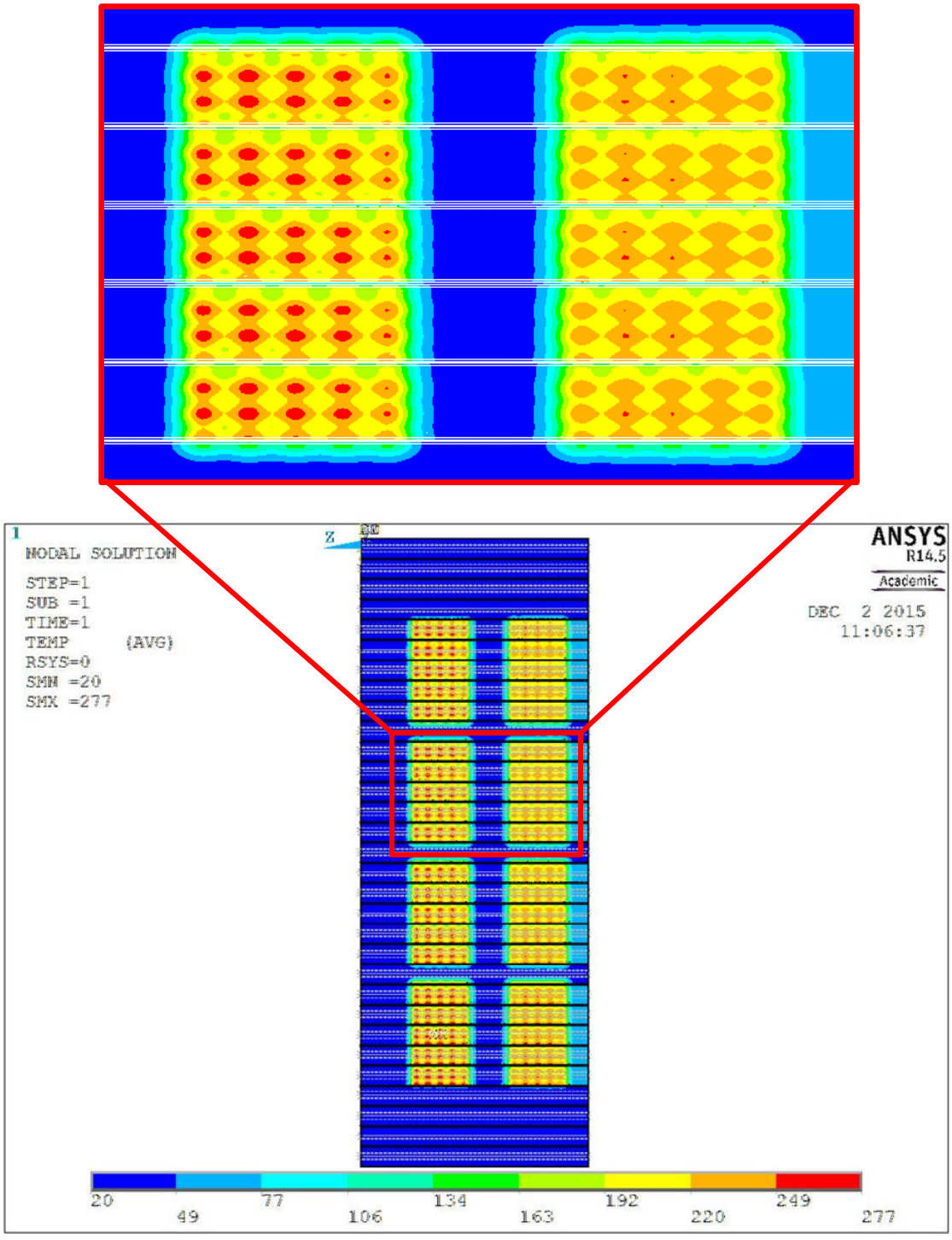

Figure 3-34 **Beam Dump left panel: contour plot of the temperature [°C] in case of $\omega_c = \omega_h = 3$ mrad (no halo)**

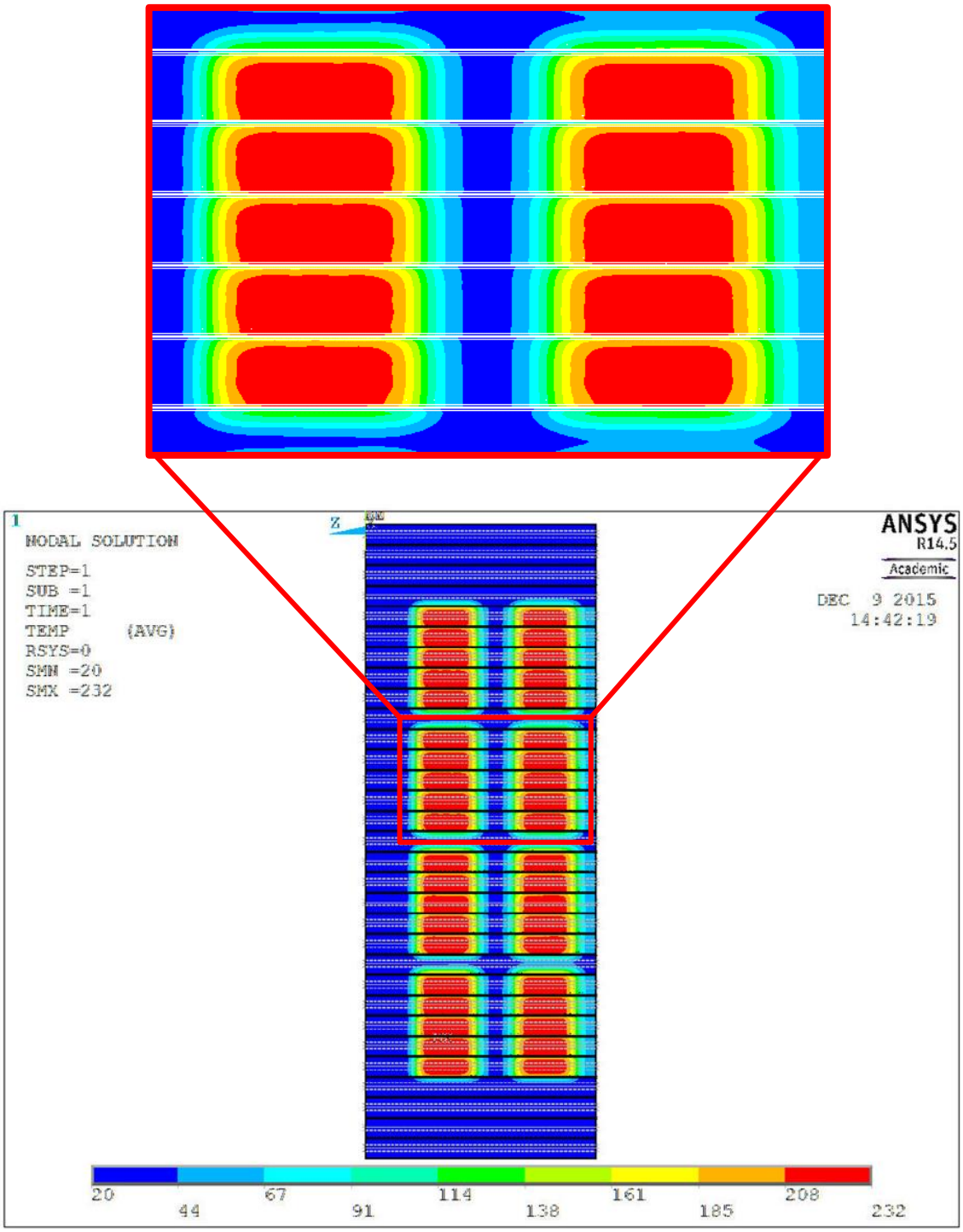

Figure 3-35 **Beam Dump left panel: contour plot of the temperature [°C] in case of $\omega_c = \omega_h = 5$ mrad (no halo)**

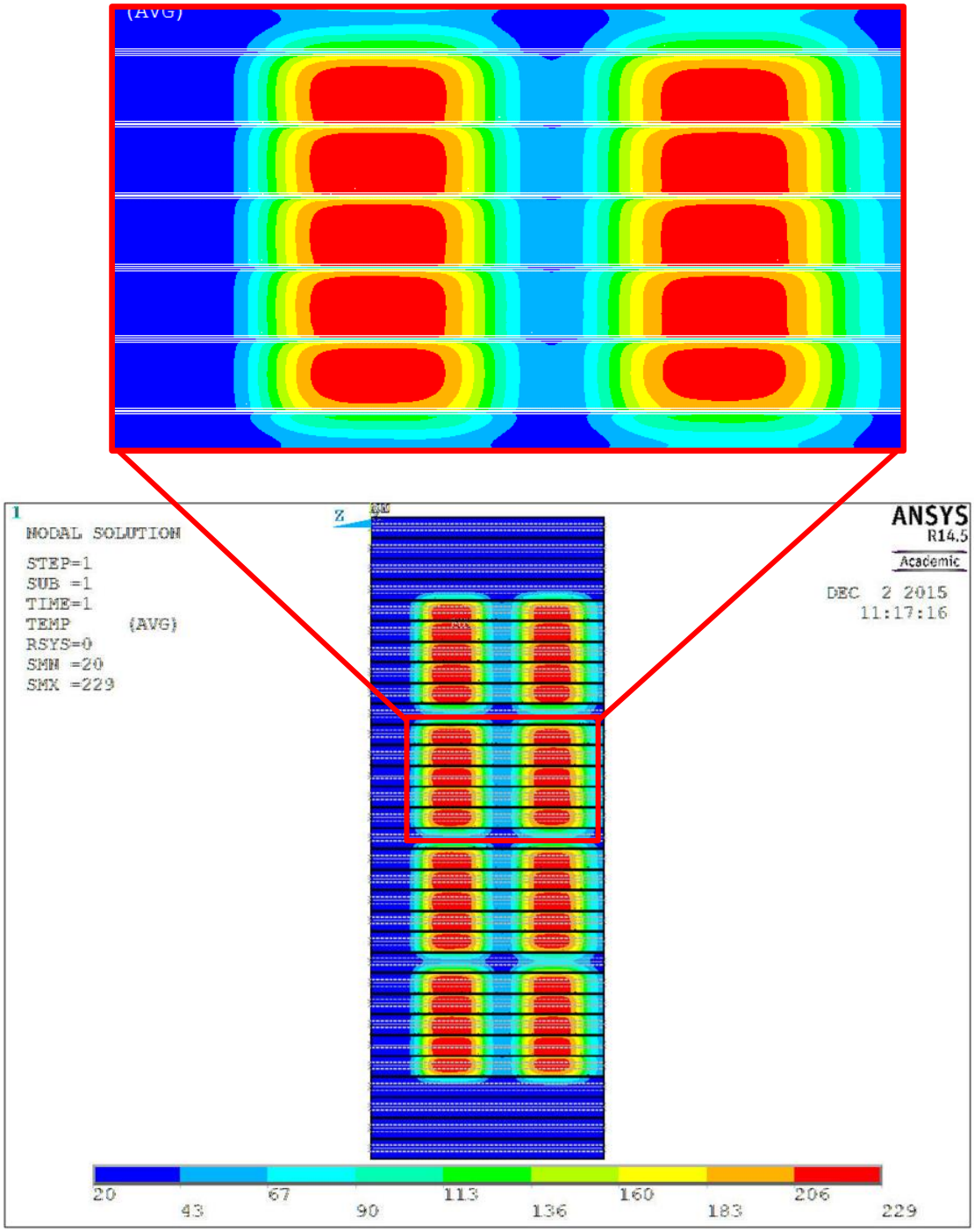

Figure 3-36 **Beam Dump left panel: contour plot of the temperature [°C] in case of $\omega_c = \omega_h = 7$ mrad (no halo)**

A particular situation has been found in case of ω_c =3 mrad that can help to diagnose this value of divergence: the temperature measured by the thermocouples along the hypervapotrons, increases from the top to the bottom side of the Beam Dump. Figure 3-37 shows the temperature profiles for the HV#7, HV#13, HV#19 and HV#25. The maximum temperature measured in the HV#7 is 206 °C while for the HV#25 the maximum is 254 °C.

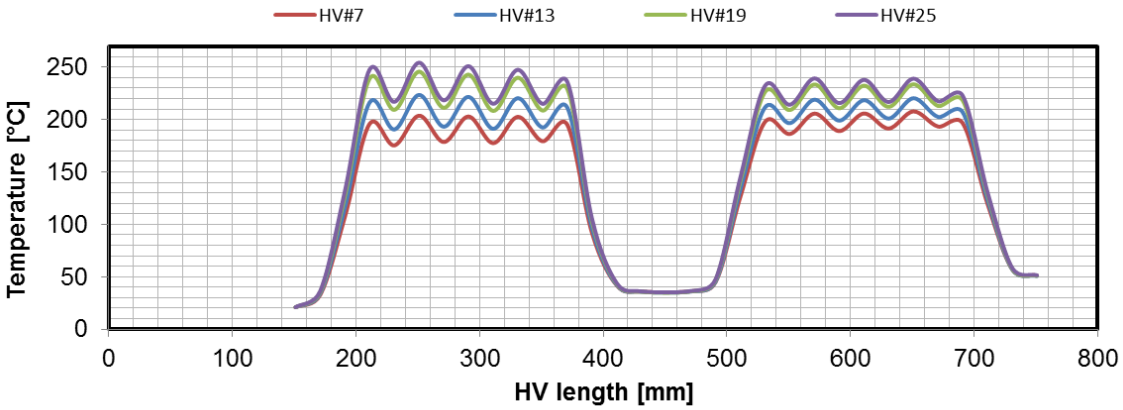

Figure 3-37 **Left panel: comparison of temperatures at 3 mm depth and at the positions of the thermocouples in case of ω_c = 3 mrad for different hypervapotrons**

The phenomenon is explained because of the position of the beamlets on the hypervapotrons: from the top to the bottom of a Beam Dump panel, the beamlets fall closer to the bottom part of the hypervapotrons where the thermocouples are located (Figure 3-38).

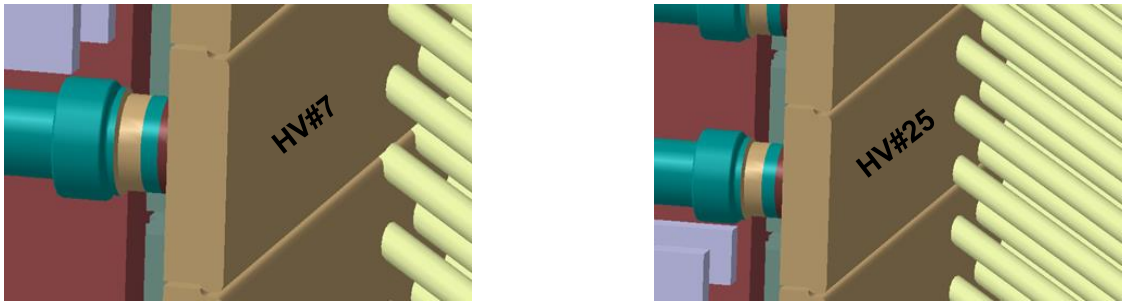

Figure 3-38 **Modelled beamlet position on HV#7 and HV#25 of the left panel**

3.6.1.2 Beam halo

The divergence of the beamlet halo (ω_h) appears difficult to measure by using the thermocouples along the hypervapotron.

In Figure 3-39 and Figure 3-40 two examples are shown: the difference of the measured temperature with or without halo is really hardly appreciable.

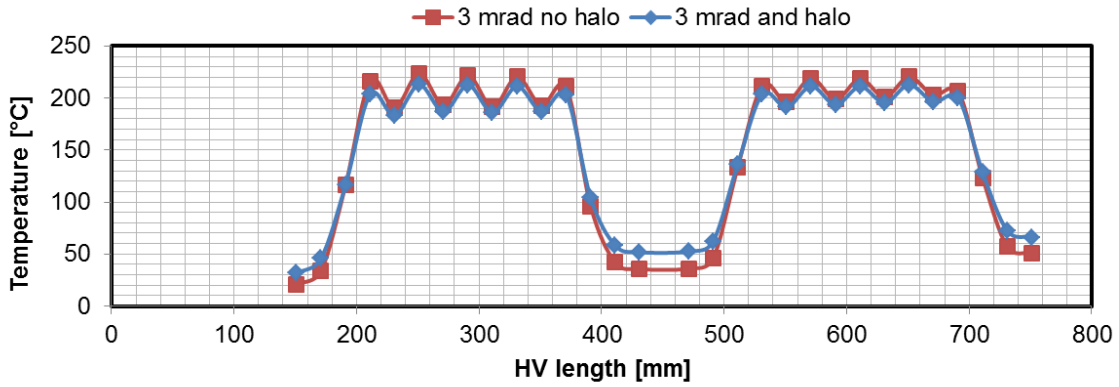

Figure 3-39 **HV#13 left panel: temperature at 3 mm depth and at the positions of the thermocouples in two cases: ω_c = 3 mrad with no halo fraction and ω_c = 3 mrad, ω_h = 30 mrad, f=15%**

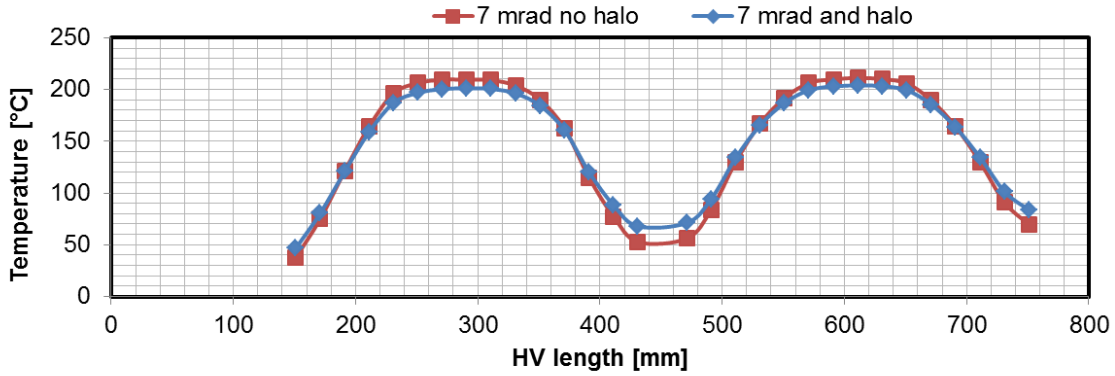

Figure 3-40 **HV#13 left panel: temperature at 3 mm depth and at the positions of the thermocouples in two cases: ω_c = 7 mrad with no halo fraction and ω_c = 7 mrad, ω_h = 30 mrad, f=15%**

The calorimetric measurements seem more useful in understanding the halo fraction. At each hypervapotron outlet there are thermocouples to measure the temperature of the water, thus knowing the inlet temperature of the coolant and the mass flow rate in each channel is possible to calculate the total power deposited on the hypervapotron by using the Eq. 43:

$$P_{th} = \dot{m}\, c_p (T_{out} - T_{in}) \qquad \text{Eq. 43}$$

where: P_{th} is the total power deposited on the hypervapotron [kW], $\dot{m}$ the mass flow rate [kg/s], c_p is the specific heat [kJ/(kg K)], T_{out} the outlet temperature of the coolant [°C] and T_{in} the inlet temperature of the coolant [°C].

The expected temperature of the water at the hypervapotron outlet can be estimate by considering the simple system in Figure 3-41: in the stationary condition the entire amount of the thermal power is rejected to the water and the outlet temperature can be calculated by using Eq. 43.

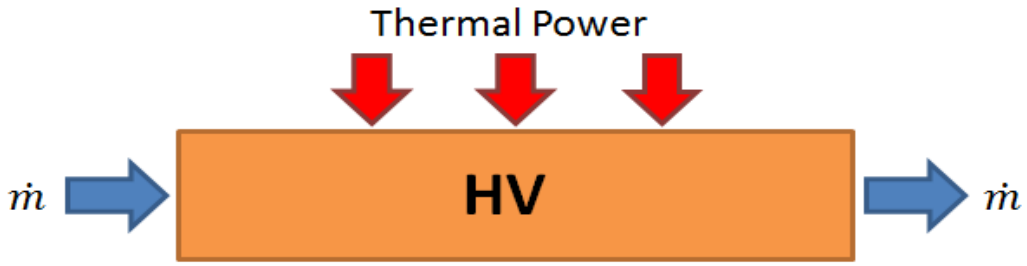

Figure 3-41 Simplified model of one hypervapotron

By considering a constant specific heat c_p of 4.186 kJ/(kg K) and a constant mass flow rate of 1.03 kg/s, the expected outlet temperatures of the water, as function of the thermal power, are plotted in Figure 3-42 for two different inlet water temperature (20 and 55 °C).

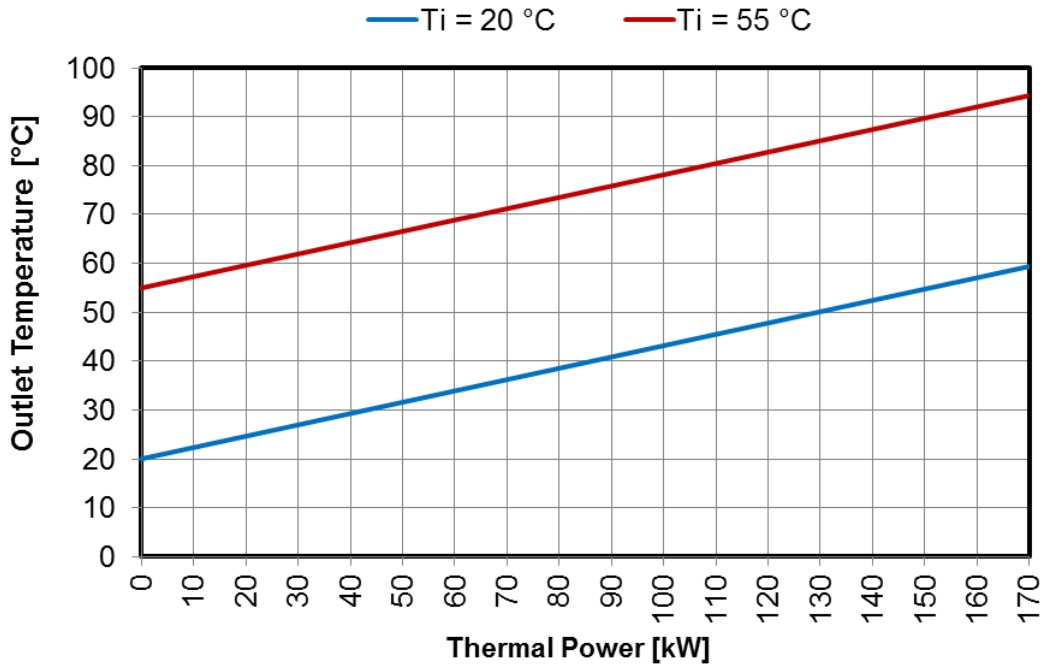

Figure 3-42 Outlet temperature as function of different thermal power at different inlet water temperature considering a mass flow rate of 1.03 kg/s

In Table 3-5 the results of the calorimetric measurements for the left panel in case of ω_c= 3 mrad with and without halo are reported. The results are then plotted in Figure 3-43 and Figure 3-44. The effect of the halo is an increase of the area over which the power is deposited and, as a consequence, an higher thermal power is detectable in the hypervapotrons between the beamlet groups (HV#10, HV#16 and HV#22) where an increase of about 10 kW has been calculated compared to the case without halo.

Table 3-5 Total power by using calorimetric measurements for the left panel of the Beam Dump in case of ω_c = 3 mrad with and without halo

	ω_c= 3 mrad, no halo			**ω_c= 3 mrad, ω_h= 30 mrad, f=15%**		
HV#	**$\dot{m}$**	**T_{out}**	**P_{th}**	**$\dot{m}$**	**T_{out}**	**P_{th}**
	kg/s	°C	kW	kg/s	°C	kW
1	1.02	20	0	1.02	20	0
2	1.02	20	0	1.02	20	0
3	1.02	20	0	1.02	20	2
4	1.02	22	9	1.02	24	15
5	1.03	53	142	1.03	51	136
6	1.03	53	142	1.03	53	140
7	1.03	53	142	1.03	53	142
8	1.03	53	142	1.03	53	141
9	1.03	53	142	1.03	52	138
10	**1.03**	**30**	**42**	**1.03**	**32**	**52**
11	1.04	53	141	1.04	52	138
12	1.04	53	141	1.04	52	140
13	1.04	52	141	1.04	52	141
14	1.04	52	141	1.04	52	140
15	1.05	52	141	1.05	51	138
16	**1.05**	**30**	**42**	**1.05**	**32**	**52**
17	1.05	52	142	1.05	52	138
18	1.04	52	142	1.04	52	140
19	1.04	53	142	1.04	52	141
20	1.04	53	142	1.04	52	141
21	1.04	53	142	1.04	52	138
22	**1.03**	**30**	**43**	**1.03**	**32**	**53**
23	1.03	53	142	1.03	52	139
24	1.03	53	143	1.03	53	141
25	1.03	53	143	1.03	53	142
26	1.03	53	143	1.03	53	141
27	1.03	53	143	1.03	52	136
28	1.02	21	6	1.02	23	12
29	1.02	20	0	1.02	20	2
30	1.02	20	0	1.02	20	0
31	1.02	20	0	1.02	20	0
			2980			2980

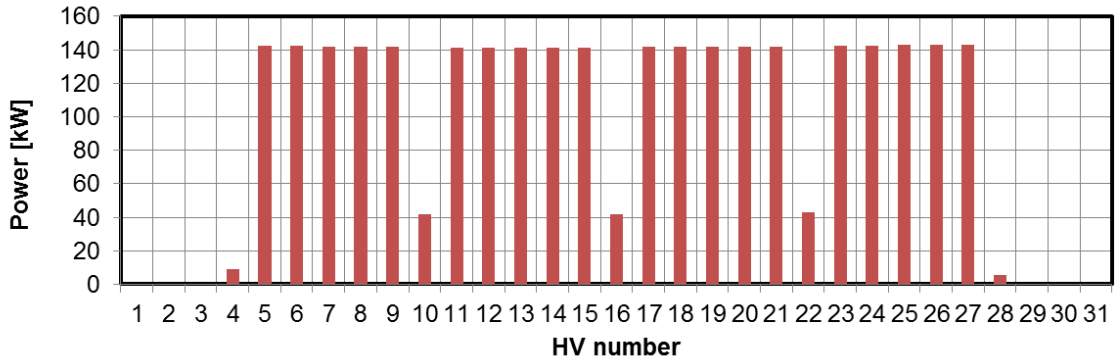

Figure 3-43 **Total power by using calorimetric measurements for the left panel of the Beam Dump in case of ω_c = 3 mrad and no halo**

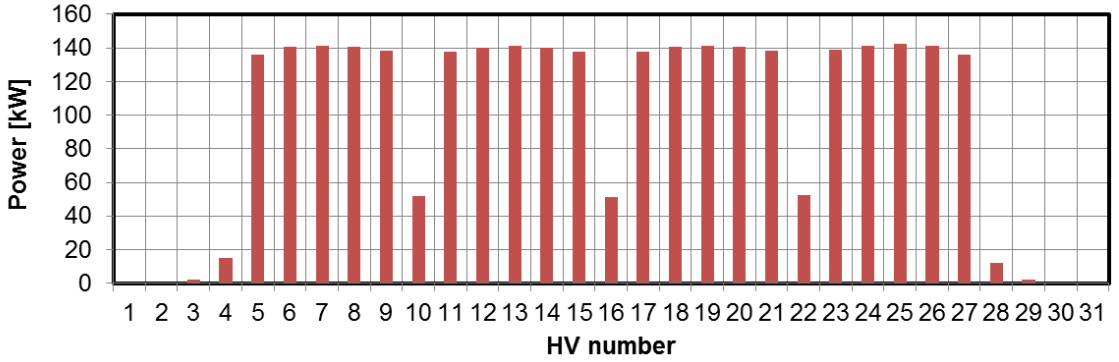

Figure 3-44 **Total power by using calorimetric measurements for the left panel of the Beam Dump in case of ω_c= 3 mrad, ω_h= 30 mrad and f=15%**

3.6.1.3 Horizontal misalignment

The horizontal misalignment of the beam (to the left or right direction) can be detected both with the calorimetric measurement and the temperature profile.

In case of beamlet core divergence of 3 mrad, the beamlets are so focused that even with a horizontal misalignment of 2 mrad, the footprint of the power is still in the correct panel. In this case the calorimetric measurements are not useful to detect the misalignment. On the contrary, the misalignment is visible by using the temperature profile along the hypervapotrons.

In Figure 3-45 and Figure 3-46 the temperature profiles with and without misalignment are reported. In particular it appears evident that in case of misalignment the profiles are shifted (respectively in the left and right direction). When the beam is shifted in the left direction (Figure 3-45) it is also possible to see that the peaks and the valleys no longer correspond to the correct thermocouple; on the contrary with a beam shifted in the right direction (Figure 3-46) the temperature profile appears more flattened.
In order to explain this effect, in Figure 3-47 the heat flux on a path along the HV#13 is shown in case of no misalignment. The vertical straight lines represent the position of the thermocouples; these lines intercept the heat flux curve where the peaks and valleys are present. A similar condition is also present in Figure 3-48 in case of 2 mrad horizontal misalignment in the left direction: the thermocouples intercept the heat flux with peaks and valley shifted. If the horizontal misalignment is of 2 mrad in the right direction, the situation is given in Figure 3-49: the straight vertical lines that represent the thermocouples position, intercept the heat flux curve more or less at the same amplitude generating the flat profile shown in Figure 3-46.

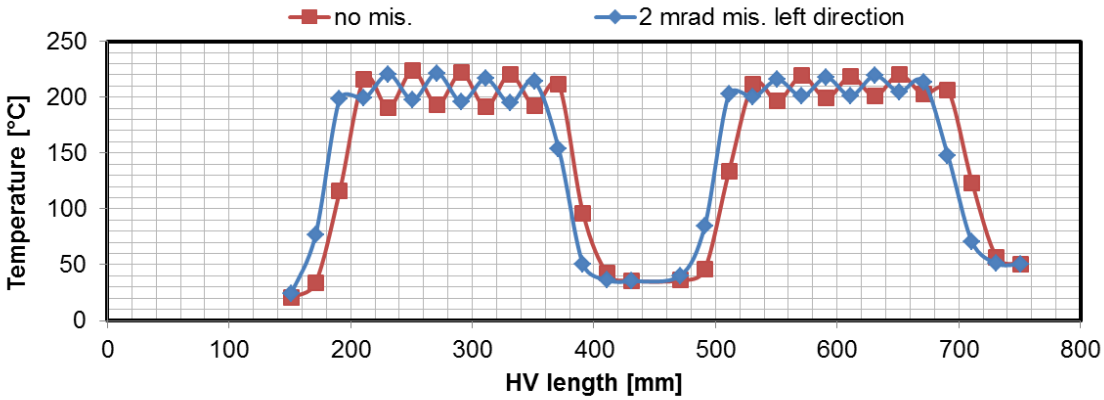

Figure 3-45 **HV#13 left panel: temperature at 3 mm depth and at the positions of the thermocouples for ω_c = 3 mrad and no halo, in case of no misalignment and with 2 mrad of horizontal misalignment in the left direction.**

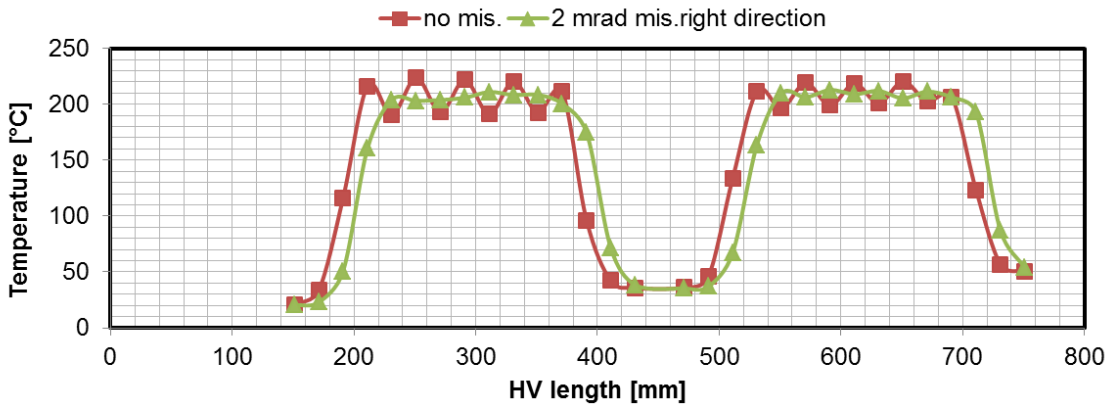

Figure 3-46 **HV#13 left panel: temperature at 3 mm depth and at the positions of the thermocouples for ω_c = 3 mrad and no halo, in case of no misalignment and with 2 mrad of horizontal misalignment in the right direction.**

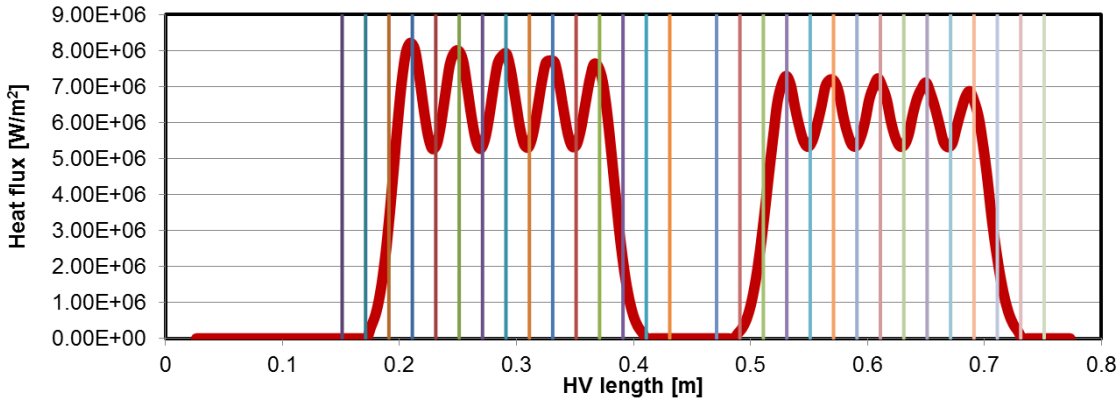

Figure 3-47 **HV#13 left panel: heat flux profile along a path with ω_c = 3 mrad and no halo in case of no misalignment. The vertical straight lines represent the position of the thermocouples.**

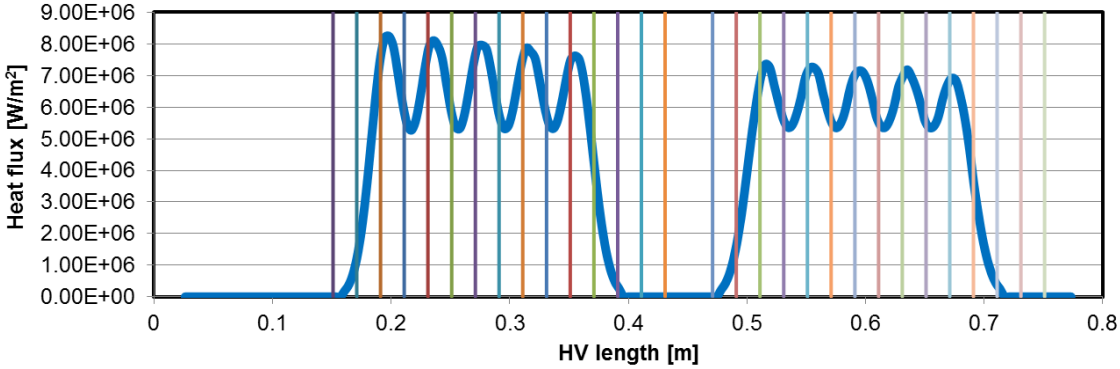

Figure 3-48 **HV#13 left panel: heat flux profile along a path with ω_c = 3 mrad and no halo in case of 2 mrad of horizontal misalignment in the left direction. The vertical straight lines represent the position of the thermocouples.**

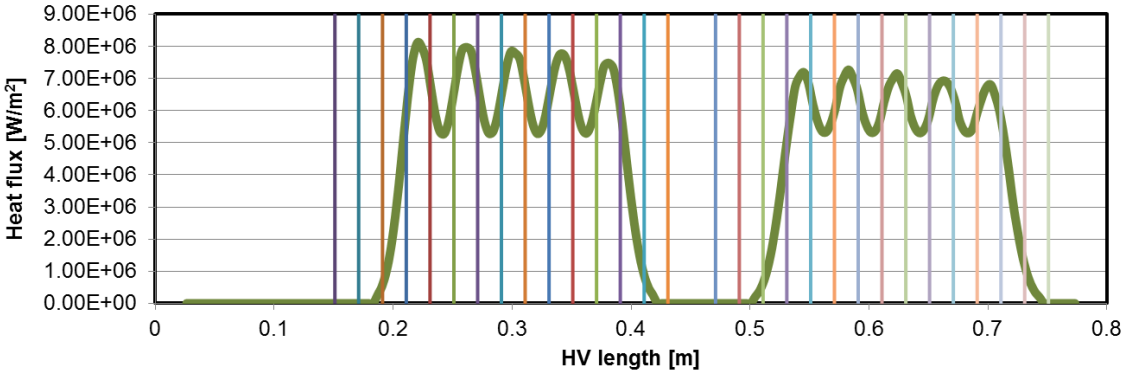

Figure 3-49 **HV#13 left panel: heat flux profile along a path with ω_c = 3 mrad and no halo in case of 2 mrad of horizontal misalignment in the right direction. The vertical straight lines represent the position of the thermocouples.**

In case of 7 mrad beamlet core divergence, the horizontal misalignment can be detected both with the calorimetric measurement and the temperature profile.

In Figure 3-50 and Figure 3-51 the temperature profiles with and without misalignment are reported: the misalignment is evident in both cases.

The calorimetric measurements are listed in Table 3-6 and plotted in Figure 3-52: an increase of 43 kW of thermal power is measured in the left panel in case of horizontal misalignment, a corresponding reduction is present (but not reported for simplicity) on the right panel.

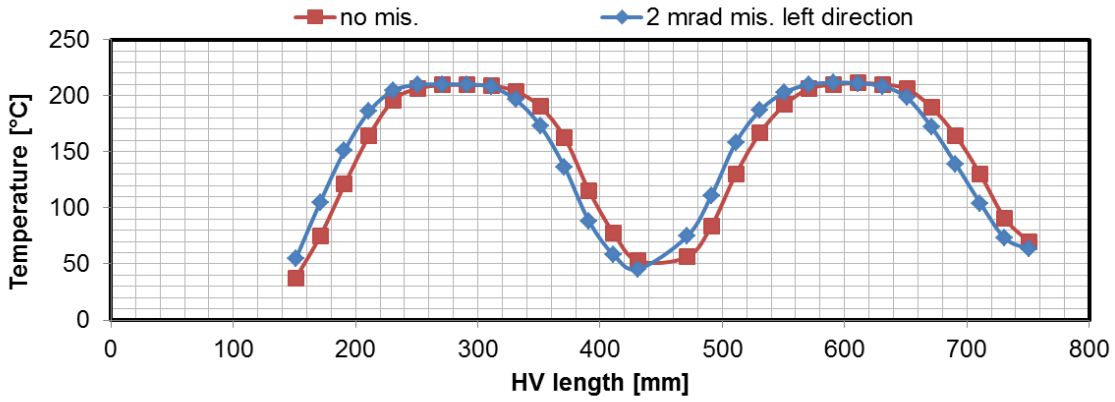

Figure 3-50 **HV#13 left panel: temperature at 3 mm depth and at the positions of the thermocouples for ω_c = 7 mrad and no halo in case of no misalignment and with 2 mrad of horizontal misalignment in the left direction.**

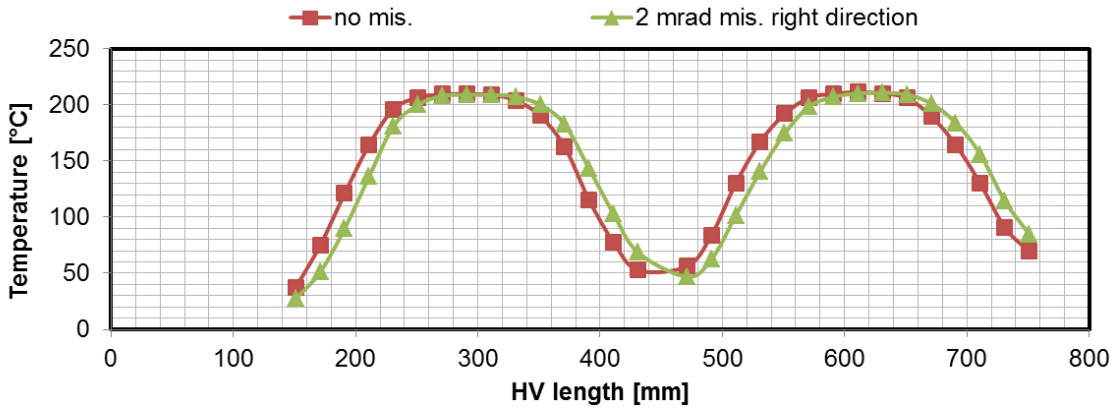

Figure 3-51 **HV#13 left panel: temperature at 3 mm depth and at the positions of the thermocouples for ω_c = 7 mrad and no halo in case of no misalignment and with 2 mrad of horizontal misalignment in the right direction.**

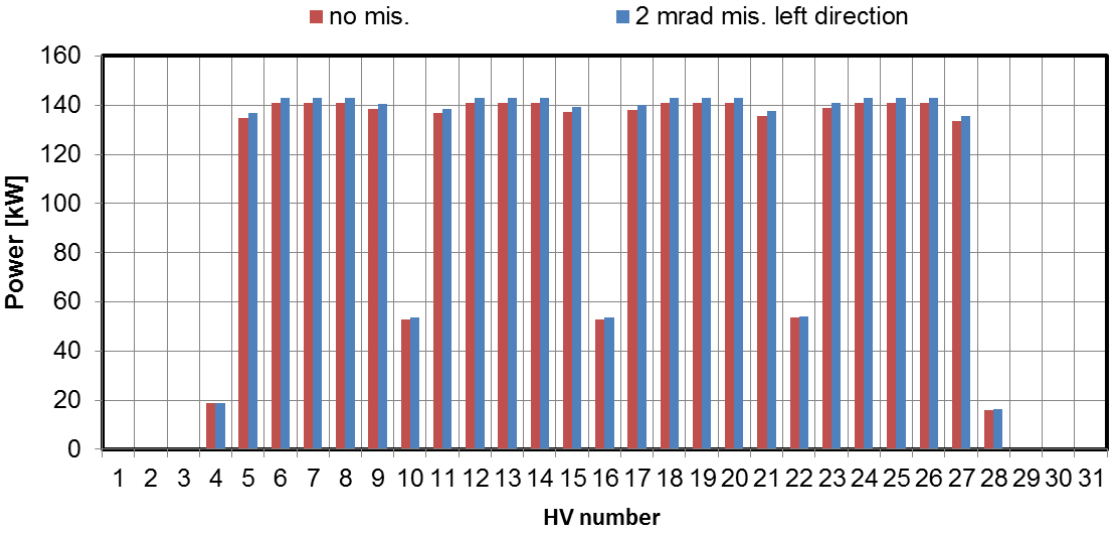

Figure 3-52 **Total power by using calorimetric measurements for the left panel of the Beam Dump in case of ω_c= 7 mrad and no halo with and without horizontal misalignment**

Table 3-6 **Total power by using calorimetric measurements for the left panel of the Beam Dump in case of ω_c = 7 mrad with and without horizontal misalignment**

	No misalignment			Horizontal misalignment of 2 mrad in the left direction		
HV#	$\dot{m}$	T_{out}	P_{th}	$\dot{m}$	T_{out}	P_{th}
	kg/s	°C	kW	kg/s	°C	kW
1	1.02	20	0	1.02	20	0
2	1.02	20	0	1.02	20	0
3	1.02	20	0	1.02	20	0
4	1.02	24	19	1.02	24	19
5	1.03	51	135	1.03	52	137
6	1.03	53	141	1.03	53	143
7	1.03	53	141	1.03	53	143
8	1.03	53	141	1.03	53	143
9	1.03	52	138	1.03	52	140
10	1.03	32	53	1.03	32	54
11	1.04	52	137	1.04	52	139
12	1.04	52	141	1.04	53	143
13	1.04	52	141	1.04	53	143
14	1.04	52	141	1.04	53	143
15	1.05	51	137	1.05	52	139
16	1.05	32	53	1.05	32	53
17	1.05	52	138	1.05	52	140
18	1.04	52	141	1.04	53	143
19	1.04	52	141	1.04	53	143
20	1.04	52	141	1.04	53	143
21	1.04	51	136	1.04	52	138
22	1.03	32	54	1.03	33	54
23	1.03	52	139	1.03	53	141
24	1.03	53	141	1.03	53	143
25	1.03	53	141	1.03	53	143
26	1.03	53	141	1.03	53	143
27	1.03	51	133	1.03	51	135
28	1.02	24	16	1.02	24	16
29	1.02	20	0	1.02	20	0
30	1.02	20	0	1.02	20	0
31	1.02	20	0	1.02	20	0
			2978			3021

3.6.1.4 Identification of the heat transfer mechanism

As already stated, the hypervapotron is able to withstand different mechanisms of thermal exchange along its cooling channel: forced convection, partial developed boiling and fully developed boiling. The results of the simulations with the nominal boundary conditions have been above presented, but the heat transfer mechanism has not been identified yet.

The most critical scenario, in terms of heat fluxes and thus temperatures, is identified with 3 mrad of core divergence and no halo, as the beamlets are well focused and the power density is the highest. In this scenario the most critical situation is present in the HV#23: in Figure 3-53 the trends of the bulk temperature, the wall temperature at the cooling channel and the onset boiling temperature are shown. The maximum wall temperature is 160 °C and the corresponding onset boiling temperature 187 °C: the boiling margin is 27 °C. As the wall temperature at the cooling channel is always under the onset boiling temperature only forced convection heat transfer is expected. The pressure drop along the same hypervapotron channel is shown in Figure 3-54.

At the channel outlet with coolant pressure of 0.9 MPa, the corresponding saturation temperature is 175 °C. As the temperature of the coolant at the outlet (about 50 °C) is well below the corresponding saturation temperature, the fully bulk boiling condition is excluded.

The temperature of the water at the Beam Dump inlet is within the range 20÷55 °C. The worst critical possibility is a scenario in which the inlet temperature is 55 °C and the beamlets well focused (3 mrad of divergence and no halo). In general it is possible to imagine the bulk and wall temperatures translated of 35 °C in Figure 3-53. In this case the nucleation of the bubbles can locally starts, but only in small regions in which the heat transfer regime correspond to the first part of the partial boiling curve, so that a real increasing of the heat transfer efficiency is not foreseen.

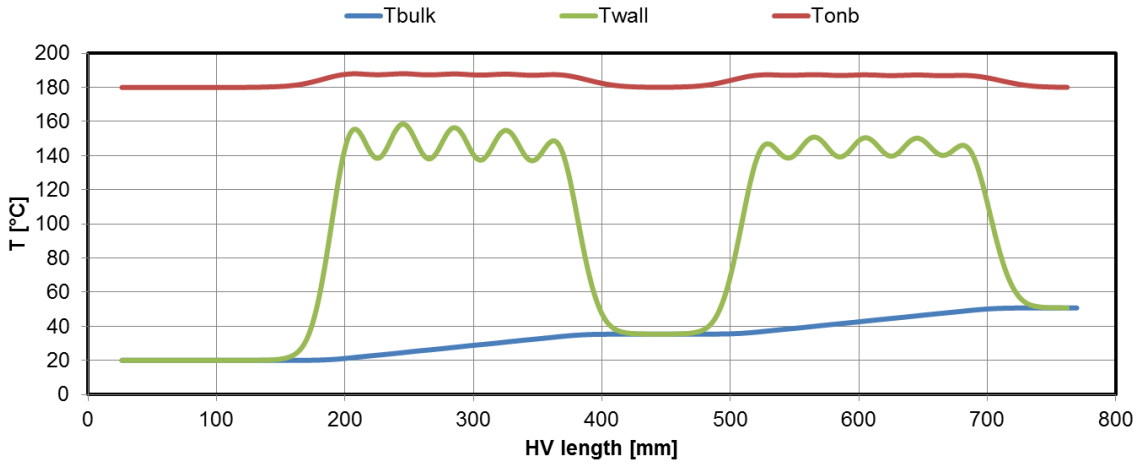

Figure 3-53 **HV#23 left panel: trends of bulk temperature, wall temperature at the cooling channel and onset boiling temperature in case of ω_c = 3 mrad and no halo**

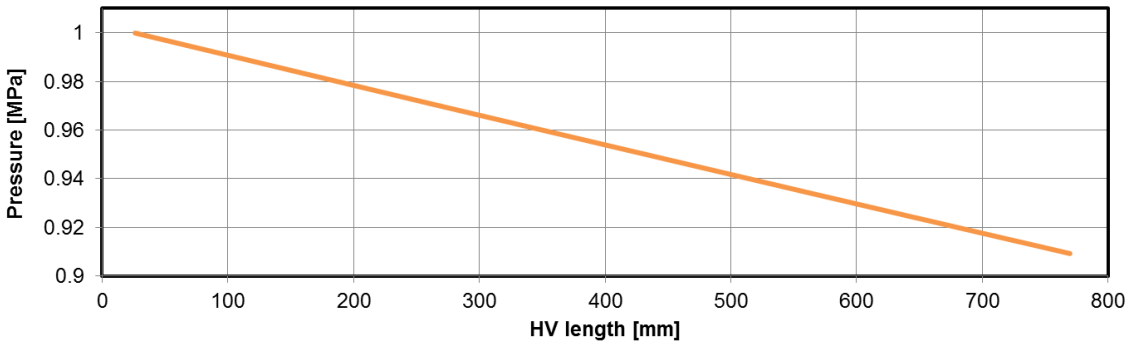

Figure 3-54 HV#23 left panel: trend of the pressure drop along the hypervapotron channel

3.6.2 Off normal conditions

Within the nominal mass flow rate of 32 kg/s the boiling regime is not achieved. Some simulations have been carried out to verify the possibility of reducing the flow rate in each panel in order to improve the calorimetric measurements and the temperature profiles. The simulations are also useful to verify the behaviour of the system in the event of a reduction of flow caused by a fault at the cooling system.

In the following the results for a simulation with changed boundary conditions are reported and discussed:

- inlet mass flow rate: 16 kg/s;
- inlet temperature of the coolant: 20 °C;
- outlet pressure: 0.97 MPa;
- heat fluxes corresponding to the scenario: ω_c= 3 mrad and no halo.

Note that the outlet pressure has been set to 0.97 MPa in order to get an inlet pressure equal to 1 MPa.

A general estimate of the heat transfer expected in the simulation is given in Figure 3-55: the plot gives the heat transfer (q) as function of the temperature of the wall at the cooling channel (T_w) within the assumptions given in the caption. By considering a bulk temperature of the coolant of 25 °C and a pressure of 1 MPa, the onset temperature of the nucleate boiling (T_{ONB}) is 188 °C. Compared to the Figure 3-27, because of the reduction of mass flow rate, the heat transfer curve for forced convection is about 40% of the previous one (at T_w=75 °C), the fully developed boiling curve is still the same because it is independent of the flow rate, and the partial boiling curve slightly changes.

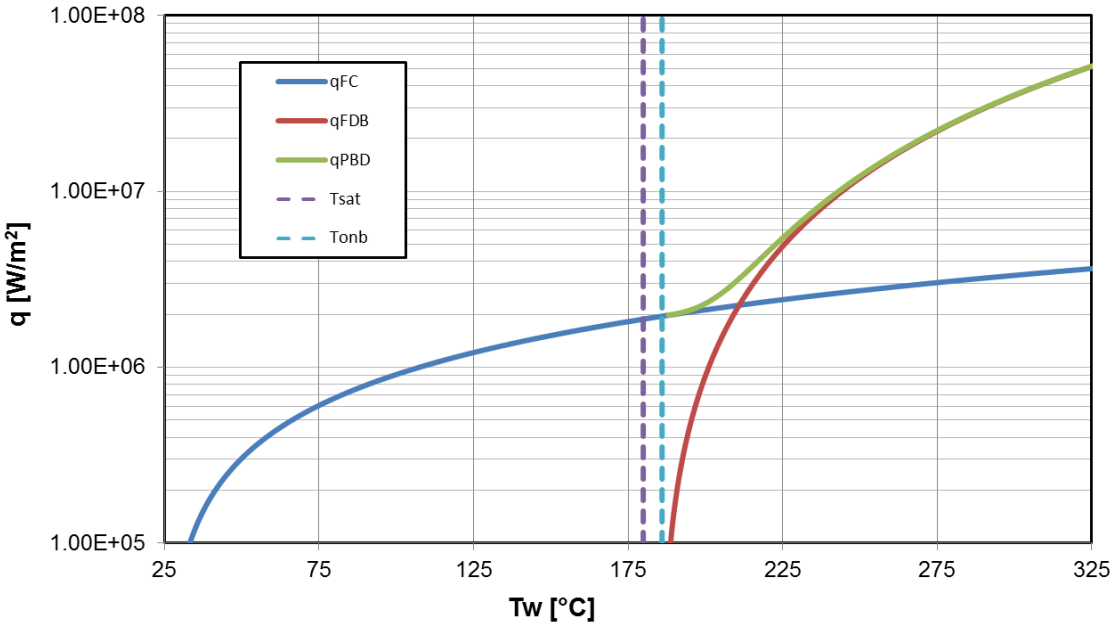

Figure 3-55 **Estimate of heat transfer for hypervapotron geometry with forced convection (q_{FC}), partial developed boiling (q_{PDB}) calculated with the Bergles and Rohsenow procedure and fully developed boiling (q_{FDB}), for T_b=25 °C, p=1 MPa, D_h=7.48 mm and $\dot{m}$=0.52 kg/s**

The temperatures measured at the thermocouple positions are shown in Figure 3-56 while the contour plot of the external temperature for the left panel is depicted in Figure 3-57 where the maximum temperature is 356 °C (instead of 277 °C reached in the nominal conditions).

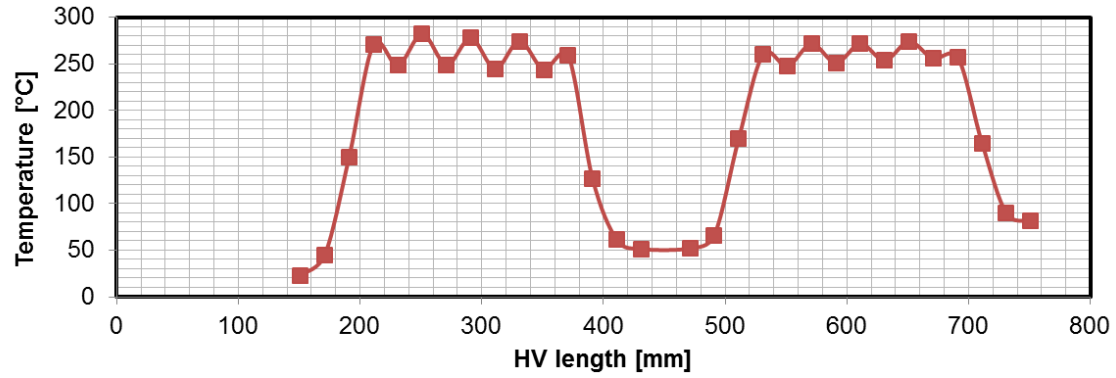

Figure 3-56 **HV#13 left panel: temperature at 3 mm depth and at the positions of the thermocouples for ω_c= 3 mrad and no halo in case of $\dot{m}$=16 kg/s**

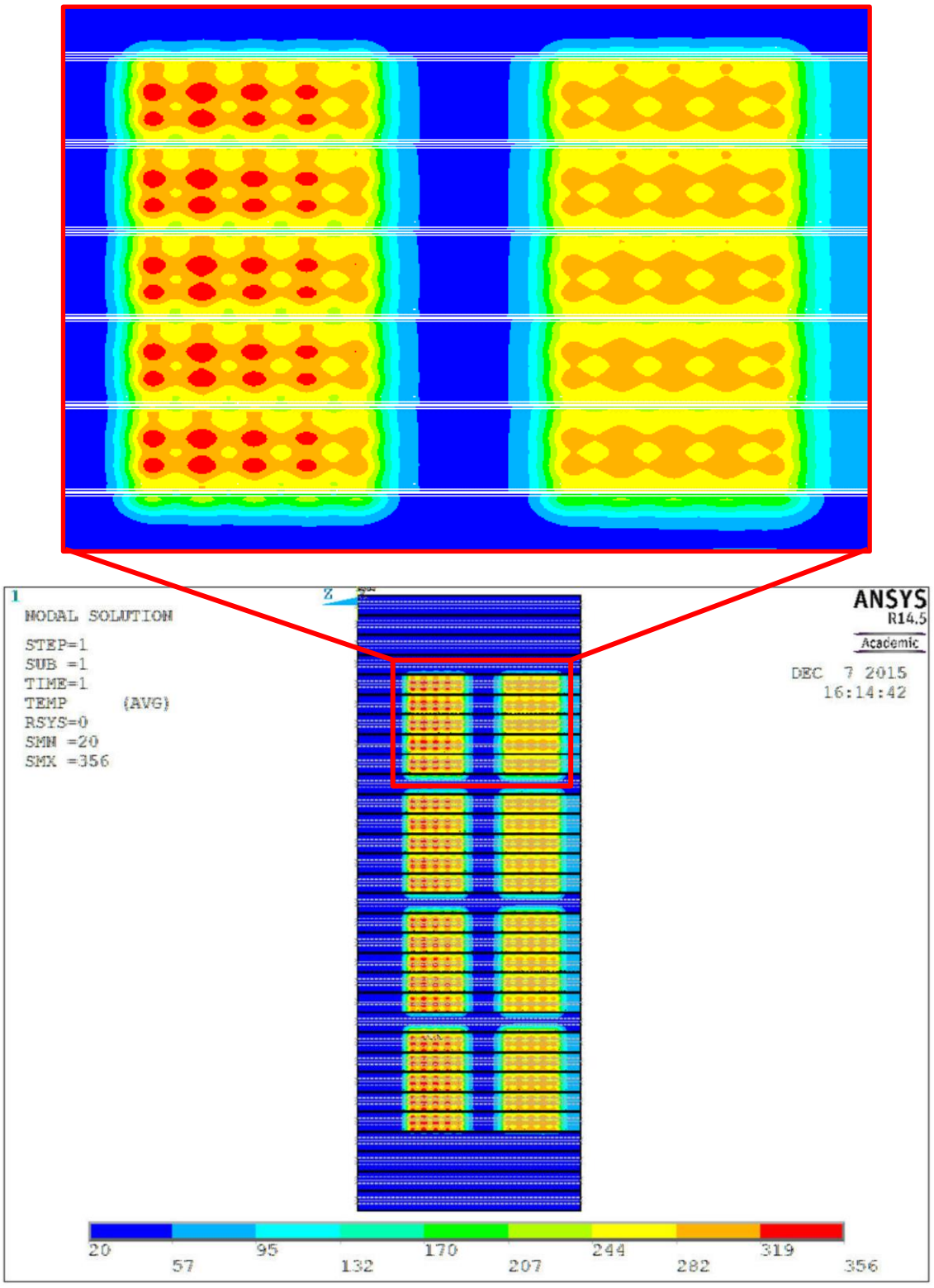

Figure 3-57 **Beam Dump left panel: contour plot of the temperature [°C] in case of ω_c = 3 mrad, no halo and reduced mass flow rate of 16 kg/s**

Figure 3-58 shows the trends of the bulk temperature along the hypervapotron, the temperature at the wall of the cooling channel, and the onset boiling temperature. The maximum wall temperature is 250 °C and the corresponding onset boiling temperature 187 °C. At the two heated regions, the wall temperature at the cooling channel exceeds the onset of boiling temperature and the bubble nucleation occurs.
The pressure drop along the same hypervapotron channel is shown in Figure 3-59.

At the outlet pressure (0.97 MPa), the corresponding saturation temperature is 178.5 °C. As the temperature of the coolant at the outlet (about 80 °C) is well below the corresponding saturation temperature, the fully bulk boiling condition is excluded.

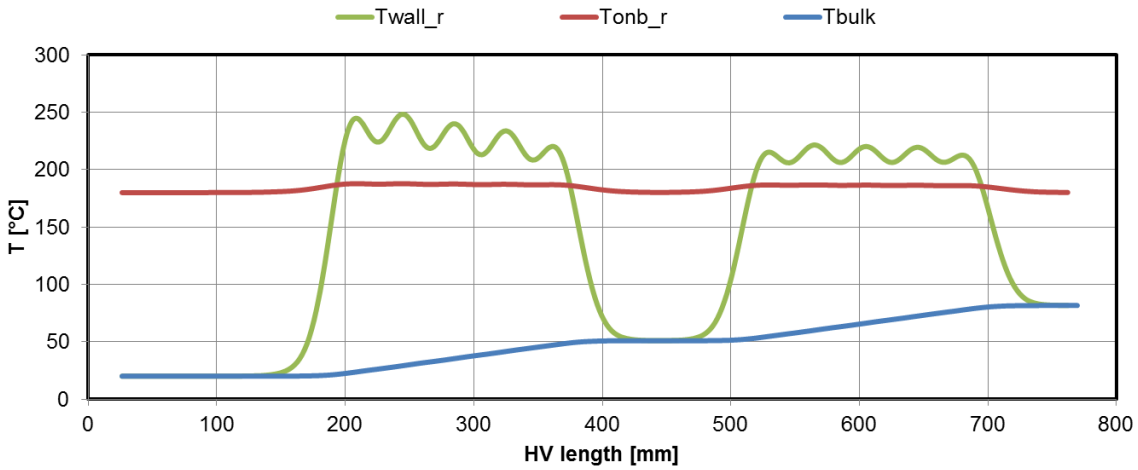

Figure 3-58 **HV#23 left panel: trends of bulk temperature, wall temperature at the cooling channel and onset boiling temperature in case of ω_c = 3 mrad and no halo and with a reduced mass flow of 16 kg/s**

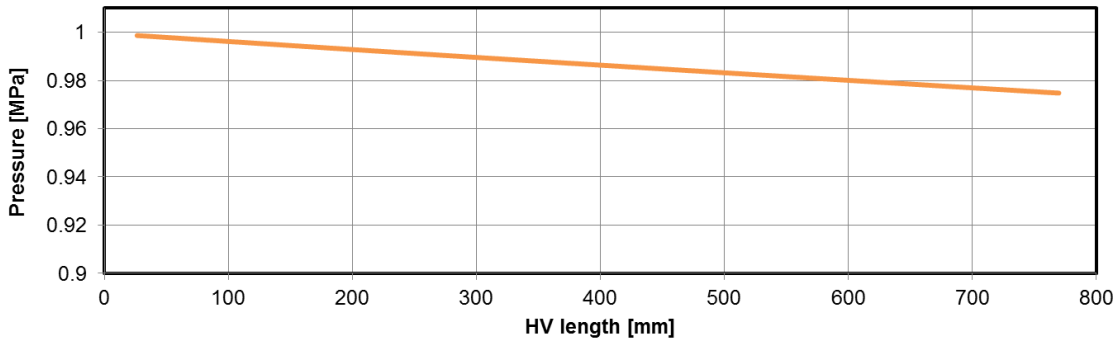

Figure 3-59 **HV#23 left panel: trend of the pressure drop along the hypervapotron channel in case of mass flow rate equals to 16 kg/s**

3.6.3 Discussion on the hypervapotron cross section

The cross section of one hypervapotron used for the thermo-hydraulic analyses is shown in Figure 3-24. The cross section of the flow (57 mm x 4 mm) is modelled without fins as required for the correlations in paragraph 3.2.1. The thickness of CuCrZr directly exposed to the beam is 5.7 mm, instead of 4 mm which is the real thickness without considering fins. This assumption has been done in order to account for the additional material of the fins.

The absence of fins constitute the major simplification in the model. By considering the real cross section with fins, the highest wall temperatures are expected at the locations in which the thickness is only 4 mm. Two simulations have been carried out to estimate the influence of the thickness: the first one with the same model used for the above results (5.7 mm of thickness) and a second one with a reduced thickness of 4 mm. The two sections are shown in Figure 3-60.
The boundary conditions for the two simulations are a constant temperature of 200 °C on the external wall of the Beam Dump, an inlet mass flow rate of 32 kg/s at 20 °C and an outlet pressure of 0.9 MPa.

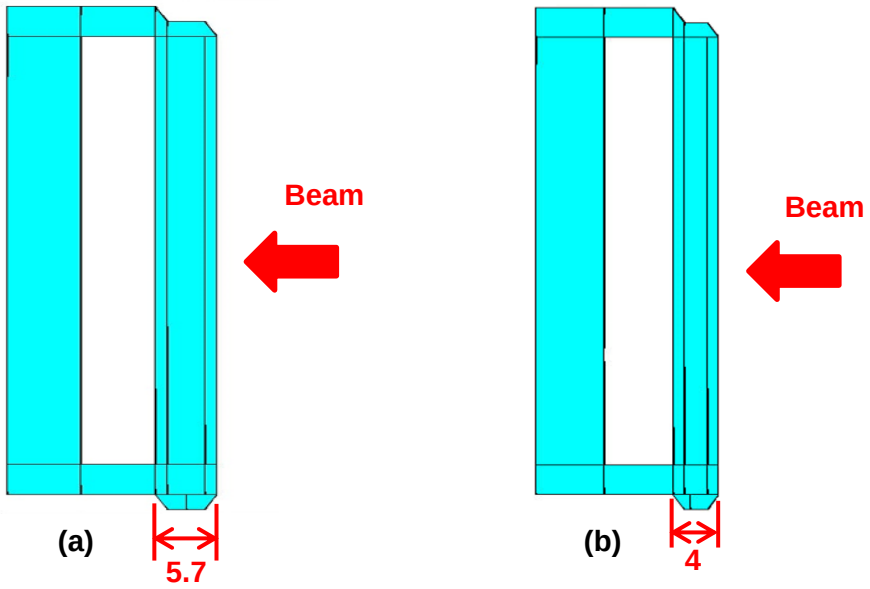

Figure 3-60 **Sections of one hypervapotron with different thickness of CuCrZr directly exposed to the beam**

The results are shown in Figure 3-61 in case of 5.7 mm thickness and in Figure 3-62 for 4 mm thickness. The wall temperature at the cooling channel differs of 6 °C between the two cases. This value can be considered as a deviation from the average value previously calculated to be taken into account.

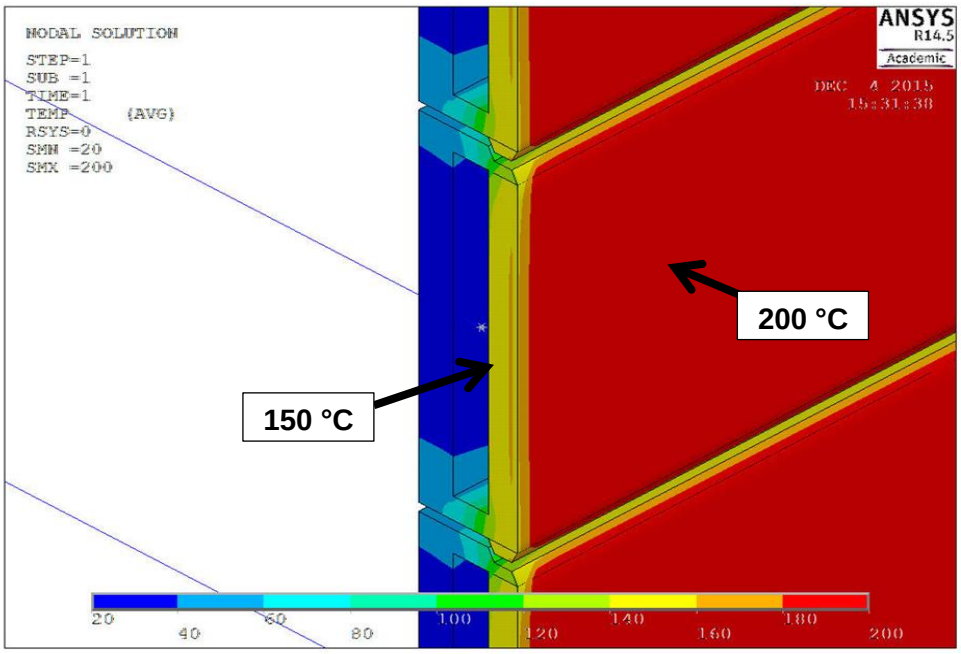

Figure 3-61 **Thickness of 5.7 mm: magnification of the temperature [°C] distribution along one hypervapotron**

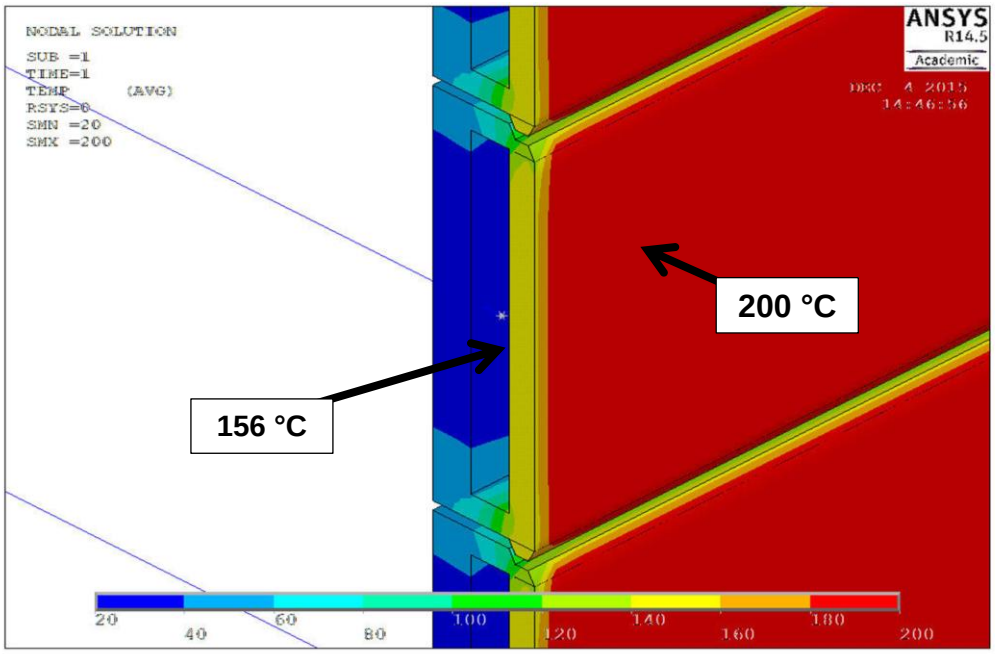

Figure 3-62 **Thickness of 4 mm: magnification of the temperature [°C] distribution along one hypervapotron**

3.6.4 Critical Heat Flux

The Critical Heat Flux at the channel wall (CHF_w) has been calculated by using the Tong-75 formula and the modified Tong-75 formula with a corrective factor C_f=1.2 valid for smooth tube (Eq. 36).

Table 3-7 reports the CHF_W in case of nominal mass flow rate (about 1 kg/s in each hypervapotron) and in case of reduced mass flow rate (about 0.5 kg/s in each hypervapotron). For both the cases the calculation has been carried out in the extreme conditions of inlet and outlet water temperature:

- nominal mass flow case: coolant bulk temperature of 20 and 85 °C (this last value is the outlet temperature when the inlet temperature is 55 °C);
- reduced mass flow case: coolant bulk temperature of 20 and 115 °C (this last value is the outlet temperature when the inlet temperature is 55 °C);

The worst results correspond to the cases with the higher bulk temperature. By considering only the Tongh-75 formula, CHF_W = 17 MW/m^2 and CHF_W = 10 MW/m^2 have been obtained respectively for the nominal and the reduced mass flow rate. The results become CHF_W = 21 MW/m^2 and CHF_W = 12 MW/m^2 when the corrective factor is considered.

Table 3-7 CHFw calculated with the modified Tong-75 formula for the SPIDER Beam Dump in different scenarios

Dh [m]	0.007475			
Cross section [m^2]	2.28E-04			
mass flow [kg/s]	1.03		0.52	
G [kg/(s m^2)]	4518		2281	
v [m/s]	4.53	4.66	2.28	2.41
p [Mpa]	1	0.90	1	0.97
Tsat [°C]	179.886	175.358	179.886	178.566
Tb [°C]	20	85	20	115
ρ_f @Tb [kg/m^3]	998.16	968.59	998.16	947.07
ρ_g @Tsat [kg/m^3]	5.16	4.62	5.16	4.89
μ [Pa s]	1.00E-03	3.33E-04	1.00E-03	2.43E-04
cp [J/(kg K)]	4184.4	4200.8	4184.4	3691.2
λ W/(m K)	5.98E-01	6.73E-01	5.98E-01	6.83E-01
Re	3.37E+04	1.01E+05	1.70E+04	7.02E+04
f	0.012962	0.006699	0.019534	0.008349
H_{fg} [J/kg]	2.01E+06	2.30E+06	2.01E+06	2.22E+06
Ja	64.27	34.68	64.27	20.51
$CHFw_{TONGH}$ [MW/m^2]	30	17	22	10
Cf	1.2			
CHFw [MW/m^2]	36	21	26	12

The maximum power density is in the scenario with ω_c = 3 mrad and no halo. The heat flux at the channel wall has been calculated with the FE model. As shown in Figure 3-63 the maximum value is equals to 63 W and corresponds to an element whose area is 1.06×10^{-5} m^2. The heat flux is thus 5.9 MW/m^2, well below all the calculated CHF.

Even though an appropriate corrective factor C_f has not been found in literature, for hypervapotron geometry with peaked power density profiles it is expected that the CHF will be higher compared to smooth tube or uniform power profile. The calculated values with C_f=1.2 can be considered as a first rough estimation.

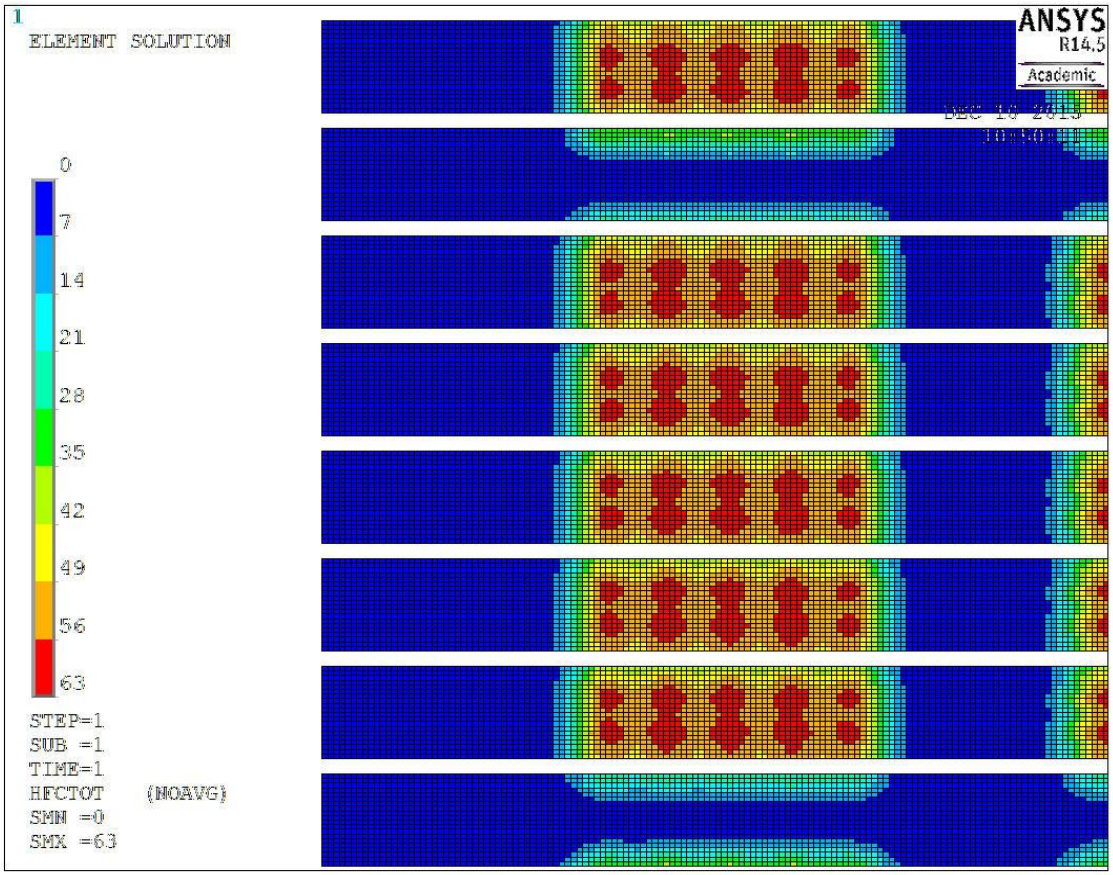

Figure 3-63 **Magnification of the heat flow [W] for the left panel in case of ω_c = 3 mrad and no halo**

Within the scenario in which the power density is the highest (ω_c = 3 mrad and no halo fraction), the corresponding Incident Heat Flux (IHF) has been already shown in Figure 3-19 where the higher value is 8.6 MW/m^2.
A further verification can be done by extrapolating the data presented by Escurbiac regarding the influence of the width in the ICHF [73]. In Figure 3-64 the ICHF as function of the HV width is shown both for uniform and picked profile. For an hypervapotron width of 65 mm is possible to extend these values obtaining 13 MW/m^2 and 20 MW/m^2 as ICHF respectively for uniform and peaked profile. Being the maximum incident heat flux on the SPIDER beam dump of 8.6 MW/m^2 (Figure 3-19) the possibility of reaching the CHF condition is excluded.

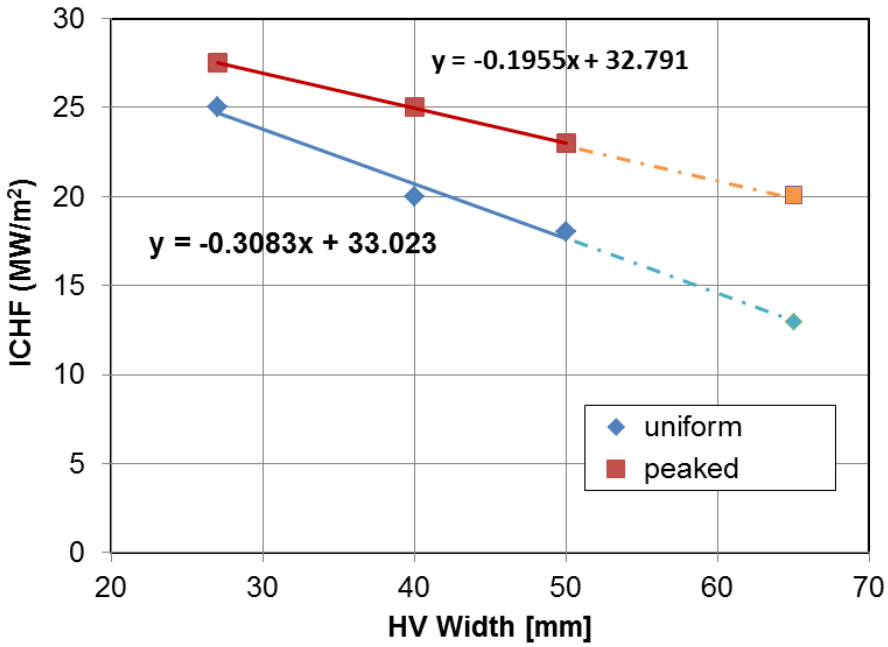

Figure 3-64 **ICHF (MW/m^2) as function of HV width (mm) for uniform and peaked profile (bulk velocity 4 m/s and sub-cooling 120 °C)**

3.7 Validation

The validation of the developed customized ANSYS APDL code has been performed with a comparison to the results obtained at the JET Neutral Beam Test Bed by Falter at al. [34]. The same results have been also used in [32] for the validations of the developed analytical model for hypervapotron performance prediction.

The test section with hypervapotron used at JET Test Bed was 500x27x19 mm^3 (Figure 3-65) with the internal fin structure as detailed in Table 3-8.

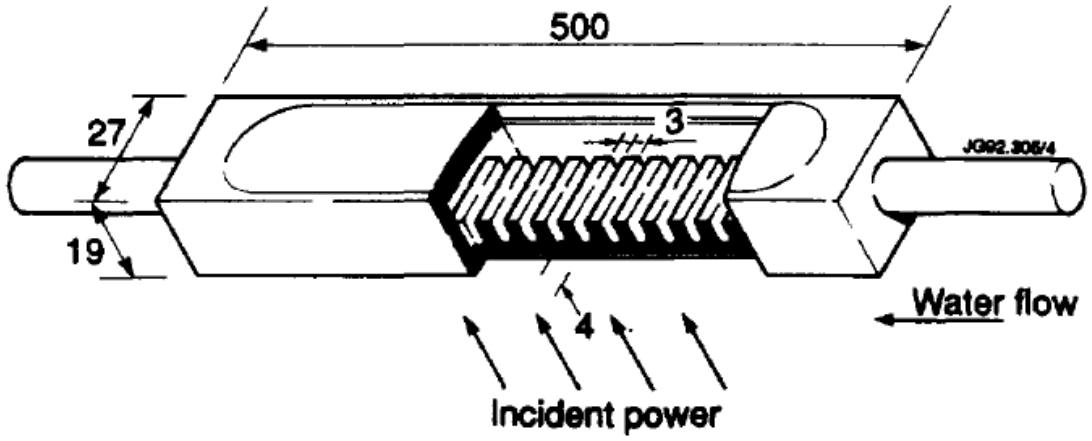

Figure 3-65 Hypervapotron test section for the JET Test Bed [34]

Table 3-8 Hypervapotron internal fin structure dimensions [34]

Fin height	4 mm
Fin width	3 mm
Groove between fins	3 mm
Water channel height	3 mm

The same geometry has been replicated in ANSYS APDL and the analyses carried out with the following boundary conditions:

- inlet mass flow rate: 0.54 kg/s;
- inlet temperature of the coolant: 20 °C;
- outlet pressure: 0.6 MPa.

In [34] is not clearly defined the shape of the beam profile which gives the power density on the hypervapotron surface, but a gaussian shape is declared. The same apparatus is described by Falter in [35], here it is stated that the power density profile is essentially flat across the elements, with a variation over the illuminated 175 mm vertical section of ±15 %.

For the validation, the power densities have been applied in the central part of one side of the hypervapotron model for 175 mm length. The maximum values, corresponding to different experimental parameters from 2.4 to 24.9 MW/m^2, have been imposed in the

centre with a linear reduction up to the 15% at the edges. This linear reduction is an attempt to take into account the total energy of the beam, even if the parameters of the gaussian distribution are unknown. The results of the comparison between the Falter experiment and the FE analyses are listed in Table 3-9 and plotted in Figure 3-66. A good agreement between these analyses and the experimental results has been found: the maximum absolute error is of 14°C at the highest power density, while the maximum percentage error is 14.5 % for the lowest power density.
Falter presented also experimental results for an higher flow rate (0.73 kg/s) but the surface temperatures are about the same for both the cases and the comparison would not add new information.

Figure 3-67 and Figure 3-68 show the contour plot of the temperatures for two different simulations. The maximum surface temperature at the cooling channel wall, located in the centre of the hypervapotron, has been taken for each simulation.

Table 3-9 Comparison of experimental and FE analysis results

Power density [MW/m^2]	Experimental temperature [°C]	FE analysis temperature [°C]	Absolute error [°C]	Percentage error [%]
2.4	55	63	8	14.5
5	110	113	3	2.7
10	220	237	17	7.7
15	310	299	-11	-3.5
20	420	410	-10	-2.4
24.9	550	564	14	2.5

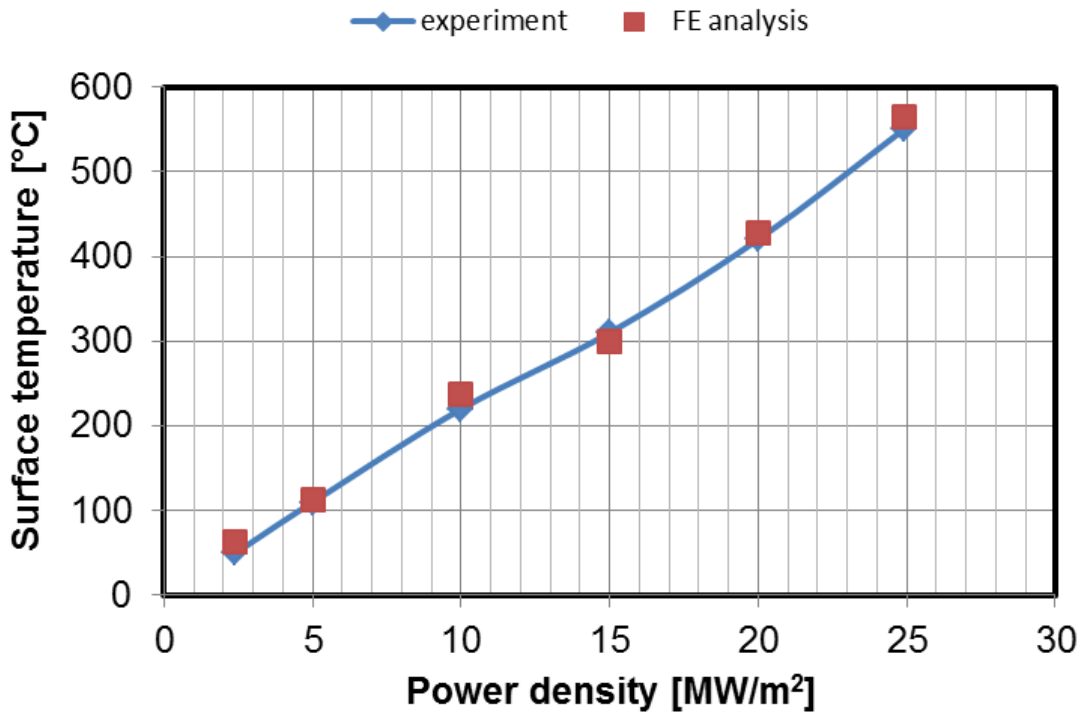

Figure 3-66 Comparison of experimental and FE analysis results

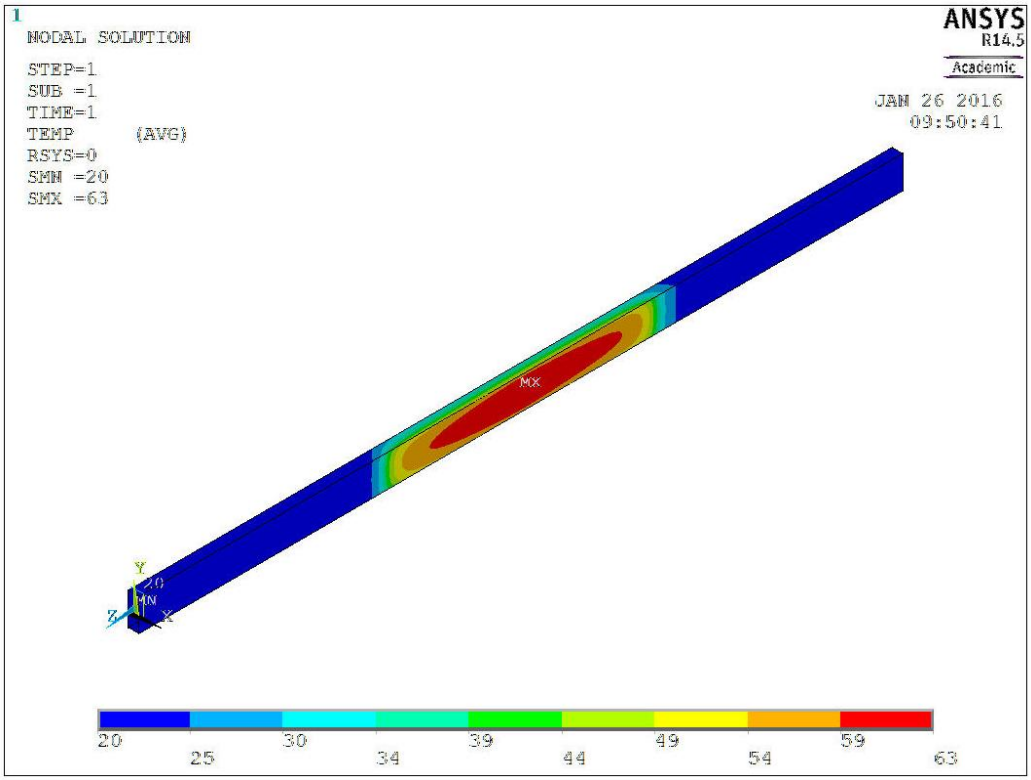

Figure 3-67 **Contour plot of wall temperatures [°C] at the cooling channel for a power density of 2.4 MW/m^2**

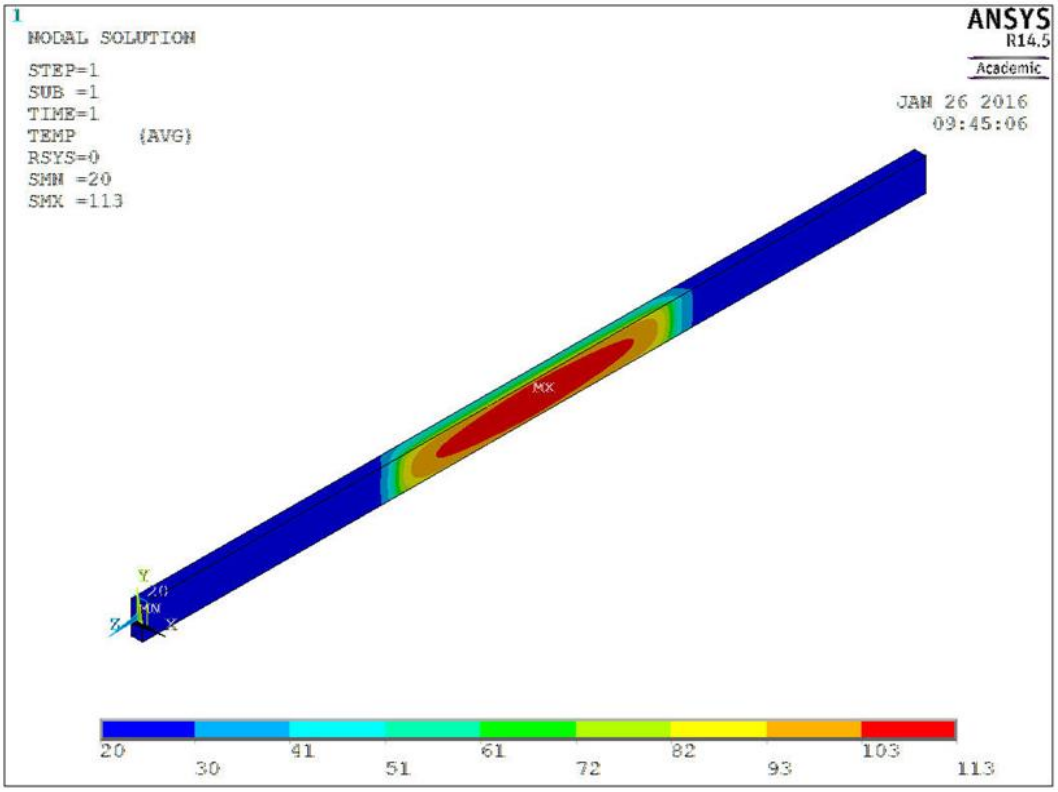

Figure 3-68 **Contour plot of temperatures [°C] at the cooling channel for a power density of 5 MW/m^2**

3.8 Discussion

The SPIDER Beam Dump has been designed to allow two main functions: dumping all the beam power coming from the RF beam source, and measuring the temperatures on the dumping panels for beam diagnostic.

31 hypervapotrons (made of CuCrZr alloy) for each panel constitute the heat transfer elements of the SPIDER beam dump. Here, different heat transfer mechanism can occur simultaneously because of a variation of surface temperature, bulk temperature, and coolant pressure. A FE model has been developed in ANSYS APDL in order to predict the behaviour of the component in different possible scenarios. As the two-phase heat transfer mechanism is not foreseen in the standard library, a customization of the code has been performed by implementing a Fortran routine with suitable thermo-hydraulic correlations and by linking it to ANSYS APDL.

The developed model has been used to carry out several analyses taking into account different beam conditions in terms of divergence, halo fraction and horizontal misalignment. The results show that, by using the thermocouples installed along the hypervapotron and at each outlet pipes, the SPIDER beam dump can be used for beam diagnostic purposes to detect divergence and horizontal misalignment.
In case of 3 mrad of core divergence is possible to recognize the peaks and valleys of temperature caused by the different beamlets, while an almost uniform temperature is produced in the central part of the heated regions for larger beam divergence; moreover the higher the divergence, the higher the temperature at the tails of the beam (a percentage increase of 81% at the first thermocouple has been calculated between the cases with ω_c=7 mrad and ω_c=3 mrad).
The horizontal misalignment can be detected only by looking at the shifted temperature profiles when the beamlets are well focused, while in case of higher divergence also the calorimetric measurements are useful. For instance, an increasing of 43 kW of thermal power is expected on the panel in which the beam is deviated in case of ω_c=7 mrad (with a corresponding reduction of power for the other panel).
The detection of the halo fraction appears hardly appreciable, but not impossible considering that other diagnostics (as tomography and spectroscopy) are foreseen.

The thermo-hydraulic proprieties given by the cooling plant (coolant pressure and inlet temperature), the beam power and its density profile doesn't lead, under normal boundary condition, to boiling heat transfer mechanism, even in the worst condition with well concentrated beamlets.
The capability of the system to withstand the thermal power during a possible flow reduction has been analysed and verified.
Temperature deviation of 6 °C from the average value has been calculated because of the addition material layer used to considered the fins.

The Critical Heat Flux has been analytically calculated with the modified Tong-75 formula by using a corrective factor C_f =1.2 not corresponding to the SPIDER beam dump hypervapotron geometry: 21 MW/m^2 is the calculated CHF with 1 kg/s mass flow, bulk temperature of 85 °C and local pressure of 0.9 MPa. Really poor correlation are available in literature and the results have to be considered as general estimation but,

as the maximum heat flux at the channel is 5.9 MW/m^2, the possibility of reaching the CHF condition is excluded.
The ICHF has been also verified considering experimental measurements and extrapolating data applicable to the present design; also in this case the verification is satisfied, even if with reduced margin of 4.4 MW/m^2 (in the worst hypothesis of uniform power density profile) that is about the 50% of the maximum applied power density.
In the end the validation of the developed code has been presented demonstrating a fitting against experimental results with a maximum error of 14% only at the lowest power density.

Chapter 4
Conclusions and future works

The research activity presented in this thesis work has been carried out in the framework of the development of the negative ion source (SPIDER) and of the full injector prototype of the ITER neutral beam (MITICA).

In fusion machines one of the most challenging issue, from an engineering point of view, is the reliability and thermal control of components faced to the plasma and particle beam. The high heat fluxes and power densities they are subjected to, make the cooling capability of these components one of the crucial aspects during the design phase.
Two main topics have been presented in the thesis: integrated thermo-hydraulic one-dimensional models with 3D sub-modelling of the MITICA beam source and beam line components, and FE model of the SPIDER beam dump.

When working with large and complex cooling pipe circuits, the 1D CFD simulations are the common choice because they act as versatile tools to evaluate the flow partitioning, the coolant temperature along the network and the pressure drop.
Three different models have been separately developed for the MITICA beam source, neutraliser and residual ion dump by using two codes (e.g. Flowmaster and ANSYS APDL). The well-known analytical models of standard elements have been used to simulate parts of the complex injector components while, to fully characterize local effects in the circuits, 3D CFD sub-modelling have been used for custom geometries.
The focus of the analyses have been different.
The model of the beam source have been used mainly to modify the flow partitioning in the entire system. Different design solutions have been explored in order to find the best compromise between flow rates, temperatures and pressure drops. A new cooling system, able to guarantee the correct flow in almost all the elements, has been proposed and adopted to be realised in the components under procurement. The new design guarantees the correct flow rate in all the component except to the PDP#1, PDP#2, PDP#3 and PDP#4 for whom the water flowing in the channels is about 40% less than the desired value. The differences with the previous solution are a parallel connection of the plasma driver plate channels, a reduction of the pipe and manifold diameters of the extraction grid and the insertion of localised pressure drops at the faraday shield lateral wall and extraction grid outlet.
The neutraliser cooling circuit has been modelled in particular to predict the outlet temperature at the most heated elements. The analysis results have been used to undertake the PED hazard classification for the MITICA Beam Line Components (BLCs). With 55 kg/s as inlet mass flow rate, the maximum temperatures are 103 °C for the panels and 120 ° for the LEEs: the CE marking of each BLC is not required as the belong to the PED category SEP meaning that they have to be designed by applying the Sound Engineering Practice.
The residual ion dump cooling circuit has been also modelled considering different designs: a balanced solution with the same tape thickness for all the swirl channels that

constitute the BSEs and a configuration with a reduced tape thickness where the expected heat loads are higher. The second design has been adopted considering the higher boiling margin in the middle panels, from 35 to 60 °C. Detailed 3D CFD analyses of a swirl channel have been carried out in order to define the main boundary conditions of the draining and dry procedure which requires Nitrogen gas with at least a minimum velocity of 30 m/s at the inlet.
The 1D models are available at Consorzio RFX for further improvements and possible modifications. Experimental comparison will be performed once MITICA will be operative. Models can be used especially during the first experimental campaigns when off-normal experimental conditions can be recognised among simulated scenarios, or un-predicted and unexpected conditions can be further simulated. The research activity has been published in [74].

The second part of the thesis has been dedicated to the SPIDER beam dump for which a FE model has been developed by using ANSYS APDL.
A programmable routine for the calculation of the local heat transfer coefficients in sub-cooled nucleate boiling conditions has been wrote in Fortran and linked to ANSYS code. Suitable heat transfer and pressure drop correlations have been implemented in the routine in order to allow coupled thermo-hydraulic analyses for hypervapotron geometries.
The customization of ANSYS APDL represents a new tool that could be used to perform simulations in two-phase heat transfer conditions for several high heat flux elements (like plasma and beam facing components) eventually with minor modifications of the correlations in case of different cooling channel geometry (for instance in case of swirl tubes).
The FE model of the SPIDER beam dump has been used to predict for the first time the temperature measurements at the thermocouple positions under different beam scenarios verifying the possibility to use the beam dump not only to remove the incident thermal power but also to characterize the beam.
Encouraging results have been obtained in diagnosing the beamlet core divergence and the horizontal misalignment. The detection of the halo fraction is rather difficult but not impossible together with the other diagnostics like tomography and spectroscopy.
A scenario with a reduced flow rate has been analysed in order to prove the ability of the beam dump to withstand higher temperature working in a fully developed boiling regime.
Scares data are available in literature for hypervapotron configuration, in particular, even if several experimental investigations have been carried out, general correlations with a wide range of validity in terms of thermodynamic proprieties and geometry are really few. The major difficulties have been encountered in the calculation of the critical heat flux for which an appropriate formula has not been found therefore its prediction has been performed following a general procedure which ensure, however, an higher safety margin. The ICHF has been also verified considering experimental measurements and extrapolating data applicable to the present design: the verification is also in this case satisfied, with a margin of 4.4 MW/m^2 (in the worst hypothesis of uniform power density profile) that is about the 50% of the maximum applied power density.

The developed customized code is fully parametric and it allow analyses on hypervapotrons with different dimensions, thus the validation has been performed comparing the obtained results at the JET Neutral Beam Test Bed facility, demonstrating a fitting against experimental results with a maximum error of 14% only at the lowest power density.
Further works is planned to extend the analyses on a wide range of beam parameters.

References

[1] J. Wesson, “Tokamaks”, Third edition, Clarendon Press Oxford, 2004

[2] J. D. Lawson, “Some criteria for a power producing thermonuclear reactor", Proc. Phys. Soc. B, Vol 70, 1957

[3] F. Wagner et al., “Regime of Improved Confinement and High Beta in Neutral-Beam-Heated Divertor Discharges of the ASDEX Tokamak”, Phys. Rev. Lett. 49, p. 1408, 1982

[4] M. Kuriyama, “Operation of the negative-ion based nbi for jt-60u," Fusion Engineering and Design, Vol. 39-40, pp. 115-121, 1998

[5] P. Sonato et al., “The ITER full size plasma source device design”, Fusion Eng. Des. 84, 269 (2009)

[6] I.G. Brown, “The physics and technology of ion sources”, Wiley-VCH Verlag GmbH & Co., Weinheim (2004)

[7] P. Sonato et al., “Design of the MITICA neutral beam injector: from physics analysis to engineering design”, Proc. 24th IAEA Fus. En. Conf., IAEA, San Diego, USA (2012)

[8] D. Marcuzzi, et al., “Detail design of the beam source for the SPIDER experiment”, Fusion Engineering and Design 85 (2010)

[9] F. Fellin et al., “Proposal of cooling plant, for SPIDER and MITICA experiments”, Fusion Engineering and Design 86 (2011)

[10] PRIMA Cooling Plant Technical Specification, Annex B

[11] Flowmaster, https://www.mentor.com/products/mechanical/flowmaster/

[12] ANSYS Mechanical APDL Tutorials, Release 14.5, ANSYS Inc.

[13] ANSYS Workbench Help, Release 14.5, ANSYS Inc.

[14] D. S. Miller, “Internal flow systems”, BHRA Fluid Engineering, Second edition, 1990

[15] P. Zaccaria et al., ”Progress in the MITICA beam source design”, Rev Sci Instrum. 2012 Feb;83(2):02B108

[16] P. Agostinetti et al., “Design of a low voltage, high current extraction system for the ITER Ion Source”, AIP Proc. 1st Int. Conf. Neg. Ions, Beams and Sources, 1097 (2008) 325-334

[17] LT Calcoli, “Plasma Driver Plate design analyses for the MITICA Beam Source”, Progress meeting Wk06, internal communication

[18] LT Calcoli, “Plasma Driver Plate (PDP): Hydraulic, thermal and structural analyses report”, internal communication

[19] LT Calcoli, “Source Case Lateral Wall”, Progress meeting Wk08, internal communication

[20] Analyses Report of the Faraday Shield Lateral Wall, RFX document ID: RFX-MITICA-TN-176 revision 0 of December the 21st 2012

[21] Analyses Report of the faraday Shield Back Plate, RFX document ID: RFX-MITICA-TN-175 revision 2 of January the 8th 2014

[22] Electromagnetic studies on the RF driver – Modelling and experimental benchmarking, RFX document ID: RFX-SPIDER-TN-030

[23] Single beamlet optics studies and function optimization of the MITICA accelerator, RFX document ID: RFX-MITICA.TN-270 revision 2 of January the 8th 2015
[24] Analyses Report supporting the Design of the MITICA Beam Source, RFX document ID: RFX_MITICA_TN_148 revision 3 of December the 16th 2014
[25] M. Dalla Palma et al., "Design and R&D for manufactoring the MITICA Neutraliser and Electron Dump", Fus. Eng. Design 88 (2013) 1020-1024
[26] Identification of the Most Heated Elements of the Neutraliser and Electron Dump, RFX document ID: RFX-MITICA-TN-121 revision 1 of December the 23rd 2011
[27] Data, Codes, and Criteria used for the analyses and verification of the Neutraliser and Electron Dump, RFX document ID: RFX-MITICA-TN-132 revision 1 of December the 23rd 2011
[28] Matlab documentation, http://it.mathworks.com/help/matlab/
[29] C.F. Colebrook and C.M. White, "Fluid friction in roughened pipes", Proceeding of the Royal Society of London, 1937, 161A:367-381
[30] BTR results of power deposition on the ERID, 07 Apr 2014, ITER IDM ref: N9Y97C v1.0
[31] C. Rotti et al. "Design of Beam Dump for SPIDER facility", Proceeding of 25th Symposium on Fusion Engineering (SOFE), 2013, IEEE
[32] C. B. Baxi and H. Falter, "A model for analytical performance prediction of hypervapotron", Fifth International Topical Meeting on Nuclear Reactor Thermal Hydraulics, 1992, Salt Like City (Utah, USA)
[33] W.M. Rosenow at al., "Handbook of Heat Transfer Fundamentals", McGraw-Hill Book Co., New York, 1983
[34] H. Falter et al., "Thermal Test Results of the JET Divertor Plate", High Heat Flux Engineering (SPIE Proceeding) Vol. 1739 (1992)
[35] H. Falter et al., "Power loading tests of the JET pumped divertor plates", Fusion Technology 1990
[36] Y.Y. Hse and R. W. Graham, "An Analytical and Experimental Study of the Thermal Boundary Layer and Equilibrium Cycle in Nucleate Boiling", NASA TN-D-594, 1961
[37] A.E. Bergles and W.M. Rohsenow, "The Determination of Forced-Convection Surface-Boiling Heat Transfer", Journal of Heat Transfer 86(3), 365-372, 1964
[38] V. Prodanovic, D. Fraser and M. Salcudean, "On the transition from partial to fully developed subcooled flow boiling", Int. Journal of Heat and Mass Transfer, 45 (2002) 4727-4738
[39] G. Guglielmini, E. Nannei and C. Pisoni, "Survey of Heat Transfer Correlations in Forced Convection Boiling", Wärme- und Stoffübertragung 13 (1980) 177-185
[40] Psychometric Data, ASAE D271.2 DEC94
[41] J.R.S. Thom, W. M. Walker, T. A. Fallon and G. F. S. Reising, "Boiling in Subcooled Water During Flow up Heated Tubes or Annuli", Presented at the Symposium on Boiling Heat Transfer in Steam Generating Units and Heat Exchangers, Manchester, 1965.

[42] J. Boscary, “Transfert thermique et flux critique dans un écoulement hélicoïdal en tube chauffé asymétriquement”, PhD Thesis, 1997
[43] J. Boscary, M. Araki, J. Schlosser, M. Akiba and F. Escourbiac, “Dimensional analysis of critical heat flux in subcooled water flow under one-side heating conditions for fusion”, Fusion Engineering and Design 43 (1998)
[44] W. H. McAdams et al., “Heat Transfer at High Rates to Water With Surface Boiling”, Industrial and Engineering Chemistry, Vol. 41, 1949, pp. 1945-1953
[45] S. S. Kutateladze, “Boiling heat Transfer”, Int. J. Heat Mass Transfer, Vol. 4, 1961, pp. 31-45
[46] W. M. Rohsenow, “Heat Transfer With Evaporation”, Chapter in Heat Transfer, University of Michigan Press, 1953
[47] K. Engelberg-Forster and R. Greif, “Heat Transfer to a Boiling Liquid-Mechanism and Correlations”, Journal of Heat Transfer, Trans. ASME, Series C. Vol. 81, 1959, pp. 43-53
[48] S. H. Chang, Y. H. Jeong and B. S. Shin, “Critical Heat Flux Enhancement”, Nuclear Engineering and Technology, Vol. 38 N. 8, 2006
[49] F. E. Tippets, “Critical Heat Fluxes and Flow Patterns in High-Pressure Boiling Water Flows”, International Journal of Heat Transfer, 1964, pp. 12-22
[50] A. R. Raffray, J. Schlosser, M. Akiba, et al., “Critical heat flux analysis and R&D for the design of the ITER divertor”, Fusion Engineering and Design 45 (1999) 377-407
[51] L. S. Tong, “A phenomenological study of critical heat flux”, ASME paper, 75-HT-68
[52] J. Schlosser, J. Boscary, F. Escourbiac, et al., ”Thermal hydraulic design of high heat flux elements for controlled fusion”, Proceedings of the 15th UIT National Heat Transfer Conference, 1997, pp. 45–59
[53] J. Schlosser and J. Boscary, “Thermal hydraulic tests at NET: ITER relevant conditions on divertor targets using swirl tubes”, NURETH 6, 1993, pp. 815–824
[54] A. Cardella, G. P. Celata and G. P. Gaspari, “Tests on the hypervapotron cooling technique for divertor application”, Fusion Technology 1990, p. 391-395
[55] A. Cardella, G. P. Celata, G. P. Gaspari, “Heat transfer and burnout at high fluxes in subcooled water”, Internation Conference on Multiphase Flow, Japan, 1991
[56] G. Cattadori et al., “Visualization of hypervapotron effect”, presented at 2nd Specialists WS on fusion thermal hydraulics, 1992
[57] D. Diremeyer, “Hypervapotron flow testing with rapid prototype modelling”, Proceedings of the 16th IEEE/NPSS Symposium on Fusion Engineering, University of Illinois (1995)
[58] C. B. Baxi, “Comparison of Swirl Tube and Hypervapotron for Cooling of ITER Divertor”, Proceedings of the 16th IEEE/NPSS Symposium on Fusion Engineering, University of Illinois (1995), pp. 186–189
[59] P. Veltri et al., “Transmission of electrons inside the cryogenic pumps of ITER Neutral Beam Injector”, Fusion Eng. Des. 88 , 1011–1014 (2013)

[60] ITER Design Description Document (WBS 5.3), Appendix 2: Beam Alignment and Transmission
[61] NIST National Institute of Standards and Technology, http://www.nist.gov/
[62] ITER Material Properties Handbook, ITER Document No. G 74 MA 16
[63] Manuale d'ausilio alla progettazione termotecnica, AICARR, 2010, Padova
[64] Beam Cycles, MIT-TQU-010, total number of pulses and pulse duration foreseen at the SPIDER and MITICA test beds, ITER IDM reference: 3R8E79 v1.0
[65] ITER Design Description Document (WBS 5.3), Appendix 4
[66] J. Milnes, Use of hypervapotrons within a magnetic ion removal system for ITER NB, MRID Hypervapotron Task Deliverable: 3.1.4.5
[67] J.D. Le Franc, H. Bruchner, P. Domenjoud, R. Morin, "Improvements made to the thermal transfer of fuel elements by using the vapotron process", Presented at 3rd International Conference on Peaceful Uses of Atomic Energy, 1964
[68] H.D. Falter and E. Thompson, "Performance of hypervapotron beam stopping elements at JET", Fusion Technology 29 (1996)
[69] H.D. Falter at al., "Vapotron as heat sink for flat high-conductivity unidirectional carbon-fiber-composite tiles", Fusion Technology 29 (1996)
[70] G. Cattadori, G.P. Gaspari, G.P. Celata, M. Cumo, at al., "Hypervapotron technique in subcooled flow boiling CHF", Experimental Thermal and Fluid Science (7), 1993, p. 230–240
[71] A. E. Bergles, "Burnout in Boiling Heat Transfer", Part. II: Sub-cooled and Low-Quality Forced Convection Systems, Nucl. Safety 18 (2), 154-167, 1977
[72] I. Smid, J. Schlosser, J. Boscary, F. Escourbiac and G. Vieider, "Comparison between various thermal hydraulic tube concepts for the ITER divertor", 1996, Fusion Technology, p. 263-266
[73] F. Escurbiac, "High heat flux and critical heat flux (CHF) tests in support to ITER HHFC", Int. HHFC Workshop, Dec. 10-12 2008, UCSD, CA
[74] M. Zaupa et al., "Steady state thermal-hydraulic analyses of the MITICA cooling circuits", Rev. Sci. Instrum. 87, 02B323 (2016)

Acknowledgements

I gratefully acknowledge the staff of Consorzio RFX, in particular the “Ingegneria del Plasma” group and NBI group. I would like to express my gratitude to Mauro Dalla Palma, Francesco Fellin, Simone Peruzzo and Emanuele Sartori for their support and availability in these three years.
Special thanks to my family.

Matteo Zaupa

Padova, 31/01/2016